Technische Universität München

TECHNISCHE UNIVERSITÄT MÜNCHEN
TUM School of Natural Sciences

Effective field theory treatment of dark matter pairs evolving as an open quantum system in a dark thermal environment

Gramos Qerimi

Vollständiger Abdruck der von der TUM School of Natural Sciences der Technischen Universität München zur Erlangung des akademischen Grades eines

Doktors der Naturwissenschaften (Dr. rer. nat.)

genehmigten Dissertation.

Vorsitz:		Prof. Dr. Elisa Resconi
Prüfer der Dissertation:	1.	Prof. Dr. Antonio Vairo
	2.	Prof. Dr. Alejandro Ibarra

Die Dissertation wurde am 15.01.2025 bei der Technischen Universität München eingereicht und durch die TUM School of Natural Sciences am 30.01.2025 angenommen.

Zusammenfassung

Der thermische Freeze-out Effekt der dunklen Materie im frühen Universum gehört zu einer der am weitverbreitetsten Mechanismen, die darauf abzielen, eine natürliche Begründung für die experimentell beobachtete Reliktdichte der dunklen Materie zu geben. Diese Arbeit widmet sich der theoretischen Studie zur chemischen Entkopplung schwerer nichtrelativistischer dunkler Materie und der anschließenden zeitlichen Entwicklung in einem expandierenden thermischen Milieu, welches den dunklen Sektor des Universums in seinen frühen Stadien abbildet. Insbesondere bedienen wir uns der Methoden der effektiven Quantenfeldtheorien bei endlicher Temperatur, um die relevanten thermischen Wechselwirkungsraten und die entsprechenden Raten im Vakuum innerhalb bestimmter Hierarchien von Energieskalen zu identifizieren und zu berechnen. Wir ermitteln die entsprechenden Observablen in verschiedenen Bezugssystemen in rigoroser Weise und heben die Genauigkeit der erhaltenen Ergebnisse hervor, welches von größter Bedeutung für eine präzise Bestimmung der gegenwärtigen Energiedichte der dunklen Materie ist. Diese Raten sind die Schlüsselkomponenten in den Evolutionsgleichungen, die die chemische Entkopplung verursachen aber auch das numerische Ergebnis der Ausbeute an dunkler Materie stark beeinflussen. Unser Ziel ist es daher, eine umfassende Forschung verschiedener Beiträge wie des Rückstoßeffekts des Massenschwerpunkts oder des Debye-Masseneffekts zu liefern und jeden von ihnen entsprechend seiner Bedeutsamkeit für die kosmische Reliktdichte miteinander zu vergleichen. Wir leiten die Quanten-Mastergleichungen für den reduzierten Dichteoperator bezüglich Paaren von dunkler Materie mit Hilfe der Konzepte offener Quantensysteme her und analysieren den semiklassischen Grenzwert, der schließlich zu den phänomenologisch gut etablierten Boltzmann-Gleichungen führt, und gewinnen auf diese Weise ein tieferes Verständnis der zugrundeliegenden Näherungen und den darausfolgenden Verlust von gewissen Quanteneffekten, die jenseits des Bereichs der semiklassischen Behandlung des dunkle-Materie-Systems liegen.

Abstract

The thermal freeze-out effect of dark matter in the early universe is one of the most prominent mechanisms that aims to come up with a natural answer for the experimentally observed dark matter relic abundance. This thesis is devoted to the theoretical study of the chemical decoupling of heavy non-relativistic dark matter states and its subsequent time evolution within an expanding thermal environment modeling the dark sector of the universe in its early stages. In particular, we scrutinize the methods of effective quantum field theories at finite temperature in order to identify and compute in a systematic manner the relevant thermal and in-vacuum interaction rates within specific hierarchies of energy scales. We calculate the corresponding observables in different reference frames in a rigorous way and highlight the accuracy of the obtained results that is of paramount importance for a precise determination of the present dark matter energy density. Those rates are the key ingredients entering the evolution equations

which induce the chemical freeze-out but also strongly affect the numerical outcome of the dark matter yield. Our aim therefore is to provide a comprehensive study of various contributions, like the center-of-mass recoil effect or the Debye-mass effect, and compare for each of them the corresponding impact on the cosmic relic abundance. We derive the quantum master equations for the reduced density operator of dark matter pairs using the concepts of open quantum systems and analyze the semi-classical limit leading ultimately to the phenomenologically well-established Boltzmann equations, in this way gaining a deeper understanding of the underlying approximations and the consequent disappearance of certain quantum effects, that are beyond the realm of a semi-classical treatment of the dark matter system.

Contents

Part I

Introduction

Chapter 1

The fate of dark matter in the early universe

In the field of cosmology and particle physics, the concept of dark matter (DM) stands as one of the most intriguing and compelling mysteries. Despite its invisible nature, the profound influence of dark matter on the large-scale structure and dynamics of the universe is unmistakable: from experimental observations it turns out that about 80% of the matter in the universe is unknown and hence can be characterized as DM affecting ordinary matter from the Standard Model (SM) via gravitation. A significant effort within theory and experiment is directed towards uncovering the identity and properties of this elusive substance. Among the various hypotheses seeking to explain the nature of dark matter [1–7], the notion of a thermal particle-like dark matter holds particular prominence. Within a theoretical framework it is assumed that dark matter particles were once in thermal equilibrium with the primordial plasma during the early stages of the universe's evolution. Due to the spatial expansion of the thermal plasma and its subsequent cooling, the dark matter underwent a phase transition via the chemical decoupling from the thermal bath and therefore freezed out retaining a steady relic abundance that ultimately shapes the cosmological landscape. The most accurate determination for the dark matter energy density at present day is provided by anisotropies in the *cosmic microwave background* (CMB) and amounts to $\Omega_{\mathrm{DM}}h^2 = 0.1200 \pm 0.0012$ [8], where h is the reduced Hubble constant.

The *thermal freeze-out* mechanism has been widely adopted to infer the present-day relic abundance of a DM candidate, and many models have been developed that introduce a new dark degree of freedom beyond the known particles of the SM, which undergoes the freeze-out. We refer the reader to some extensive reviews, e.g. refs. [9,10]. The various models have usually the following paradigm in common: Assuming a dark heavy particle X of large mass M, its chemical freeze-out, usually induced by dark matter annihilation processes, occurs once the temperature T of the thermal bath drops below $\approx M/25$. Hence, since $T \ll M$ at freeze-out and thereafter, the dark particle can be considered to evolve *non-relativistically*, which calls for the exploitation of the *effective field theory* (EFT) formalism within the concept of quantum field theories (QFTs)

in particle physics. Non-relativistic and potential non-relativistic effective field theories, dubbed as NREFTs and pNREFTs, respectively, can be adopted for a systematic description of the non-relativistic dark matter dynamics in the expanding thermal bath, by isolating and emphasizing the relevant physical events at each temperature stage (i.e. time period) in a consistent way [11]. Under the condition that the intrinsic and extrinsic energy scales, or at least a few of them, can be hierarchically ordered, EFT techniques allow one to effectively disentangle the contribution from each scale and highlight its range of validity. The better the scale separation, the better the EFT predictions. As mentioned above, in most of the models proposing the thermal DM freeze-out as a viable explanation for the observed DM abundance, the scale arrangement $M \gg T$ follows necessarily. If we consider more specific theories, where the dark particles interact via long-range mediators (either with the SM bath or with themselves, [12–14]) with a weak coupling α, then many more energy scales will appear due the combination of M or T and α. But M and T can produce another scale as well, as we will see in the following. Despite chemical equilibrium is lost at the freeze-out regime, kinetic equilibrium is usually assumed to be kept for longer since dark matter is yet embedded as an ingredient in the hot thermal medium, which means that the momenta $\boldsymbol{p}_X$ of the dark particles follow a thermal distribution. This is quite often a key assumption within practical phenomenological applications, in order to be able to write down integrated Boltzmann equations (as particularly simplified evolution equations) for the DM number density. They can be solved numerically and hence enable one to obtain a first theoretical estimate of the relic abundance associated to the underlying dark matter model [15–45]; allowing one to link the particle model parameters, such as couplings and the DM mass, with the observed relic density, or possibly rule out the model under study. Under the assumption of kinetic equilibrium, thermalized heavy particles have a kinetic energy of the order of the bath temperature, hence the modulus of the particle momentum scales as $|\boldsymbol{p}_X| \sim \sqrt{MT}$. Such a scale is much larger than the temperature around and after the freeze-out, $\sqrt{MT} = T\sqrt{M/T} \gg T$ for $M \gg T$, and at the same time it is much smaller than M, $\sqrt{MT} = M\sqrt{T/M} \ll M$ for $M \gg T$. The emergence of the scale $\sqrt{MT}$ out of an intrinsic hard scale M and a thermal scale T is a peculiar property for thermalized dark matter. Typically in heavy quark or quarkonium physics, the heavy quarks or the heavy quarkonium produced in a quark-gluon plasma (QGP) may be treated as external probes, which are indeed not, or just partly, thermalized with the plasma constituents. In such a scenario, the momentum can be taken to be of the order of the thermal scale T, as opposed to $\sqrt{MT}$ that is induced by kinetic equilibrium. In any case, we presume that any physical model may have several emergent energy scales, perhaps hidden at first sight, that need to be taken into consideration when exploiting the EFT framework.

The discussion so far shall give the reader a first glimpse of what this work will be build on: After choosing a specific model of interest, the first step consists of identifying the energy scales of the physical system and exploring if the scales do arrange in a hierarchical order during the passing of time around and after the freeze-out. If so, we will construct the (p)NREFTs to the associated model, that will effectively describe the dynamics of the relevant degrees of freedom. We will determine the power counting of

the effective interactions and compute the relevant thermal rates underlining the level of accuracy. The ultimate goal is to analyze its effects on the dark matter relic abundance. In particular, this work is divided into several parts: We begin with a more precise specification of the freeze-out mechanism that sets the present relic density of dark matter (sec. 2). We consider as a particular example the dark U(1) model that features the freeze-out effect, classify the internal and thermal scales and the associated hierarchical ordering among them [46–49], construct the appropriate EFTs at finite temperature (sec. 3–4), and compute systematically the in-vacuum and thermal interaction rates (sec. 5–6) that are the necessary ingredients for an accurate theoretical determination of the relic abundance via semi-classical Boltzmann equations (sec. 7). We also inspect the relative impact of the several processes and its contributions with respect to the present dark matter energy density. In the sections 8–10, we reiterate the computation, however in a purely dark SU(N) theory at finite temperature [50], in order to compare possible differences in the results to the abelian analogue. The sections 11–13 are devoted to an out-of-equilibrium study of the dark matter evolution in terms of a reduced density operator within the framework of open quantum systems (OQS), in this way gaining a more thorough theoretical picture of the dark quantum system and providing a better understanding and control of the underlying assumptions that need to be taken into account in order to justify the semi-classical treatment of the dark matter dynamics. In the appendices A–F we provide diverse complementing material that is used throughout the main body of this work. Finally, conclusions and outlook are in chapter VI.

This thesis is partly based on previously published articles in [51, 52], conference proceedings [53, 54], and recent work that is under preparation for publication [55].

Chapter 2

Thermal freeze-out mechanism

The thermal freeze-out of dark matter, a conceptual phenomenon belonging to the intersection field between cosmology, i.e. physics at the largest observable length scales, and particle physics, i.e. physics at distances below the subatomic range, can be characterized by a time phase where thermal dark matter, hypothesized to be particle-like, decouples from the residual hot thermal bath that models the early stages of the primordial universe. Hence, it freezes out. The rest of the thermal bath, to which the dark matter particles cease to interact, can be classified as the ordinary baryonic matter built up by the fundamental degrees of freedom from the Standard Model, but it can also constitute other, yet unknown, components such as dark radiation or other dark particles, which have comparatively smaller masses than the dark matter particle that decouples. In this sense we distinguish the dark matter, which undergoes the freeze-out process, from the residual dark degrees of freedom by its much heavier mass M; we call it the *heavy* dark matter, the others the *light* dark particles of mass $m_i \ll M$, where the index i denotes the different species in case there are more than one.[1]

In order for the heavy dark matter subsystem to deviate from its thermal equilibrium state, the underlying interactions with the thermal bath need to go out-of-equilibrium, such that an initial detailed balance situation, among processes that change the dark matter particle number, is lost. In the models that we scrutinize in this work, those number-changing processes are the annihilation (creation) of heavy dark matter into (from) the dark light constituents. Since the universe expands in space and time and it consequently cools down, the initial symmetry between the reaction rates of the forward (annihilation) process and reverse (creation) process breaks down. By thermal freeze-out we thus understand the chemical freeze-out of dark matter, while it is still in kinetic equilibrium with the bath, where the particle momenta are distributed according to a time-independent phase space density function. All the other bath particles, both from the Standard Model sector as well as the dark sector, stay in chemical and kinetic equilibrium throughout the freeze-out period and for long times afterwards. The early

[1] In this work, we will encounter both situations where $m_i \neq 0$ and $m_i = 0$. The latter will correspond to dark radiation, for instance dark photons. As for the heavy DM particle, we will consider masses of around $M \sim$ TeV.

expanding universe drives the thermal heavy DM system into a non-equilibrium state, reducing the interaction rate for the creation of the heavy DM particle below the expansion rate. This happens to be the case as soon as the temperature of the universe drops below the rest mass of the heavy dark matter, $T \lesssim M$, such that it cannot be produced anymore, while the annihilations can still happen.[2] Hence, the thermal freeze-out happens at some critical time, the freeze-out time $t_{\rm F}$, that can be related to the freeze-out temperature $T_{\rm F}$, at which the creation process becomes ineffective.

Similarly as in the heavy ion collisions, where the temperature evolution of the quark-gluon plasma is modeled as an expanding medium that progressively cools down, for the thermal environment that models the early universe, the temperature evolution is determined by the expansion rate of the universe, namely the Hubble rate. In the Standard Model of cosmology, the Lambda-CDM model with a Friedmann-Lemaître-Robertson-Walker (FLRW) metric, it is defined as $H = \dot{a}(t)/a(t)$, where a is time-dependent scale factor. The equation that relates time with temperature can be obtained by combining the concepts of general relativity and thermodynamics. Assuming a flat universe, where the curvature κ is put to zero in the FLRW metric, one finds [56]

$$\frac{dT}{dt} = -\frac{\sqrt{24\pi}}{M_{\rm Pl}} \frac{s(T)}{c(T)} \sqrt{\rho(T)}\,, \tag{2.1}$$

where $s(T)$, $\rho(T)$ and $c(T) = T(ds/dT)$ are the entropy density, energy density and heat capacity, respectively, and $M_{\rm Pl} \approx 1.22 \times 10^{19}$ GeV is the Planck mass. It is convenient to determine the speed of sound $c_s(T)$ in order to derive a more compact form for the time dependence of the temperature,

$$c_s^2(T) = \frac{\partial p}{\partial \rho} = \frac{s(T)}{c(T)}\,. \tag{2.2}$$

where p is the pressure in the bath, related to ρ and s via the thermodynamic equation $p = Ts - \rho$.[3] Since the freeze-out is certainly happening during the radiation dominated epoch for large $M \sim$ TeV, it follows that $c_s^2 \approx 1/3$ for the thermal bath,[4] and we can write

$$\frac{dT}{dt} = -T\sqrt{\frac{8\pi}{3}} \frac{3c_s^2(T)}{M_{\rm Pl}} \sqrt{\rho} \approx -TH(T)\,, \tag{2.3}$$

[2]Since $T \lesssim M$, at freeze-out and in the subsequent time evolution, the heavy dark particle is non-relativistic, while all the other particles in the bath are relativistic as long as $T \gg m_i$ or $T \gg m_i^{\rm S.M.}$, where $m_i^{\rm S.M.}$ denotes to the masses of the Standard Model degrees of freedom.

[3]Equation $\rho = Ts - p$ comes from the fundamental thermodynamic relation for quasistatic processes, $E = TS - pV + \mu N$, divided by the volume V and where the last term does not contribute since the chemical potential μ for antiparticles comes with an opposite sign compared to the one for particles. Hence in sum the μN-term cancels out for models with a dark matter-antimatter symmetry.

[4]The Friedmann equation in flat space is given by $H^2 = 8\pi G\rho/3$, where $G = 1/M_{\rm Pl}^2$ is Newton's gravitational constant. In a radiation dominated universe, the energy density is $\rho = g_{\rm eff}(T)\pi^2 T^4/(30)$, the entropy density is $s = h_{\rm eff}(T)2\pi^2 T^3/(45)$ and the heat capacity is $c = i_{\rm eff}(T)2\pi^2 T^3/(15)$, where $g_{\rm eff}, h_{\rm eff}$ are temperature-dependent functions accounting for the number of effective degrees of freedom in the thermal bath that contribute to the energy and entropy, respectively, and $i_{\rm eff} = h_{\rm eff} + T(dh_{\rm eff}/dT)/3$ [57].

where we inserted the Hubble rate

$$H(T) = \sqrt{\frac{8\pi}{3}}\frac{\sqrt{\rho}}{M_{\rm Pl}} \simeq 1.66\sqrt{g_{\rm eff}(T)}\frac{T^2}{M_{\rm Pl}}\,. \tag{2.4}$$

Assuming that $g_{\rm eff}$, $h_{\rm eff}$ and hence also $c_s = [(1/3)\times[1+(T/h_{\rm eff})(dh_{\rm eff}/dT)/3]]^{1/2}$ vary slowly with T,[5] then as a solution to the differential equation (2.3), it follows that the temperature changes with time as[6]

$$T = \sqrt{\frac{T_0^2}{1+2\xi(t-t_0)T_0^2}}\,, \tag{2.5}$$

where $\xi \equiv 1.66 g_{\rm eff}^{1/2}/M_{\rm Pl}$ and t_0, T_0 the integration constants for time and temperature, respectively. Choosing them to be the initial values, then from eq. (2.5) we can verify that at at later times, i.e. $t \gg t_0$, the temperature decreases, i.e. $T < T_0$. Hence, the universe indeed cools down with the passing of time, and by (2.5) we have a one-to-one correspondence between time and temperature. In the main body of this work we will show some numerical results for the interaction rates of interest, plotted as functions of M/T for fixed values of M. These results can straightforwardly be related to as functions over time upon using (2.5), in this way we can always visualize the interaction rates as evolving in time. We remark that, since the temperature scales with time as $T \sim t^{-1/2}$

[5]Since we assume the dark sector to be in thermal equilibrium with the Standard Model sector (or at least in the early stages of the universe evolution), in $g_{\rm eff}$ we need to take into account the relativistic degrees of freedom from both sectors. In case the two sectors were not in thermal equilibrium, and therefore do not necessarily share the same temperature, one would need to take into account only the relativistic degrees of freedom from the dark sector to which the heavy dark matter is coupled. In case of a dark abelian U(1) or non-abelian SU(N) gauge theory, which will be the models of interest in this work, with n_f charged dark light fermions, we have

$$g_{\rm eff}^{\rm U(1)} = 2 + 2\times 2\frac{7}{8}n_f\,,$$

where the dark photon has two physical polarizations and the dark light Dirac fermions get a factor of four accounting for the spin and antiparticle degrees of freedom, and

$$g_{\rm eff}^{\rm SU(N)} = 2\times(N^2-1) + N\times 2\times 2\times\frac{7}{8}n_f\,,$$

where N^2-1 counts the different dark color charges of the dark gauge field in the adjoint representation, and N the dark color charges of the light dark fermions in the fundamental representation.

[6]We can compare the solution (2.5) with Bjorken's result for the temperature evolution of a spatially homogeneous and isotropic thermal medium that extends to infinity and where heavy nuclei collide only centrally [58]:

$$T = T_0\left(\frac{t_0}{t}\right)^{c_s^2}\,,$$

where at high T the speed of sound squared is $c_s^2 \approx 1/3$ in the deconfined plasma. It may give a first qualitatively accurate estimation for the temperature behaviour of the quark-gluon plasma (QGP) with evolving time, at least at zeroth order in the approximations. Since $T \sim t^{-1/3}$, we can justify that the temperature evolution is quasi-static at late times [59].

according to equation (2.5), with increasing time the temperature changes only slowly and therefore, to a certain degree of accuracy, we may neglect the time dependence and the evolution is then called to be *quasistatic* at large t; in agreement with the speed of sound $c_s^2 \approx \sqrt{1/3} < 1$ being subluminal [58, 60].

We turn back to the study of the freeze-out mechanism of the heavy dark particle, where in this work we will consider it to be a Dirac fermion that is charged under an internal gauge group. One can usually inspect the loss of detailed balance between dark matter annihilation and creation processes, which in turn impacts the evolution of the heavy dark matter particle number in the thermal bath, by a rate equation which takes the form of a Boltzmann equation for the particle number density n [57, 61, 62]:[7]

$$(\partial_t + 3H)n = -\frac{1}{2}\langle\sigma_{\rm ann} v_{\rm rel}\rangle(n^2 - n_{\rm eq}^2)\,, \tag{2.6}$$

where $v_{\rm rel} = |\boldsymbol{v}_1 - \boldsymbol{v}_2|$ is the relative velocity of the annihilating pair in the center-of-mass frame and $n_{\rm eq}$ is the number density in thermal, i.e. kinetic and chemical, equilibrium and is given by

$$\begin{aligned} n_{\rm eq} &= 2g_X \int \frac{d^3p}{(2\pi)^3} e^{-E_X/T} = \frac{g_X}{\pi^2} T M^2 K_2\left(\frac{M}{T}\right) \\ &\approx 2g_X \left(\frac{MT}{2\pi}\right)^{3/2} e^{-M/T}\,, \end{aligned} \tag{2.7}$$

where the $g_X = 2$ for the two spin configurations of the fermion. The result in the first line of (2.7) in terms of the modified Bessel function of the second kind, K_2, is for a relativistic particle with energy E_X. For a DM particle of mass M, from the numerical solution of (2.6) and the phase at which n starts to deviate from $n_{\rm eq}$, one can infer that the chemical freeze-out occurs at a temperature $T_{\rm F} \approx M/25$. Therefore, at freeze-out the dark matter particles are *non-relativistic*.[8] We can therefore expand the result in the first line of (2.7) up to leading order in $T \ll M$, which gives the analytic expression in the second line.[9]

It is convenient to recast the Boltzmann equation (2.6) in terms of the yield $Y \equiv n/s$, where its time derivative can be written as

$$\dot{Y} = \frac{\dot{n}}{s} - \frac{n}{s^2}\dot{s} = \frac{\dot{n}}{s} + 3H\frac{n}{s}\,, \tag{2.8}$$

[7] The heavy dark matter number density $n = 2n_X$ is the sum of the particle and antiparticle densities n_X and $n_{\bar{X}}$, respectively, where $n_{\bar{X}} = n_X$ since we do not consider any initial asymmetry between the number of particles and antiparticles. In the case of annihilation of identical particles, e.g. Majorana fermions, the factor 1/2 on the right-hand side of eq. (2.6) should be replaced by 1.

[8] The freeze-out temperature can also be estimated by equating the expansion with the annihilation cross section $H \sim n_{\rm eq}\langle\sigma_{\rm ann} v_{\rm rel}\rangle$, namely $T^2/M_{\rm Pl} \sim \left(\frac{MT}{2\pi}\right)^{3/2} e^{-M/T}\alpha^2/M^2$ where α is some fine structure constant depending on the specific dark matter model.

[9] One can, alternatively, obtain the second line of equation (2.7) by expanding $E_X \approx M + \boldsymbol{p}^2/(2M)$ and performing the Gaussian integral over the particle momentum $\boldsymbol{p}$.

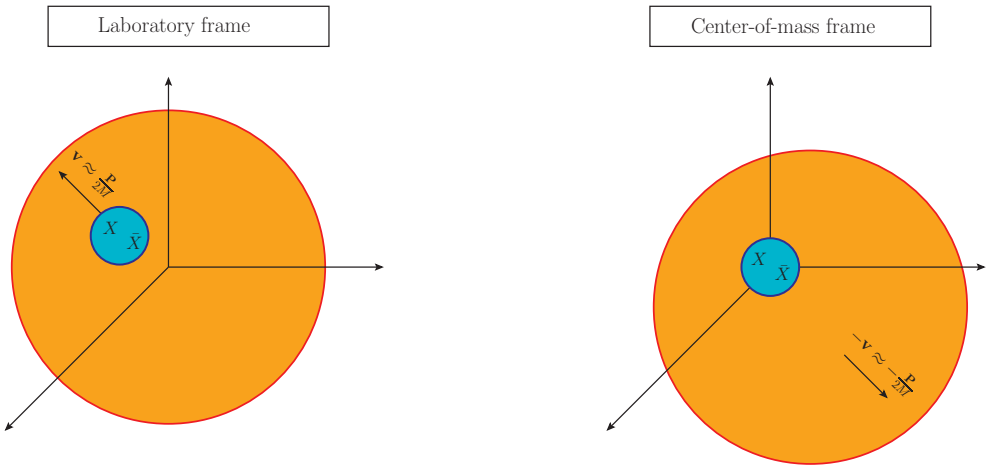

Figure 2.1: Schematic representation of the laboratory frame (left) vs the center-of-mass frame (right). The blue and orange shaded circular areas depict the heavy fermion-antifermion pair and the thermal bath, respectively.

where in the second equality we used the fact that the total entropy per comoving volume $S = a^3 s$ is constant, which gives $\dot{s} = -3Hs$. Dividing eq. (2.6) by the entropy density s, and substituting the time derivative by a derivative over $z \equiv M/T$, we obtain [57]

$$\frac{dY}{dz} = \frac{1}{6H}\frac{ds}{dz}\langle\sigma_{\rm ann} v_{\rm rel}\rangle (Y^2 - Y_{\rm eq}^2)\,, \tag{2.9}$$

where the yield at equilibrium is $Y_{\rm eq} = n_{\rm eq}/s = 45\, g_X z^2 K_2(z)/(4\pi^4 h_{\rm eff})$. Equation (2.9) can be solved numerically up to late times (in particular we solve it up to the smallest temperature value considered in this work: $T = M/10^5$), and the numerical solution of the present DM yield can eventually be related to the present-day relic density of dark matter, $\Omega_{\rm DM} = M s_0 Y_0/\rho_{\rm crit,0}$, where Y_0, s_0 and $\rho_{\rm crit,0}$ denote the present yield, entropy density and critical energy density, respectively.[10] The values for s_0 and $\rho_{\rm crit,0}$ can be taken from e.g. [63, 64], and one obtains $\Omega_{\rm DM}h^2 = (M/{\rm GeV})\, Y_0/(3.645 \times 10^{-9})$, where h is the reduced Hubble constant.

It is crucial to calculate $\langle\sigma_{\rm ann} v_{\rm rel}\rangle$ accurately because the present-day DM energy density $\Omega_{\rm DM}h^2$, as predicted by a given model, depends on it through the solution of eq. (2.9). The DM mass is in turn fixed as a function of the other model parameters to reproduce $\Omega_{\rm DM}h^2$. A solid prediction for DM mass benchmarks compatible with the relic density is needed to establish the viability of models, guide the experimental searches and put DM phenomenology on a sound theoretical ground. In chapters 7 and 10 we

[10] We can assume that the present DM relic abundance is the one of the heavy DM species only, if the other dark degrees of freedom are considered to have negligible rest masses, i.e. $m_i \ll M$, which is the case for the DM theory models considered in this work.

will provide contour plots for the numerical solutions in the parameter space for the exemplary gauge theories $\mathrm{U}(1)_{\mathrm{DM}}$ and $\mathrm{SU}(N)_{\mathrm{DM}}$, respectively. However, determining $\langle\sigma_{\mathrm{ann}}v_{\mathrm{rel}}\rangle$ by including the full features of each model, and the thermal environment, is not straightforward. In the particular models $\mathrm{U}(1)_{\mathrm{DM}}$ or $\mathrm{SU}(N)_{\mathrm{DM}}$ of the dark sector, the charged heavy dark matter particle self-interacts via long-range dark gauge fields. It leads to non-perturbative phenomena such as the Sommerfeld-effect [65, 66], or the formation of heavy dark meta-stable bound states [15, 67], that in turn will impact significantly the annihilation rate $\langle\sigma_{\mathrm{ann}}v_{\mathrm{rel}}\rangle$, extend the usual single evolution equation (2.6) or (2.9) into a network of coupled Boltzmann equations (for more details, see chapter 7), and therefore alter the present relic abundance [68]. By exploiting the methods of effective field theories (EFTs) at finite temperature, we will be able to account for these effects in a systematic manner.

As a final remark, we want to highlight that the rates, for instance the annihilation cross section times relative velocity $\sigma_{\mathrm{ann}}v_{\mathrm{rel}}$ and its thermally averaged version, that enter in the evolution equations for the DM number density, but also the DM energy density itself, are in general frame-dependent, and here written in the center-of-mass frame of the annihilating pair. In a general reference frame, however, the expressions change, e.g. $v_{\mathrm{rel}} \to v_{\mathrm{M\o l}}$, but more on it will come in the subsequent chapters. Hence, one always needs to specify first the particular reference frame for the coordinates, on which the outcomes for the rates or densities are then based. In this work, we will consider two coordinate systems for the annihilating DM particle-antiparticle pair with respect to the thermal environment. We call *laboratory frame* (lab) the reference frame where the thermal bath is at rest. In this case, the center of mass of the fermion-antifermion pair is moving with velocity $\boldsymbol{v} \approx \boldsymbol{P}/(2M)$. The laboratory frame is sometimes also called *cosmic comoving frame*. In addition we are going to consider the aforementioned *center-of-mass frame* of the heavy DM pair, where the thermal bath is moving with velocity about $-\boldsymbol{P}/(2M)$. The center-of-mass and laboratory frame are shown in figure 2.1 for the case of a dark matter fermion-antifermion pair moving in a thermal bath.

Part II

Physical setup: scale hierarchies, tower of EFTs

Chapter 3

$\mathrm{U(1)_{DM}}$: hierarchies of energy scales

There exists a variety of models for the dark sector, that can be classified according to the long-range interactions between bosonic or fermionic heavy dark particles.[1] A particularly simple renormalizable and hence UV-complete model is $\mathrm{U(1)_{DM}}$, i.e. where the dark sector consists of a dark Dirac fermion X of large mass M that is charged under an abelian gauge group [74–78]. We denote the corresponding dark photon with γ. The Lagrangian density reads

$$\mathcal{L}_{\mathrm{U(1)_{DM}}} = \bar{X}(i\not{D} - M)X - \frac{1}{4}F_{\mu\nu}F^{\mu\nu} + \sum_{i=1}^{n_f} \bar{f}_i(i\not{D} - m_i)f_i + \mathcal{L}_{\mathrm{portal}}\,, \tag{3.1}$$

where the covariant derivative is $D_\mu = \partial_\mu + igA_\mu$, with A_μ the dark photon field and $F_{\mu\nu} = \partial_\mu A_\nu - \partial_\nu A_\mu$; we define the fine structure constant as $\alpha \equiv g^2/(4\pi)$. The term $\mathcal{L}_{\mathrm{portal}}$ comprises additional interactions coupling the dark photon with the SM degrees of freedom, for example through a mixing with the neutral components of the SM gauge fields, also called kinetic mixing [79–81]. Such interactions are responsible for the eventual decay of the dark photons, in this way avoiding that their number density dominates the universe at later stages. For the purpose of this work, we do not consider the effect of portal interactions when computing the cross sections and decay widths of dark matter particles, however we still assume they are responsible for keeping the Standard Model and dark sector at the same temperature.[2] From now on we set $\mathcal{L}_{\mathrm{portal}} = 0$. Moreover,

[1] For instance in refs. [69,70] the authors consider different models involving either a scalar or a Dirac fermion field as possible candidates for a heavy dark matter particle, that couples to a massive vector mediator. For a coupling between a fermionic dark particle and a massless or massive scalar mediator, see e.g. ref. [31, 71–73]. In these models the mass of a long-range mediator is usually considered to be generated by the Higgs mechanism of a spontaneously broken gauge theory; otherwise the considered models would be non-renormalizable at large energies.

[2] Since the dark photon acquires a non-vanishing coupling with the Standard Model fermions, the dark and Standard Model sector are maintained in thermal equilibrium through the portal interaction even for very small values of the mixing parameter, see e.g. [14]. In our work, we assume the dark

additional fermionic degees of freedom are coupled to the dark photon. We consider n_f dark light Dirac fields f_i with masses m_i, which can be distinguished from each other by the index i.[3] In practice, when evaluating the self-energy of the dark photon, see appendix D.2, we will put $m_i = 0$ for all the light dark fermions.[4] At temperatures $T \ll M$, they are responsible for quantum corrections to the dark photon propagator, whose pole develops a real and an imaginary part [49, 82, 83].[5] The real part introduces a screening (Debye) mass $m_{\rm D}$ of order gT for the temporal dark photon, whereas the imaginary part of the pole originates from $2 \to 2$ scatterings (i.e. bath-particle scatterings) with plasma constituents, also referred to as Landau damping [20, 22, 23, 27, 29]. There is an additional contribution to the imaginary part due to $1 \to 3$ and the reversed $3 \to 1$ processes, involving an off-shell dark-photon decay into a $f_i - \bar{f}_i$ pair and vice versa. We will cope with these phenomena in the next chapter and in appendix D.2.

The Lagrangian (3.1) describes also processes involving two dark fermions close to threshold, i.e. processes where the fermions are non-relativistic and move with an absolute value of the relative velocity $v_{\rm rel} \ll 1$. For $v_{\rm rel} \sim \alpha$, (ladder) photons exchanged between the pair contribute with a relative factor of order $\alpha/v_{\rm rel} \sim 1$ and need to be resummed. The resummation generates bound-state poles of order $M\alpha^2$ at negative energies and a continuous scattering spectrum at positive energies. The typical momentum exchanged between the pair when $v_{\rm rel} \sim \alpha$ is $M\alpha$, which is of the order of the inverse Bohr radius of the bound state. The dynamically generated scales $M\alpha$ and $M\alpha^2$ are the more separated the smaller α is: $M \gg M\alpha \gg M\alpha^2$. We call them *soft* and *ultrasoft* scales, respectively, to distinguish them from the *hard* scale associated with the mass M. These energy scales affect significantly various processes in the near threshold momentum region, like dark fermion pair annihilation, formation and transition via emission or absorption of photons. The use of the full Lagrangian (3.1) to compute near threshold observables is in general unpractical as all energy scales get entangled in the amplitudes. It is more convenient, instead, to take advantage of the fact that the energy scales are hierarchically ordered and replace systematically (3.1) with a hierarchy of (non-relativistic) effective field theories along what has been done for near threshold fermion pairs in QED and QCD [11, 46, 47].

Another relevant energy scale is the inverse correlation length characterizing the medium made of the dark fermions, dark photons and SM particles. The bath medium is thermalized and we identify the inverse of its correlation length with the temperature T.[6] The relativistic dark photons and light fermions, that form the dark sector of the thermal

gauge coupling to be much larger than the mixing-induced coupling, hence we practically neglect portal interactions when computing the cross sections and widths of dark matter particles.

[3] We could in principle add also some light dark scalars to the Lagrangian (3.1), which couple to the gauge field A_μ as well. But we drop them in this work.

[4] In ref. [82] the the photon self-energy in QED for a finite electron mass is derived. For the purpose of our work, it is not crucial to retain the light fermion masses in the calculation.

[5] The situation is somewhat different in the non-abelian case, where quantum corrections to the dark gluon propagator may be induced also by dark gluon self interactions [48, 50, 84, 85], cf. chapters 8–10.

[6] In the literature one sometimes finds the temperature scale with an additional π attached, i.e. πT. By $\pi T \sim T$ we approximate the two scales to be of the same order and thus equivalent. We can drop π.

bath, have thus energies and momenta of order T; except the non-relativistic dark matter particle X where, despite chemically decoupled from the bath after the the freeze-out, it has kinetically equilibrated velocities following a Maxwell–Boltzmann distribution, from which it follows that $v \sim \sqrt{T/M} \ll 1$. Then there is the aforementioned dynamically generated Debye mass scale, explicitly written in eq. (D.39), which vanishes if we remove the light fermions from the dark sector by putting $n_f = 0$ contrarily to $m_{\rm D}$ in the non-abelian model, cf. (9.31). We assume $T \gg m_{\rm D}$, which leads to the requirement $\sqrt{n_f \alpha} \ll 1$. Hence, whenever we consider light fermions in the theory, we keep the coupling as well as n_f sufficiently small, with $\alpha \lesssim 0.1$ and $n_f \in \{1, 2\}$. The smaller the coupling, the better the approximation. Otherwise we can relax the upper boundary for the coupling constant to somewhat larger values as long as α remains week, i.e. $\alpha \lesssim 0.5$ as has been considered in ref. [51], in return of ejecting the Landau damping phenomenon from the theory.

The aim of the following sections is to compute near threshold observables affecting the evolution of the dark matter density in the early universe, cf. eq. (2.6). In particular, we compute annihilation, dissociation and formation cross sections of dark matter fermion-antifermion pairs. We compute these quantities by means of the tower of non-relativistic effective field theories depicted in figure 3.1. While the scales $M, M\alpha, M\alpha^2$ are inherently separated for non-relativistic dark matter, there is an ambiguity between the order of some of these internal scales and the thermal scales T and $m_{\rm D}$ when time proceeds along the thermal freeze-out era.

3.1 Far-off from freeze-out: $M\alpha \gtrsim \sqrt{MT} \gg M\alpha^2 \gtrsim T \gg m_{\rm D}$

If we assume that T is about the ultrasoft scale $M\alpha^2$ or smaller, the typical momentum of the thermalized dark fermions is then $Mv_{\rm rel} \sim \sqrt{MT} \lesssim M\alpha$, which implies $v_{\rm rel} \lesssim \alpha$. Then it also holds that $\sqrt{MT} \gtrsim M\alpha^2$. These conditions qualify $Mv_{\rm rel}$ as a soft scale and $Mv_{\rm rel}^2 \sim T$ as an ultrasoft scale. Our ensemble of thermalized heavy dark fermions and antifermions realizes, therefore, the following hierarchy of energy scales

$$M \gg M\alpha \gtrsim \sqrt{MT} \gg M\alpha^2 \gtrsim T \gg m_{\rm D}\,. \tag{3.2}$$

The hierarchy (3.2) is of phenomenological interest for the study of near threshold effects in the minimal dark matter model under consideration [15, 36]. Indeed, since the decoupling from chemical equilibrium happens at around $T_{\rm F} \approx M/25$ according to the discussion in the preceding chapter, the condition (3.2) may be fulfilled for most of the time after the decoupling.[7] The case $M\alpha^2 \gtrsim T$ has been extensively studied in [51].

[7] If, more conservatively, we identify the absolute value of the ground state energy, $M\alpha^2/4$, with the ultrasoft scale, the condition $M\alpha^2/4 \gtrsim T$ is fulfilled for all times after decoupling if $\alpha \gtrsim 0.4$. For such large values, however, we spoil the assumption $T \gg m_{\rm D}$, and the hierarchy arrangement in (3.2) now instead would read as follows

$$M \gg M\alpha \gtrsim \sqrt{MT} \gg M\alpha^2 \gtrsim T \sim m_{\rm D}\,.$$

In ref. [51] we considered the $n_f = 0$ case, resulting in $m_{\rm D} = 0$ for the abelian case, hence the hierarchy of energy scales was more simple, i.e. $M \gg M\alpha \gtrsim \sqrt{MT} \gg M\alpha^2 \gtrsim T$.

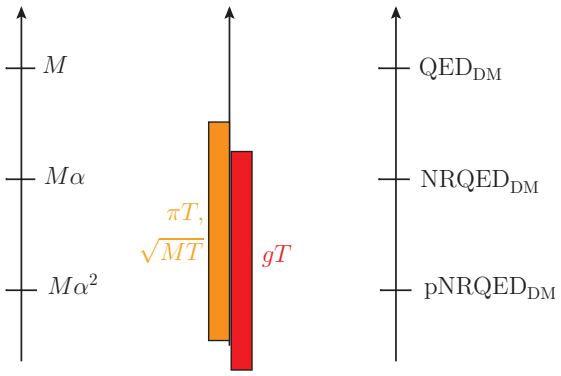

Figure 3.1: Hierarchy of energy scales and effective field theories considered in this chapter for the DM Lagrangian density defined in eq. (3.1). A similar tower of EFTs applies for the non-abelian model given in eq. (8.1) and the corresponding hierarchies of energy scales considered in section 8. The red bar denotes the energy range for the thermal Debye mass scale $m_{\mathrm{D}} \sim gT$.

Although interactions with light dark fermions were not considered there, for small T their contributions to the rates near threshold are suppressed, as we are going to show in the subsequent chapters. The information about the bath-particle scatterings also enters in the running of the coupling constant, which was absent in ref. [51] for the $\mathrm{U}(1)_{\mathrm{DM}}$ model because of $n_f = 0$. As a solution to the renormalization group equation (8.3) at one-loop order with the first coefficient of the beta function in $\mathrm{U}(1)_{\mathrm{DM}}$, $\beta_0 = -4n_f/3$, it reads

$$\alpha(\mu) = \frac{\alpha(2M)}{1 + \frac{\beta_0}{2\pi}\alpha(2M)\log\left(\frac{\mu}{2M}\right)}\,, \tag{3.3}$$

where $\alpha(2M)$, renormalized at the hard scale $2M$, is taken as a free parameter in the abelian model (3.1), together with the DM mass M and number n_f of light fermion species. In the $\mathrm{U}(1)_{\mathrm{DM}}$ case in [51]: $\alpha = \text{const}$, which can be immediately seen from (3.3) upon setting n_f to zero.

3.2 Close to freeze-out: $\sqrt{MT} \gg M\alpha \gg T \gg M\alpha^2 \sim m_{\mathrm{D}}$

At temperatures larger than the ultrasoft scale $M\alpha^2$ but smaller than the soft scale $M\alpha$, which in the early expanding universe corresponds to a time window prior to the one considered in section 3.1, the thermal and internal energy scales arrange as follows

$$M \gg \sqrt{MT} \gg M\alpha \gg T \gg m_{\mathrm{D}}, M\alpha^2\,. \tag{3.4}$$

This hierarchy is realized to a good extent at the thermal freeze-out and shortly after.[8]

[8]The condition $M\alpha \gg T_{\mathrm{F}} \approx M/25$ requires for the values of the coupling to be larger than 0.04. Then we can safely assume that the freeze-out of a bound dark fermion pair happens at a scale lower than its

The two hierarchies in (3.2) and (3.4) enable us to integrate out from the parent $\mathrm{QED}_{\mathrm{DM}}$ model the energy scales starting from the highest scale, the hard scale M, where we obtain a non-relativistic effective field theory (NREFT) for the dark sector, here dubbed $\mathrm{NRQED}_{\mathrm{DM}}$, followed by a potential NREFT (pNREFT), denoted as $\mathrm{pNRQED}_{\mathrm{DM}}$, upon integrating out the subsequent soft scale by means of a multipole expansion. From now on, by ultrasoft scales we mean the energy scales below the soft scale, to which the temperature belongs to according to the hierarchical arrangement of the scales in (3.2) and in (3.4). Only modes of the order of the ultrasoft scale are dynamical degrees of freedom in $\mathrm{pNRQED}_{\mathrm{DM}}$.[9] Since $T \ll M\alpha$, the matching can be done as in vacuum, and the matching coefficients of the effective theory can be eventually written in terms of potentials. There is, however, a small caveat that one needs to take into account for the case in (3.4). The second largest scale is not the soft but the $\sqrt{MT}$ scale, which may have an impact on the $\mathrm{pNRQED}_{\mathrm{DM}}$ Lagrangian. We have carefully inspected the contributions of the energy and momentum modes at the scale $\sqrt{MT}$, and we found that they are either zero or exponentially suppressed for the dark photon, heavy and light fermion propagators, as well as for the heavy fermion-dark photon vertex. Non-vanishing contributions will appear in the heavy fermion-antifermion scatterings eventually giving thermal corrections to the potentials.[10] In (3.4), we did not specify further the order between the two lowest scales, which are yet entangled. It comprises the two limiting cases $m_{\mathrm{D}} \gg M\alpha^2$ and $m_{\mathrm{D}} \ll M\alpha^2$. For an exemplary study of (muonic) hydrogen atom in QED within an analogous EFT-framework as above, we refer the reader to refs. [49, 82]. As an application of NRQED to the computation of radiative corrections for the hyperfine splitting of positronium or muonium, we recommend refs. [86, 87].

soft Bohr-momentum scale. Instead for the case of smaller couplings than 0.04, the freeze-out certainly happens at a temperature scale above $M\alpha$, and can not be captured within the hierarchies (3.2) and (3.4). We will not consider such small parameter values for the coupling in this work. Together with the constraint from $T \gg m_{\mathrm{D}}$ on α, we choose the following range on the allowed parameter values for the coupling constant in the subsequent chapters for the dark abelian model: $0.05 \lesssim \alpha \lesssim 0.1$. Instead, whenever we set $n_f = 0$ or consider only annihilations (where m_{D} effects are negligible), we enlarge the benchmark values to $0.05 \lesssim \alpha \lesssim 0.5$.

[9] Only for very small couplings $\alpha \lesssim 0.04$, the freeze-out temperature $T_{\mathrm{F}} \approx M/25$ can not be ultrasoft and hence the freeze-out not be described by $\mathrm{pNRQED}_{\mathrm{DM}}$ as the multipole expansion would be spoiled. Therefore $\mathrm{pNRQED}_{\mathrm{DM}}$ would need to be discarded and instead $\mathrm{NRQED}_{\mathrm{DM}}$ retained.

[10] More precisely, we expect the thermal corrections to the potentials, from the matching of four-fermion Green functions with loop momenta of order $\sqrt{MT}$, to stem from the vacuum part of the internal propagators in the loops, since the thermal part is exponentially suppressed because of the distribution functions $n_{\mathrm{B/F}}(\sqrt{MT}) \approx \exp\left(-\sqrt{M/T}\right) \ll 1$.

Chapter 4

Effective field theories for the dark sector

4.1 NRQED$_{\rm DM}$

At energies much smaller than M, the effective degrees of freedom in the thermal bath are non-relativistic heavy dark fermions and antifermions, low energy dark photons and massless fermions, and the SM particles. The effective field theory that follows from (3.1) by integrating out dark photons and fermions of energy or momentum of order M has the form of NRQED [46]. It is organized as an expansion in $1/M$ and α and its Lagrangian density up to $\mathcal{O}(1/M^2)$ reads[1]

$$\begin{aligned}
&\mathcal{L}_{\mathrm{NRQED_{DM}}} \\
&= \psi^\dagger \left(iD_0 - M + \frac{\mathbf{D}^2}{2M} + c_{\rm F}\frac{\boldsymbol{\sigma}\cdot g\mathbf{B}}{2M} + c_{\rm D}\frac{\boldsymbol{\nabla}\cdot g\mathbf{E}}{8M^2} + ic_{\rm S}\frac{\boldsymbol{\sigma}\cdot(\mathbf{D}\times g\mathbf{E} - g\mathbf{E}\times\mathbf{D})}{8M^2} \right)\psi \\
&\quad + \chi^\dagger \left(iD_0 + M - \frac{\mathbf{D}^2}{2M} - c_{\rm F}\frac{\boldsymbol{\sigma}\cdot g\mathbf{B}}{2M} + c_{\rm D}\frac{\boldsymbol{\nabla}\cdot g\mathbf{E}}{8M^2} + ic_{\rm S}\frac{\boldsymbol{\sigma}\cdot(\mathbf{D}\times g\mathbf{E} - g\mathbf{E}\times\mathbf{D})}{8M^2} \right)\chi \\
&\quad - \frac{1}{4}F^{\mu\nu}F_{\mu\nu} + \frac{d_2}{M^2}F^{\mu\nu}\mathbf{D}^2F_{\mu\nu} + \frac{d_s}{M^2}\psi^\dagger\chi\,\chi^\dagger\psi + \frac{d_v}{M^2}\psi^\dagger\,\boldsymbol{\sigma}\,\chi\cdot\chi^\dagger\,\boldsymbol{\sigma}\,\psi + \sum_{i=1}^{n_f}\bar{f}_i i\not{D} f_i\,.
\end{aligned} \tag{4.1}$$

Here, ψ is the two-component Pauli spinor that annihilates a dark matter fermion, $\chi^\dagger$ is the Pauli spinor that annihilates an antifermion, σ^i are the Pauli matrices, $\mathbf{E}$ is the (dark) electric field, $E^i = F^{i0}$, and $\mathbf{B}$ is the (dark) magnetic field, $B^i = -\epsilon_{ijk}F^{jk}/2$. The first two lines in eq. (4.1) describe how non-relativistic dark fermions and antifermions propagate and interact with low-energy dark photons of energy smaller than M. The third line describes the propagation and effective self interaction of the photons; it also

[1] At order $1/M^2$ also local four-fermion operators like $(\psi^\dagger\psi + \chi^\dagger\chi)\sum_{i=1}^{n_f}\bar{f}_i f_i + \text{h.c.}$ appear which are responsible for heavy-light DM scatterings. We do not write those terms explicitly in (4.1) as they do not develop an imaginary part and hence do not account for annihilation processes.

contains two four-fermion operators and the n_f dark massless fermions f_i with thermal energies and momenta of order $T \ll M$.

To keep track of the thermalization of the physical fields, we do not redefine the fermion and antifermion fields ψ and χ to reabsorb their mass terms, which we leave explicit. In the matching, the thermal scales and any other energy scale below M can be set to zero. Hence, upon our assumption $M \gg T$, no finite temperature effect enters the EFT Lagrangian (4.1).

The one-loop expressions of the matching coefficients $c_{\rm F}$, $c_{\rm D}$, $c_{\rm S}$ and d_2 in the $\overline{\rm MS}$ scheme can be found in ref. [88] taking the abelian limit. They are regularized in dimensional regularization, and the μ dependence cancels against low-energy matrix elements when computing observables in the EFTs. The coefficients of the kinetic operators are fixed to be one at all orders in the coupling by reparametrization (Poincaré) invariance [89, 90]. As for the four-fermion dimension-six operators, the matching coefficients d_s, d_v at order α^2 can be inferred from e.g. [91]. Its imaginary parts inherit the information about the annihilation processes that are non-dynamical in NREFTs as they happen at the hard scale $2M$. More details will be provided in the next chapter. Here we only comment that the four-fermion operators shown in eq. (4.1) encode the annihilation of S-wave fermion-antifermion pairs, where the annihilation of the heavy pairs with non-vanishing orbital angular momentum comes from the higher-dimensional four-fermion operators. For instance, dimension-eight four-fermion operators encode the annihilation of P-wave fermion-antifermion pairs but also the first relativistic correction to the S-wave annihilations, cf. eq. (5.12).

4.2 pNRQED$_{\rm DM}$

Consistently with the hierarchies of energy scales in (3.2) and (3.4), the next degrees of freedom to integrate out to describe threshold phenomena at the ultrasoft scale are dark photons of energy or momentum of order $Mv_{\rm rel}$, which encompasses the scales $M\alpha$ and $\sqrt{MT}$. At energies much smaller than $Mv_{\rm rel}$ the dynamical degrees of freedom are dark fermions and antifermions with energy of order $Mv_{\rm rel}^2$, and ultrasoft dark photons with energy and momentum of order $Mv_{\rm rel}^2$, which encompasses the scales $M\alpha^2$ and T.[2] The Lagrangian term for the massless thermal fermions does not change since $T \ll M\alpha$. The effective field theory is pNRQED$_{\rm DM}$, i.e. the dark version of pNRQED [92, 93]. We integrate out the soft scale by setting to zero all lower energy scales. The matching is done at weak coupling, i.e. order by order in α, although the EFT is suited to accommodate a non-perturbative framework as well [11, 94].

Threshold phenomena affect the heavy fermion-antifermion pairs, hence it is convenient to project the EFT on the fermion-antifermion Hilbert space and express it in terms of gauge singlet fermion-antifermion bilocal fields $\phi(t, \boldsymbol{r}, \boldsymbol{R})$, where $\boldsymbol{r} \equiv \boldsymbol{r}_1 - \boldsymbol{r}_2$

[2] We remark that for excited Coulombic states, further distinctions of scales due to the principal quantum number may turn out to be necessary, as $M\alpha^2/n^2 \leq M\alpha^2$ and similarly for the Bohr momentum $M\alpha/n \leq M\alpha$. Nevertheless, to keep the analysis of the results simple, we refrain in this paper to put stronger constraints on the excited Coulombic states.

is the distance between a fermion located at $\boldsymbol{r}_1$ and an antifermion located at $\boldsymbol{r}_2$ and $\boldsymbol{R} \equiv (\boldsymbol{r}_1 + \boldsymbol{r}_2)/2$ is the center of mass coordinate.[3] In order to ensure that the photons are ultrasoft, photon fields are *multipole* expanded in $\boldsymbol{r}$. Hence the pNRQED$_{\rm DM}$ Lagrangian density for the dark matter theory (3.1) is organized as an expansion in $1/M$, inherited from NRQED$_{\rm DM}$, $\boldsymbol{r}$ and α (at weak coupling). In the laboratory frame, up to leading order in $\boldsymbol{r}$ and in the center-of-mass momentum $\boldsymbol{P}$ of the heavy pair, it reads

$$\begin{aligned}\mathcal{L}_{\rm pNRQED_{DM}} \;=\; & \int d^3r \left\{ \phi^\dagger(t,\boldsymbol{r},\boldsymbol{R}) \left[i\partial_0 - H(\boldsymbol{r},\boldsymbol{p},\boldsymbol{P},\boldsymbol{S}_1,\boldsymbol{S}_2) \right] \phi(t,\boldsymbol{r},\boldsymbol{R}) \right. \\ & \left. + \phi^\dagger(t,\boldsymbol{r},\boldsymbol{R}) \left[\boldsymbol{r}\cdot g\boldsymbol{E}(t,\boldsymbol{R}) + \frac{\boldsymbol{r}}{2}\cdot \left\{ \frac{\boldsymbol{P}}{2M}\times\,,\, g\boldsymbol{B}(t,\boldsymbol{R}) \right\} \right] \phi(t,\boldsymbol{r},\boldsymbol{R}) \right\} \\ & - \frac{1}{4}F_{\mu\nu}F^{\mu\nu} + \sum_{i=1}^{n_f} \bar{f}_i i \not{D} f_i \,, \end{aligned} \tag{4.2}$$

where $\{\dots,\dots\}$ stands for the anticommutator. The Hamiltonian reads

$$H(\boldsymbol{r},\boldsymbol{p},\boldsymbol{P},\boldsymbol{S}_1,\boldsymbol{S}_2) = 2M + \frac{\boldsymbol{p}^2}{M} + \frac{\boldsymbol{P}^2}{4M} + V(\boldsymbol{r},\boldsymbol{p},\boldsymbol{P},\boldsymbol{S}_1,\boldsymbol{S}_2) + \dots \,, \tag{4.3}$$

where the dots stand for higher order relativistic corrections of the kinetic term. The fermion-antifermion potential can be expanded as

$$V(\boldsymbol{r},\boldsymbol{p},\boldsymbol{P},\boldsymbol{S}_1,\boldsymbol{S}_2) = V^{(0)} + \frac{V^{(1)}}{M} + \frac{V^{(2)}}{M^2} + \dots \,, \tag{4.4}$$

and $\boldsymbol{S}_1 = \boldsymbol{\sigma}_1/2$ and $\boldsymbol{S}_2 = \boldsymbol{\sigma}_2/2$ are the spin operators acting on the fermion and antifermion, respectively. The static potential is the Coulomb potential:

$$V^{(0)} = -\frac{\alpha}{r} \,. \tag{4.5}$$

If $T \sim M\alpha^2$, cf. hierarchy (3.2), the potential does not get, by construction, thermal contributions at any order. The power counting of the EFT goes as follows: the inverse of the relative coordinate r scales like $Mv_{\rm rel}$, whereas the inverse of the center-of-mass coordinate R can at most change by $M\alpha^2$ or T, if the DM fermion-antifermion pair recoils against ultrasoft dark photons. The fact that the variation in R is larger than r guarantees the validity of the multipole expansion. Hence, pNRQED$_{\rm DM}$ is valid as long as $T \ll M\alpha$. The dots in eq. (4.4) stand for irrelevant operators of higher order

[3] The Hilbert space of a fermion-antifermion pair is spanned by the vector

$$|\phi\rangle = \sum_{ij} \int d^3r_1\, d^3r_2\; \phi_{ij}(\boldsymbol{r}_1,\boldsymbol{r}_2) \psi^{i\dagger}(\boldsymbol{r}_1)\chi^j(\boldsymbol{r}_2)|0\rangle \,,$$

where ϕ_{ij} is the spin-dependent heavy-pair wavefunction, to be distinguished from the heavy-pair field operator ϕ in eq. (4.6), which is spectrally divided into a bound-state and scattering-state configuration via the Fourier-decomposition.

Figure 4.1: Feynman diagrams for electric and magnetic-dipole transitions between fermion-antifermion scattering states (double line) and bound states (single line). The wavy lines stand for the photon external fields. The circle with a cross denotes the electric-dipole vertex $i\boldsymbol{r}\cdot g\boldsymbol{E}$ and the square denotes the magnetic-dipole vertex $i\boldsymbol{r}\cdot\{\boldsymbol{P}\times, g\boldsymbol{B}\}/(4M)$ due to the Röntgen term [90]. The momentum $\boldsymbol{P}$ is the sum of the center-of-mass momentum of the incoming fermion-antifermion pair and the momentum of the incoming photon. The vertices follow from the Lagrangian (4.2).

in the $1/M$ expansion. The relative momentum $\boldsymbol{p}=-i\boldsymbol{\nabla}_{\boldsymbol{r}}$ and the center of mass momentum $\boldsymbol{P}=-i\boldsymbol{\nabla}_{\boldsymbol{R}}$ are the conjugate variables of $\boldsymbol{r}$ and $\boldsymbol{R}$, respectively.[4] We refer to appendix A for more details about the center-of-mass coordinates and its Lorentz boost transformation relations among different reference frames. At order r, the term proportional to the dark electric field is an electric-dipole interaction term; it provides the leading ultrasoft interaction between fermion and dark photon fields in pNRQED$_{\rm DM}$. The term proportional to the dark magnetic field provides the leading ultrasoft interaction between DM fermion and photon fields in pNRQED$_{\rm DM}$ that is proportional to the center-of-mass momentum $\boldsymbol{P}$. It is sometimes also called *Röntgen term* [98]. The Röntgen term originates form the *Lorentz force* $\boldsymbol{F}=\boldsymbol{v}\times g\boldsymbol{B}$[5], and it shows up as a man-

[4]The potential (4.4) gets affected from the center-of-mass motion as well as the relative motion of the heavy pair. For example at dimension six, we can write the center-of-mass-momentum dependent corrections entering $V^{(2)}$ [90, 95–97]:

$$\delta V^{(2)}(\boldsymbol{r},\boldsymbol{P})=-\frac{1}{8}\boldsymbol{P}^2V^{(0)}(r)+\frac{1}{8}(\boldsymbol{r}\cdot\boldsymbol{P})^2\frac{V^{(0)\prime}(r)}{r}-\frac{1}{8}(\boldsymbol{r}\times\boldsymbol{P})\cdot(\boldsymbol{\sigma}_1-\boldsymbol{\sigma}_2)\frac{V^{(0)\prime}(r)}{r},$$

where $V^{(0)\prime}(r)$ is the derivative of the static potential, $\boldsymbol{\sigma}_1$ the Pauli matrix acting on the fermion and $\boldsymbol{\sigma}_2$ the Pauli matrix acting on the antifermion. Of the same order is also the kinetic energy correction $-\boldsymbol{P}^4/(64M^3)-(\boldsymbol{p}\cdot\boldsymbol{P})^2/(4M^3)-\boldsymbol{p}^2\boldsymbol{P}^2/(8M^3)$.

[5]There is an additional magnetic interaction term proportional to the relative momentum and $\boldsymbol{R}$, which we drop since we are interested only at dipole interactions of order $\boldsymbol{r}$. We get this term together with the Röntgen term by computing the corresponding part in the Hamiltonian $H\supset-(\boldsymbol{r}_1\cdot\boldsymbol{F}_1+\boldsymbol{r}_2\cdot\boldsymbol{F}_2)$, where the Lorentz forces acting on the fermion and antifermion are $\boldsymbol{F}_1=\boldsymbol{v}_1\times g\boldsymbol{B}(\boldsymbol{r}_1)$ and $\boldsymbol{F}_2=\boldsymbol{v}_2\times(-g)\boldsymbol{B}(\boldsymbol{r}_2)$, respectively. Then we switch to the center-of-mass coordinates, cf. (A.1) and (A.2), from which it follows that $\boldsymbol{v}_{1/2}=\dot{\boldsymbol{r}}_{1/2}=(\boldsymbol{V}\pm\boldsymbol{v}_{\rm rel}/2)$, where $\boldsymbol{V}=\dot{\boldsymbol{R}}$ is the spatial center-of-mass velocity of the pair. Next, we multipole expand the magnetic field to zeroth order,

$$\boldsymbol{B}(t,\boldsymbol{r}_{1/2})=\boldsymbol{B}(t,\boldsymbol{R}\pm\boldsymbol{r}/2)=\boldsymbol{B}(t,\boldsymbol{R})\pm(\boldsymbol{r}\cdot\boldsymbol{\nabla}_{\boldsymbol{R}})\boldsymbol{B}(t,\boldsymbol{R})/2+\cdots\approx\boldsymbol{B}(t,\boldsymbol{R})\equiv\boldsymbol{B}\,.$$

Finally, putting everything together we obtain $H\supset-g[\boldsymbol{r}\cdot(\boldsymbol{V}\times\boldsymbol{B})+\boldsymbol{R}\cdot(\boldsymbol{v}_{\rm rel}\times\boldsymbol{B})]$, where the first term corresponds to the Röntgen interaction. We symmetrize it in quantum theory according to the Weyl ordering, which results in $-g\boldsymbol{r}\cdot\{\boldsymbol{V}\times,\boldsymbol{B}\}/2$, and $\boldsymbol{V}=\boldsymbol{P}/2M$ at leading order in the non-relativistic limit.

ifestation of the Poincaré invariance of QED [90]. It is suppressed in the center-of-mass velocity $\boldsymbol{v}$ compared to the electric-dipole term. The matching coefficient of the electric dipole and Röntgen interaction has been taken equal to one.

At order r^0 in the multipole expansion, cf. first line in (4.2), the equation of motion of the fermion-antifermion pair is a Schrödinger equation with potential $V(\boldsymbol{r}, \boldsymbol{p}, \boldsymbol{P}, \boldsymbol{S}_1, \boldsymbol{S}_2)$. Hence the leading order fermion-antifermion propagator in pNRQED$_{\rm DM}$ automatically accounts for bound-state effects and multiple Coulomb rescatterings, called the Sommerfeld enhancement, in physical observables. This can be seen explicitly in (D.14), where V enters through the Hamiltonian as a pole in the heavy-pair propagator.[6] Fermion-antifermion pairs above threshold form scattering states of positive energy and fermion-antifermion pairs below threshold form bound states of negative energy. It may be therefore convenient to decompose the bi-local field $\phi(t, \boldsymbol{r}, \boldsymbol{R})$ into a scattering component and a bound-state component [99],

$$\phi_{ij}(t, \boldsymbol{r}, \boldsymbol{R}) = \int \frac{d^3P}{(2\pi)^3} \left[\sum_n e^{-iE_n t + i\boldsymbol{P}\cdot\boldsymbol{R}}\, \Psi_n(\boldsymbol{r})\, S_{ij}\, \phi_n(\boldsymbol{P}) + \sum_{\rm spin} \int \frac{d^3p}{(2\pi)^3} e^{-iE_p t + i\boldsymbol{P}\cdot\boldsymbol{R}}\, \Psi_{\boldsymbol{p}}(\boldsymbol{r})\, S_{ij}\, \phi_{\boldsymbol{p}}(\boldsymbol{P}) \right], \tag{4.6}$$

where $\phi_n^\dagger(\boldsymbol{P})$ creates a Coulombic bound state, $|n, \boldsymbol{P}\rangle = \phi_n^\dagger(\boldsymbol{P})|0\rangle$, with center of mass momentum $\boldsymbol{P}$, quantum numbers n,[7] energy E_n and wavefunction $\Psi_n(\boldsymbol{r})\, S_{ij}$, whereas $\phi_p^\dagger(\boldsymbol{P})$ creates a scattering state, $|\boldsymbol{p}, \boldsymbol{P}\,\rangle = \phi_{\boldsymbol{p}}^\dagger(\boldsymbol{P})|0\rangle$, with center of mass momentum $\boldsymbol{P}$, relative momentum $\boldsymbol{p}$, energy E_p and wavefunction $\Psi_{\boldsymbol{p}}(\boldsymbol{r})\, S_{ij}$. The indices i, j are spin indices. In particular, S-wave dark fermion-antifermion pairs may be either in a spin-singlet state, in which case $S_{ij} = \delta_{ij}/\sqrt{2}$, or in a spin-triplet state, in which case $S_{ij} = (\boldsymbol{\sigma}\cdot\boldsymbol{\epsilon})_{ij}/\sqrt{2}$, where $\boldsymbol{\sigma}$ are the Pauli matrices and $\boldsymbol{\epsilon}$ is the polarization vector of the spin-triplet pair. The sum over spin in the second line of eq. (4.6) is a sum over all spin configurations; in the first line, this sum is included in the sum over the quantum numbers n. If the dark fermion-antifermion pair is bound we may call it *darkonium*, which, in the S-wave case, we may further distinguish into a spin-singlet *paradarkonium* state, and a spin-triplet *orthodarkonium* state. Various transitions between scattering and bound states are induced by the dipole vertices from the terms in the second line of (4.2), which are shown in figure 4.1. We discuss these dipole interactions in chapter 6. As a final remark, the spectrum of bound states below the mass threshold in the center-of-mass frame is given at order α^2 by

$$(E_n)_{\rm cm} = 2M + E_n^b\,, \tag{4.7}$$

[6] The expression of the potential $V(\boldsymbol{r}, \boldsymbol{p}, \boldsymbol{P}, \boldsymbol{S}_1, \boldsymbol{S}_2)$ in the center of mass frame including $V^{(0)}$, $V^{(1)}$ and $V^{(2)}$ can be found in ref. [47].

[7] With n we comprise the principal quantum number n, the orbital angular momentum quantum number ℓ and the magnetic quantum number m. Then $\Psi_n(\boldsymbol{r}) = R_{n\ell}(r) Y_\ell^m(\hat{\boldsymbol{r}})$ where $R_{n\ell}(r)$ is the radial part of the bound-state wavefunction, cf. (C.3), and $Y_\ell^m(\hat{\boldsymbol{r}})$ the spherical harmonics.

with binding energy $E_n^b = -M\alpha^2/(4n^2) = -(Ma_0^2n^2)^{-1}$ and Bohr radius $a_0 = 2/(M\alpha)$. In the center-of-mass frame, the continuum spectrum of scattering states above the mass threshold is given at leading order in the relative momentum by

$$(E_p)_{\rm cm} = 2M + \frac{\boldsymbol{p}^2}{M}\,. \tag{4.8}$$

In the laboratory frame, the spectrum and wavefunctions get corrections that depend on the center-of-mass momentum $\boldsymbol{P}$. The leading-order correction to the spectrum is the center-of-mass kinetic energy $\boldsymbol{P}^2/(4M)$, which is of the same order as E_n^b or $\boldsymbol{p}^2/M$ if $P \sim p \sim \sqrt{MT}$ and $M\alpha^2 \sim T$. Higher order corrections are computed in appendix B.

Part III

Interactions: cross sections and widths, Boltzmann equations

Chapter 5

Annihilations in EFTs

5.1 Free annihilations in NRQED$_{\rm DM}$

We are interested in describing the annihilation processes of heavy dark matter pairs. Annihilations happen at the hard scale $2M$ and the corresponding energy modes are integrated out in the non-relativistic EFT, here NRQED$_{\rm DM}$.[1] The local four-fermion operators of dimension six, listed in the third line of the Lagrangian (4.1), encode the annihilation of S-wave fermion-antifermion pairs. The leading order contribution to the imaginary part of these irrelevant operators comes from the two-photon and two-fermion annihilation processes $X\bar{X} \to \gamma\gamma$ and $X\bar{X} \to f_i\bar{f}_i$, respectively for a spin-singlet and spin-triplet configuration, see figure 5.1. The four-fermion matching coefficients d_s and d_v at leading order (LO) read

$$\mathrm{Im}[d_s]_{\rm LO} = \pi\alpha^2\,, \quad \mathrm{Im}[d_v]_{\rm LO} = \frac{n_f}{3}\pi\alpha^2\,, \tag{5.1}$$

where they are obtained by cutting the loop diagrams along the internal photon or light fermion propagators [100,101]. The matching procedure can be systematically performed at higher order in the coupling. The four-fermion Wilson coefficients are known up to next-to-next-to leading order (NNLO), see refs. [91, 102] and the review [103]. At NLO,

[1] EFTs, suitable to describe a physical system effectively at scales $\mu \ll M$, where μ denotes the energy scale at which only the light degrees of freedom (l.d.o.f.) are dynamical, have the following general structure of the Lagrangian density:

$$\mathcal{L}_{\rm EFT}(\text{l.d.o.f.}) = \mathcal{L}(\text{l.d.o.f.}) + \sum_i \frac{c_i}{M^{d_i-4}}\mathcal{O}_i\,,$$

where $\mathcal{L}$(l.d.o.f.) denotes the subset of the parent renormalizable relativistic theory, $\mathcal{L}$, comprising only the dynamical l.d.o.f., whereas the irrelevant operators $\mathcal{O}_i$ are generated due to the non-relativistic expansion in μ/M. The dimensionless Wilson coefficients c_i encode the physics at the large scale M and the radiative corrections at that scale.

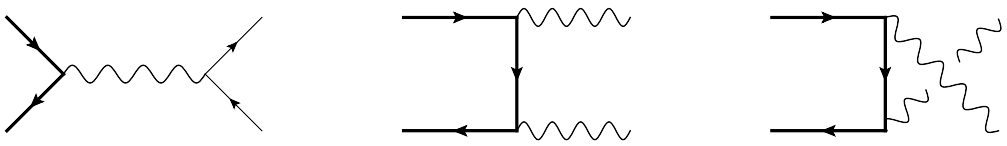

Figure 5.1: Annihilation processes for a heavy dark fermion-antifermion pair (thick lines) into a light dark fermion-antifermion pair (thin lines), cf. left diagram, or into two dark photons (wavy lines), cf. middle and right diagram, at leading order in α. Radiative corrections to these processes, but also annihilations with more products in the final state, for instance three outgoing photons, happen at least at $\mathcal{O}(\alpha^3)$.

the expressions in (5.1) are modified due to the radiative corrections as follows:

$$\mathrm{Im}[d_s]_{\mathrm{NLO}} = \pi\alpha^2 \left[1 + \frac{\alpha}{\pi}\left(\frac{\pi^2}{4} - 5\right)\right], \tag{5.2}$$

$$\mathrm{Im}[d_v]_{\mathrm{NLO}} = \frac{n_f}{3}\pi\alpha^2 \left[1 + \frac{\alpha}{\pi}\left(\frac{4}{3}\frac{\pi^2 - 9}{n_f} - 4\right)\right]. \tag{5.3}$$

From the optical theorem, it follows that the spin-averaged annihilation cross section, σ_{ann}, can be written in full generality as[2] [57, 63]

$$\sigma_{\mathrm{ann}} v_{\mathrm{Møl}} = \frac{\mathrm{Im}[\mathcal{M}_{\mathrm{NR}}(\psi\chi \to \psi\chi)]}{2}, \tag{5.4}$$

where $\mathcal{M}_{\mathrm{NR}}(\psi\chi \to \psi\chi)$ is the $2 \to 2$ scattering amplitude with initial and final states normalized non-relativistically,[3] and $v_{\mathrm{Møl}}$ is the so-called Møller velocity, which is the flux of incoming particles divided by the energies of the two colliding particles carrying four-momenta $p_i = (E_i, \boldsymbol{p}_i)$,

$$v_{\mathrm{Møl}} = \frac{\sqrt{(p_1 \cdot p_2)^2 - M^4}}{E_1 E_2}. \tag{5.5}$$

The Møller velocity has a simple expression in terms of the particle velocities $\boldsymbol{v}_i \equiv \boldsymbol{p}_i/E_i$:

$$v_{\mathrm{Møl}}^2 = v_{\mathrm{rel}}^2 - (\boldsymbol{v}_1 \times \boldsymbol{v}_2)^2, \tag{5.6}$$

where $v_{\mathrm{rel}} \equiv |\boldsymbol{v}_1 - \boldsymbol{v}_2|$ is the relative velocity of the colliding particles. Note that in the non-relativistic limit, the relative velocity is of order $1/M$, whereas $|\boldsymbol{v}_1 \times \boldsymbol{v}_2|$ is of

[2] Cross sections are computed by summing over the final state polarizations and averaging over the initial state ones. In the case of annihilation cross sections and bound state formation cross sections (cf. sec. 6.1), the initial state polarizations are the $4 = 2 \times 2$ spin orientations of the incoming fermion-antifermion pair. In the case of ionization cross sections (sec. 6.2), the initial state polarizations are the $4 = 2 \times 2$ spin orientations of the incoming fermion-antifermion pair and the two polarizations of the incoming photon (or $2 \times (N^2 - 1)$ polarizations in case of non-abelian gauge fields, cf. section 9.2).

[3] The relation between a relativistically normalized state, $|\mathrm{R}\rangle$, and a non-relativistically normalized one, $|\mathrm{NR}\rangle$, is $|\mathrm{R}\rangle = \sqrt{2E}\,|\mathrm{NR}\rangle$, E being the energy of the state.

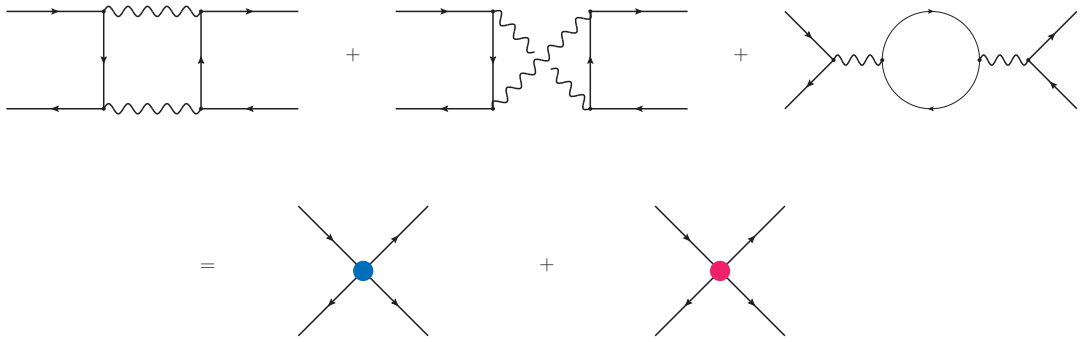

Figure 5.2: Matching between annihilation diagrams in the relativistic theory at one loop (upper three diagrams) and the corresponding four-fermion interactions in $\mathrm{NRQED}_{\mathrm{DM}}$ (lower two diagrams). The associated imaginary parts of the matching coefficients d_s and d_v at order α^2 are given in (5.1). They correspond to S-wave spin-singlet and spin-triplet annihilations, respectively. The thick solid lines denote the incoming and outgoing heavy DM particle and antiparticle, whereas wavy lines stand for the dark photon and thin solid lines for light dark fermions. The imaginary part of the matching coefficients encode the annihilation processes depicted in figure 5.1.

order $1/M^2$. We can write $\boldsymbol{p}_1 = \boldsymbol{p} + \boldsymbol{P}/2$ and $\boldsymbol{p}_2 = -\boldsymbol{p} + \boldsymbol{P}/2$, where $\boldsymbol{p}$ is the relative and $\boldsymbol{P}$ the center-of-mass momentum, cf. section A.1. From this it follows that in the center-of-mass frame (cm) of the dark fermion-antifermion pair, where $\boldsymbol{P}_{\mathrm{cm}} = \boldsymbol{0}$, $(\boldsymbol{p}_1)_{\mathrm{cm}} = -(\boldsymbol{p}_2)_{\mathrm{cm}} = \boldsymbol{p}_{\mathrm{cm}}$ and $(E_1)_{\mathrm{cm}} = (E_2)_{\mathrm{cm}} = \sqrt{\boldsymbol{p}_{\mathrm{cm}}^2 + M^2}$, it holds that

$$(\boldsymbol{v}_1)_{\mathrm{cm}} = -(\boldsymbol{v}_2)_{\mathrm{cm}} = \frac{\boldsymbol{p}_{\mathrm{cm}}}{\sqrt{\boldsymbol{p}_{\mathrm{cm}}^2 + M^2}}\,, \tag{5.7}$$

and from relation (5.6) in the center-of-mass frame, where $(\boldsymbol{v}_1)_{\mathrm{cm}} \times (\boldsymbol{v}_2)_{\mathrm{cm}} = \boldsymbol{0}$, it follows

$$(v_{\mathrm{M\o l}})_{\mathrm{cm}} = (v_{\mathrm{rel}})_{\mathrm{cm}} = 2|(\boldsymbol{v}_1)_{\mathrm{cm}}| = 2\frac{|\boldsymbol{p}_{\mathrm{cm}}|}{M}\left[1 - \frac{\boldsymbol{p}_{\mathrm{cm}}^2}{2M^2} + \mathcal{O}\left(\frac{\boldsymbol{p}_{\mathrm{cm}}^4}{M^4}\right)\right]. \tag{5.8}$$

We see that $(v_{\mathrm{rel}}^{(0)})_{\mathrm{cm}} \equiv 2|\boldsymbol{p}_{\mathrm{cm}}|/M$ is the relative velocity at leading order in the non-relativistic expansion. In the center-of-mass frame of the fermion-antifermion pair, the thermal bath is moving with velocity about $-\boldsymbol{P}/(2M)$, where $\boldsymbol{P}$ is the center-of-mass momentum in the thermal bath frame, cf. fig. 2.1.

We turn back to the computation of the spin-averaged annihilation cross section. Accounting only for the lowest-order dimension-six four-fermion operators written explicitly in (4.1), that are momentum independent, from the optical theorem (5.4) we obtain for the S-wave annihilation cross section at zeroth order in the momenta in the center-of-mass frame (in fact, it is the same in any reference):

$$\sigma_{\mathrm{ann}}^{\mathrm{NR}} v_{\mathrm{rel}} \;=\; \frac{\mathrm{Im}[d_s] + 3\mathrm{Im}[d_v]}{M^2}\,, \tag{5.9}$$

where $v_{\rm rel} \equiv (v_{\rm rel}^{(0)})_{\rm cm}$ is the relative velocity used in the literature for heavy composite systems. Computing next-to-leading order (NLO) annihilation cross sections has been for long pursued in a variety of models, e.g. [104–111]. The expression at NLO in α of the S-wave annihilation cross section in the abelian dark matter model (3.1) reads

$$(\sigma_{\rm ann}^{\rm NR} v_{\rm rel})_{\rm NLO} = \frac{\pi\alpha^2}{M^2}\left[1 + n_f + \frac{\alpha}{\pi}\left(\frac{19}{12}\pi^2 - 17 - 4n_f\right)\right] . \tag{5.10}$$

At leading order, one recovers the well known result (cf. ref. [112] for the specific case $n_f = 0$, i.e. the free annihilation of a fermion and an antifermion into two photons)

$$(\sigma_{\rm ann}^{\rm NR} v_{\rm rel})_{\rm LO} = (1 + n_f)\frac{\pi\alpha^2}{M^2} . \tag{5.11}$$

Whether or not we set $n_f = 0$ in (3.1), the NLO corrections are negative and make the cross section smaller. Taking $\alpha = 0.4$, the NLO cross section is reduced by about 17% with respect to the LO cross section (even larger couplings have been considered in the literature, see e.g. [15]). If we keep one light fermion in the model ($n_f = 1$), then the NLO cross section decreases by about 34% with respect to the LO cross section, for the same value of the coupling; by about 40% for $n_f = 2$ and by more than a half if we would add more than ten light fermions. We see that radiative corrections can have a significant impact on the observable, and it is therefore crucial to state the order of accuracy by the power counting whenever a result is provided.

We can increase the order of precision not only by considering loop corrections to the matching coefficients, like it was done for $\mathrm{Im}[d_s]$ and $\mathrm{Im}[d_v]$ up to NLO in α in eqs. (5.2) and (5.3), but also by adding irrelevant four-fermion operators of dimension higher than six to the Lagrangian (4.1), in this way accounting for the velocity corrections of S-wave annihilations at higher order. Higher dimensional four-fermion operators also account for the annihilation of fermion-antifermion pairs with higher orbital angular momentum, i.e. P-waves, D-waves and so on. Effective field theories provide a straightforward framework to compute higher-order corrections to the annihilation cross section, either in terms of the aforementioned α corrections to the matching coefficients of the four-fermion operators, or by including higher dimensional four-fermion operators to the $\mathrm{NRQED}_{\rm DM}$ Lagrangian, and eventually provide the relativistic and radiative corrections to the associated interaction rate, here the annihilation cross section, in terms of velocities and the coupling, respectively.[4]. The irrelevant four-fermion operators of dimension eight are[5] [115, 116]

[4]In this respect, we refer the interested reader to the following refs. [113, 114], where EFT-methods were exploited for dark matter models involving neutralino fields in the context of the Minimal Supersymmetric Standard Model (MSSM), or ref. [100] for the case of heavy quarkonium in QCD.

[5]Four-fermion operators of dimensionality seven are forbidden because of parity conservation. At dimension eight there are two additional four-fermion operators that couple to a soft dark magnetic field (at dimension nine they couple to a soft dark electric field), and one of them develops an imaginary part in the associated matching coefficient at $\mathcal{O}(\alpha^2)$ [115]. We do not consider such interactions in this work, as for instance $X\bar{X} + \gamma_{\rm soft} \to f_i\bar{f}_i$.

$$
\begin{aligned}
&\delta\mathcal{L}^{\text{dim.8}}_{\text{NRQED}_{\text{DM}}} \\
&= \frac{g(^1S_0)}{2M^4}\left[\psi^\dagger\left(-\frac{i}{2}\overleftrightarrow{\nabla}\right)^2\chi\,\chi^\dagger\psi + \text{h.c.}\right] + \frac{g(^3S_1)}{2M^4}\left[\psi^\dagger\left(-\frac{i}{2}\overleftrightarrow{\nabla}\right)^2\boldsymbol{\sigma}\chi\cdot\chi^\dagger\boldsymbol{\sigma}\psi + \text{h.c.}\right] \\
&+ \frac{g(^3S_1,{}^3D_1)}{2M^4}\left[\psi^\dagger\sigma^i\chi\,\chi^\dagger\sigma^j\left(-\frac{i}{2}\right)^2\overleftrightarrow{\nabla}^{(i}\overleftrightarrow{\nabla}^{j)}\psi + \text{h.c.}\right] \\
&+ \frac{g_{\text{a cm}}}{M^4}\nabla^i(\psi^\dagger\sigma^j\chi)\nabla^i(\chi^\dagger\sigma^j\psi) + \frac{g_{\text{b cm}}}{M^4}\boldsymbol{\nabla}\cdot(\psi^\dagger\boldsymbol{\sigma}\chi)\boldsymbol{\nabla}\cdot(\chi^\dagger\boldsymbol{\sigma}\psi) + \frac{g_{\text{c cm}}}{M^4}\boldsymbol{\nabla}(\psi^\dagger\chi)\cdot\boldsymbol{\nabla}(\chi^\dagger\psi) \\
&+ \frac{f(^1P_1)}{M^4}\psi^\dagger\left(-\frac{i}{2}\overleftrightarrow{\nabla}\right)\chi\cdot\chi^\dagger\left(-\frac{i}{2}\overleftrightarrow{\nabla}\right)\psi + \frac{f(^3P_0)}{3M^4}\psi^\dagger\left(-\frac{i}{2}\overleftrightarrow{\nabla}\cdot\boldsymbol{\sigma}\right)\chi\,\chi^\dagger\left(-\frac{i}{2}\overleftrightarrow{\nabla}\cdot\boldsymbol{\sigma}\right)\psi \\
&+ \frac{f(^3P_1)}{2M^4}\psi^\dagger\left(-\frac{i}{2}\overleftrightarrow{\nabla}\times\boldsymbol{\sigma}\right)\chi\cdot\chi^\dagger\left(-\frac{i}{2}\overleftrightarrow{\nabla}\times\boldsymbol{\sigma}\right)\psi \\
&+ \frac{f(^3P_2)}{M^4}\psi^\dagger\left(-\frac{i}{2}\overleftrightarrow{\nabla}^{(i}\sigma^{j)}\right)\chi\,\chi^\dagger\left(-\frac{i}{2}\overleftrightarrow{\nabla}^{(i}\sigma^{j)}\right)\psi\ ,
\end{aligned}
\tag{5.12}
$$

and encode the first correction to the S-wave annihilation in the relative velocity (second and third line) and in the center-of-mass velocity (fourth line), but also the first non-vanishing contribution to the P-wave annihilation (last three lines). In eq. (5.12) the gradient $\overleftrightarrow{\nabla}$ acts on both directions, $\overleftrightarrow{\nabla} \equiv \overrightarrow{\nabla} - \overleftarrow{\nabla}$ with $\overrightarrow{\nabla} = \boldsymbol{\nabla}$, and we use the conventional notation $T^{(ij)} \equiv (T^{ij}+T^{ji})/2 - T^{kk}\delta^{ij}/3$. The terms in (5.12) are obtained from more general operators, where the gradient $\boldsymbol{\nabla}$ is replaced by the spatial covariant derivative $\boldsymbol{D}$. We characterize the fermion-antifermion pair as in atomic spectroscopy by ${}^{2S+1}L_J$, i.e. by its total spin $S = (0,1)$, total orbital angular momentum $L = (0,1,\dots)$ and the total angular momentum quantum number $J = S+L$. One can then compute the annihilation cross section upon using the optical theorem (5.4) in any reference frame, and from the operators in (5.12) one would obtain the leading relative and center-of-mass momentum-dependent corrections to the S-wave annihilation in (5.9), and in addition a non-vanishing contribution from the P-wave annihilation. The imaginary parts of the matching coefficients in (5.12) at order α^2 are given by [115, 117, 118]

$$
\text{Im}\left[g(^1S_0)\right] = -\frac{4}{3}\pi\alpha^2\,,\ \text{Im}\left[g(^3S_1)\right] = -\frac{4}{9}n_f\pi\alpha^2\,,\ \text{Im}\left[g(^3S_1,{}^3D_1))\right] = -\frac{n_f}{3}\pi\alpha^2, \tag{5.13}
$$

$$
\text{Im}\left[f(^1P_1)\right] = \text{Im}\left[f(^3P_1)\right] = 0\,,\ \text{Im}\left[f(^3P_0)\right] = 3\pi\alpha^2\,,\ \text{Im}\left[f(^3P_2)\right] = \frac{4}{5}\pi\alpha^2\,, \tag{5.14}
$$

$$
\text{Im}\left[g_{\text{a cm}}\right] = -\frac{1}{4}\text{Im}\left[d_v\right]\ ,\ \text{Im}\left[g_{\text{b cm}}\right] = 0\,,\ \text{Im}\left[g_{\text{c cm}}\right] = -\frac{1}{4}\text{Im}\left[d_s\right]\ , \tag{5.15}
$$

where we dropped the subscript LO since we will not go to higher order in α for the annihilations of order $1/M^4$. Those matching coefficients in (5.13)–(5.15), that depend on n_f, incorporate the annihilation into two massless fermions, the others are generated from the annihilations into two photons. The matching coefficients in (5.13) and (5.15) account for spin-singlet and spin-triplet S-wave annihilations, the ones in (5.14) for spin-singlet and spin-triplet P-wave annihilations. The relations in (5.15) are exact, i.e. valid at all orders, and follow from (reparametrization) Poincaré invariance of QED.

If we consider only the dimension-eight four-fermion operators listed in the fourth row of eq. (5.12), then we get the spin-averaged S-wave annihilation cross section in the laboratory frame at order $\boldsymbol{P}^2/M^2$ in the center-of-mass momentum and at zeroth order in the relative momentum:

$$(\sigma_{\text{ann}} v_{\text{Møl}})_{\text{lab}}(\boldsymbol{P}) = \frac{\text{Im}[d_s] + 3\text{Im}[d_v]}{M^2}\left(1 - \frac{\boldsymbol{P}^2}{4M^2}\right) = \sigma_{\text{ann}}^{\text{NR}} v_{\text{rel}}\left(1 - \frac{\boldsymbol{P}^2}{4M^2}\right), \tag{5.16}$$

which does not depend on the relative momentum, since the other operators in (5.12) are dropped. The result in eq. (5.16) could also have been derived by Lorentz-boosting $\sigma_{\text{ann}} v_{\text{Møl}}$ from the center-of-mass frame to the laboratory frame. In particle physics, the cross section is defined in such a way to be Lorentz invariant, cf. equation (F.1) where $d\sigma$ is expressed in terms of Lorentz-invariant factors, hence boosting $\sigma_{\text{ann}} v_{\text{Møl}}$ just means boosting $v_{\text{Møl}}$. According to its definition (5.5), the Møller velocity transforms under a Lorentz transformation as the inverse of an energy square since the flux is Lorentz invariant. In particular, transforming from the center-of-mass to the laboratory frame we get

$$\begin{aligned}(v_{\text{Møl}})_{\text{lab}} &= \frac{\sqrt{(p_1 \cdot p_2)^2 - M^4}}{\gamma(\sqrt{\boldsymbol{p}^2 + M^2} - \boldsymbol{p}\cdot\boldsymbol{v})\,\gamma(\sqrt{\boldsymbol{p}^2 + M^2} + \boldsymbol{p}\cdot\boldsymbol{v})} = \frac{(v_{\text{Møl}})_{\text{cm}}}{\gamma^2\,(1 - (\boldsymbol{p}\cdot\boldsymbol{v})^2/(\boldsymbol{p}^2 + M^2))} \\ &= (v_{\text{Møl}})_{\text{cm}}\left(1 - \frac{\boldsymbol{P}^2}{4M^2} + \dots\right),\end{aligned} \tag{5.17}$$

where $\gamma = 1/\sqrt{1 - \boldsymbol{v}^2}$ is the Lorentz factor, $\boldsymbol{v}$ is the center-of-mass velocity, $\boldsymbol{p}$ the relative momentum in the center-of-mass frame, $\boldsymbol{P}$ the center-of-mass momentum in the laboratory frame and the dots stand for higher-order terms in the $1/M$ expansion. Therefore, Lorentz-boosting eq. (5.9) to the laboratory frame leads precisely to eq. (5.16).

5.2 pNRQED$_{\text{DM}}$: Sommerfeld-enhanced annihilations and decays

Concerning the annihilation of dark fermions and antifermions, we accounted only for velocity suppressed operators and radiative corrections in $\alpha(2M)$ to the annihilation cross section so far, but not for the multiple soft photon rescatterings, which is important near threshold. Multiple soft dark photon exchanges between the annihilating dark fermion-antifermion pair modify the fermion-antifermion wavefunction near threshold and lead to a significant change in the annihilation cross section. These soft photon exchanges are already encoded in pNRQED$_{\text{DM}}$ in the potential (4.4). The fermion-antifermion wavefunction in pNRQED$_{\text{DM}}$, which at leading order in the multipole expansion is the solution of the Schrödinger equation with the potential (4.4), accounts by construction for the effect of multiple soft photon rescattering. The four-fermion operators responsible for annihilation in NRQED$_{\text{DM}}$ give rise to contact potentials in pNRQED$_{\text{DM}}$,

$$\mathcal{L}_{\text{pNRQED}_{\text{DM}}} \supset -\int d^3r\; \phi^\dagger(t, \boldsymbol{r}, \boldsymbol{R})\; \delta V^{\text{ann}}\; \phi(t, \boldsymbol{r}, \boldsymbol{R}), \tag{5.18}$$

and the annihilation process of S- and P-wave fermion-antifermion pairs is described by the imaginary local potential [116]

$$\begin{aligned}
\mathrm{Im}\,[\delta V^{\mathrm{ann}}] &= -\frac{\delta^3(\boldsymbol{r})}{M^2}\left[2\mathrm{Im}\,[d_s] - \boldsymbol{S}^2\left(\mathrm{Im}\,[d_s] - \mathrm{Im}\,[d_v]\right)\right] \\
&+ \frac{\mathcal{T}^{ij}_{SJ}}{M^4}\boldsymbol{\nabla}^i_{\boldsymbol{r}}\left[\delta^3(\boldsymbol{r})\boldsymbol{\nabla}^j_{\boldsymbol{r}}\,\mathrm{Im}\left[f(^{2S+1}P_J)\right]\right] + \frac{\Omega^{ij}_{SJ}}{2M^4}\left\{\boldsymbol{\nabla}^i_{\boldsymbol{r}}\boldsymbol{\nabla}^j_{\boldsymbol{r}}\,,\,\delta^3(\boldsymbol{r})\right\}\mathrm{Im}\left[g(^{2S+1}P_J)\right] \\
&+ \frac{\delta^3(\boldsymbol{r})}{M^4}\nabla^i_{\boldsymbol{R}}\nabla^j_{\boldsymbol{R}}\left[2\,\mathrm{Im}\,[g_{\mathrm{c\,cm}}]\,\delta_{ij} - \boldsymbol{S}^2\left(\mathrm{Im}\,[g_{\mathrm{c\,cm}}] - \mathrm{Im}\,[g_{\mathrm{a\,cm}}]\right)\delta_{ij} + S^iS^j\,\mathrm{Im}\,[g_{\mathrm{b\,cm}}]\right]\,,
\end{aligned} \tag{5.19}$$

where an implicit summation over the total spin S and total angular momentum J index is understood, and the operators $\mathcal{T}^{ij}_{SJ}$, Ω^{ij}_{SJ} are written in terms of the spin as [116, 119]

$$\begin{aligned}
&\Omega^{ij}_{00} = \delta^{ij}(2-\boldsymbol{S}^2)\,,\ \ \Omega^{ij}_{11} = \delta^{ij}\boldsymbol{S}^2\,,\ \ \Omega^{ij}_{11}(^3S_1, {}^3D_1) = S^iS^j - \frac{\delta^{ij}}{3}\boldsymbol{S}^2\,, \\
&\mathcal{T}^{ij}_{01} = \delta^{ij}(2-\boldsymbol{S}^2)\,,\ \ \mathcal{T}^{ij}_{10} = \frac{1}{3}S^iS^j\,,\ \ \mathcal{T}^{ij}_{11} = \frac{1}{2}\epsilon^{kia}\epsilon^{kja'}S^aS^{a'}\,,\ \ \mathcal{T}_S \equiv \frac{1}{3}\Omega^{ii}_{SS}\,, \\
&\mathcal{T}^{ij}_{12} = \left[\frac{1}{2}(\delta^{ik}S^a + \delta^{ia}S^k) - \frac{1}{3}\delta^{ka}S^i\right]\left[\frac{1}{2}(\delta^{jk}S^a + \delta^{ja}S^k) - \frac{1}{3}\delta^{ka}S^j\right] = \frac{1}{2}\delta^{ij}\boldsymbol{S}^2 + \frac{1}{6}S^iS^j\,.
\end{aligned} \tag{5.20}$$

In equation (5.19), the expression in the first line encodes the S-wave annihilation at leading order, the second expression in the second row its correction at first order in the relative momentum and the expressions in the third line its correction at first order in the center-of-mass momentum. The first expression in the second line describes the P-wave annihilation at leading order.

5.2.1 Radiative vs. velocity corrections

The resummation of multiple soft photon exchanges within the dark fermion-antifermion pair leads to a modification of the pair wavefunction close to threshold from free to either a bound-state wavefunction or a scattering wavefunction. This modification ultimately alters the annihilation cross section and decay width. The spin averaged annihilation cross section may be computed from the optical theorem analogously to eq. (5.4):

$$\sigma_{\mathrm{ann}}v_{\mathrm{M\o l}} = \frac{\mathrm{Im}[\mathcal{M}_{\mathrm{NR}}(\phi\to\phi)]}{2}\,, \tag{5.21}$$

where the amplitude $\mathcal{M}_{\mathrm{NR}}(\phi\to\phi)$ describes the propagation of the fermion-antifermion field ϕ projected on scattering states. The amplitude is given by the expectation value of $-\mathrm{Im}\,[\delta V^{\mathrm{ann}}]$ on the fermion-antifermion wavefunction for scattering states.[6] Considering

[6] To be more explicit:

$$\mathrm{Im}[\mathcal{M}_{\mathrm{NR}}(\phi\to\phi)] = -\sum_{S=0,1}\sum_{m_S=0,\pm1}\int d^3r\ \langle \boldsymbol{p},\boldsymbol{P},S,m_S|\phi^\dagger(\boldsymbol{r},\boldsymbol{R},t)\,\mathrm{Im}\,[\delta V^{\mathrm{ann}}]\,\phi(\boldsymbol{r},\boldsymbol{R},t)|\boldsymbol{p},\boldsymbol{P},S,m_S\rangle\,.$$

all terms listed in (5.19), we obtain for the spin-averaged annihilation cross section at leading order in $\alpha(2M)$ in the laboratory frame[7]

$$
\begin{aligned}
(\sigma_{\rm ann} v_{\rm M\o l})_{\rm lab}\,(\boldsymbol{p},\boldsymbol{P}) &= \frac{\mathrm{Im}[d_s]_{\rm LO} + 3\,\mathrm{Im}[d_v]_{\rm LO}}{M^2}\,\Big(|\Psi_{\boldsymbol{p}}(\boldsymbol{0})|^2\Big)_{\rm lab} \\
&+ \frac{\mathrm{Im}[f(^3P_0)] + 5\,\mathrm{Im}[f(^3P_2)]}{3M^4}\int d^3r_{\rm lab}\;\delta^3(\boldsymbol{r}_{\rm lab})\,\big[\boldsymbol{\nabla}_{\boldsymbol{r}}\Psi^*_{\boldsymbol{p}}(\boldsymbol{r})\big]_{\rm lab}\cdot\big[\boldsymbol{\nabla}_{\boldsymbol{r}}\Psi_{\boldsymbol{p}}(\boldsymbol{r})\big]_{\rm lab} \\
&- \frac{\mathrm{Im}[g(^1S_0)] + 3\,\mathrm{Im}[g(^3S_1)]}{2M^4}\int d^3r_{\rm lab}\;\delta^3(\boldsymbol{r}_{\rm lab})\,\Big[\big[\Delta_{\boldsymbol{r}}\Psi^*_{\boldsymbol{p}}(\boldsymbol{r})\big]_{\rm lab}\,(\Psi_{\boldsymbol{p}}(\boldsymbol{r}))_{\rm lab} \\
&\qquad\qquad + \big(\Psi^*_{\boldsymbol{p}}(\boldsymbol{r})\big)_{\rm lab}\,\big[\Delta_{\boldsymbol{r}}\Psi_{\boldsymbol{p}}(\boldsymbol{r})\big]_{\rm lab}\Big] \\
&- \frac{\mathrm{Im}\,[g_{\rm c\,cm}] + 3\,\mathrm{Im}\,[g_{\rm a\,cm}]}{M^4}\int d^3r_{\rm lab}\;\delta^3(\boldsymbol{r}_{\rm lab})\,\big(\Psi^*_{\boldsymbol{p},\boldsymbol{P}}(\boldsymbol{r},\boldsymbol{R},t)\big)_{\rm lab}\,\big[\Delta_{\boldsymbol{R}}\Psi_{\boldsymbol{p},\boldsymbol{P}}(\boldsymbol{r},\boldsymbol{R},t)\big]_{\rm lab}
\end{aligned}
\tag{5.22}
$$

where we drop the subscript LO in the matching coefficients of the associated dimension-eight operators, and show only terms with non-vanishing Wilson coefficients at $\mathcal{O}(\alpha^2)$, cf. eqs. (5.13)–(5.15). Terms involving the imaginary matching coefficient $\mathrm{Im}\left[g(^3S_1, {}^3D_1))\right]$ cancel out once we evaluate the spin operators projected on the scattering state, cf. footnote 6. We compute the integrals over the relative distance $\boldsymbol{r}_{\rm lab}$,[8] and the spin-averaged S-wave annihilation cross section in the laboratory frame at leading order in α and at order $\boldsymbol{p}^2_{\rm lab}/M^2$ and $\boldsymbol{P}^2/M^2$ in the relative and center-of-mass momentum, respectively, reads therefore,[9]

[7] The full spatial scattering-state wavefunction in the laboratory frame, cf. (4.6), is $\Psi_{\boldsymbol{p},\boldsymbol{P}}(\boldsymbol{r},\boldsymbol{R},t) = e^{-iE_p t + i\boldsymbol{P}\cdot\boldsymbol{R}}\,\Psi_{\boldsymbol{p}}(\boldsymbol{r})$. Hence it follows that $\Psi^*_{\boldsymbol{p},\boldsymbol{P}}(\boldsymbol{r},\boldsymbol{R},t)\,[\Delta_{\boldsymbol{R}}\Psi_{\boldsymbol{p},\boldsymbol{P}}(\boldsymbol{r},\boldsymbol{R},t)] = (-\boldsymbol{P}^2)\,|\Psi_{\boldsymbol{p}}(\boldsymbol{r})|^2$.

[8] In order to evaluate the integrals in the second line, we can perform the partial-wave decomposition of the wavefunction and use the vector spherical harmonics $\vec{\Psi}^m_\ell(\hat{\boldsymbol{r}}) = r\,\boldsymbol{\nabla}_{\boldsymbol{r}} Y^m_\ell(\hat{\boldsymbol{r}})$, together with the completeness relations

$$
\int d\Omega\,\vec{\Psi}^m_\ell(\hat{\boldsymbol{r}})\cdot\Big(\vec{\Psi}^{m'}_{\ell'}(\hat{\boldsymbol{r}})\Big)^* = \ell(\ell+1)\delta_{\ell,\ell'}\delta_{m,m'}\,,\quad \sum_{m=\ell}^{\ell}\vec{\Psi}^m_\ell(\hat{\boldsymbol{r}})\cdot\Big(\vec{\Psi}^m_\ell(\hat{\boldsymbol{r}})\Big)^* = \frac{2\ell+1}{4\pi}\,.
$$

As for the integrals in the third and fourth line of (5.22), we can use the Schrödinger equation with respect to the relative motion at leading order in the potential and in the energy of the scattering state, and substitute $\Delta_{\boldsymbol{r}}\Psi_{\boldsymbol{p}}(\boldsymbol{r}) = (-\boldsymbol{p}^2 - M\alpha/r)\Psi_{\boldsymbol{p}}(\boldsymbol{r})$. The integration of the first term is straightforward, however the second term involving the Coulomb potential is infrared divergent. If we regularize the three-dimensional integral in dimensional regularization, then we can show that it vanishes:

$$
\int d^3r\,\delta^3(\boldsymbol{r})|\Psi_{\boldsymbol{p}}(\boldsymbol{r})|^2\frac{1}{r} \;=\; \int d^3r\,\delta^3(\boldsymbol{r})|\Psi_{\boldsymbol{p}}(\boldsymbol{r})|^2\int d^3k\,e^{i\boldsymbol{k}\cdot\boldsymbol{r}}\frac{4\pi}{\boldsymbol{k}^2} \;=\; |\Psi_{\boldsymbol{p}}(\boldsymbol{0})|^2\int d^3k\,\frac{4\pi}{\boldsymbol{k}^2} \;=\; 0\,,
$$

because the integral in $\boldsymbol{k}$ is scaleless. Dimensional regularization is the correct choice, since the matching between the EFTs is done in this particular scheme.

[9] Since the terms in eq. (5.22) involving the integrals in $\boldsymbol{r}_{\rm lab}$ are already of order $1/M^4$, we can approximate those integrals by the ones in the center-of-mass frame, since corrections due to this substitution would be of higher order than $\mathcal{O}(\boldsymbol{p}^2_{\rm lab}/M^2, \boldsymbol{P}^2/M^2)$. It simplifies the computation, because we can use the analytic expression (C.4) for the wavefunction of the scattering state in the center-of-mass frame. More information about Lorentz-boost transformations of heavy-pair wavefunctions between different reference frames is given in sec. A.2.

$$
\begin{aligned}
&(\sigma_{\rm ann} v_{\rm M\o l})_{\rm lab}\,(\boldsymbol{p},\boldsymbol{P}) \\
&\quad = (1+n_f)\frac{\pi\alpha^2}{M^2}\,\left(|\Psi_{\boldsymbol{p}0}(\boldsymbol{0})|^2\right)_{\rm lab}(\boldsymbol{P})\left(1-\frac{\boldsymbol{P}^2}{4M^2}\right) \\
&\qquad + (1+n_f)\frac{\pi\alpha^2}{M^2}\,\left(|\Psi_{\boldsymbol{p}0}(\boldsymbol{0})|^2\right)_{\rm cm}\left[-\frac{4\boldsymbol{p}_{\rm cm}^2}{3M^2}+\frac{7\boldsymbol{p}_{\rm cm}^2}{3M^2}\left(\frac{1+(a_0|\boldsymbol{p}_{\rm cm}|)^{-2}}{1+n_f}\right)\right]\,, \qquad (5.23)
\end{aligned}
$$

where the index 0 in the squared wavefunctions denotes that only the partial wave with $\ell = 0$ contributes at the origin $\boldsymbol{r} = \boldsymbol{0}$ (note that the information about the P-wave annihilation is encoded in the term involving the prefactor $(1+(a_0|\boldsymbol{p}_{\rm cm}|)^{-2})$. According to eq. (A.32), we can replace $\left(|\Psi_{\boldsymbol{p}0}(\boldsymbol{0})|^2\right)_{\rm lab}(\boldsymbol{P})$ with the corresponding quantity in the center-of-mass frame, $\left(|\Psi_{\boldsymbol{p}0}(\boldsymbol{0})|^2\right)_{\rm cm} \equiv S_{\rm ann}(\zeta)$, where $S_{\rm ann}(\zeta)$ is called *Sommerfeld factor* [65] and reads (see e.g. [120, 121])

$$
S_{\rm ann}(\zeta) = \frac{2\pi\zeta}{1-e^{-2\pi\zeta}}\,, \qquad\qquad \zeta \equiv \frac{\alpha(\mu_{\rm s})}{v_{\rm rel}} = \frac{1}{a_0|\boldsymbol{p}_{\rm cm}|}\,. \qquad (5.24)
$$

where $\alpha(\mu_{\rm s})$ is evaluated at the soft scale $\mu_{\rm s} \sim M\alpha$, and we remind that $\alpha = \alpha(2M)$. Hence, the spin-averaged S-wave annihilation cross section in the laboratory frame at leading order in α and at order $\boldsymbol{P}^2/M^2$, $\boldsymbol{p}^2/M^2$ can be written as

$$
\begin{aligned}
(\sigma_{\rm ann} v_{\rm M\o l})_{\rm lab}\,(\boldsymbol{p},\boldsymbol{P}) &= (\sigma_{\rm ann}^{\rm NR} v_{\rm rel})_{\rm LO}\, S_{\rm ann}(\zeta) \\
&\quad \times\left[1-\frac{\boldsymbol{P}^2}{4M^2}-\frac{4\boldsymbol{p}_{\rm cm}^2}{3M^2}+\frac{7\boldsymbol{p}_{\rm cm}^2}{3M^2}\left(\frac{1+(a_0|\boldsymbol{p}_{\rm cm}|)^{-2}}{1+n_f}\right)\right]\,, \qquad (5.25)
\end{aligned}
$$

where $p_{\rm cm} \equiv |\boldsymbol{p}_{\rm cm}|$ and $(\sigma_{\rm ann}^{\rm NR} v_{\rm rel})_{\rm LO}$ has been defined in eq. (5.11). In the above expression, the center-of-mass relative momentum $\boldsymbol{p}_{\rm cm}$ in the Sommerfeld factor is expressed in terms of the relative momentum in the laboratory frame through eq. (A.17), while the $\boldsymbol{p}_{\rm cm}$ in the square brackets in (5.25) can be substituted directly by the relative momentum in the laboratory frame.

In the center-of-mass frame, instead, the spin averaged annihilation cross section at $\mathcal{O}(\alpha^2, v_{\rm rel}^2)$ becomes (note that the subscript cm and lab on the left-hand side of (5.26) and (5.25), respectively, means that the momenta are taken in that specific reference frame)[10]

$$
(\sigma_{\rm ann} v_{\rm rel})_{\rm cm}(\boldsymbol{p}) = (\sigma_{\rm ann}^{\rm NR} v_{\rm rel})_{\rm LO}\,\left[\left(1-\frac{5}{24}v_{\rm rel}^2\right)S_{\rm ann}(\zeta)+\frac{7}{12}\frac{v_{\rm rel}^2}{1+n_f}S_{\rm ann}^{\ell=1}(\zeta)\right]\,, \qquad (5.26)
$$

where $S_{\rm ann}^{\ell=1}(\zeta) = (1+\zeta^2)S_{\rm ann}(\zeta)$ is the Sommerfeld enhancement for a scattering state in a P-wave [120,121]. We observe that even at leading order in the non-relativistic velocity

[10] Note that in order to obtain the result (5.26) from the previous eq. (5.25) (upon switching to the center-of-mass frame, i.e. $\boldsymbol{P} = \boldsymbol{0} \to \boldsymbol{p}_{\rm lab} = \boldsymbol{p}_{\rm cm}$, $(v_{\rm M\o l})_{\rm lab} = (v_{\rm M\o l})_{\rm cm}$), one has to insert (5.8) for the Møller velocity in the center-of-mass frame, expand the whole equation up to order $(\boldsymbol{p}_{\rm cm}/M)^2$, and finally rewrite $\boldsymbol{p}_{\rm cm} = M\boldsymbol{v}_{\rm rel}/2$ in terms of the relative velocity in the center-of-mass frame.

expansion (upon neglecting the local potentials of higher order in pNRQED$_{\rm DM}$ (second and third row in (5.19)) that arise from the associated dimension-eight four-fermion operators in NRQED$_{\rm DM}$) where only S-waves do annihilate, the corresponding annihilation cross section is $\boldsymbol{p}$-dependent due to the Sommerfeld factor being still persistent, i.e.

$$(\sigma^{\rm NR}_{\rm ann} v_{\rm rel})_{\rm cm}(\boldsymbol{p}) = (\sigma^{\rm NR}_{\rm ann} v_{\rm rel})\, S_{\rm ann}(\zeta)\,, \tag{5.27}$$

where we consider the momentum-independent free S-wave annihilation cross section $(\sigma^{\rm NR}_{\rm ann} v_{\rm rel})$, defined (5.9), to encompass also radiative corrections of order α^3. Equation (5.27) shows manifestly the factorization of the different energy scales: the hard dynamics is contained in the NRQED$_{\rm DM}$ matching coefficients $\mathrm{Im}(d_s)$ and $\mathrm{Im}(d_v)$, whereas the soft dynamics is contained in the wavefunction squared $|\Psi_{\boldsymbol{p}0}(\boldsymbol{0})|^2$. For $v_{\rm rel} \lesssim \alpha$, the annihilation cross section is significantly enhanced by the Sommerfeld factor and the prediction from the Boltzmann equation (2.6) on the DM particle density n changes accordingly.[11]

Our aim in the following is to examine the relative importance of NLO radiative corrections to the hard matching coefficients $\mathrm{Im}[d_s]$ and $\mathrm{Im}[d_v]$, which are corrections of order α^3, with respect to the leading relativistic corrections in the relative and total velocity of the dark fermion-antifermion pair.[12] In the center-of-mass frame, it means that we compare the annihilation cross section (5.26), which is of order α^2 and $v^2_{\rm rel}$ and hence comprises S- and P-wave annihilations at leading order in the coupling, with the S-wave annihilation cross section (5.26) of order α^3 and $v^0_{\rm rel}$. In the left panel of fig. 5.3, we plot the annihilation cross section in the center-of-mass frame at different orders of accuracy as a function over M/T from regions around the freeze-out (here $T = M/10$) up to late times, where $T = M/10^5$. The coupling is fixed at the hard scale, $\alpha = \alpha(2M) = 0.1$, and runs at one loop. The cross section is thermally averaged according to (B.15), because the thermal motion of the bath can be neglected at the hard annihilation scale, and normalized by $\pi\alpha^2/M^2$, which corresponds to the free annihilation cross section into two photons at LO in α and zeroth order in the velocity in the center-of-mass frame. As expected, the NLO correction to the matching coefficients decreases the annihilation cross section (dashed lines are below the dotted lines), while velocity corrections increase it (solid lines are above the dotted lines). The cross sections grow monotonically with decreasing temperature due to the Sommerfeld enhancement, and increasing the number n_f of light fermions in the model increases the cross section due to the additional annihilation channels (black lines above orange lines). Then on the

[11] A derivation of the Sommerfeld enhancement for S-wave pair annihilation that includes the regime of very small momenta (velocities) for the unbound pair has been presented in [66,122,123]. The main result is a saturation of the Sommerfeld factor and a regular behaviour for $v_{\rm rel} \to 0$. Diagrammatically this amounts to resum the annihilation term, namely the local four-fermion interactions shown in figure 5.1 (right). In this work, we assume to be away from such regime for unbound states. For bound states this resummation is never needed because the momentum of the particle in the pair is constrained to be of order $M\alpha$. Finally, it is worth noticing that the thermally averaged cross section (B.15) removes the singularity at vanishing $v_{\rm rel}$.

[12] Relativistic corrections also affect the dark fermion-antifermion pair wavefunctions. We do not consider these corrections here.

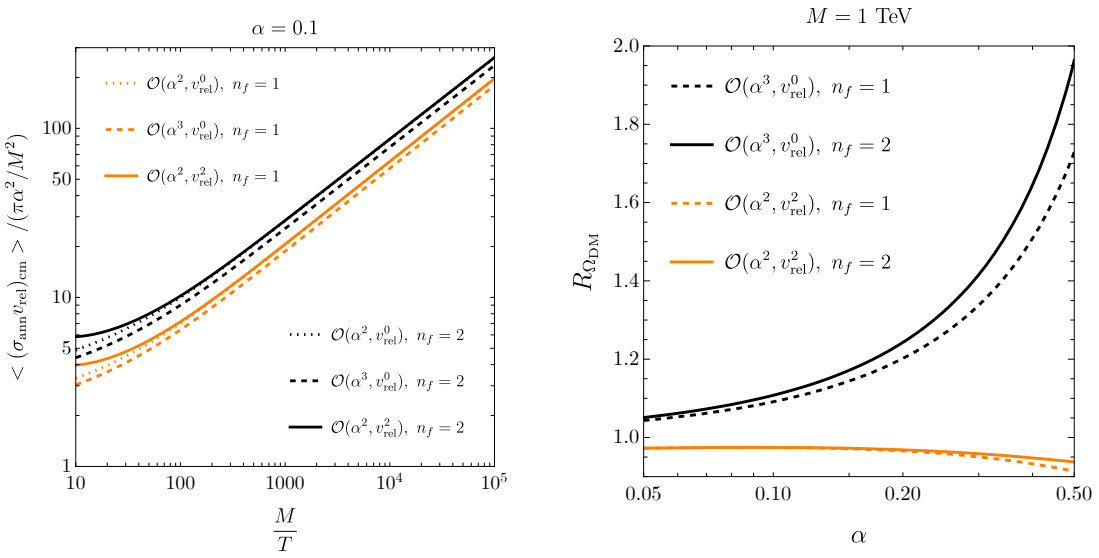

Figure 5.3: (Left) Thermally averaged annihilation cross section in the center-of-mass frame, normalized by $\pi\alpha^2/M^2$, at different orders in the radiative α-expansion and relativistic $v_{\rm rel}$-expansion; plotted as a function of M/T and the coupling runs at one loop with starting value $\alpha = \alpha(2M) = 0.1$. Orange lines are for $n_f = 1$, black lines for $n_f = 2$. (Right) Ratios of the present relic densities, showing either radiative corrections (black lines) or velocity corrections (orange lines); as a function of $\alpha = \alpha(2M)$. Dashed lines are for $n_f = 1$, solid lines for $n_f = 2$.

right panel of fig. 5.3, we visualize the numerical impact of the α- and $v_{\rm rel}$-corrections on the present DM energy density $\Omega_{\rm DM}h^2$. We therefore plot the ratio $R_{\Omega_{\rm DM}}$ of $\Omega_{\rm DM}h^2$, as obtained from the S-wave annihilation cross section with matching coefficients at $\mathcal{O}(\alpha^3)$, over the present energy density when the matching coefficients are of order α^2 (black lines). We do the same for the velocity corrections and matching coefficients at LO (orange lines), and plot the ratios over the coupling $\alpha = \alpha(2M)$. In order to get the present relic density, we solve the Boltzmann equation (2.9) up to $T = M/10^5$, and relate the numerical result for the yield Y_0 to the present relic abundance $\Omega_{\rm DM}h^2 \sim Y_0$. As already elaborated before, the NLO corrections to the matching coefficients make the cross section smaller, and hence a more abundant dark matter population is found for each value of α; with the largest increase by almost a factor of two for $\alpha = 0.5$ and $n_f = 2$ (black solid line). Accordingly, we find $R_{\Omega_{\rm DM}} > 1$, as shown in the plot. As for the velocity corrections, the trend is different. The corrections to the cross section make it larger for each α, and accordingly we find a smaller DM energy density that results in $R_{\Omega_{\rm DM}} < 1$. The P-wave contribution overcomes the negative correction of the velocity dependent S-wave correction, especially at large values of α; the largest decrease is by about 10% for $\alpha = 0.5$ and $n_f = 1$. Hence, we conclude that the radiative corrections to the annihilation process have a stronger impact on the present relic abundance than the relativistic velocity corrections. In the weak-coupling regime up to $\alpha(2M) \lesssim 0.1$,

however, the individual corrections on the present relic density are of the more or less of same order and do barely depend on the number n_f of the light fermions. The α-corrections increase $\Omega_{\rm DM}h^2$ up to 7–10%, while the $v_{\rm rel}$-corrections decrease it by about 5%. Hence it seems that at the level of the present relic abundance the radiative and relativistic velocity corrections partly balance each other as long as the couplings are sufficiently small. We checked that the results have a rather mild dependence on the specific value of the DM mass, and for the right plot in fig. 5.3 it is set to the specific value $M = 1$ TeV.

As a final remark, if we discard the resummation of the soft scale, i.e. neglect the Coulomb rescattering effects from multiple soft photon exchanges by setting ζ to zero, from which it follows that $S_{\rm ann}(0) = S^{\ell=1}_{\rm ann}(0) = 1$, we recover the result (F.3) in appendix F.1, which corresponds to the annihilation cross section one would obtain in NRQED$_{\rm DM}$ from the dimension-six and dimension-eight four-fermion operators, cf. (5.12), by applying the optical theorem (5.4) in the center-of-mass frame. Appendix F is devoted to an alternative study of the annihilation processes without the usage of the EFT-formalism, especially in sec. F.2 we follow the Bethe–Salpeter approach to incorporate the Sommerfeld effect at the diagrammatic level, while in pNRQED$_{\rm DM}$, cf. eq. (4.2), it is already built-in due to the emergence of the potential and Coulombic wavefunctions.

5.2.2 Lorentz-boost behaviour among reference frames

At the order of $\boldsymbol{P}^2/M^2$ and $\boldsymbol{p}^2/M^2$ in the non-relativistic velocity expansion, and by comparing the annihilation cross section in the laboratory frame, eq. (5.25), with the annihilation cross section in the center-of-mass frame, cf. eq. (5.26), we observe that

$$(\sigma_{\rm ann} v_{\rm Møl})_{\rm lab}\,(\boldsymbol{p},\boldsymbol{P}) = (\sigma_{\rm ann} v_{\rm Møl})_{\rm cm}\,(\boldsymbol{p})\left(1-\frac{\boldsymbol{P}^2}{4M^2}\right), \tag{5.28}$$

which represents again the Lorentz transformation property of the Møller velocity with respect to boosts from the center-of-mass to the laboratory frame, cf. equation (5.17). Hence Lorentz-boost invariance of the annihilation cross section $\sigma_{\rm ann}$ is not violated by the soft-photon resummation and therefore by the Sommerfeld effect, and the Lorentz-boost relation (5.28) between the two reference frames equals the relation (5.16) in NRQED$_{\rm DM}$.

Apart from annihilation processes of scattering states, in pNRQED$_{\rm DM}$ heavy dark fermion-antifermion bound pairs can annihilate as well. At leading order in α, spin-singlet bound states, paradarkonia, decay via annihilation into two dark photons, while spin-triplet bound states, orthodarkonia, decay into two light dark fermions. The decay width can be computed from

$$\Gamma_{\rm ann} = 2\,{\rm Im}[\mathcal{M}_{\rm NR}(\phi\to\phi)]\,, \tag{5.29}$$

which is analogous to eq. (5.21), but now we do not average over the spin of the initial states as we project ϕ onto the specific bound state that is decaying. Proceeding like

in the case of the annihilation cross section, it follows that the paradarkonium S-wave annihilation width in the laboratory frame at order $\boldsymbol{P}^2/M^2$, $\alpha(2M)^2$ and $\alpha(\mu_{\rm s})^2$ (the latter coming from the $1/M^4$ local potentials with respect to the relative motion) is given by

$$\begin{aligned}(\Gamma_{\rm ann}^{n,\rm para})_{\rm lab}(\boldsymbol{P}) = \frac{4{\rm Im}\,[d_s]_{\rm LO}}{M^2}\,\left(|\Psi_{n00}(\boldsymbol{0})|^2\right)_{\rm lab}(\boldsymbol{P})\,\left(1-\frac{\boldsymbol{P}^2}{4M^2}\right)\\ +\frac{4{\rm Im}\,[d_s]_{\rm LO}}{M^2}\,\left(|\Psi_{n00}(\boldsymbol{0})|^2\right)_{\rm cm}\,\frac{1}{3}\left(\frac{\alpha(\mu_{\rm s})}{2n}\right)^2,\end{aligned} \tag{5.30}$$

where the term in the second line comes from the local potential involving the imaginary matching coefficient ${\rm Im}\left[g(^1S_0)\right]$, that has been rewritten as $-4\,{\rm Im}\,[d_s]_{\rm LO}/3$ according to eq. (5.13). In a similar way we obtain for the orthodarkonium S- and P-wave annihilation width

$$\begin{aligned}\left(\Gamma_{\rm ann}^{n,\rm ortho}\right)_{\rm lab}(\boldsymbol{P}) = \frac{4{\rm Im}\,[d_v]_{\rm LO}}{M^2}\,\left(|\Psi_{n00}(\boldsymbol{0})|^2\right)_{\rm lab}(\boldsymbol{P})\,\left(1-\frac{\boldsymbol{P}^2}{4M^2}\right)\\ +\frac{4{\rm Im}\,[d_v]_{\rm LO}}{M^2}\,\left(|\Psi_{n00}(\boldsymbol{0})|^2\right)_{\rm cm}\,\frac{1}{3}\left(\frac{\alpha(\mu_{\rm s})}{2n}\right)^2\left[1+7\frac{n^2-1}{n_f}\right],\end{aligned} \tag{5.31}$$

where in the second line the first term in the square brackets comes from the local potential involving the imaginary matching coefficient ${\rm Im}\left[g(^3S_1)\right]$ rewritten to $-4\,{\rm Im}\,[d_v]_{\rm LO}/3$ according to eq. (5.13), and the second term in the square brackets accounts for the spin-triplet P-wave annihilations (that vanishes for the ground state, where $n=1$). Using eq. (A.31), we can replace $\left(|\Psi_{n00}(\boldsymbol{0})|^2\right)_{\rm lab}(\boldsymbol{P})$ with $\gamma\left(|\Psi_{n00}(\boldsymbol{0})|^2\right)_{\rm cm} \approx (1+\boldsymbol{v}^2/2)\left(|\Psi_{n00}(\boldsymbol{0})|^2\right)_{\rm cm} = (1+\boldsymbol{P}^2/(8M^2))\left(|\Psi_{n00}(\boldsymbol{0})|^2\right)_{\rm cm}$. We then get for the paradarkonium S-wave annihilation width in the laboratory frame at leading order in $\alpha(2M)$ and at order $\boldsymbol{P}^2/M^2$ and $\alpha(\mu_{\rm s})^2$ (terms proportional to $\alpha(\mu_{\rm s})^2\times(\boldsymbol{P}^2/M^2)$ are of higher order)

$$(\Gamma_{\rm ann}^{n,\rm para})_{\rm lab}(\boldsymbol{P}) = \frac{4{\rm Im}\,[d_s]_{\rm LO}}{M^2}\left(|\Psi_{n00}(\boldsymbol{0})|^2\right)_{\rm cm}\left[1-\frac{\boldsymbol{P}^2}{8M^2}+\frac{1}{3}\left(\frac{\alpha(\mu_{\rm s})}{2n}\right)^2\right], \tag{5.32}$$

and similarly for the orthodarkonium decay width:[13]

$$\begin{aligned}\left(\Gamma_{\rm ann}^{n,\rm ortho}\right)_{\rm lab}(\boldsymbol{P}) = \frac{4{\rm Im}\,[d_v]_{\rm LO}}{M^2}\left(|\Psi_{n00}(\boldsymbol{0})|^2\right)_{\rm cm}\\ \times\left[1-\frac{\boldsymbol{P}^2}{8M^2}+\frac{1}{3}\left(\frac{\alpha(\mu_{\rm s})}{2n}\right)^2\left(1+7\frac{n^2-1}{n_f}\right)\right],\end{aligned} \tag{5.33}$$

[13]We notice that there is a profound connection between the $v_{\rm rel}$-corrections to the annihilation cross section, cf. eq. (5.25), and the $\alpha(\mu_{\rm s})$-corrections to the decay widths (5.32) and (5.33). One can relate at leading order in quantum mechanics the relative momentum of a scattering state with the Bohr momentum of a bound state through the correspondence $p_{\rm cm} \leftrightarrow i\frac{M\alpha(\mu_{\rm s})}{2n}$, i.e. $v_{\rm rel} \leftrightarrow i\,\alpha(\mu_{\rm s})/n$.

which is now expressed in terms of the square of the bound-state wavefunction in the center-of-mass frame at the origin, $\left(|\Psi_{n00}(\mathbf{0})|^2\right)_{\rm cm} = |R_{n0}(\mathbf{0})|^2/(4\pi)$.[14]

Since $\frac{4\pi\alpha^2}{M^2}\left(|\Psi_{n00}(\mathbf{0})|^2\right)_{\rm cm}\left[1+\frac{1}{3}\left(\alpha(\mu_{\rm s})/(2n)\right)^2\right]$ is the paradarkonium annihilation width in the center-of-mass frame, $(\Gamma^{n,\rm para}_{\rm ann})_{\rm cm}$, eq. (5.32) simply states the expected Lorentz dilation of time intervals (upon neglecting $\mathcal{O}[\alpha(\mu_{\rm s})^2\times(\boldsymbol{P}^2/M^2)]$ terms):

$$(\Gamma^{n,\rm para}_{\rm ann})_{\rm lab}(\boldsymbol{P}) = \frac{(\Gamma^{n,\rm para}_{\rm ann})_{\rm cm}}{\gamma} \approx (\Gamma^{n,\rm para}_{\rm ann})_{\rm cm}\left(1-\frac{\boldsymbol{P}^2}{8M^2}\right). \tag{5.34}$$

The same relation also holds for the orthodarkonium decay width. We remark that the results for the decay widths (5.32) and (5.33) are valid only for bound states with quantum numbers n, $\ell=(0,1)$, $m=(0,\pm1)$, i.e. only for S- and P-waves. D-wave annihilations are generated from four-fermion operators of higher dimensionality than eight.

In computing annihilation cross sections and widths we have neglected the thermal distribution of the photons in the final state. This is justified by the fact that the energy of the final state photons is of order M. Therefore, according to the two hierarchies (3.2) and (3.4) considered in this work, the corresponding Bose–Einstein distribution is exponentially suppressed: $n_{\rm B}(M)\approx e^{-M/T}$.

[14]For the ground state it holds $|R_{10}(\mathbf{0})|^2 = 4/a_0^3 = (M\alpha)^3/2$, which leads to $\left(\Gamma^{1,\rm para}_{\rm ann}\right)_{\rm lab}(\boldsymbol{P}) = \frac{M\alpha(2M)^2\alpha(\mu_{\rm s})^3}{2}\left(1-\frac{\boldsymbol{P}^2}{8M^2}+\alpha(\mu_{\rm s})^2/6\right)$, where $M\alpha(2M)^2\alpha(\mu_{\rm s})^3/2$ is the 1S paradarkonium annihilation width at LO in the center-of-mass frame.

Chapter 6

Dipole transitions at finite temperature

In the laboratory frame, i.e. in the reference frame where the thermal bath is at rest and the center of mass of the dark fermion-antifermion pair is moving, near-threshold processes such as the formation of bound states or their dissociation into scattering states are due at order $\boldsymbol{r}$ in pNRQED$_{\rm DM}$ to the two dipole interaction operators in the second line of eq. (4.2). The corresponding vertices are shown in figure 4.1. The photons emitted or absorbed in the bound-state formation (*bsf*) and bound-state dissociation (*bsd*) processes respectively are below the *soft* scale, i.e. they carry energy and momentum of order smaller than $M\alpha$, which justifies the multipole expansion for a system that fulfills the hierarchy of energy scales for temperatures close to the freeze-out, cf. eq. (3.4), and for lower temperatures, cf. eq. (3.2).

Under the two hierarchies (3.2) and (3.4), the electric-dipole operator is the leading operator responsible for bound-state formation and bound-state dissociation. Together with kinetic energy corrections to the electric-dipole vertex, the magnetic-dipole vertex accounts for the leading correction to bound-state formation and bound-state dissociation due to the center-of-mass motion of the dark fermion-antifermion pair relative to the thermal bath. Its effect is suppressed by $P/M \sim v \sim \sqrt{T/M}$ (if $P \sim \sqrt{MT}$) with respect to the effect of the electric-dipole vertex. The dipole vertices induce bound-state to bound-state and scattering-state to scattering-state transitions as well, which amount to (de-)excitation processes and thermal (emission) absorption processes, respectively. Transitions among continuous scattering states of unbound pairs count as elastic processes, and thermal emissions are known under the name of *bremsstrahlung* processes.

The laboratory frame may be a convenient frame where to compute recoil effects, because thermal distributions have there a particularly simple form. For instance, the thermal distribution of photons in a thermal bath at rest is the Bose–Einstein distribution

$$n_{\rm B}(E) = \frac{1}{e^{E/T} - 1} \,. \tag{6.1}$$

The Bose–Einstein distribution for a moving thermal bath is given in eq. (6.65) and

requires the introduction of a velocity-dependent effective temperature. We will discuss the treatment of dipole transitions in the center-of-mass frame in more detail in section 6.1.2.2 for the bsf process, and in section 6.2.2 for the bsd process. We will mention it briefly also in case of (de-)excitation processes in sec. 6.3.

All these dipole processes among bound and scattering states happen at energy scales below the soft scale, and hence can be summarized to as *near-threshold* or *close-to-threshold* processes, where the threshold can be understood as the energy barrier separating unbound scattering states from bound states with negative binding energy. We will compute the associated interaction rates to these dipole processes at finite temperature, which involves propagators in the real-time formalism. The explicit expression of the photon propagator in Coulomb gauge at leading order is written in (D.4)–(D.5) and can be found in ref. [124], whereas the expression of the dark fermion-antifermion pair propagator, cf. (D.14), can be found in [51]. The light-fermion propagator is given in (D.15).[1]

6.1 Formation of bound states

We begin with the study of the bound-state formation process due to the dipole transitions in a dark thermal bath. In sec. 6.1.1 we will neglect the recoil effect by discarding the Röntgen term from the Lagrangian (4.2). In this way the formation of a bound state can only happen via the electric-dipole operator. In the subsequent sec. 6.1.2 we will reinstate it again, which allows additionally for the bound-state formation via the magnetic-dipole operator.

6.1.1 Cross section in the laboratory frame without recoil

We derive the bound-state formation cross section in the laboratory frame where the medium is at rest. This choice made, the cross section depends on the center of mass momentum $\boldsymbol{P}$. The center of mass momentum in the thermal average of the cross section times $v_{\rm rel}$ scales like $\sqrt{MT}$, which is the momentum scale in the Boltzmann distribution. Since $\sqrt{MT} \ll M$, we may systematically expand the rates in the center of mass momentum $\boldsymbol{P}/M$, and if we retain the leading order term, this amounts to set $\boldsymbol{P} = \boldsymbol{0}$ in the cross section,[2] which is our choice in the following sections (6.1.1.1) and (6.1.1.2).

[1] In real-time formalism, propagators are 2×2 matrices. However, the fermion-antifermion propagator gets a particularly simple form in the heavy-fermion limit, as thermal corrections are exponentially suppressed and the 12-component vanishes [48]. The interaction rates can be computed either from the imaginary part of the 11-component or from the 21-component of the associated self energy. In case of bound-state formation, the corresponding self-energy is depicted in fig. 6.1.

[2] We come to the same conclusion if we choose the reference frame of the center of mass of the dark fermion-antifermion pair. In this case, the velocity of the medium is about $\sqrt{T/M}$, which is much smaller than one, the velocity of light. Expanding in it, the thermal distribution of the dark photons reduces at leading order to the thermal distribution of the medium at rest, i.e. eq. (6.1) [125].

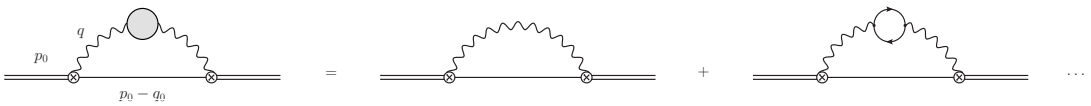

Figure 6.1: Self-energy diagram of the scattering state at dipole order r^2 and at zeroth order in velocity expansion (left-hand side). The diagram on the left-hand side involves a resummed dark electric-electric correlator (grey shaded loop), which can be expanded in the weakly coupled abelian model, here up to next-to-leading order in α, where the first diagram on the right-hand side is of order α and the second diagram is of order α^2. The external double solid lines represent the unbound pair, the internal single solid lines represent a bound state. The wavy lines denote the dark photon, the n_f light dark fermions in the loop are represented by single arrowed lines. These diagrams are generated by the electric-dipole interaction only, cf. left vertex in fig. 4.1.

6.1.1.1 Heavy-pair self-energy up to next-to-leading order

The bound-state formation cross section in the laboratory frame at leading order in $\boldsymbol{r}$ and at zeroth order in $\boldsymbol{P}$ can be determined from the self-energy diagram of the scattering state in figure 6.1.[3] From the optical theorem it follows that

$$(\sigma_{\rm bsf}\, v_{\rm M\o l})_{\rm lab}(\boldsymbol{p}) = -2\langle\, \boldsymbol{p}|{\rm Im}[\Sigma^{11}(p_0)]|\boldsymbol{p}\,\rangle_{\rm lab} = \langle\, \boldsymbol{p}|[-i\Sigma^{21}(p_0)]|\boldsymbol{p}\,\rangle_{\rm lab}\,, \tag{6.2}$$

where in the second equality we used the cutting rules at finite T, cf. ref. [126], in order to relate the imaginary part of the time-ordered self-energy to the 21-component of the self-energy Σ_s^{21}. [4] We refer the reader to appendix D for more details about the Schwinger-Keldysh contour and the associated CTP indices $\{1,2\}$, which lead to the four combinations $\{\Sigma^T, \Sigma^>, \Sigma^<, \Sigma^{\bar{T}} = (\Sigma^T)^*\}$ of the self-energy (and similarly for the propagators).

Since in this section we consider the incoming scattering state with vanishing total momentum, $\boldsymbol{P} = \boldsymbol{0}$, its energy $(p_0)_{\rm lab}$ and relative momentum $(\boldsymbol{p})_{\rm lab}$ equal the expressions in the center-of-mass frame, and $(v_{\rm M\o l})_{\rm lab} = v_{\rm rel}$. We will drop the subscript *lab* from now on. Hence $p_0 = E_p = 2M + \boldsymbol{p}^2/M$ at leading order, and in the laboratory frame where the thermal bath is static, we can freely choose the center-of-mass coordinate to be at the origin $\boldsymbol{R} = \boldsymbol{0}$. In dimensional regularization $D = 4 - 2\epsilon$, the physical

[3] In case of dissociations and bound-to-bound transitions, one has just to invert the double- and single-line heavy pair propagators in figure 6.1, or consider only single-line propagators, respectively. The photonic part and the vertices remain unchanged. For scattering-to-scattering transitions, only double-solid lines need to be considered.

[4] More explicitly, employing the cutting rules we get

$${\rm Im}[\Sigma^{11}] = -\frac{1}{2i}(\Sigma^> + \Sigma^<) \approx \frac{i}{2}\Sigma^>\,,$$

where the 12-component $\Sigma^<$ is exponentially suppressed due to the off-diagonal structure of the DM pair propagator, cf. (D.14).

11-component of the self-energy reads

$$\begin{aligned}\Sigma^{11}(p_0) &= -ig^2\int_0^\infty dt\; r^i e^{it(p_0-H)} r^j \langle E^i(t,\boldsymbol{R}) E^j(0,\boldsymbol{R}')\rangle^{11} \\ &= \frac{-ig^2}{D-1}\int_0^\infty dt\; r^i e^{it(p_0-H)} r^i \langle \boldsymbol{E}(t,0)\boldsymbol{E}(0,0)\rangle^{11} \\ &= \frac{-ig^2}{D-1}\int_0^\infty dt\; r^i e^{it(p_0-H)} \mu^{4-D}\int \frac{d^Dq}{(2\pi)^D} e^{-iq_0t} r^i \langle \boldsymbol{E}\boldsymbol{E}\rangle^{11}(q) \\ &= -ig^2\frac{\mu^{4-D}}{D-1}\int \frac{d^Dq}{(2\pi)^D} r^i \frac{i}{p_0-q_0-H+i\epsilon} r^i \langle \boldsymbol{E}\boldsymbol{E}\rangle^{11}(q)\,, \end{aligned} \tag{6.3}$$

where in the second equality we used the rotational symmetry in case of vanishing center-of-mass momentum of the heavy pair, and in the third equality we transformed the electric-electric correlator into momentum space. The time-ordered DM propagator enters as $i[p_0-q_0-H+i\epsilon]^{-1}$ in the last line of (6.3), and the dark electric field correlator can be written in terms of the dark photon two-point function

$$\begin{aligned}\langle E_i(x)E_i(0)\rangle &= (-\partial_0 g_{\mu i} + \partial_i g_{\mu 0})(\partial_0 g_{\nu i} - \partial_i g_{\nu 0})\langle A^\mu(x)A^\nu(0)\rangle \\ &= -\partial_0^2 D_{ii}(x) - \boldsymbol{\nabla}^2 D_{00}(x)\,,\end{aligned} \tag{6.4}$$

or equivalently in the momentum space

$$\begin{aligned}\langle E_iE_i\rangle(q) &= (iq_0 g_{\mu i} - iq_i g_{\mu 0})(-iq_0 g_{\nu i} + iq_i g_{\nu 0})\langle A^\mu A^\nu\rangle(q) \\ &= q_0^2 D_{ii}(q) + \boldsymbol{q}^2 D_{00}(q)\,.\end{aligned} \tag{6.5}$$

Projecting the imaginary part of equation (6.3) onto a scattering state $|\boldsymbol{p}\rangle$ and inserting a complete set of bound states with quantum numbers n in between the DM propagator and one of the quantum-mechanical relative position operators r^i, one can determine the bound-state formation cross section:

$$(\sigma_{\rm bsf}\, v_{\rm rel})(\boldsymbol{p}) = -2g^2\frac{\mu^{4-D}}{D-1}\sum_n |\langle n|\boldsymbol{r}|\boldsymbol{p}\rangle|^2 \int \frac{d^Dq}{(2\pi)^D}\; {\rm Im}\left[\frac{\langle \boldsymbol{E}\boldsymbol{E}\rangle^{11}(q_0,\boldsymbol{q})}{p_0-q_0-E_n+i\epsilon}\right]\,, \tag{6.6}$$

where $H|n\rangle = E_n|n\rangle$, $E_n = 2M - M\alpha(\mu_{\rm s})^2/(4n^2)$ is the eigenenergy of the bound state n, and the energy scale μ_s is of order of the Bohr momentum. Alternatively, according to equation (6.2), it may be equivalently extracted from the 21-component of the scattering-state self-energy, eventually leading to

$$(\sigma_{\rm bsf}\, v_{\rm rel})(\boldsymbol{p}) = g^2\frac{\mu^{4-D}}{D-1}\sum_n |\langle n|\boldsymbol{r}|\boldsymbol{p}\rangle|^2 \int \frac{d^{D-1}q}{(2\pi)^{D-1}} \langle \boldsymbol{E}\boldsymbol{E}\rangle^{>}(\Delta E_n^p, \boldsymbol{q})\,. \tag{6.7}$$

The bound-state formation cross section depends on the quantum-mechanical electric dipole matrix element $\langle n|\boldsymbol{r}|\boldsymbol{p}\rangle$, whose general expression can be inferred from appendix C.1, and on the $D-1$ dimensional integral of the 21-component of the dark electric-electric correlator with fixed energy $\Delta E_n^p \equiv E_p - E_n = \boldsymbol{p}^2/M + M\alpha(\mu_{\rm s})^2/(4n^2) \geq 0$. The latter quantity is the key subject to be studied in the following.

If we stay at leading order in the coupling α, hence neglect the two-loop self-energy diagram in fig. 6.1, we insert the free dark photon propagator in Coulomb gauge, cf. eqs. (D.4) and (D.5), into (6.5), and obtain

$$\begin{aligned}\langle \boldsymbol{E}\boldsymbol{E}\rangle^{>}_{\rm LO}(\Delta E_n^p,\boldsymbol{q}) &= (\Delta E_n^p)^2 D_{ii}^{>,\rm LO}(\Delta E_n^p,\boldsymbol{q}) + \boldsymbol{q}^2 D_{00}^{>,\rm LO}(\Delta E_n^p,\boldsymbol{q}) \\ &= 4\pi\,(\Delta E_n^p)^2\,\delta[(\Delta E_n^p)^2-\boldsymbol{q}^2]\,[1+n_{\rm B}(\Delta E_n^p)]\,,\end{aligned} \tag{6.8}$$

which upon plugging in into (6.7) and integrating over the three-momentum $\boldsymbol{q}$ gives

$$(\sigma_{\rm bsf}\,v_{\rm rel})^{\rm LO}(\boldsymbol{p}) = \sum_n (\sigma^n_{\rm bsf}\,v_{\rm rel})^{\rm LO}(\boldsymbol{p}) = \frac{4}{3}\alpha\sum_n |\langle n|\boldsymbol{r}|\boldsymbol{p}\rangle|^2\,(\Delta E_n^p)^3\,[1+n_{\rm B}(\Delta E_n^p)]\,, \tag{6.9}$$

where $\alpha = g^2/(4\pi)$. The bound-state formation cross section at leading order in the coupling is already known since a while [15]. It corresponds to the electric-dipole process

$$(X\bar{X})_p \to \gamma + (X\bar{X})_n\,, \tag{6.10}$$

where a bound state $(X\bar{X})_n$ is formed from a scattering state $(X\bar{X})_p$ via the emission of an ultrasoft dark photon. As a specific example of the above expression, we consider the formation of the lowest-lying 1S bound state, whose wavefunction is $\langle \boldsymbol{r}|1{\rm S}\rangle = R_{10}(r)/(4\pi)$. In this case, only scattering states in the partial wave $\ell = 1$ contribute, whose wavefunction is $\langle \boldsymbol{r}|\boldsymbol{p}1\,\rangle = \Psi_{\boldsymbol{p}1}(\boldsymbol{r})$. The bound-state formation cross section reads

$$\begin{aligned}(\sigma^{\rm 1S}_{\rm bsf}v_{\rm rel})^{\rm LO}(\boldsymbol{p}) &= \frac{g^2}{3\pi}\,[1+n_{\rm B}(\Delta E_1^p)]\,|\langle 1{\rm S}|\boldsymbol{r}|\boldsymbol{p}1\rangle|^2(\Delta E_1^p)^3 \\ &= \frac{\alpha^7\pi^2\,2^{10}}{3\,M^2\,v_{\rm rel}^5\left(1+\frac{\alpha^2}{v_{\rm rel}^2}\right)^2}\frac{e^{-4\frac{\alpha}{v_{\rm rel}}{\rm arccot}\frac{\alpha}{v_{\rm rel}}}}{1-e^{-2\pi\frac{\alpha}{v_{\rm rel}}}}\,[1+n_{\rm B}(\Delta E_1^p)]\,,\end{aligned} \tag{6.11}$$

with $p = Mv_{\rm rel}/2$ and $\Delta E_1^p = \frac{Mv_{\rm rel}^2}{4}\left(1+\frac{\alpha^2}{v_{\rm rel}^2}\right)$. The squared dipole matrix element is written in eq. (C.19). By rewriting the result in (6.11) in terms of $\zeta = \alpha/v_{\rm rel}$, we recover in the zero temperature limit, i.e. by setting the Bose–Einstein distribution to zero, the expression derived in refs. [15,127], and also the abelian limit of the non-abelian version given in eq. (9.21) [50]. We also agree with the finite temperature expression presented in ref. [29]. The formation cross section for the first excited bound state 2S, with quantum numbers $n = 2$ and $\ell = m = 0$, is given by

$$\begin{aligned}(\sigma^{\rm 2S}_{\rm bsf}v_{\rm rel})^{\rm LO}(\boldsymbol{p}) &= \frac{g^2}{3\pi}\,[1+n_{\rm B}(\Delta E_2^p)]\,|\langle 2{\rm S}|\boldsymbol{r}|\boldsymbol{p}1\rangle|^2(\Delta E_2^p)^3 \\ &= \frac{2^7\pi^2\alpha^7}{3M^2v_{\rm rel}^5}\frac{\left(1+\frac{\alpha^2}{v_{\rm rel}^2}\right)}{\left(1+\frac{1}{4}\frac{\alpha^2}{v_{\rm rel}^2}\right)^3}\frac{e^{-4\frac{\alpha}{v_{\rm rel}}\,{\rm arccot}\left(\frac{1}{2}\frac{\alpha}{v_{\rm rel}}\right)}}{1-e^{-2\pi\frac{\alpha}{v_{\rm rel}}}}\,[1+n_{\rm B}(\Delta E_2^p)]\,,\end{aligned} \tag{6.12}$$

where the squared dipole matrix element is written in eq. (C.21), and for the 2P state, with $n = 2$, $\ell = 1$ and with a summation over the orbital magnetic quantum number $m = (0,\pm 1)$, it reads

$$
\begin{aligned}
(\sigma^{2\mathrm{P}}_{\mathrm{bsf}} v_{\mathrm{rel}})^{\mathrm{LO}}(\boldsymbol{p}) &= \sum_{m=-1}^{m=1} (\sigma^{2\mathrm{P}_m}_{\mathrm{bsf}} v_{\mathrm{rel}})^{\mathrm{LO}}(\boldsymbol{p}) \\
&= \frac{2^5\pi^2\alpha^9}{3^3} \frac{\left(\sqrt{1+\frac{\alpha^2}{4v_{\mathrm{rel}}^2}} - 4\sqrt{1+\frac{\alpha^2}{v_{\mathrm{rel}}^2}}\right)^2 + 2\left(\sqrt{1+\frac{\alpha^2}{4v_{\mathrm{rel}}^2}} + 2\sqrt{1+\frac{\alpha^2}{v_{\mathrm{rel}}^2}}\right)^2}{M^2 v_{\mathrm{rel}}^7 \left(1+\frac{\alpha^2}{4v_{\mathrm{rel}}^2}\right)^4} \\
&\quad \times \frac{e^{-4\frac{\alpha}{v_{\mathrm{rel}}}\,\mathrm{arccot}\left(\frac{\alpha}{2v_{\mathrm{rel}}}\right)}}{1-e^{-2\pi\frac{\alpha}{v_{\mathrm{rel}}}}} \left[1+n_{\mathrm{B}}(\Delta E_2^p)\right] . \qquad (6.13)
\end{aligned}
$$

where the squared dipole matrix elements for $m = (0, \pm 1)$ are written in eq.(C.23) and (C.25). Since at $\mathcal{O}(\alpha^2)$ the binding energies depend only on the principal quantum number n, the states 2S and $2\mathrm{P}_{m=0,\pm1}$ have the same binding energy $E_2^b = -M\alpha^2/16$. The formation cross section of a 3S bound state, that has quantum numbers $n = 3$, $\ell = m = 0$, and binding energy $E_3^b = -M\alpha^2/(4 \cdot 3^2)$, reads

$$
(\sigma^{3\mathrm{S}}_{\mathrm{bsf}} v_{\mathrm{rel}})^{\mathrm{LO}}(\boldsymbol{p}) = \frac{2^{10}\pi^2}{3^4} \frac{\alpha^7 \left(1+\frac{\alpha^2}{v_{\mathrm{rel}}^2}\right)}{M^2 v_{\mathrm{rel}}^5} \frac{\left(1+\frac{7\alpha^2}{3^3 v_{\mathrm{rel}}^2}\right)^2}{\left(1+\frac{\alpha^2}{3^2 v_{\mathrm{rel}}^2}\right)^5} \frac{e^{-4\frac{\alpha}{v_{\mathrm{rel}}}\,\mathrm{arccot}\left(\frac{\alpha}{3v_{\mathrm{rel}}}\right)}}{1-e^{-2\pi\frac{\alpha}{v_{\mathrm{rel}}}}} \left[1+n_{\mathrm{B}}(\Delta E_3^p)\right] . \qquad (6.14)
$$

Our results agree with the ones in ref. [17]. In figure 6.2 left, we plot the bound-state formation cross section normalized by $\pi\alpha^2/M^2$ for the 1S (orange solid line), 2S (brown dotted line), 2P (purple dashed line) and 3S (red dash-dotted line) state, thermally averaged according to (B.15), for $\alpha = 0.1$.[5] As a reference, we plot also the thermally averaged Sommerfeld enhancement factor (5.24), presented by the black solid line, where we see that only the 1S-bsf is larger than S_{ann} (by a factor of two to three for the whole temperature range $10 \leq M/T \leq 10^5$), while the 2P-bsf (summed over $m = 0, \pm 1$) is of the same order and the 2S-, 3S-bsf cross sections are suppressed. We can therefore truncate the summation in n in (6.9) up to the first few excited states, where the formation of the ground state dominates over all the other bound states. We remark that in the dipole limit, if we select the spin of the final state, the bound-state formation cross section for paradarkonium in general is given by $\sigma^{1\mathrm{S,para}}_{\mathrm{bsf}} = \sigma^{1\mathrm{S}}_{\mathrm{bsf}}/4$ and for orthodarkonium it is $\sigma^{1\mathrm{S,ortho}}_{\mathrm{bsf}} = 3\,\sigma^{1\mathrm{S}}_{\mathrm{bsf}}/4$. Despite that the near-threshold processes are spin-blind at order $\boldsymbol{r}^2$, we will need to split them into its spin-singlet and spin-triplet parts when plugging them into the coupled Boltzmann equations that we will show in sec. 7.2.

In the derivation of the bound-state formation cross section we have implicitly assumed that the dark pair propagator and electric-field correlator are the ones in kinetic equilibrium, and $\sigma^{\mathrm{LO}}_{\mathrm{bsf}}$ encompasses therefore the Bose-enhancement factor $[1 + n_{\mathrm{B}}]$ in (6.9) due to the emitted photon. The result does not apply if the thermal bath is out of kinetic equilibrium. However, as argued in chapter 2, at freeze-out the thermal environment evolves rather slowly and hence can be assumed to be quasistatic to a certain

[5] Note that we thermally average in the laboratory frame where the bath is at rest. But since we omit the center-of-mass motion in this section, the relative velocity in the laboratory frame coincides with the one in the center-of-mass frame.

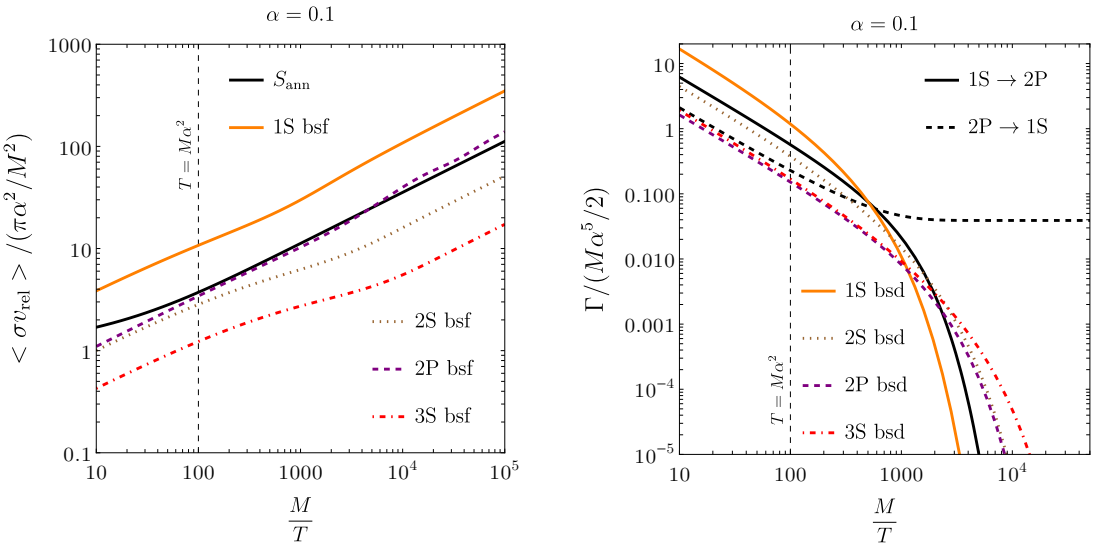

Figure 6.2: (Left) Ratios of the thermally averaged formation cross sections of the first few excited bound states at leading order, cf. eq. (6.9), over $\pi\alpha^2/M^2$, as functions of M/T. As a comparison, we plot also the thermally averaged Sommerfeld factor. (Right) Ratios of the 1S, 2S, 2P and 3S dissociation widths and 1S $\leftrightarrow$ 2P (de-)excitation widths over $M\alpha^5/2$ at leading order in the coupling. The vertical lines mark the position where $T = M\alpha^2$, i.e. the regime where the temperature is of order of the ultrasoft scale.

degree of accuracy. Hence we can rely on the Maxwell–Boltzmann- and Bose-statistics of the fermion-antifermion meson and the dark photons, respectively, and therefore use the corresponding thermal propagator expressions (here (D.14), (D.4) and (D.5) at leading order). Even though detailed balance is lost with respect to annihilation and creation processes, it is maintained between bound-state formation and bound-state dissociation as long as the bath is hot enough, called the *ionization*-equilibrium regime [23], and for instance for the ground state it holds that

$$\frac{1}{16}\langle\sigma^{\rm 1S}_{\rm bsf} v_{\rm rel}\rangle\, n^2_{\rm eq} = \Gamma^{\rm 1S}_{\rm bsd} n^{\rm para}_{\rm 1S,eq} \qquad \text{and} \qquad \frac{3}{16}\langle\sigma^{\rm 1S}_{\rm bsf} v_{\rm rel}\rangle\, n^2_{\rm eq} = \Gamma^{\rm 1S}_{\rm bsd}\, n^{\rm ortho}_{\rm 1S,eq}\,. \tag{6.15}$$

We can compute the dissociation width from the detailed balance conditions in (6.15), for the first three excited states and plot the results in the right panel of fig. 6.2. We will show the analytic results for the widths in the next chapter, where they will be derived in a direct way. There is also a detailed balance relation between excitation and de-excitation processes, which for two discrete bound states n and n', with $n > n'$, reads

$$n_{\rm B}(E_n)\,\Gamma^{n\to n'}_{\text{de-ex.}} = n_{\rm B}(E_{n'})\,\Gamma^{n'\to n}_{\text{ex.}}\,, \tag{6.16}$$

and for the particular example of $n = 2{\rm P}$ and $n' = 1{\rm S}$, we add the corresponding bound-state to bound-state widths in the right panel of fig. 6.2. Bound-to-bound transitions

will be treated in more detail in sec. 6.3. Hence, from now on kinetic equilibrium is always presupposed.

At next-to-leading order in the coupling, one needs to take into account the two-loop self-energy displayed in figure 6.1, hence we need to compute the next-to-leading order correction to the 21-component of the electric-field correlator (6.8):

$$\begin{aligned}\delta\langle \boldsymbol{EE}\rangle^{>}_{\rm NLO}(q) &= q_0^2 D_{ii}^{>,\rm NLO}(q) + \boldsymbol{q}^2 D_{00}^{>,\rm NLO}(q)\\ &= 2[1+n_{\rm B}(q_0)]\,{\rm Im}\left[q_0^2 D_{i\lambda}^{R,\rm LO}(q)\Pi_R^{\lambda\rho}(q)D_{\rho i}^{R,\rm LO}(q) + \boldsymbol{q}^2 D_{0\lambda}^{R,\rm LO}(q)\Pi_R^{\lambda\rho}(q)D_{\rho 0}^{R,\rm LO}(q)\right]\\ &\equiv \delta\langle \boldsymbol{EE}\rangle^{>,n_{\rm F}=0}_{\rm NLO}(q) + \delta\langle \boldsymbol{EE}\rangle^{>,n_{\rm F}\neq 0}_{\rm NLO}(q)\,,\end{aligned} \tag{6.17}$$

where $q_0 = \Delta E_n^p$ and in the last line we separated the electric correlator into two terms according to the splitting of the retarded polarization tensor into a vacuum ($n_{\rm F}(q_0)=0$) and a thermal ($n_{\rm F}(q_0)\neq 0$) part as in (D.17).[6]

We insert the retarded photon propagator at LO, cf. eqs. (D.8) and (D.9), and the vacuum part of the retarded polarization tensor (D.18), renormalized in the $\overline{\rm MS}$ scheme, and we obtain for the $n_{\rm F}(q_0)=0$ part of the 21-correlator

$$\begin{aligned}&\delta\langle \boldsymbol{EE}\rangle^{>,n_{\rm F}=0}_{\rm NLO}(q)\\ &= 2[1+n_{\rm B}(q_0)]{\rm Im}\left[q_0^2 D_{i\lambda}^{R,\rm LO}(q)\Pi_{R,\overline{\rm MS}}^{\lambda\rho,T=0}(q)D_{\rho i}^{R,\rm LO}(q) + \boldsymbol{q}^2 D_{0\lambda}^{R,\rm LO}(q)\Pi_{R,\overline{\rm MS}}^{\lambda\rho,T=0}(q)D_{\rho 0}^{R,\rm LO}(q)\right]\\ &= [1+n_{\rm B}(q_0)]\frac{n_f g^2}{6\pi^2}{\rm Im}\left[\frac{q^2(\boldsymbol{q}^2-3q_0^2)}{((q_0+i\epsilon)^2-\boldsymbol{q}^2)^2}\left[\ln\left(\frac{(q_0+i\epsilon)^2-\boldsymbol{q}^2}{-\mu^2}\right)-\frac{5}{3}\right]\right].\end{aligned} \tag{6.18}$$

Inserting this expression into (6.7) and integrating over $\boldsymbol{q}$ using the residue theorem, we obtain the next-to-leading order correction to the bsf cross section coming from the $n_{\rm F}(q_0)=0$ part ,

$$\delta(\sigma_{\rm bsf}\,v_{\rm rel})^{\rm NLO}_{n_{\rm F}=0}(\boldsymbol{p}) = \sum_n (\sigma^n_{\rm bsf}\,v_{\rm rel})^{\rm LO}(\boldsymbol{p})\frac{n_f}{3\pi}\alpha\,\left[\ln\left(\frac{4(\Delta E_n^p)^2}{\mu^2}\right)-\frac{10}{3}\right], \tag{6.19}$$

where $(\sigma^n_{\rm bsf}\,v_{\rm rel})^{\rm LO}$ can be read off from eq. (6.9). At first sight the bsf cross section (6.19) seems to depend on the renormalization scale μ. However, from the one-loop running of the coupling in (3.3) we deduce that[7]

$$\alpha(\mu) = \frac{\alpha(\mu_{\rm us})}{1-\frac{\beta_0}{4\pi}\alpha(\mu_{\rm us})\ln\left(\frac{\mu_{\rm us}^2}{\mu^2}\right)} \approx \alpha(\mu_{\rm us})\left[1-\frac{n_f}{3\pi}\alpha(\mu_{\rm us})\ln\left(\frac{\mu_{\rm us}^2}{\mu^2}\right)\right], \tag{6.20}$$

[6] In order to make the notation more transparent, note that while we distinguish contributions to the 21-electric correlator coming from either a vanishing or non-vanishing Fermi–Dirac distribution in $\Pi_R^{\lambda\rho}(q)$, the Bose–Einstein distribution $n_{\rm B}(q_0)$ is included in $\delta\langle \boldsymbol{EE}\rangle^{>,n_{\rm F}=0}_{\rm NLO}(q)$ as well as in $\delta\langle \boldsymbol{EE}\rangle^{>,n_{\rm F}\neq 0}_{\rm NLO}(q)$.

[7] We can expand the expression in (6.20) because the coupling is weak at the ultrasoft scale μ_s, and the electric-field correlator (6.18) has been computed in dimensional regularization at a scale μ of the order of μ_s.

where $\mu_{\rm us}$ is chosen to be at the ultrasoft scale at which the bsf process happens, $\mu_{\rm us} \approx M\alpha^2$. Substituting the coupling in (6.9) by the expression (6.20), then it follows that the sum of the bsf cross section at LO, (6.9), and the NLO correction term (6.19) gives

$$\begin{aligned}(\sigma_{\rm bsf}\, v_{\rm rel})^{\rm LO+NLO}_{n_{\rm F}=0}(\boldsymbol{p}) &\equiv (\sigma_{\rm bsf}\, v_{\rm rel})^{\rm LO}(\boldsymbol{p}) + \delta(\sigma_{\rm bsf}\, v_{\rm rel})^{\rm NLO}_{n_{\rm F}=0}(\boldsymbol{p}) \\ &= \sum_n (\sigma_{\rm bsf}\, v_{\rm rel})^{\rm LO}_n(\boldsymbol{p}) \left\{ 1 + \frac{n_f}{3\pi}\alpha(\mu_{\rm us}) \left[\ln\left(\frac{4(\Delta E^p_n)^2}{\mu^2_{\rm us}} \right) - \frac{10}{3} \right] \right\}, \end{aligned} \tag{6.21}$$

that now is scale independent and the NLO correction is suppressed if $n_f\alpha(\mu_{\rm us}) \ll 1$. We notice that this condition is certainly fulfilled for the considered hierarchies (3.2) and (3.4), where $T \gg m_{\rm D}$ implies $\sqrt{n_f\alpha(T)} \ll 1$.[8]

Next, we compute the $n_{\rm F}(q_0) \neq 0$ part in (6.17), that depends on the thermal retarded polarization tensor given in (D.21), and obtain

$$\begin{aligned}&\delta\langle \boldsymbol{E}\boldsymbol{E}\rangle^{>,n_{\rm F}\neq 0}_{\rm NLO}(q) \\ &= 2[1+n_{\rm B}(q_0)]{\rm Im}\left[2q_0^2 \Delta^R_{\rm LO}(q)\Pi^{R,T\neq 0}_{\rm trans}(q)\Delta^R_{\rm LO}(q) + \boldsymbol{q}^2 D^{R,{\rm LO}}_{00}(q)\Pi^{R,T\neq 0}_{00}(q) D^{R,{\rm LO}}_{00}(q) \right] \\ &= n_f g^2 [1+n_{\rm B}(q_0)] \int \frac{d^3k}{(2\pi)^3} \frac{n_{\rm F}(|\boldsymbol{k}|)}{|\boldsymbol{k}||\boldsymbol{k}+\boldsymbol{q}|} {\rm Im}\left[\sum_{\sigma_{1,2}=\pm 1} \frac{\sigma_2 T_{00}/\boldsymbol{q}^2|_{k_0=\sigma_1|\boldsymbol{k}|}}{q_0+\sigma_1|\boldsymbol{k}|+\sigma_2|\boldsymbol{k}+\boldsymbol{q}|+i\epsilon} \right. \\ &\qquad \left. + \frac{1}{((q_0+i\epsilon)^2-\boldsymbol{q}^2)^2} \left(\sum_{\sigma_{1,2}=\pm 1} \frac{\sigma_2 2q_0^2 T_{\rm trans}|_{k_0=\sigma_1|\boldsymbol{k}|}}{q_0+\sigma_1|\boldsymbol{k}|+\sigma_2|\boldsymbol{k}+\boldsymbol{q}|+i\epsilon} \right) \right], \end{aligned} \tag{6.22}$$

where $\Delta^R_{\rm LO}(q)$, $\Pi^{R,T\neq 0}_{00}(q)$, $\Pi^{R,T\neq 0}_{\rm trans}(q)$, $T_{00/{\rm trans}}$ are given in eqs. (D.9), (D.24), (D.25) and (D.23), respectively. We insert (6.22) into (6.7) and first integrate over the momentum $\boldsymbol{q}$ using the residue theorem[9], then add up the individual terms and integrate over the angular coordinate $\theta = \sphericalangle(\boldsymbol{q},\boldsymbol{k})$, and end up with a single integral expression in $|\boldsymbol{k}|$ that

[8] The coupling, that enters in the Debye mass expression (D.39), is evaluated at the energy scale of the order of the temperature. As discussed in sec. 3, if we require that $T \gg m_{\rm D}$, i.e. $\sqrt{n_f\alpha(T)} \ll 1$, then for non-vanishing $n_f = 1$ or $n_f = 2$ we consider sufficiently small couplings $\alpha(2M) \lesssim 0.1$. Since in the U(1) model the coupling decreases with decreasing energy scale, it holds that $n_f\alpha(\mu_{\rm s}) \ll \sqrt{n_f\alpha(T)}$.

[9] Equation (6.22) has two single poles at $|\boldsymbol{q}|_\pm = -|\boldsymbol{k}|\cos\theta \pm \sqrt{\boldsymbol{k}^2\cos\Theta^2 + q_0^2 + 2\sigma_1 q_0|\boldsymbol{k}|}$, which would physically correspond to putting the light dark fermions on-shell and hence belongs to the process of bsf via bath-particle scattering as well as the off-shell decay of the intermediate dark photon into a light dark particle and antiparticle. Moreover equation (6.22) has a double pole at $|\boldsymbol{q}| = q_0$ and corresponds to putting the dark photon on-shell, which corresponds to bsf via on-shell photo-emission.

is finite and numerically solvable[10],

$$\delta(\sigma_{\rm bsf}\, v_{\rm rel})^{\rm NLO}_{n_{\rm F}\neq 0}(\boldsymbol{p}) = \sum_n (\sigma^n_{\rm bsf}\, v_{\rm rel})^{\rm LO}(\boldsymbol{p}) \frac{n_f \alpha}{\pi (\Delta E^p_n)^3} \int_0^\infty d|\boldsymbol{k}|\; 2 n_{\rm F}(|\boldsymbol{k}|) \Bigg[-2|\boldsymbol{k}|\Delta E^p_n + 2|\boldsymbol{k}|\Delta E^p_n \ln\left|\frac{\boldsymbol{k}^2 - (\Delta E^p_n)^2}{(\Delta E^p_n)^2}\right| + [2|\boldsymbol{k}|^2 + (\Delta E^p_n)^2] \ln\left|\frac{|\boldsymbol{k}| + \Delta E^p_n}{|\boldsymbol{k}| - \Delta E^p_n}\right| \Bigg] . \tag{6.23}$$

The complete bsf cross section up to NLO in the coupling is given by the sum of (6.21) and (6.23), and can be written as

$$\begin{aligned}(\sigma_{\rm bsf}\, v_{\rm rel})^{\rm LO+NLO}(\boldsymbol{p}) &= (\sigma_{\rm bsf}\, v_{\rm rel})^{\rm LO+NLO}_{n_{\rm F}=0}(\boldsymbol{p}) + \delta(\sigma_{\rm bsf}\, v_{\rm rel})^{\rm NLO}_{n_{\rm F}\neq 0}(\boldsymbol{p}) \\ &= \sum_n (\sigma_{\rm bsf}\, v_{\rm rel})^{\rm LO}_n(\boldsymbol{p}) \left\{ 1 + \frac{n_f}{\pi}\alpha(\mu_{\rm us}) \left[\mathcal{X}_{\rm vac}(\Delta E^p_n, \mu_{\rm us}) + \mathcal{X}_{\rm th}(\Delta E^p_n/T) \right] \right\},\end{aligned} \tag{6.24}$$

where $\mathcal{X}_{\rm vac}$ can be read off from (6.21) and $\mathcal{X}_{\rm th}$ is written as an integral over a dimensionless variable $t \equiv |\boldsymbol{k}|/T$, and reads [29, 128]

$$\mathcal{X}_{\rm th}(x) = \frac{2}{x^3} \int_0^\infty \frac{dt}{e^t + 1} \left[(2t^2 + x^2) \ln\left|\frac{t+x}{t-x}\right| + 2tx \ln\left|\frac{t^2 - x^2}{x^2}\right| - 2xt \right] , \tag{6.25}$$

which can be integrated numerically. The bound-state formation at NLO may proceed via different mechanisms in addition to the thermal photo-dissociation in (6.10). For $n_f \neq 0$, the scattering state can collide inelastically with the constituents from the thermal bath that turns it into a bound state. Or the emitted photon can decay into a light fermion-antifermion pair. These additional processes can be inferred from cutting the two-loop diagram in fig. 6.1 through the light-fermion loop and we can relate it to the *Landau damping* phenomenon in a QED plasma, that is known for the reverse process of bound-state dissociation through these bath-particle scattering processes. While the in-vacuum loop corrections in (6.21) are suppressed for small couplings, the thermal loop corrections $n_f \alpha \mathcal{X}_2/\pi$ may become large if the temperature exceeds the typical ultrasoft energy scale ΔE^p_n. Hence for the hierarchy of energy scales shown in (3.4), the thermal loop corrections need to be resummed, which is displayed by the grey shaded loop in figure 6.1. It is the topic in the next section.

6.1.1.2 Thermal Debye-mass resummation

At temperatures close to the thermal freeze-out regime, where it holds that $T \gg \Delta E^p_n$ for weak coupling $\alpha \ll 0.4$, we can calculate the 11-component of the self-energy in eq. (6.3) by splitting the loop integral into various energy regions according to the hierarchies among them, given in (3.4). We start with the largest dynamical scale in the pNRQED$_{\rm DM}$ model, namely the temperature, and integrate over energy and momentum

[10] Following the arguments in [29, 128], potential collinear divergences from the individual terms in (6.23) cancel each other when summing them up.

modes in the loop of the order of T, i.e. $\{q_0, |\boldsymbol{q}|\} \sim T$, by expanding the heavy DM pair propagator in the energy difference operator $\Delta E \equiv p_0 - H \ll q_0 \sim T$ up to zeroth order,

$$\frac{i}{p_0 - H - q_0 + i\epsilon} = \frac{i}{-q_0 + i\epsilon}\left[1 + \mathcal{O}\left(\frac{p_0 - H}{q_0}\right)\right] . \tag{6.26}$$

We insert it into (6.3), that now reads

$$\Sigma^{11}_{(T)}(p_0) = -ig^2 \frac{\mu^{4-D}}{D-1}\boldsymbol{r}^2 \int \frac{d^D q}{(2\pi)^D} \frac{i}{-q_0 + i\epsilon}[q_0^2 D^{11}_{ii}(q) + \boldsymbol{q}^2 D^{11}_{00}(q)] . \tag{6.27}$$

The subscript (T) for the self-energy denotes the corresponding energy region. If we insert the leading order expression for the dark photon propagator in Coulomb gauge given in (D.4)–(D.5) into eq. (6.27), we obtain a vanishing integral.[11] Instead, if we insert the next-to-leading order expression for the dark photon propagator into (6.27), which we can expand since $q \sim T \gg m_{\rm D}$, we obtain[12]

$$\Sigma^{11}_{(T)}(p_0) = -ig^2 \frac{\mu^{4-D}}{D-1}\boldsymbol{r}^2 \int \frac{d^D q}{(2\pi)^D} \pi\delta(q_0)\, \boldsymbol{q}^2 D^{11,\rm NLO}_{00}(q) , \tag{6.28}$$

and hence the imaginary part reads

$$\begin{aligned} \mathrm{Im}\left[\Sigma^{11}_{(T)}\right] &= -g^2 \frac{\mu^{4-D}}{D-1}\boldsymbol{r}^2 \int \frac{d^D q}{(2\pi)^D} \pi\delta(q_0)\, \boldsymbol{q}^2 \ \mathrm{Re}\left[D^{11,\rm NLO}_{00}(q)\right] \\ &= -\frac{g^2}{2} \frac{\mu^{4-D}}{D-1}\boldsymbol{r}^2 \int \frac{d^D q}{(2\pi)^D} \pi\delta(q_0)\, \boldsymbol{q}^2 \frac{-i\Pi^S_{00}(q)}{\boldsymbol{q}^4} , \end{aligned} \tag{6.29}$$

where in the second line we split the dark photon propagator according to (D.7) into its real symmetric and imaginary antisymmetric parts. Since (6.29) is non-zero for $q_0 = 0$, it follows that $|\boldsymbol{q}| \sim T \gg q_0$, and we use the appropriate symmetric polarization tensor in eq. (D.34) to obtain

$$\begin{aligned} \mathrm{Im}\left[\Sigma^{11}_{(T)}\right] &= -4g^4 n_f T \boldsymbol{r}^2 \frac{\mu^{4-D}}{D-1} \int \frac{d^{D-1} q}{(2\pi)^D} \frac{1}{|\boldsymbol{q}|^3} \int_{|\boldsymbol{q}|/2}^{\infty} d|\boldsymbol{k}||\boldsymbol{k}| n_{\rm F}(|\boldsymbol{k}|) \\ &= \frac{\alpha}{6}\boldsymbol{r}^2 T m_{\rm D}^2 \left[\frac{1}{\epsilon} + \gamma_{\rm E} + \frac{2}{3} - 4\ln 2 - 2\frac{\zeta'(2)}{\zeta(2)} - \ln\left(\frac{T^2}{\pi\mu^2}\right)\right] , \end{aligned} \tag{6.30}$$

where $\zeta(2) = \pi^2/6$ is Riemann's zeta function. The quantity in eq. (6.30) is infrared divergent and scale dependent. However, at this stage, this is not a concern. It is in

[11] In fact the vacuum part of the free dark photon propagator results in a scaleless integral for all terms in the expansion in (6.26). As for the thermal part, contributions up to the third order in the expansion of the heavy pair propagator can be shown to either vanish in dimensional regularization or be real and hence they do not contribute to the bsf cross section in (6.2). Further terms of higher order in $\Delta E/T$ in (6.26) can be omitted, since the potentially non-vanishing contributions to the scattering-state self-energy scale less than $\alpha r^2 (\Delta E)^3$ and hence below our accuracy of interest [129].

[12] Since the electric-electric correlator is even in q_0, only the even part of the zeroth order expression of the DM pair propagator contributes.

fact the manifestation, or an artifact, of the separation of energy scales and indicates that the result in (6.30) is not valid in the energy region much below the temperature scale. As soon as we add the contribution from the lower scales, the divergence and the renormalization scale μ will, and must, cancel out.

Higher order corrections, coming from the contributions to the heavy pair propagator beyond the zeroth order expansion (comprised in the $\mathcal{O}(\dots)$-term in the expanded propagator (6.26)), are suppressed by a factor $\alpha r^2 m_{\mathrm{D}}^2 T \times (\Delta E/T)^2 \ll \alpha r^2 m_{\mathrm{D}}^2 T$. Similarly, corrections to the dark photon propagator are suppressed by $\alpha r^2 m_{\mathrm{D}}^2 T \times (m_{\mathrm{D}}/T)^2 \ll \alpha r^2 m_{\mathrm{D}}^2 T$ and hence beyond the accuracy of this work. In a similar manner, one could calculate the real part of the self-energy, which gives thermal corrections to the potential of the heavy DM pair, see for instance ref. [130] in case of heavy quarkonium in a QGP or refs. [49, 82] for hydrogen and muonic atoms.

In the next step, we need to look at the lower energy region, where the energy and momentum modes in the loop are the order of the Debye mass or the ultrasoft energy difference, i.e. $\{q_0, |\boldsymbol{q}|\} \sim m_{\mathrm{D}} \sim \Delta E$. Since we consider contributions from the modes simultaneously of the order of m_{D} and ΔE, we cannot expand the DM pair propagator as in (6.26) and must therefore keep both the transversal and longitudinal parts of electric-field correlator. Moreover, the resummation of the loop corrections to the dark photon propagator is essential, since $q \sim m_{\mathrm{D}}$. Instead of computing $\mathrm{Im}[\Sigma^{11}]$, we choose to evaluate the 21-component of the scattering-state self-energy,

$$\begin{aligned}\Sigma^{>}_{(m_{\mathrm{D}}\sim\Delta E)}(p_0) &= ig^2 \frac{\mu^{4-D}}{D-1} r^i \int \frac{d^D q}{(2\pi)^D} 2\pi\delta(\Delta E - q_0)[\boldsymbol{q}^2 D^{>}_{00}(q) + q_0^2 D^{>}_{ii}(q)] r^i \\ &= \Sigma^{>,\,\mathrm{long}}_{(m_{\mathrm{D}}\sim\Delta E)}(p_0) + \Sigma^{>,\,\mathrm{trans}}_{(m_{\mathrm{D}}\sim\Delta E)}(p_0)\,.\end{aligned} \tag{6.31}$$

First, we compute the longitudinal part. We abbreviate the resummed longitudinal retarded/advanced dark photon propagator in (D.50) as

$$D^{R/A}_{00}(q) = \frac{i}{\boldsymbol{q}^2 + l(q) \pm i l'(q)}\,, \tag{6.32}$$

where $l(q) \equiv \mathrm{Re}\left[\Pi^{R/A,T\neq 0}_{00}(q)\right]$, cf. (D.35), and $\pm l'(q) \equiv \mathrm{Im}\left[\Pi^{R/A,T\neq 0}_{00}(q)\right]$, cf. (D.36). Then it follows for the resummed longitudinal 21-propagator that

$$D^{>}_{00}(q) = [1 + n_{\mathrm{B}}(q_0)]\left[D^{R}_{00}(q) - D^{A}_{00}(q)\right] \approx \frac{\pi T}{|\boldsymbol{q}|} \frac{m_{\mathrm{D}}^2 \Theta(-q^2)}{[\boldsymbol{q}^2 + l(q)]^2 + l'(q)^2}\,, \tag{6.33}$$

and the corresponding longitudinal part of $\Sigma^{>}$ reads

$$\begin{aligned}\Sigma^{>,\,\mathrm{long}}_{(m_{\mathrm{D}}\sim\Delta E)}(p_0) &= ig^2 \frac{\mu^{4-D}}{D-1} r^i \int \frac{d^D q}{(2\pi)^D} 2\pi\delta(\Delta E - q_0)\boldsymbol{q}^2 D^{>}_{00}(q) r^i \\ &= ig^2 \frac{\mu^{4-D}}{D-1} r^i \int \frac{d^D q}{(2\pi)^D} 2\pi\delta(\Delta E - q_0)\boldsymbol{q}^2 \frac{\pi T}{|\boldsymbol{q}|} \frac{m_{\mathrm{D}}^2 \Theta(-q^2)}{[\boldsymbol{q}^2 + l(q)]^2 + l'(q)^2} r^i\,.\end{aligned} \tag{6.34}$$

The above expression is ultraviolet divergent, which signals that its validity is spoiled at energy regions much larger than $m_{\rm D}$ or ΔE. However, as mentioned before, it cancels the IR-divergence in $\Sigma^{>}_{(T)} = -2i\ {\rm Im}\left[\Sigma^{11}_{(T)}\right]$, cf. (6.30). In order to see the cancellation explicitly, we extract the divergent part out of (6.34) by writing

$$\begin{aligned}\Sigma^{>,\,\rm long}_{(m_{\rm D}\sim\Delta E)}(p_0) &= ig^2\frac{\mu^{4-D}}{D-1}r^i\int\frac{d^Dq}{(2\pi)^D}2\pi\delta(\Delta E-q_0)\frac{\pi T}{|\boldsymbol{q}|^3}m_{\rm D}^2\Theta(-q^2)\\ &\qquad\times\left[1+\frac{1-[1+l(q)/\boldsymbol{q}^2]^2-[l'(q)/\boldsymbol{q}^2]^2}{[1+l(q)/\boldsymbol{q}^2]^2+[l'(q)/\boldsymbol{q}^2]^2}\right]r^i \qquad (6.35)\\ &= \Sigma^{>,\,\rm long,\,div}_{(m_{\rm D}\sim\Delta E)}(p_0)+\Sigma^{>,\,\rm long,\,fin}_{(m_{\rm D}\sim\Delta E)}(p_0)\,.\end{aligned}$$

The integration of the first term in the square bracket in the second line of (6.35), which contains the UV-divergence, gives

$$\begin{aligned}\Sigma^{>,\,\rm long,\,div}_{(m_{\rm D}\sim\Delta E)}(\Delta E) &= 2i\pi^2g^2\,T\,m_{\rm D}^2\frac{\mu^{4-D}}{D-1}\frac{2\,\sqrt{\pi}^{D-1}}{(2\pi)^D\,\Gamma\left(\frac{D-1}{2}\right)}\,r^i\int_{\Delta E}^{\infty}d|\boldsymbol{q}|\,|\boldsymbol{q}|^{D-5}r^i\\ &= i\frac{\alpha}{3}\,Tm_{\rm D}^2\,r^{\,i}\left[\frac{1}{\epsilon}-\gamma_{\rm E}+\frac{8}{3}-\ln\left(\frac{(\Delta E)^2}{\pi\mu^2}\right)\right]r^i\,.\end{aligned} \qquad (6.36)$$

The integration of the second term in the square bracket is finite and can be done numerically. We write the expression as

$$\Sigma^{>,\,\rm long,\,fin}_{(m_{\rm D}\sim\Delta E)}(\Delta E) = i\frac{2}{3}\alpha\,Tm_{\rm D}^2\,r^i\,\mathcal{Y}^{\rm long}_{\rm th}\left(\frac{\Delta E}{m_{\rm D}}\right)r^i\,, \qquad (6.37)$$

where we define the dimensionless finite integral

$$\mathcal{Y}^{\rm long}_{\rm th}(x)\equiv\int_1^{\infty}\frac{dt}{t}\frac{(xt)^4-[(xt)^2+\tilde{l}(t)]^2-\tilde{l}'(t)^2}{[(xt)^2+\tilde{l}(t)]^2+\tilde{l}'(t)^2}\,, \qquad (6.38)$$

with the dimensionless integration variable $t\equiv|\boldsymbol{q}|/\Delta E$ and the functions

$$\tilde{l}(x)\equiv 1+\frac{1}{2x}\ln\left|\frac{1-x}{1+x}\right|,\ \ \tilde{l}'(x)\equiv\frac{\pi}{2x}\,. \qquad (6.39)$$

Hence, summing (6.36) and (6.37), the longitudinal part of the scattering-state self-energy reads

$$\begin{aligned}\Sigma^{>,\,\rm long}_{(m_{\rm D}\sim\Delta E)}(\Delta E) &= i\frac{\alpha}{3}Tm_{\rm D}^2r^i\left[\frac{1}{\epsilon}-\gamma_{\rm E}+\frac{8}{3}-\ln\left(\frac{(\Delta E)^2}{\pi\mu^2}\right)+2\mathcal{Y}^{\rm long}_{\rm th}\left(\frac{\Delta E}{m_{\rm D}}\right)\right]r^i\\ &= -2i\ {\rm Im}\left[\Sigma^{11,\,\rm long,\,div}_{(m_{\rm D}\sim\Delta E)}(\Delta E)\right]\,.\end{aligned} \qquad (6.40)$$

Note that in the limit $\Delta E/m_{\rm D}\to\infty$, where the function $\mathcal{Y}^{\rm long}_{\rm th}$ vanishes, eq. (6.40) agrees with the abelian version of the result in ref. [84]. Hence the correction term $2\mathcal{Y}^{\rm long}_{\rm th}$

accounts for the less strict relation $\Delta E \sim m_{\rm D}$ compared to the hierarchy $\Delta E \gg m_{\rm D}$ considered in that reference.

Now we consider the finite transversal part in (6.31),

$$\Sigma^{>,\,\rm trans}_{(m_{\rm D}\sim\Delta E)}(p_0) = i\frac{g^2}{3} r^i \int \frac{d^4q}{(2\pi)^4} 2\pi\delta(\Delta E - q_0) q_0^2 D^{>}_{ii}(q) r^i \,. \tag{6.41}$$

Starting from the 21-component of the dark photon propagator

$$D^{>}_{ii}(q) = [1 + n_{\rm B}(q_0)] \left[D^R_{ii}(q) - D^A_{ii}(q)\right] \,, \tag{6.42}$$

and using the resummed retarded/advanced propagators in (D.51), we obtain

$$\begin{aligned}\Sigma^{>,\,\rm trans}_{(m_{\rm D}\sim\Delta E)}(\Delta E) = i\frac{2}{3} g^2 T r^i \Delta E \int \frac{d^3q}{(2\pi)^3} \Bigg[&\frac{i}{(\Delta E)^2 - \boldsymbol{q}^2 + t(\Delta E, \boldsymbol{q}) + i t'(\Delta E, \boldsymbol{q}) + i\epsilon} \\ &- \frac{i}{(\Delta E)^2 - \boldsymbol{q}^2 + t(\Delta E, \boldsymbol{q}) - i t'(\Delta E, \boldsymbol{q}) - i\epsilon} \Bigg] r^i \,,\end{aligned} \tag{6.43}$$

where we define $t(q) \equiv \mathrm{Re}\left[\Pi^{R,T\neq 0}_{\rm trans}(q)\right]$, cf. (D.37), and $\pm t'(q) \equiv \mathrm{Im}\left[\Pi^{R,T\neq 0}_{\rm trans}(q)\right]$, cf. (D.38). Equation (6.43) can be written as

$$\begin{aligned}\Sigma^{>,\,\rm trans}_{(m_{\rm D}\sim\Delta E)}(\Delta E) &= i\frac{2}{3}\alpha\, T m_{\rm D}^2 r^i \mathcal{Y}^{\rm trans}_{\rm th}\left(\frac{\Delta E}{m_{\rm D}}\right) r^i \\ &= -2i\ \mathrm{Im}\left[\Sigma^{11,\,\rm trans}_{(m_{\rm D}\sim\Delta E)}(\Delta E)\right] \,,\end{aligned} \tag{6.44}$$

where we define the dimensionless finite integral

$$\begin{aligned}&\mathcal{Y}^{\rm trans}_{\rm th}(x) \\ &\quad\equiv \frac{2}{\pi} x^4 \int_0^\infty dt\ t^2 \left[\frac{i}{(1-t^2)x^2 - \tilde{t}(t) + i\tilde{t}'(t) + i\epsilon} - \frac{i}{(1-t^2)x^2 - \tilde{t}(t) - i\tilde{t}'(t) - i\epsilon}\right] \\ &\quad= \frac{2}{\pi} x^4 \left[\int_0^1 dt\ t^2 2\pi\delta[(1-t^2)x^2 - \tilde{t}(t)] + \int_1^\infty dt\ t^2 \frac{2\tilde{t}'(t)}{[(1-t^2)x^2 - \tilde{t}(t)]^2 + \tilde{t}'(t)^2}\right] \,,\end{aligned} \tag{6.45}$$

with the dimensionless integration variable $t \equiv |\boldsymbol{q}|/\Delta E$ and the functions

$$\tilde{t}(x) \equiv \frac{1}{2x^2}\left[1 - \frac{1}{2x}(1-x^2)\ln\left|\frac{1+x}{1-x}\right|\right] \,,\ \ \tilde{t}'(x) \equiv \frac{\pi}{4x^3}(x^2-1)\Theta(x^2-1) \,. \tag{6.46}$$

In the last equality in eq. (6.45), the integral is split into two integration regions, that can be associated with distinct physical processes that contribute to heavy-pair transitions. For example, by considering bound-state formation, the first term in eq. (6.45) contributes to the radiative formation via the emission of an on-shell timelike dark photon with momentum $|\boldsymbol{q}| < \Delta E$, namely $(X\bar{X})_p \to (X\bar{X})_n + \gamma^*$; it is *timelike* because the photon is corrected with a light-fermion loop, which slows it down below the speed

of light. The second term in eq. (6.45) contributes to the $2 \to 2$ scattering process with light dark fermions from the plasma, the process being $(X\bar{X})_p + f_i \to (X\bar{X})_n + f_i$ (and similarly with antifermions $\bar{f}_i$). In this case, the interaction is mediated by an off-shell spacelike dark photon with momentum $|\boldsymbol{q}| > \Delta E$. The $1 \to 3$ process, where an intermediate off-shell timelike dark photon decays into a massless dark fermion-antifermion pair, is not captured here, since $\hat{k}(x) \neq 0$ only for $x > 1$. This is a more general statement for $T \gg \Delta E$, irrespective of the relative size between the Debye mass scale and ΔE. One may see this by expanding the Heaviside functions in eqs. (D.27) and (D.29) for large temperatures $T \gg \Delta E$, at all orders, it always leads to $\Theta(-q^2)$, cf. eqs. (D.36) and (D.38). Therefore, in the large temperature regime, the $1 \to 3$ process involving an intermediate off-shell photon with timelike momentum, $q^2 > 0$, cannot occur.

Similar arguments apply to the reversed $3 \to 1$ process in the situation of a bound-state dissociation. However, at temperatures $T \sim \Delta E$, the $1 \to 3$ interaction channel can give a finite contribution to the bsf process. But at this temperature regime the $1 \to 3$ off-shell photo-decay as well as the $2 \to 2$ Landau damping process appear as small next-to-leading order effects and are therefore suppressed compared to the leading order bound-state formation via an on-shell dark photon emission, as will be seen in fig. 6.3 upon plotting the thermally averaged cross section as a function of the inverse temperature, M/T.

Summarizing the result for the total self-energy, the sum of eqs. (6.40) and (6.44) leads to

$$\begin{aligned}
&\Sigma^{>}_{(m_\mathrm{D}\sim\Delta E)}(\Delta E) \\
&\quad = i\frac{\alpha}{3} T m_\mathrm{D}^2\, r^i \left[\frac{1}{\epsilon} - \gamma_\mathrm{E} + \frac{8}{3} - \ln\left(\frac{(\Delta E)^2}{\pi\mu^2}\right) + 2\mathcal{Y}^{\mathrm{long}}_{\mathrm{th}}\left(\frac{\Delta E}{m_\mathrm{D}}\right) + 2\mathcal{Y}^{\mathrm{trans}}_{\mathrm{th}}\left(\frac{\Delta E}{m_\mathrm{D}}\right)\right] r^i \\
&\quad = -2i\ \mathrm{Im}\left[\Sigma^{11}_{(m_\mathrm{D}\sim\Delta E)}(\Delta E)\right] ,
\end{aligned} \tag{6.47}$$

and adding the contribution in (6.30) coming from the scale T, we eventually end up with

$$\begin{aligned}
\mathrm{Im}\left[\Sigma^{11}(\Delta E)\right] &= \mathrm{Im}\left[\Sigma^{11}_{(T)}\right] + \mathrm{Im}\left[\Sigma^{11}_{(m_\mathrm{D}\sim\Delta E)}(\Delta E)\right] \\
&= \frac{\alpha}{3} T m_\mathrm{D}^2\, r^i \left[\gamma_\mathrm{E} - 1 - \frac{\zeta'(2)}{\zeta(2)} + \ln\left(\frac{\Delta E}{4T}\right) - \mathcal{Y}^{\mathrm{long}}_{\mathrm{th}}\left(\frac{\Delta E}{m_\mathrm{D}}\right) - \mathcal{Y}^{\mathrm{trans}}_{\mathrm{th}}\left(\frac{\Delta E}{m_\mathrm{D}}\right)\right] r^i .
\end{aligned} \tag{6.48}$$

We compute the bound-state formation cross section from the optical theorem, cf. eq. (5.21), taking into account the resummation of the Debye-mass scale in (6.48), and neglect the in-vacuum correction at NLO, cf. $\mathcal{X}_{\mathrm{vac}}$ in (6.24), since $n_f\alpha(\mu_s) \ll \sqrt{n_f\alpha(T)}$ for the considered parametric values of n_f and $\alpha(2M)$ in this work (we refer to the

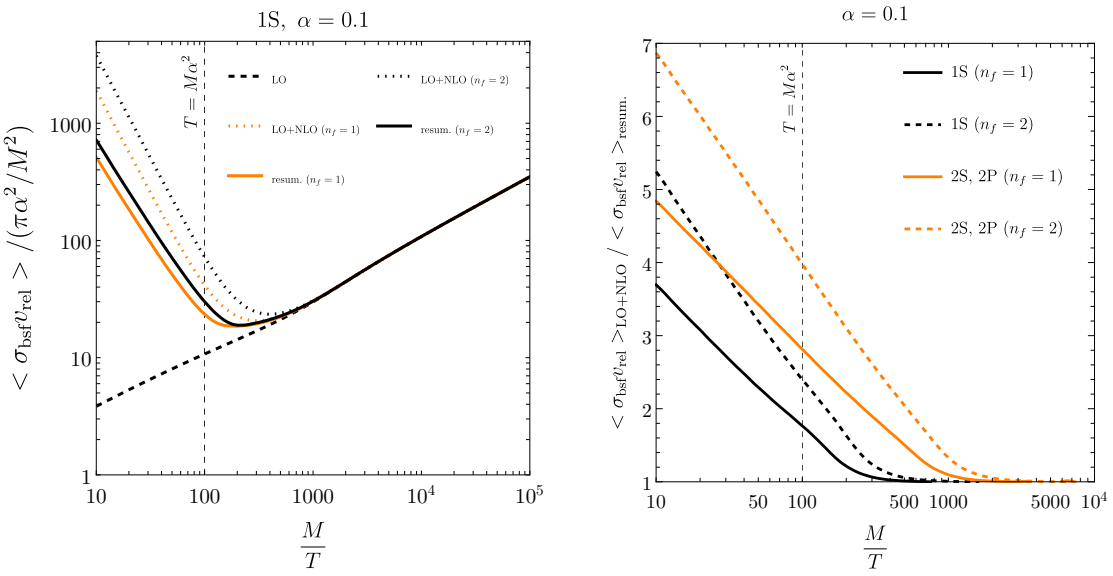

Figure 6.3: (Left) Ratios of the thermally averaged formation cross sections of the first few excited bound states at leading order, cf. eq. (6.9), over $\pi\alpha^2/M^2$, as functions of M/T. As a comparison, we plot also the thermally averaged Sommerfeld factor. (Right) Ratios of the 1S, 2S, 2P and 3S dissociation widths and 1S $\leftrightarrow$ 2P (de-)excitation widths over $M\alpha^5/2$ at leading order in the coupling. The vertical lines mark the position where $T = M\alpha^2$, i.e. the regime where the temperature is of order of the ultrasoft scale.

discussion in footnote 8 in the previous subsection). It reads

$$(\sigma_{\rm bsf}\, v_{\rm rel})_{\rm resum.}(\boldsymbol{p}) = \sum_n (\sigma^n_{\rm bsf}\, v_{\rm rel})^{\rm LO}(\boldsymbol{p})\Big|_{T\gg\Delta E^p_n} \times\left(\frac{m_{\rm D}}{2\Delta E^p_n}\right)^2\left[2 - 2\gamma_{\rm E} + 2\frac{\zeta'(2)}{\zeta(2)} - \ln\left(\frac{(\Delta E^p_n)^2}{16T^2}\right) + 2\mathcal{Y}^{\rm long}_{\rm th}\left(\frac{\Delta E^p_n}{m_{\rm D}}\right) + 2\mathcal{Y}^{\rm trans}_{\rm th}\left(\frac{\Delta E^p_n}{m_{\rm D}}\right)\right], \tag{6.49}$$

where $(\sigma^n_{\rm bsf}\, v_{\rm rel})^{\rm LO}(\boldsymbol{p})\big|_{T\gg\Delta E^p_n} \approx (4\alpha/3)|\langle n|\boldsymbol{r}|\boldsymbol{p}\rangle|^2 T(\Delta E^p_n)^2$ is the bsf cross section at leading order for a given bound state $|n\rangle$ with specific quantum numbers n, cf. eq. (6.9), in the limit of large temperatures $T \gg \Delta E^p_n$. We are now able to compare quantitatively the corrections from the $m_{\rm D}$-scale to the result obtained at leading order, cf. (6.9), but also to the result truncated at NLO, cf. (6.24). We integrate the expressions in (6.38) and (6.45) numerically and, similarly as in the left plot of fig. 6.2, we show the thermally averaged bsf cross sections for the ground state at LO (dashed line for $n_f = 1$ and $n_f = 2$), up to NLO (dotted lines) and with resummation effects (solid lines) on the left panel of fig. 6.3. Orange lines are for $n_f = 1$, black lines for $n_f = 2$, and we choose again $\alpha = 0.1$ at the hard scale $2M$, and run the coupling at one loop. The solid and dotted lines approach the dashed line with decreasing temperature. This indeed meets the expectations, since at small T the dominant bsf process is via on-shell emission of

a thermal dark photon. However, for large temperatures, where the thermal scale $m_{\rm D}$ becomes important and eventually needs to be resummed, we observe a corresponding smaller cross section (solid line) with respect to the cross section at fixed NLO (dotted curve). In order to see more closely the amount of discrepancy between the naive truncation of the loop corrections at NLO, and the resummation of the scale $m_{\rm D}$, we plot the ratio between the two cross sections for the ground state (black lines) as well as the first excited states 2S and 2P (orange lines) in the right panel of figure 6.3. Since the excited states 2S and 2P have the same binding energy, the ratio does not change. We observe an overestimation of the bsf cross section at NLO compared to the resummed cross section by a factor up to 4-7 in the large temperature region, depending on the number n_f of light fermions. The more fermions species the larger the NLO- and resummation effects due to the screening of the photon in the thermal bath. The screening effect, however, disappears in the small-T limit, independently of the value of n_f. But, as will be shown in the follow-up chapter, the discrepancy will have an impact when studying the dark matter density evolution in the early universe.

6.1.2 Center-of-mass recoil effects

In this section, we compute the bound-state formation cross section in pNRQED$_{\rm DM}$, within the hierarchy of energy scales (3.2), at leading order in the coupling expansion and first order in the temperature and recoil energy over M ratio. It generalizes the process in (6.10), i.e. $(X\bar{X})_p \to \gamma + (X\bar{X})_n$, where the thermal motion of the center-of-mass of the incoming scattering state $(X\bar{X})_p$ is now reinstated. It is the dominating process in the ultrasoft temperature regime (3.2). We make use of the optical theorem (5.21) and express the rate in terms of self-energy diagrams whose vertices are shown in figure 4.1. It follows that the self-energy of the scattering state at leading order in α, corresponding to the first diagram in fig. 6.1 and , is now extended to four self-energies depicted in fig. 6.4. We will check explicitly that the cross section obtained in the laboratory frame agrees with the one derived by boosting the cross section obtained in the center-of-mass frame.

6.1.2.1 Bound-state formation in the laboratory frame

The self-energy diagrams shown in fig. 6.4 depend on four correlators:
the electric-electric correlator

$$\langle E_i(t,\boldsymbol{R})E_j(0,\boldsymbol{R}')\rangle = \int \frac{d^4k}{(2\pi)^4} e^{-ik^0t+i\boldsymbol{k}\cdot(\boldsymbol{R}-\boldsymbol{R}')}\left[k_0^2 D_{ij}(k) + k_i k_j D_{00}(k)\right] , \tag{6.50}$$

the magnetic-magnetic correlator

$$\langle B_i(t,\boldsymbol{R})B_j(0,\boldsymbol{R}')\rangle = \epsilon_{ilm}\epsilon_{jnr}\int \frac{d^4k}{(2\pi)^4} e^{-ik^0t+i\boldsymbol{k}\cdot(\boldsymbol{R}-\boldsymbol{R}')}k_l k_n D_{mr}(k) , \tag{6.51}$$

the electric-magnetic correlator

$$\langle B_i(t,\boldsymbol{R})E_j(0,\boldsymbol{R}')\rangle = -\epsilon_{ilm}\int \frac{d^4k}{(2\pi)^4} e^{-ik^0t+i\boldsymbol{k}\cdot(\boldsymbol{R}-\boldsymbol{R}')}k_l k_0 D_{mj}(k) , \tag{6.52}$$

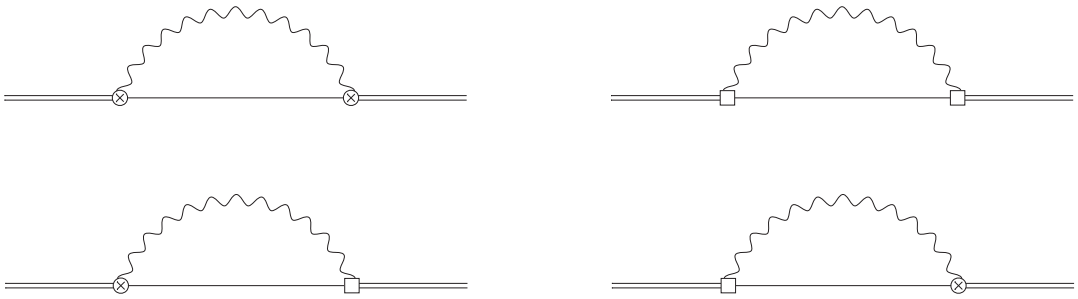

Figure 6.4: Self-energy diagrams in pNRQED$_{\rm DM}$ with an initial scattering state (solid double line) and an intermediate bound state (solid line) contributing up to relative order T/M in the laboratory frame. The electric electric diagram on the upper left contains the leading-order diagram, cf. one-loop diagram in fig. 6.1. The other diagrams are suppressed by T/M or $\Delta E_n^p/M$. Since the dark photon in the loop carries a spatial momentum $\boldsymbol{k}$, the bound fermion-antifermion pair recoils by a spatial momentum $\boldsymbol{P}-\boldsymbol{k}$. Electric and magnetic couplings are as in figure 4.1.

and the magnetic-electric correlator

$$\langle E_i(t,\boldsymbol{R})B_j(0,\boldsymbol{R}')\rangle = -\epsilon_{jlm}\int\frac{d^4k}{(2\pi)^4}e^{-ik^0t+i\boldsymbol{k}\cdot(\boldsymbol{R}-\boldsymbol{R}')}k_lk_0D_{im}(k)\,, \tag{6.53}$$

where $D_{\mu\nu}$ is the dark photon propagator at leading order in the real-time formalism; we use the expressions (D.4)–(D.5) in Coulomb gauge and drop the superscript LO.[13] The correlators are gauge invariant and therefore may be evaluated in any gauge. The bound-state formation cross section can be computed from the imaginary part of the 11-componentd of the four self-energies, which is the approach that we follow in this section. In the laboratory frame, the dark fermion-antifermion pair moves with momentum $\boldsymbol{P}$. After emitting a dark photon of spatial momentum $\boldsymbol{k}$, the fermion-antifermion pair recoils by a spatial momentum $\boldsymbol{P}-\boldsymbol{k}$. Therefore, the propagator of the recoiling fermion-antifermion pair is in pNRQED$_{\rm DM}$

$$\frac{i}{E_p+\boldsymbol{P}^2/(4M)-(E_n+(\boldsymbol{P}-\boldsymbol{k})^2/(4M))-k_0+i\epsilon} = \frac{i}{\Delta E_n^p+(2\boldsymbol{P}\cdot\boldsymbol{k}-\boldsymbol{k}^2)/(4M)-k_0+i\epsilon}\,, \tag{6.54}$$

where we have defined[14]

$$\Delta E_n^p \equiv (\Delta E_n^p)_{\rm lab} \equiv (E_p)_{\rm lab}-(E_n)_{\rm lab} > 0 \tag{6.55}$$

[13] We remark that at large temperatures close to the freeze-out, where bath-particle scattering effects need to be taken into account, the Debye-mass resummation alters the dark photon propagator significantly from its expression at leading order. The computation of recoil effects within the hierarchy (3.4) may be of interest in future works.

[14] In the energy difference $(\Delta E_n^p)_{\rm lab}$ one needs to add the center-of-mass correction terms to the potential and kinetic energy, given in footnote 4 in sec. 4.2, since these corrections may contribute

the energy difference between the scattering state and the bound state in the laboratory frame. The time-ordered 11-component of the electric-electric self-energy diagram (upper left diagram in fig. 6.4), projected onto a scattering state with relative momentum $\boldsymbol{p} \equiv \boldsymbol{p}_{\rm lab}$ and center-of-mass momentum $\boldsymbol{P}$, reads

$$\begin{aligned}\left(-i\Sigma^{11}_{ee}\right)(\boldsymbol{p},\boldsymbol{P}) = -g^2 \sum_n \int \frac{d^4k}{(2\pi)^4} \frac{i}{\Delta E^p_n + \frac{2\boldsymbol{P}\cdot\boldsymbol{k}-\boldsymbol{k}^2}{4M} - k_0 + i\epsilon} \\ \times \left[|\langle n|\boldsymbol{r}|\boldsymbol{p}\rangle|^2 k_0^2 - \langle n|\boldsymbol{r}\cdot\boldsymbol{k}|\boldsymbol{p}\rangle|^2\right] \left[\frac{i}{k^2+i\epsilon} + 2\pi\delta(k^2) n_{\rm B}(|k_0|)\right],\end{aligned} \tag{6.56}$$

where we have summed over all intermediate bound states. The time-ordered 11-component of the magnetic-magnetic self-energy diagram (upper right diagram in fig. 6.4) reads

$$\begin{aligned}\left(-i\Sigma^{11}_{mm}\right)(\boldsymbol{p},\boldsymbol{P}) = -\frac{g^2}{4M^2}\epsilon_{ijk}\epsilon_{lmn}\epsilon_{krs}\epsilon_{ntu} \sum_n \int \frac{d^4k}{(2\pi)^4} \frac{i}{\Delta E^p_n + \frac{2\boldsymbol{P}\cdot\boldsymbol{k}-\boldsymbol{k}^2}{4M} - k_0 + i\epsilon} \\ \times \left(P_i - \frac{k_i}{2}\right)\left(P_l - \frac{k_l}{2}\right)\langle \boldsymbol{p}|r^j|n\rangle\langle n|r^m|\boldsymbol{p}\rangle k_r k_t \left(\delta_{su} - \frac{k_s k_u}{\boldsymbol{k}^2}\right)\left[\frac{i}{k^2+i\epsilon} + 2\pi\delta(k^2) n_{\rm B}(|k_0|)\right].\end{aligned} \tag{6.57}$$

The time-ordered 11-component of the electric-magnetic self-energy diagram (lower left diagram in fig. 6.4) is given by

$$\begin{aligned}\left(-i\Sigma^{11}_{em}\right)(\boldsymbol{p},\boldsymbol{P}) = \frac{g^2}{2M}\epsilon_{ijk}\epsilon_{klm} \sum_n \int \frac{d^4k}{(2\pi)^4} \left(P_i - \frac{k_i}{2}\right) \frac{i}{\Delta E^p_n + \frac{2\boldsymbol{P}\cdot\boldsymbol{k}-\boldsymbol{k}^2}{4M} - k_0 + i\epsilon} \\ \times \langle \boldsymbol{p}|r^j|n\rangle\langle n|r^s|\boldsymbol{p}\rangle k_l k_0 \left(\delta_{sm} - \frac{k_s k_m}{\boldsymbol{k}^2}\right)\left[\frac{i}{k^2+i\epsilon} + 2\pi\delta(k^2) n_{\rm B}(|k_0|)\right],\end{aligned} \tag{6.58}$$

and the time-ordered 11-component of the magnetic-electric self-energy diagram (lower right diagram in fig. 6.4) reads

$$\begin{aligned}\left(-i\Sigma^{11}_{me}\right)(\boldsymbol{p},\boldsymbol{P}) = \frac{g^2}{2M}\epsilon_{ijk}\epsilon_{klm} \sum_n \int \frac{d^4k}{(2\pi)^4} \frac{i}{\Delta E^p_n + \frac{2\boldsymbol{P}\cdot\boldsymbol{k}-\boldsymbol{k}^2}{4M} - k_0 + i\epsilon} \left(P_i - \frac{k_i}{2}\right) \\ \times \langle \boldsymbol{p}|r^s|n\rangle\langle n|r^j|\boldsymbol{p}\rangle k_l k_0 \left(\delta_{sm} - \frac{k_s k_m}{\boldsymbol{k}^2}\right)\left[\frac{i}{k^2+i\epsilon} + 2\pi\delta(k^2) n_{\rm B}(|k_0|)\right].\end{aligned} \tag{6.59}$$

The term $(2\boldsymbol{P}\cdot\boldsymbol{k} - \boldsymbol{k}^2)/(4M)$, that enters the heavy-pair propagator in each of the eqs. (6.56)–(6.59), is a recoil correction to the kinetic energy. It is indeed a correction, since the term $\boldsymbol{P}\cdot\boldsymbol{k}/(2M)$ is suppressed by $\sqrt{T/M}$ and the term $-\boldsymbol{k}^2/(4M)$ by T/M with

at order T/M and $\Delta E^p_n/M$ through the electric-electric self-energy diagram in the upper left corner of fig. 6.4, and the insertions into the other diagrams lead to corrections of higher order. As for the electric-electric diagram, the leading recoil correction due to $\delta V(\boldsymbol{r},\boldsymbol{P})$ is proportional to the energy shift $\langle \boldsymbol{p}|\delta V(\boldsymbol{r},\boldsymbol{P})|\boldsymbol{p}\rangle - \langle n|\delta V(\boldsymbol{r},\boldsymbol{P}-\boldsymbol{k})|n\rangle$. Terms that do not depend on $\boldsymbol{k}$ are absorbed into ΔE^p_n, terms linear in $\boldsymbol{k}$ give rise to odd integrands in $\boldsymbol{k}$, while terms proportional to $\boldsymbol{k}^2$ give rise to corrections of order $(\Delta E^p_n/M)^2$, which are beyond our accuracy. A similar reasoning holds for the kinetic energy correction.

respect to ΔE_n^p and T. Hence, the expansion of the propagator (6.54) up to terms of relative order T/M reads

$$\begin{aligned}\frac{i}{\Delta E_n^p + (2\boldsymbol{P}\cdot\boldsymbol{k} - \boldsymbol{k}^2)/(4M) - k_0 + i\epsilon} &= \frac{i}{\Delta E_n^p - k_0 + i\epsilon} \\ &+ \frac{i}{(\Delta E_n^p - k_0 + i\epsilon)^2}\left(-\frac{2\boldsymbol{P}\cdot\boldsymbol{k} - \boldsymbol{k}^2}{4M}\right) + \frac{i}{(\Delta E_n^p - k_0 + i\epsilon)^3}\left(\frac{\boldsymbol{P}\cdot\boldsymbol{k}}{2M}\right)^2 + \dots ,\end{aligned} \tag{6.60}$$

where the dots stand for higher-order terms. We expand the heavy-pair propagators in (6.56)–(6.59) according to (6.60), and integrate over the four-momentum k. The sum of the imaginary parts of the four self-energies, upon using the optical theorem (5.21), gives the bound-state formation cross section

$$\begin{aligned}(\sigma_{\rm bsf}\, v_{\rm M\o l})_{\rm lab}(\boldsymbol{p},\boldsymbol{P}) &= \sum_n (\sigma_{\rm bsf}^n\, v_{\rm M\o l})_{\rm lab}(\boldsymbol{p},\boldsymbol{P}) \\ &= -2\,{\rm Im}\left[\left(\Sigma_{ee}^{11}\right)(\boldsymbol{p},\boldsymbol{P}) + \left(\Sigma_{mm}^{11}\right)(\boldsymbol{p},\boldsymbol{P}) + \left(\Sigma_{em}^{11}\right)(\boldsymbol{p},\boldsymbol{P}) + \left(\Sigma_{me}^{11}\right)(\boldsymbol{p},\boldsymbol{P})\right] .\end{aligned} \tag{6.61}$$

Including all corrections of relative order $\boldsymbol{P}^2/M^2 \sim T/M$ and $\Delta E_n^p/M$, the bound-state formation cross section in the laboratory frame reads

$$\begin{aligned}(\sigma_{\rm bsf}\, v_{\rm M\o l})_{\rm lab}(\boldsymbol{p},\boldsymbol{P}) = \frac{4}{3}\alpha \sum_n (\Delta E_n^p)^3\,(1 + n_{\rm B}(\Delta E_n^p)) \\ \times \left(|\langle n|\boldsymbol{r}|\boldsymbol{p}\rangle_{\rm lab}|^2 F_1^n(p,P) + \left|\langle n|\boldsymbol{r}\cdot\frac{\boldsymbol{P}}{2M}|\boldsymbol{p}\rangle_{\rm lab}\right|^2 F_2^n(p,P)\right),\end{aligned} \tag{6.62}$$

with

$$\begin{aligned}F_1^n(p,P) = 1 &- \frac{3}{4}\frac{\Delta E_n^p}{M} + \frac{\boldsymbol{P}^2}{4M^2} + n_{\rm B}(\Delta E_n^p)\,\frac{\Delta E_n^p}{4M}\,\frac{\Delta E_n^p}{T} \\ &- n_{\rm B}(\Delta E_n^p)\,\frac{\boldsymbol{P}^2}{4M^2}\frac{\Delta E_n^p}{T}\left[1 - \frac{\Delta E_n^p}{5T} - \frac{2}{5}n_{\rm B}(\Delta E_n^p)\frac{\Delta E_n^p}{T}\right],\end{aligned} \tag{6.63}$$

and

$$F_2^n(p,P) = 1 - \frac{1}{10}\,n_{\rm B}(\Delta E_n^p)\,\frac{(\Delta E_n^p)^2}{T^2}\,(1 + 2\,n_{\rm B}(\Delta E_n^p)) . \tag{6.64}$$

Note that $\Delta E_n^p/T$ may be of order one according to our hierarchy of energy scales (3.2). The statistical factor $1 + n_{\rm B}(\Delta E_n^p)$ in (6.62) reflects the fact the dark photon is emitted into the thermal bath. From the recoil factors (6.63) and (6.64) we deduce that the recoil corrections can be split into in-vacuum and thermal contributions, and that even in the zero-total-momentum-limit a residual recoil correction remains, since $F_1^n(p, P = 0) \neq 1$. Contrarily to the result in eq. (6.9), due to the appearance of the quantum-mechanical matrix element involving the scalar product $\boldsymbol{r}\cdot\boldsymbol{P}/(2M)$, cf. second term in the second line of eq. (6.62), rotational invariance is broken because of the aligned center-of-mass momentum vector.

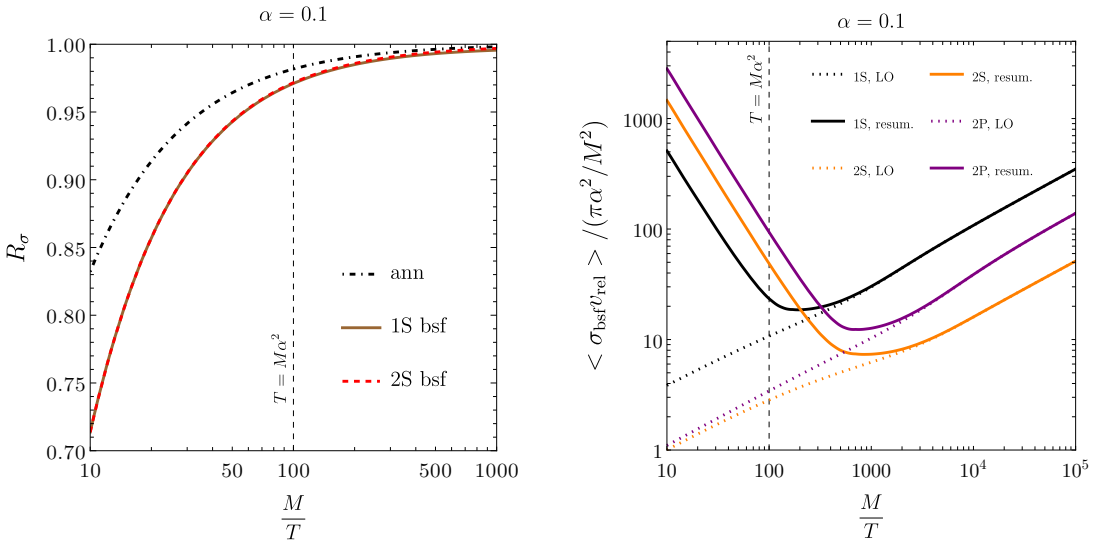

Figure 6.5: (Left) Ratios of thermally averaged cross sections in the laboratory frame with recoil corrections and the corresponding thermally averaged cross sections without recoil corrections plotted as a function of M/T for coupling $\alpha = 0.1$. The black dash-dotted line follows from the annihilation cross section (5.28), and the brown solid and red dashed lines from the bound-state formation cross section (6.62) for the 1S and 2S state, respectively. (Right) Thermally averaged bsf cross sections for the 1S (black lines), 2S (orange lines) and 2P state (purple lines), normalized by $\pi\alpha^2/M^2$. Dashed lines are for the results at LO, cf. (6.9), solid lines as obtained from (6.49). The coupling $\alpha = \alpha(2M) = 0.1$ runs at one loop and $n_f = 1$. The vertical lines mark the position where $T = M\alpha^2$.

In order to quantify the effect of the recoil corrections due to the center-of-mass motion on the bsf cross section, we compare the result (6.62) with the corresponding leading-order expression without recoil corrections in (6.9). In the left plot of fig. 6.5 we show the ratio R_σ of the the thermally averaged bsf cross sections (6.62) and (6.9), for the 1S and 2S state (denoted by the brown solid and red dashed line, respectively). The thermal average in the laboratory frame has been defined in appendix B. Similarly, for dark matter fermion pair annihilation (black dash-dotted line), we take the ratio of the thermal average of (5.28) in the laboratory frame and the corresponding thermally averaged annihilation cross section without center-of-mass momentum dependence in (5.27). For the coupling $\alpha = 0.1$, the effect of the center-of-mass recoil corrections to the bound-state formation cross section is up to 3% at temperatures such that $M/T \gtrsim 1/\alpha^2 = 100$. The recoil corrections increase for larger couplings, for instance for $\alpha = 0.5$ they are around 20-25% around the thermal freeze-out.[15] We checked that for the whole range of considered couplings up to $\alpha = 0.5$, recoil corrections are larger for bound-state

[15]We remind that for such large coupling, the condition $M\alpha^2 \gtrsim T$ is fulfilled even at freeze-out temperature.

formation cross sections than for annihilation. The reason is that processes happening at the hard scale, like annihilations, depend weakly on the thermal medium.[16] In general, it holds that the ratio is $R_\sigma < 1$, since the annihilation and bound-state formation cross sections are both Lorentz contracted in the laboratory frame, although to a different degree.

In order to have a direct comparison between the recoil corrections due to the center-of-mass motion and the corrections coming from the resummation of the Debye-mass scale, we show in the right panel of figure 6.5 the 1S-, 2S- and 2P-bsf cross sections at LO (dotted lines), cf. eq. (6.9), and the resummed expressions (solid lines), cf. eq. (6.49), for $n_f = 1$. We can see two main differences. While the recoil effect seems independent of the specific internal quantum numbers n of the outgoing bound state (the brown solid and red dashed lines overlap), the m_D-resummation increases the formation cross section of the higher excited states more than the ground state at large temperatures, and hence the scale m_D has a strong influence on the internal motion of the heavy pair. The second difference lies in the size of the corrections, where we see that the resummation increases the rate by orders of magnitude with increasing T, while the recoil corrections are only of the order of percentage.[17] In chapter 7, we are going to contrast again the recoil with resummation effects, but then on the level of the DM relic abundance.

6.1.2.2 Bound-state formation in the center-of-mass frame

In the following, we consider the dark-matter pair at rest, while the thermal bath moves with constant velocity $-\boldsymbol{v}$; see fig. 2.1 for a pictorial illustration.[18] We provide the bound-state formation cross section in the center-of-mass frame of the dark-matter fermion-antifermion pair. In the following, the relative momentum, $\boldsymbol{p}$, and distance, $\boldsymbol{r}$, in quantities marked with the subscript cm are to be understood as measured in the center-of-mass frame. The Bose–Einstein distribution for thermal dark photons in the

[16] For the Coulombic bound states considered in this work, the leading thermal correction to the annihilation cross section or width comes from a loop diagram with two electric dipole vertices and the insertion of an imaginary contact potential (5.19). This is suppressed by at least $\alpha(a_0 T)^2 \lesssim \alpha T/M$ with respect to the leading width.

[17] We have to remark, however, that the recoil effect has been considered only for the bsf process given in (6.10), which is fine as long as the temperature is at most ultrasoft, i.e. if for the hierarchy 3.2. It remains to check how large the recoil corrections become if we go to larger T, cf. hierarchy 3.4, where the thermal motion of the heavy particles become faster in the bath, and where the Landau-damping phenomenon becomes important.

[18] A general formula for the center-of-mass velocity of the heavy pair with respect to the moving thermal medium as seen from a generic laboratory frame is given by [131]

$$\boldsymbol{v} = \frac{-P^0 \boldsymbol{w} + \frac{\boldsymbol{P}\cdot\boldsymbol{w}}{\boldsymbol{w}^2}\boldsymbol{w} + \left(\boldsymbol{P} - \frac{\boldsymbol{P}\cdot\boldsymbol{w}}{\boldsymbol{w}^2}\boldsymbol{w}\right)\sqrt{1-\boldsymbol{w}^2}}{P^0 - \boldsymbol{P}\cdot\boldsymbol{w}}\,,$$

where P^0 and $\boldsymbol{P}$ are the total energy and center-of-mass momentum of the dark-matter pair with respect to the laboratory frame, respectively, and $\boldsymbol{w}$ is the velocity of the thermal medium with respect to the laboratory frame. If the laboratory frame coincides with the center-of-mass frame of the pair, then $\boldsymbol{P} = 0$ and $\boldsymbol{v} = -\boldsymbol{w}$. Instead, if the laboratory frame coincides with the frame where the medium is at rest, then $\boldsymbol{w} = 0$ and $\boldsymbol{v} = \boldsymbol{P}/P^0$.

moving bath reads [125, 132]

$$n_{\rm B}(|k^\mu u_\mu|) = \frac{1}{e^{|k^\mu u_\mu|/T} - 1}\,, \tag{6.65}$$

where $u^\mu = (1, -\boldsymbol{v})\,\gamma$, and, as in the rest of the paper, $\gamma = 1/\sqrt{1-\boldsymbol{v}^2}$ is the Lorentz factor. In the laboratory frame, where the bath is at rest ($\boldsymbol{v} = 0$), we have $k^\mu u_\mu = k^0$, and the distribution (6.65) reduces to (6.1). For on-shell thermal dark photons from the bath, we can write

$$\frac{k^\mu u_\mu}{T} = \frac{k^0 - |\boldsymbol{v}||\boldsymbol{k}|\cos\theta}{T\sqrt{1-\boldsymbol{v}^2}} = \frac{|\boldsymbol{k}|}{T}\frac{1 - |\boldsymbol{v}|\cos\theta}{\sqrt{1-\boldsymbol{v}^2}} \equiv \frac{|\boldsymbol{k}|}{T_{\rm eff}}\,, \tag{6.66}$$

where θ is the angle between the medium velocity $-\boldsymbol{v}$ and the dark photon momentum $\boldsymbol{k}$. The *effective temperature*, $T_{\rm eff}$, is defined as [133]

$$T_{\rm eff}(|\boldsymbol{v}|, \theta) = \frac{T\sqrt{1-\boldsymbol{v}^2}}{1 - |\boldsymbol{v}|\cos\theta}\,. \tag{6.67}$$

It may be understood as the temperature experienced by an observer at rest; it is different from T because of the Doppler effect.[19] Expanding the distribution function (6.65) for small medium velocities $|\boldsymbol{v}| \ll 1$ up to order $\boldsymbol{v}^2$, we get[20]

$$n_{\rm B}(|k^\mu u_\mu|) = n_{\rm B}(|\boldsymbol{k}|)\left[1 + (1 + n_{\rm B}(|\boldsymbol{k}|))\left(-\frac{\boldsymbol{v}\cdot\boldsymbol{k}}{T} - \frac{|\boldsymbol{k}|}{T}\frac{\boldsymbol{v}^2}{2} + \frac{(\boldsymbol{k}\cdot\boldsymbol{v})^2}{2T^2}(2n_{\rm B}(|\boldsymbol{k}|) + 1)\right)\right]. \tag{6.68}$$

In the center-of-mass frame, the dark fermion-antifermion pair recoils by a spatial momentum $-\boldsymbol{k}$ when emitting a photon of spatial momentum $\boldsymbol{k}$. The resulting propagator, when the incoming pair is in a scattering state and the outcoming one in a bound state, can be expanded in the center-of-mass kinetic energy $\boldsymbol{k}^2/(4M)$, which is suppressed by T/M with respect to ΔE_n^p and T, leading to

$$\frac{i}{(\Delta E_n^p)_{\rm cm} - \boldsymbol{k}^2/(4M) - k_0 + i\epsilon} = \frac{i}{(\Delta E_n^p)_{\rm cm} - k_0 + i\epsilon} + \frac{i}{((\Delta E_n^p)_{\rm cm} - k_0 + i\epsilon)^2}\frac{\boldsymbol{k}^2}{4M} + \dots\,. \tag{6.69}$$

Higher-order terms are beyond our accuracy. The bound-state formation cross section in the center-of-mass frame up to relative order $\boldsymbol{v}^2$, which in our case is about T/M and

[19] Depending on the angle θ, i.e. whether the medium moves towards the observer ($0 \le \theta < \pi/2$) or away from the observer ($\pi/2 < \theta \le \pi$), the temperature measured by the observer is larger or smaller than T, T being the temperature of the thermal bath in the medium rest frame. The maximum and minimum temperature is for $\theta = 0$ and $\theta = \pi$, respectively,

$$T_{\rm max} = T\sqrt{\frac{1+|\boldsymbol{v}|}{1-|\boldsymbol{v}|}}\,, \qquad T_{\rm min} = T\sqrt{\frac{1-|\boldsymbol{v}|}{1+|\boldsymbol{v}|}}\,.$$

[20] Because of the hierarchy (3.2), we consider here only the case of a thermal bath moving at small velocity. For the case of a thermal bath of photons moving at high velocity, see ref. [125].

$\Delta E_n^p/M$, can be again computed by cutting the four self-energy diagrams in fig. 6.4, and reads

$$\begin{aligned}(\sigma_{\rm bsf}\, v_{\rm M\o l})_{\rm cm}(\boldsymbol{p},\boldsymbol{v}) &= -2\,{\rm Im}\left[\left(\Sigma_{ee}^{11}\right)(\boldsymbol{p},\boldsymbol{v})+\left(\Sigma_{mm}^{11}\right)(\boldsymbol{p},\boldsymbol{v})+\left(\Sigma_{em}^{11}\right)(\boldsymbol{p},\boldsymbol{v})+\left(\Sigma_{me}^{11}\right)(\boldsymbol{p},\boldsymbol{v})\right]\\ &= \frac{4}{3}\alpha\sum_n (\Delta E_n^p)_{\rm cm}^3\,(1+n_{\rm B}((\Delta E_n^p)_{\rm cm}))\Big(|\langle n|\boldsymbol{r}|\boldsymbol{p}\rangle_{\rm cm}|^2\tilde{F}_1^n(p,v)+|\langle n|\boldsymbol{r}\cdot\boldsymbol{v}|\boldsymbol{p}\rangle_{\rm cm}|^2\tilde{F}_2^n(p,v)\Big)\,,\end{aligned} \tag{6.70}$$

with

$$\begin{aligned}\tilde{F}_1^n(p,v) =& 1-\frac{3}{4}\frac{(\Delta E_n^p)_{\rm cm}}{M}+n_{\rm B}((\Delta E_n^p)_{\rm cm})\,\frac{(\Delta E_n^p)_{\rm cm}}{4M}\,\frac{(\Delta E_n^p)_{\rm cm}}{T}\\ &-n_{\rm B}((\Delta E_n^p)_{\rm cm})\,\boldsymbol{v}^2\frac{(\Delta E_n^p)_{\rm cm}}{T}\left[\frac{1}{2}-\frac{(\Delta E_n^p)_{\rm cm}}{5T}-\frac{2}{5}n_{\rm B}((\Delta E_n^p)_{\rm cm})\frac{(\Delta E_n^p)_{\rm cm}}{T}\right],\end{aligned} \tag{6.71}$$

and

$$\tilde{F}_2^n(p,v) = -\frac{1}{10}\,n_{\rm B}((\Delta E_n^p)_{\rm cm})\,\frac{(\Delta E_n^p)_{\rm cm}^2}{T^2}\,(1+2\,n_{\rm B}((\Delta E_n^p)_{\rm cm}))\,, \tag{6.72}$$

where we have made explicit in which reference frame the matrix elements and the energy difference are computed, and we have neglected relative corrections smaller than $\boldsymbol{v}^2$ and $\Delta E_n^p/M$.

6.1.2.3 Boost-invariance of the cross section at finite T

So far we have computed the bound-state formation cross section in the laboratory frame as well as in the center-of-mass frame directly from the imaginary part of the four self-energy diagrams in fig. 6.4 by means of the optical theorem. We can show that the two results for the bsf cross section can be related to each other by transforming the matrix elements and the energy difference from the center-of-mass frame to the laboratory frame:

$$\begin{aligned}|\langle n|\boldsymbol{r}|\boldsymbol{p}\rangle_{\rm cm}|^2 &= |\langle n|\boldsymbol{r}|\boldsymbol{p}\rangle_{\rm lab}|^2\left(1+\frac{\boldsymbol{v}^2}{2}\right)+|\langle n|\boldsymbol{r}\cdot\boldsymbol{v}|\boldsymbol{p}\rangle_{\rm lab}|^2\,,\\ |\langle n|\boldsymbol{r}\cdot\boldsymbol{v}|\boldsymbol{p}\rangle_{\rm cm}|^2 &= |\langle n|\boldsymbol{r}\cdot\boldsymbol{v}|\boldsymbol{p}\rangle_{\rm lab}|^2\,,\\ (\Delta E_n^p)_{\rm cm} &= \gamma(\Delta E_n^p)_{\rm lab} = (\Delta E_n^p)_{\rm lab}\left(1+\frac{\boldsymbol{v}^2}{2}\right),\end{aligned} \tag{6.73}$$

which follow from eqs. (A.23) and (A.34) upon expanding up to order $\boldsymbol{v}^2$. We insert them into eq. (6.70), set $\boldsymbol{v}=\boldsymbol{P}/(2M)$ and keep only terms up to order $\boldsymbol{P}^2/M^2$. Then the relation between the bound-state formation cross section in the laboratory frame (6.62) and the bound-state formation cross section in the center-of-mass frame (6.70) is

$$(\sigma_{\rm bsf}\, v_{\rm M\o l})_{\rm lab}(\boldsymbol{p},\boldsymbol{P}) = (\sigma_{\rm bsf}\, v_{\rm M\o l})_{\rm cm}(\boldsymbol{p},\boldsymbol{P}/(2M))\left(1-\frac{\boldsymbol{P}^2}{4M^2}\right), \tag{6.74}$$

This relation is consistent with the discussion in section 5.2.2: the cross section is Lorentz invariant and the transformation (6.74) just reflects the Lorentz transformation (5.17)

of the Møller velocity. Hence, Lorentz-boost invariance of the cross section is not broken by the thermal medium. We remind that the relative momentum in $(\sigma_{\rm bsf}\, v_{\rm Møl})_{\rm lab}(\boldsymbol{p}, \boldsymbol{P})$ is measured in the laboratory frame, the one in $(\sigma_{\rm bsf}\, v_{\rm Møl})_{\rm cm}(\boldsymbol{p}, \boldsymbol{P}/(2M))$ is measured in the center-of-mass frame and the center-of-mass momentum $\boldsymbol{P}$ is measured in the laboratory frame.

6.2 Dissociation of bound states

6.2.1 Results at LO, NLO and with Debye-mass resummation in a static medium without recoil

In the previous section we introduced briefly the dissociation of bound states as the reversed process to the bound-state formation, and that the interplay between both processes keeps the heavy pairs in ionization equilibrium at large T. Moreover, from the detailed balance relations (6.15) we have shown how the corresponding dissociation width may be related from the bsf cross section, and have plotted the result in the right panel of fig. 6.2. One can verify the detailed balance condition (6.15) by computing the width directly within pNRQED$_{\rm DM}$ at finite T, as was done for the bsf cross section. If we neglect the center-of-mass motion of the heavy pair and exchange the double solid lines with the single solid lines in fig. (6.1), then from the optical theorem we can relate the bsd width of an incoming bound state with quantum numbers n and energy E_n to the imaginary part of the self-energy via

$$\Gamma^n_{\rm bsd} = -2\,\langle n|{\rm Im}[\Sigma^{11}(E_n)]|n\rangle = \langle n|[-i\Sigma^{21}(E_n)]|n\rangle\,. \tag{6.75}$$

At leading order in the coupling α and projecting on intermediate unbound fermion-antifermion pairs of relative momentum $\boldsymbol{p}$, which selects the part of ${\rm Im}[\Sigma^{11}(E_n)]$ or $\Sigma^{21}(E_n)$ with negative $\Delta E = E_n - E_p = -\Delta E^p_n$, we get

$$\Gamma^{n,{\rm LO}}_{\rm bsd} = \frac{g^2}{3\pi}\int\frac{d^3p}{(2\pi)^3}\, n_{\rm B}(\Delta E^p_n)\;|\langle n|\boldsymbol{r}|\boldsymbol{p}\rangle|^2\,(\Delta E^p_n)^3\,, \tag{6.76}$$

corresponding to the *photo-dissociation* process through the reaction

$$\gamma + (X\bar{X})_n \to (X\bar{X})_p\,. \tag{6.77}$$

It is a purely *thermal* width, because it depends on the Bose–Einstein distribution $n_{\rm B}(\Delta E^p_n)$ that vanishes in the $T = 0$ limit, which reflects the fact that the decay of a bound state into an unbound pair is kinematically forbidden in vacuum. Hence, as the plasma temperature decreases, fewer darkonium states can be ionized. The thermal width can be also understood in general as an integral over a temperature-dependent bound-state dissociation cross section, $\sigma^n_{\rm bsd}$, or as a convolution of the in-vacuum *ionization* (ion) cross section of the bound-state, which we denote $\sigma^n_{\rm ion}$, with the thermal

distribution of the incoming photon, here at LO:

$$\begin{aligned}\Gamma_{\rm bsd}^{n,\rm LO} &= 2\int\frac{d^3p}{(2\pi)^3}\sigma_{\rm bsd}^{n,\rm LO}(\boldsymbol{p}) = 2\int\frac{d^3p}{(2\pi)^3}\,n_{\rm B}(\Delta E_n^p)\,\sigma_{\rm bsd}^{n,\rm LO}(\boldsymbol{p})\\ &= 2\int_{|\boldsymbol{k}|\geq|E_n^b|}\frac{d^3k}{(2\pi)^3}\,n_{\rm B}(|\boldsymbol{k}|)\,\sigma_{\rm ion}^{n,\rm LO}(\boldsymbol{k})\,,\end{aligned} \tag{6.78}$$

where 2 is the number of final state photon polarizations and the relative velocity between the darkonium and the photon from the bath has been set equal to one. The bound-state formation and ionization cross sections are related via the temperature-dependent Milne relation [51]

$$\frac{\sigma_{\rm ion}^n(\boldsymbol{p})}{\sigma_{\rm bsf}^n(\boldsymbol{p})} = \frac{M^2v_{\rm rel}^2}{8(\Delta E_n^p)^2}\frac{1}{1+n_{\rm B}(\Delta E_n^p)}\,, \tag{6.79}$$

which reduces to the in-vacuum Milne relation in ref. [15] in the $T=0$ limit at fixed relative velocity $v_{\rm rel}$.

We provide some explicit expressions for the dissociation widths for the ground state and the first few excited states. For photo-dissociation of the lowest-lying darkonium, eq. (6.76) can be equivalently written as an integral over the momentum $\boldsymbol{k}$ of the absorbed dark photon:[21]

$$\Gamma_{\rm bsd}^{\rm 1S,LO} = \int_{|\boldsymbol{k}|\geq|E_1^b|}\frac{d^3k}{(2\pi)^3}\,n_{\rm B}(|\boldsymbol{k}|)\,\frac{4}{3}\alpha\,\frac{M^{\frac{3}{2}}}{2}\,|\boldsymbol{k}|\,\sqrt{|\boldsymbol{k}|+E_1^b}\,|\langle 1{\rm S}|\boldsymbol{r}|\boldsymbol{p}1\rangle|^2\Big|_{|\boldsymbol{p}|=\sqrt{M(|\boldsymbol{k}|+E_1^b)}}\,, \tag{6.80}$$

where $E_n^b \equiv E_n - 2M$; in particular, $E_1^b = -M\alpha^2/4$ is the binding energy of the 1S state. Note that the photon needs to have a threshold momentum to trigger the breaking of the bound state. The result agrees in the abelian limit with the gluo-dissociation width of a color singlet quark-antiquark bound state in the temperature regime $T\sim M\alpha_s^2$ [50,134], which we will reproduce in sec. 9.2, cf. eq. (9.23). The gluo-dissociation width of a heavy quarkonium in the static limit was obtained in ref. [48] and for a hydrogen atom in QED in ref. [49]. Comparing the above equation with eq. (6.80) and using the expression of the dipole matrix element in the center-of-mass frame given in appendix C, we obtain

$$\sigma_{\rm ion}^{\rm 1S,LO}(|\boldsymbol{k}|) = \alpha\frac{2^9\pi^2}{3}\frac{|E_1^b|^3}{M|\boldsymbol{k}|^4}\frac{e^{-\frac{4}{w_1(|\boldsymbol{k}|)}\arctan(w_1(|\boldsymbol{k}|))}}{1-e^{-\frac{2\pi}{w_1(|\boldsymbol{k}|)}}}\,, \tag{6.81}$$

with $w_1(|\boldsymbol{k}|)\equiv\sqrt{|\boldsymbol{k}|/|E_1^b|-1}$. The result in eq. (6.81) agrees with the ionization cross section given in ref. [15], where it was obtained through the Milne relation.[22] Here, we did not rely on an explicit use of the Milne relation, but on thermal field theory alone.

[21] Due to the selection rule of the electric dipole matrix element, only a transition into a scattering state with orbital angular momentum quantum number $\ell=1$ is possible.

[22] One has to express eq. (6.80) in terms of the momentum of the scattering state, $|\boldsymbol{p}| = Mv_{\rm rel}/2$, i.e. $|\boldsymbol{k}| = M(v_{\rm rel}^2+\alpha^2)/4 = \Delta E_1^p$ and $w_1(|\boldsymbol{k}|) = v_{\rm rel}/\alpha$.

Thermal field theory provides, by construction, the dissociation width with the correct temperature dependence. For the excited states 2S, 2P and 3S, with binding energies $E_2^b = -M\alpha^2/16$ and $E_3^b = -M\alpha^2/36$, respectively, the widths are

$$\Gamma_{\rm bsd}^{\rm 2S,LO} = \int_{|\boldsymbol{k}|\geq|E_2^b|} \frac{d^3k}{(2\pi)^3}\; n_{\rm B}(|\boldsymbol{k}|)\frac{4}{3}\alpha\frac{M^{\frac{3}{2}}}{2}|\boldsymbol{k}|\sqrt{|\boldsymbol{k}|+E_2^b}\;|\,\langle 2S|\boldsymbol{r}|\boldsymbol{p}1\rangle\,|^2\Big|_{|\boldsymbol{p}|=\sqrt{M(|\boldsymbol{k}|+E_2^b)}}\,, \tag{6.82}$$

$$\Gamma_{\rm bsd}^{\rm 2P,LO} = \frac{1}{3}\sum_{m=0,\pm1}\int_{|\boldsymbol{k}|\geq|E_2^b|}\frac{d^3k}{(2\pi)^3}\,n_{\rm B}(|\boldsymbol{k}|)\,\frac{4}{3}\alpha\frac{M^{\frac{3}{2}}}{2}|\boldsymbol{k}|\sqrt{|\boldsymbol{k}|+E_2^b} \times\left|\sum_{\ell'=0,2}\langle 2{\rm P}_m|\boldsymbol{r}|\boldsymbol{p}\ell'\rangle\right|^2\Bigg|_{|\boldsymbol{p}|=\sqrt{M(|\boldsymbol{k}|+E_2^b)}}\,, \tag{6.83}$$

$$\Gamma_{\rm bsd}^{\rm 3S,LO} = \int_{|\boldsymbol{k}|\geq|E_3^b|}\frac{d^3k}{(2\pi)^3}\;n_{\rm B}(|\boldsymbol{k}|)\,\frac{4}{3}\alpha\frac{M^{\frac{3}{2}}}{2}|\boldsymbol{k}|\sqrt{|\boldsymbol{k}|+E_3^b}\;\left|\langle 3S|\boldsymbol{r}|\boldsymbol{p}1\rangle\right|^2\Big|_{|\boldsymbol{p}|=\sqrt{M(|\boldsymbol{k}|+E_3^b)}}\,, \tag{6.84}$$

where we averaged the thermal dissociation width of the 2P state over m. The associated ionization widths are

$$\sigma_{\rm ion}^{\rm 2S,LO}(|\boldsymbol{k}|) = \alpha\frac{2^{12}\pi^2}{3}\left(4+w_2(|\boldsymbol{k}|)^2\right)\frac{|E_2^b|^4}{M|\boldsymbol{k}|^5}\frac{e^{-\frac{8}{w_2(|\boldsymbol{k}|)}\arctan(w_2(|\boldsymbol{k}|))}}{1-e^{-\frac{4\pi}{w_2(|\boldsymbol{k}|)}}}\,, \tag{6.85}$$

$$\sigma_{\rm ion,LO}^{\rm 2P_{m=0}}(|\boldsymbol{k}|) = \alpha\frac{2^{12}\pi^2}{3^3}\Big(\sqrt{w_2(|\boldsymbol{k}|)^2+1}-4\sqrt{w_2(|\boldsymbol{k}|)^2+4}\Big)^2\frac{|E_2^b|^5}{M|\boldsymbol{k}|^6}\frac{e^{-\frac{8}{w_2(|\boldsymbol{k}|)}\arctan(w_2(|\boldsymbol{k}|))}}{1-e^{-\frac{4\pi}{w_2(|\boldsymbol{k}|)}}}\,, \tag{6.86}$$

$$\sigma_{\rm ion,LO}^{\rm 2P_{m=\pm1}}(|\boldsymbol{k}|) = \alpha\frac{2^{12}\pi^2}{3^3}\Big(\sqrt{w_2(|\boldsymbol{k}|)^2+1}+2\sqrt{w_2(|\boldsymbol{k}|)^2+4}\Big)^2\frac{|E_2^b|^5}{M|\boldsymbol{k}|^6}\frac{e^{-\frac{8}{w_2(|\boldsymbol{k}|)}\arctan(w_2(|\boldsymbol{k}|))}}{1-e^{-\frac{4\pi}{w_2(|\boldsymbol{k}|)}}}\,, \tag{6.87}$$

$$\sigma_{\rm ion}^{\rm 3S,LO}(|\boldsymbol{k}|) = \alpha 2^9\pi^2 3^2(3^2+w_3(|\boldsymbol{k}|)^2)\left(\frac{7}{3}+w_3(|\boldsymbol{k}|)^2\right)^2\frac{|E_3^b|^6}{M|\boldsymbol{k}|^7}\frac{e^{-\frac{12}{w_3(|\boldsymbol{k}|)}\arctan(w_3(|\boldsymbol{k}|))}}{1-e^{-\frac{6\pi}{w_3(|\boldsymbol{k}|)}}}\,, \tag{6.88}$$

where we define $w_2(|\boldsymbol{k}|) \equiv \sqrt{|\boldsymbol{k}|/|E_2^b|-1}$ and $w_3(|\boldsymbol{k}|) \equiv \sqrt{\boldsymbol{k}|/|E_3^b|-1}$. One can check explicitly that each of the expressions in (6.80) and (6.82)–(6.84), once numerically integrated over $\boldsymbol{k}$, satisfies the detailed balance relation in (6.15) upon plugging in the thermally averaged bsf cross sections, written explicitly in eqs. (6.11)–(6.14). The same applies to the ionization widths in (6.81) and (6.85)–(6.88), which satisfy the Milne relation (6.79).

In the right panel of figure 6.2, we have plotted the corresponding photo-dissociation widths. At very small temperatures the thermal width for the 1S state (orange solid line)

vanishes faster than the one for the 2S state (brown dotted line), 2P state (purple dashed line) and 3S state (red dot-dashed line), whereas at higher temperatures the 1S thermal width is larger than the ones of the excited states. Hence, at large T the dissociation of the 1S state is dominating over all excited states by at least a factor of four, and at small T the widths are all negligible due to the exponentially suppressed Bose–Einstein distribution function. It is therefore sufficient to take only the dissociation of ground state and the first few excited states into consideration, when studying the dynamics of meta-stable darkonium in a thermal bath.

The bsd width at higher order in the coupling, corresponding to at least the two-loop self-energy displayed in figure 6.1 but with double solid and single solid lines exchanged, can be computed in an analogous way as for the bsf cross section in the preceding section, and the modification compared to the result at LO, cf. (6.76) is through the more involved electric-field correlator, i.e.

$$\Gamma^n_{\rm bsd} = g^2 \frac{\mu^{4-D}}{D-1} \int \frac{d^3p}{(2\pi)^3} |\langle n|\boldsymbol{r}|\boldsymbol{p}\rangle|^2 \int \frac{d^{D-1}q}{(2\pi)^{D-1}} \langle \boldsymbol{E}\boldsymbol{E}\rangle^{>}(-\Delta E^p_n, \boldsymbol{q})\,. \tag{6.89}$$

which reduces to (6.76) upon plugging in the simple leading order expression (6.8), where $1+n_{\rm B}(-\Delta E^p_n) = -n_{\rm B}(\Delta E^p_n)$. Up to next-to-leading order, the dissociation width reads

$$\Gamma^{n,\rm LO+NLO}_{\rm bsd} = 2\int \frac{d^3p}{(2\pi)^3} \sigma^{n,\rm LO}_{\rm bsd}(\boldsymbol{p}) \left\{ 1 + \frac{n_f}{\pi}\alpha(\mu_{\rm us}) \left[\mathcal{X}_{\rm vac}(\Delta E^p_n, \mu_{\rm us}) + \mathcal{X}_{\rm th}(\Delta E^p_n/T) \right] \right\}, \tag{6.90}$$

where the dimensionless functions $\mathcal{X}_{\rm vac}, \mathcal{X}_{\rm th}$ can be inferred from (6.21) and (6.25), respectively.[23] The bsd cross section at LO, $\sigma^{n,\rm LO}_{\rm bsd}$, has been defined in the first line of eq. (6.78). As in the bsf case, the vacuum contribution $\mathcal{X}_{\rm vac}$ is suppressed, since $n_f\alpha(\mu_{\rm us}) \ll 1$ in this work, and hence can be neglected, while the thermal part $\mathcal{X}_{\rm th}$ becomes large if $T \gg \Delta E^p_n$, such that $m_{\rm D} \sim \Delta E^p_n$. Perturbation theory breaks down for loop momenta of the order of the Debye mass scale, and the series needs to be resummed. Similarly as in the case of bound-state formation, cf. eq. (6.49), the $m_{\rm D}$-resummed bsd width is

$$\begin{aligned}(\Gamma^n_{\rm bsd})_{\rm resum.} &= 2\int \frac{d^3p}{(2\pi)^3} \sigma^{n,\rm LO}_{\rm bsd}(\boldsymbol{p})\Big|_{T\gg\Delta E^p_n} \\ &\times \left(\frac{m_{\rm D}}{2\Delta E^p_n}\right)^2 \left[2 - 2\gamma_{\rm E} + 2\frac{\zeta'(2)}{\zeta(2)} - \ln\left(\frac{(\Delta E^p_n)^2}{16T^2}\right) + 2\mathcal{Y}^{\rm long}_{\rm th}\left(\frac{\Delta E^p_n}{m_{\rm D}}\right) + 2\mathcal{Y}^{\rm trans}_{\rm th}\left(\frac{\Delta E^p_n}{m_{\rm D}}\right)\right],\end{aligned} \tag{6.91}$$

where $\sigma^{n,\rm LO}_{\rm bsd}(\boldsymbol{p})\big|_{T\gg\Delta E^p_n} \approx (4\alpha/3)|\langle n|\boldsymbol{r}|\boldsymbol{p}\rangle|^2 T(\Delta E^p_n)^2/2$ is the spin-averaged and temperature dependent bound-state dissociation cross section at leading order, which can be read off from the integrand in (6.76), in the limit of large temperatures $T \gg \Delta E^p_n$. The dimensionless functions $\mathcal{Y}^{\rm long}_{\rm th}$ and $\mathcal{Y}^{\rm trans}_{\rm th}$ are defined in eqs. (6.38) and (6.45), respectively.

[23] The functions $\mathcal{X}_{\rm vac}(x)$ and $\mathcal{X}_{\rm th}(x)$ are symmetric upon the change of the argument $x \to -x$ that occurs when switching from bound-state formation to bound-state dissociation.

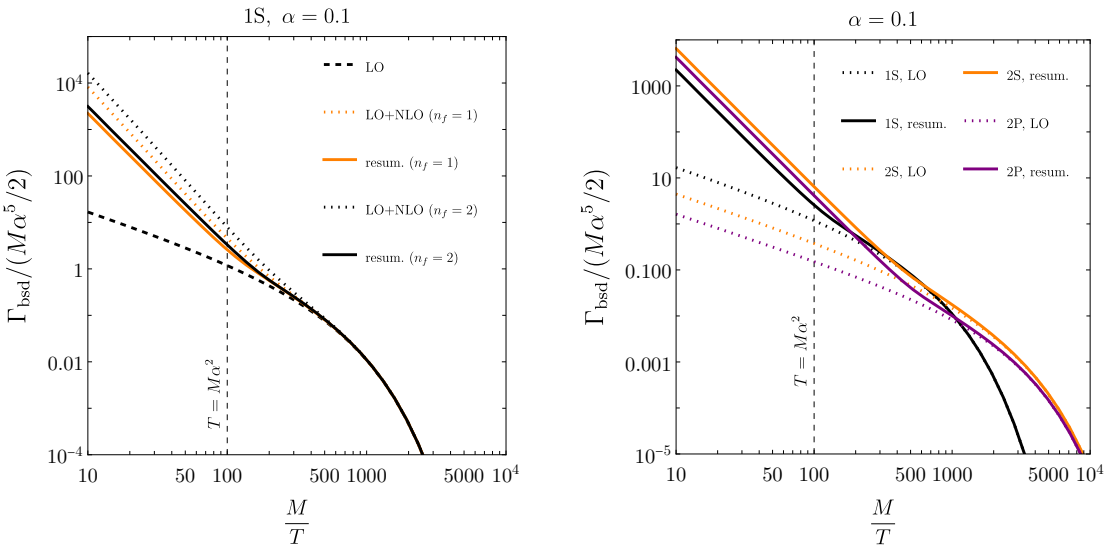

Figure 6.6: (Left) Ratios of the thermally averaged formation cross sections of the first few excited bound states at leading order, cf. eq. (6.9), over $\pi\alpha^2/M^2$, as functions of M/T. As a comparison, we plot also the thermally averaged Sommerfeld factor. (Right) Ratios of the 1S, 2S, 2P and 3S dissociation widths and 1S $\leftrightarrow$ 2P (de-)excitation widths over $M\alpha^5/2$ at leading order in the coupling. The vertical lines mark the position where $T = M\alpha^2$, i.e. the regime where the temperature is of order of the ultrasoft scale.

In the left panel of fig. 6.6, we plot the bsd width, normalized by $M\alpha^5/2$, for the ground state at leading order (black dashed line for $n_f = \{1, 2\}$), including next-to-leading order corrections at fixed order (orange and black dotted lines for $n_f = 1$ and $n_f = 2$, respectively) and with Debye mass resummation (orange and black solid lines for $n_f = 1$ and $n_f = 2$, respectively). We choose again $\alpha(2M) = 0.1$ for the running coupling at one loop. At low temperatures, of the order of the ultrasoft scale or smaller, the curves approach each other and are exponentially suppressed. The dominant process is via photo-dissociation. At larger T, the bath-particle scattering starts becoming relevant, eventually being the dominant process enhancing the width by at least two orders of magnitudes for the largest temperatures that we consider, $T = M/10$. However, as in the case of the bsf process, see figure 6.3 left, the width at fixed NLO leads to an overestimation by a factor up to five compared to the Debye-mass resummed width. In figure 6.6 right, we add the widths of the first excited states 2S (orange lines) and 2P (purple lines) for $n_f = 1$, where we have averaged the 2P-bsd width over the magnetic quantum number $m = \{0, \pm 1\}$ of the incoming bound state. Dotted lines are for the width at LO, only accounting for the photo-dissociation process, solid lines are when incorporating the Debye mass resummation. At low T, the widths of the excited states are larger than the one of the ground state because it is more likely to dissociate a bound pair with a smaller (closer to threshold) binding energy. However, at larger temperatures, the widths of the excited states still are larger compared to the 1S width, contrary to the

results at LO. The resummation of the Debye mass has a greater impact on the excited states than on the ground state, as we already observed in the bound-state formation process, see the right plot in fig. 6.5.

6.2.2 Width in different reference frames: recoil correction, Lorentz contraction

For the particular hierarchical arrangement of the energy scales according to (3.2), bound-state dissociation happens most likely when a bound state $(X\bar{X})_n$ absorbs a thermal dark photon from the bath and dissociates into a scattering state $(X\bar{X})_p$ through the reaction $\gamma + (X\bar{X})_n \to (X\bar{X})_p$, cf. (6.77). The bound-state dissociation width with recoil corrections can be determined from the imaginary parts of the self-energy diagrams shown in figure 6.4 with the propagators of the scattering states (double line) and bound states (single line) exchanged, because now the incoming and outgoing pair is bound, while the pair in the loop is unbound. We project the self energies onto bound states with quantum numbers n and center-of-mass momentum $\boldsymbol{P}$ in the laboratory frame, and label them accordingly. The dissociation width can then be computed in the laboratory frame, up to corrections of relative order T/M and $\Delta E_n^p/M$, as

$$(\Gamma^n_{\rm bsd})_{\rm lab}(\boldsymbol{P}) = -2\,{\rm Im}\left[\left(\Sigma^{11}_{ee}\right)(n,\boldsymbol{P}) + \left(\Sigma^{11}_{mm}\right)(n,\boldsymbol{P}) + \left(\Sigma^{11}_{em}\right)(n,\boldsymbol{P}) + \left(\Sigma^{11}_{me}\right)(n,\boldsymbol{P})\right]. \tag{6.92}$$

The propagator of the recoiling unbound fermion-antifermion pair in the loop reads

$$\begin{aligned}\frac{i}{E_n + \boldsymbol{P}^2/(4M) - (E_p + (\boldsymbol{P}-\boldsymbol{k})^2/(4M)) - k_0 + i\epsilon} \\ = \frac{i}{-\Delta E_n^p + (2\boldsymbol{P}\cdot\boldsymbol{k} - \boldsymbol{k}^2)/(4M) - k_0 + i\epsilon}\,,\end{aligned} \tag{6.93}$$

where we notice the sign difference in front of ΔE_n^p with respect to eq. (6.54). The recoil term, $(2\boldsymbol{P}\cdot\boldsymbol{k} - \boldsymbol{k}^2)/(4M) \ll \Delta E_n^p$, is the same as in the bound-state formation process, and we can the propagator in the recoil correction to the kinetic energy as in sec. 6.1.2.1. Including all corrections of order $\boldsymbol{P}^2/M^2 \sim T/M$ and $\Delta E_n^p/M$, the bound-state dissociation width in the laboratory frame reads

$$\begin{aligned}&(\Gamma^n_{\rm bsd})_{\rm lab}(\boldsymbol{P}) \\ &= \frac{4}{3}\alpha \int \frac{d^3p}{(2\pi)^3}(\Delta E_n^p)^3 n_{\rm B}(\Delta E_n^p)\left(|\langle n|\boldsymbol{r}|\boldsymbol{p}\rangle_{\rm lab}|^2 D_1^n(p,P) + \left|\langle n|\boldsymbol{r}\cdot\frac{\boldsymbol{P}}{2M}|\boldsymbol{p}\rangle_{\rm lab}\right|^2 D_2^n(p,P)\right),\end{aligned} \tag{6.94}$$

with

$$\begin{aligned}D_1^n(p,P) =& 1 + \frac{3}{4}\frac{\Delta E_n^p}{M} + \frac{\boldsymbol{P}^2}{4M^2} - (1+n_{\rm B}(\Delta E_n^p))\,\frac{\Delta E_n^p}{4M}\,\frac{\Delta E_n^p}{T} \\ &- (1+n_{\rm B}(\Delta E_n^p))\,\frac{\boldsymbol{P}^2}{4M^2}\,\frac{\Delta E_n^p}{T}\left[1 + \frac{\Delta E_n^p}{5T} - \frac{2}{5}(1+n_{\rm B}(\Delta E_n^p))\frac{\Delta E_n^p}{T}\right],\end{aligned} \tag{6.95}$$

and

$$D_2^n(p,P) = 1 - \frac{1}{10}\,(1+n_{\rm B}(\Delta E_n^p))\,\frac{(\Delta E_n^p)^2}{T^2}\,(1+2\,n_{\rm B}(\Delta E_n^p))\,. \tag{6.96}$$

The statistical factor $n_{\rm B}(\Delta E_n^p)$ in (6.94) reflects the fact the dark photon is absorbed from the thermal bath. As elaborated in the previous sections, the dissociation width does not contain a vacuum part because bound-state dissociation is kinematically forbidden in vacuum. Hence, the bound-state dissociation width is a purely thermal width also when including the recoil effect.

We can compute the bsd width in the center-of-mass frame, following similar steps as in sec. 6.1.2.2 for the bsf cross section, where we set $\boldsymbol{P}=\boldsymbol{0}$ and the thermal bath is moving with velocity $-\boldsymbol{v}$. At relative order $\boldsymbol{v}^2$ and $\Delta E_n^p/M$, we get

$$\begin{aligned}
&(\Gamma_{\rm bsd}^n)_{\rm cm}(\boldsymbol{v}) \\
&= \frac{4}{3}\alpha \int \frac{d^3p}{(2\pi)^3} (\Delta E_n^p)_{\rm cm}^3\, n_{\rm B}((\Delta E_n^p)_{\rm cm}) \Big(|\langle n|\boldsymbol{r}|\boldsymbol{p}\rangle_{\rm cm}|^2 \tilde{D}_1^n(p,v) + |\langle n|\boldsymbol{r}\cdot\boldsymbol{v}|\boldsymbol{p}\rangle_{\rm cm}|^2 \tilde{D}_2^n(p,v)\Big)\,,
\end{aligned} \tag{6.97}$$

with

$$\begin{aligned}
\tilde{D}_1^n(p,v) =\; & 1 + \frac{3}{4}\frac{(\Delta E_n^p)_{\rm cm}}{M} - (1+n_{\rm B}((\Delta E_n^p)_{\rm cm}))\,\frac{(\Delta E_n^p)_{\rm cm}}{4M}\,\frac{(\Delta E_n^p)_{\rm cm}}{T} \\
& - (1+n_{\rm B}((\Delta E_n^p)_{\rm cm}))\,\boldsymbol{v}^2\frac{(\Delta E_n^p)_{\rm cm}}{T}\left[\frac{1}{2} + \frac{(\Delta E_n^p)_{\rm cm}}{5T} - \frac{2}{5}\,(1+n_{\rm B}((\Delta E_n^p)_{\rm cm}))\,\frac{(\Delta E_n^p)_{\rm cm}}{T}\right],
\end{aligned} \tag{6.98}$$

and

$$\tilde{D}_2^n(p,v) = -\frac{1}{10}\,(1+n_{\rm B}((\Delta E_n^p)_{\rm cm}))\,\frac{(\Delta E_n^p)_{\rm cm}^2}{T^2}\,(1+2\,n_{\rm B}((\Delta E_n^p)_{\rm cm}))\,, \tag{6.99}$$

where we have made explicit in which reference frame the matrix elements and the energy difference are computed. The momentum integral in (6.97) is over the relative momentum in the center-of-mass frame.

The relation between the bound-state dissociation width in the laboratory frame (6.94) and the bound-state dissociation width in the center-of-mass frame (6.97) is

$$(\Gamma_{\rm bsd}^n)_{\rm lab}(\boldsymbol{P}) = \frac{(\Gamma_{\rm bsd}^n)_{\rm cm}(\boldsymbol{v})}{\gamma} \approx (\Gamma_{\rm bsd}^n)_{\rm cm}(\boldsymbol{P}/(2M))\left(1 - \frac{\boldsymbol{P}^2}{8M^2}\right)\,, \tag{6.100}$$

if we transform the matrix elements and the energy difference according to (6.73), the momentum-space volume as $d^3p_{\rm cm} = d^3p_{\rm lab}/\gamma$ (see eq. (A.21)), set $\boldsymbol{v} = \boldsymbol{P}/(2M)$ and keep only terms up to order $\boldsymbol{P}^2/M^2$. Equation (6.100) expresses the Lorentz dilation of time intervals, and is independent of the presence of the thermal bath (cf. the Lorentz contraction of the in-vacuum decay width for paradarkonium in (5.34)). In order to grasp the impact of the recoil on the dissociation width, we plot in figure 6.7 the ratios of the 1S- and 2S-bsd widths to be inferred from (6.94), thermally averaged in the laboratory frame according to (B.9), and the associated widths at LO, cf. eqs. (6.80) and (6.82), as functions of M/T with $\alpha = 0.1$. We also plot the ratios R_Γ of the thermally averaged

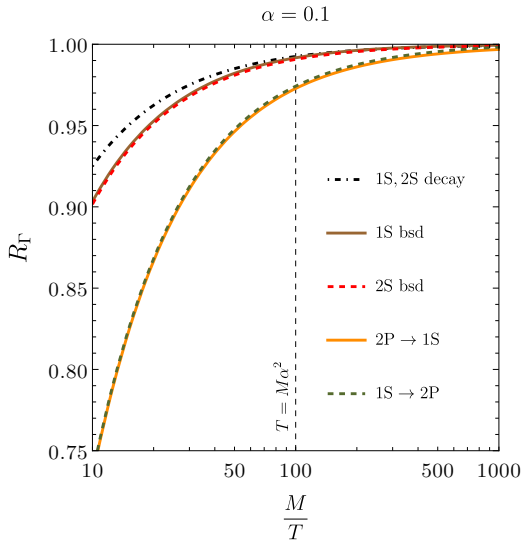

Figure 6.7: Ratios of thermally averaged widths in the laboratory frame with recoil corrections and the corresponding thermally averaged widths without recoil corrections plotted as a function of M/T for coupling $\alpha = 0.1$. The black dash-dotted line denotes the ratio when taking the thermal average of (5.34), the brown solid and red dashed lines when taking the thermal average of (6.94) for the 1S and 2S state, respectively, the orange solid line when taking the thermal average of (6.103) for the transition 2P $\to$ 1S, and the green dashed line when taking the thermal average of (6.104) for the transition 1S $\to$ 2P. The vertical line marks the position where $T = M\alpha^2$.

1S and 2S paradarkonium decay widths in the laboratory frame with recoil corrections, cf. (5.34), and the corresponding ones without recoil corrections. We observe that the recoil effect is independent of the discrete quantum number n of the bound states (brown solid and red dashed lines overlap for the 1S and 2S bsd) as in the bsf case, and that the recoil corrections are slightly larger for the dissociation than the annihilation (black dot-dashed line for the 1S and 2S state), with values up to 10% at the largest considered temperature. Again $R_\Gamma < 1$ because of the Lorentz contraction of the widths when going from the center-of-mass to the laboratory frame, inducing the known time dilatation effect for time intervals.

6.3 Bound-state to bound-state transitions: (de-)excitations

In this section, we derive the transition rates between two dark matter bound states. Bound-state to bound-state transitions include *de-excitations* of excited bound states into bound states of lower energy by emission of a dark photon, $(X\bar{X})_n \to \gamma + (X\bar{X})_{n'}$, and *excitations* of bound states into bound states of higher energy due to the absorption

of a dark photon from the bath, $\gamma + (X\bar{X})_n \to (X\bar{X})_{n'}$.[24] At higher order in the coupling, thermal interactions with the bath particles may induce (de-)excitations as well, and for large temperatures, such that the hierarchy (3.4) is fulfilled, those bath-particle scattering processes need to be resummed. Since these processes are mediated by the dipole operator, the angular momentum of the bound state must change by one unit, $|\Delta\ell| = 1$, whereas the spin is left unchanged. In pNRQED$_{\rm DM}$, both excitation and de-excitation processes can be described by cutting the same self-energy diagrams as for scattering-state to bound-state transitions shown in figures 6.1 and 6.4, except that the matter states inside and outside the loop are bound states (i.e. we replace the external double solid with a single solid line). The computation of the de-excitation transition width goes like the computation of the bound-state formation cross section done in section 6.1, whereas the computation of the excitation transition width goes like the computation of the bound-state dissociation width done in section 6.2. The results may be read directly from the results listed in those sections by replacing the scattering state $|\boldsymbol{p}\rangle$ with the bound state $|n\rangle$ in the case of the de-excitation transition width and with the bound state $|n'\rangle$ in the case of the excitation transition width.[25]

At large temperatures and omitting the recoil corrections due to the center-of-mass motion, the result for the de-excitation width $\Gamma^n_{\text{de-ex.}} \equiv \sum_{n'<n} \Gamma^{n\to n'}_{\text{de-ex.}}$ up to fixed NLO and with Debye mass resummation equals the expressions for the bsf cross section at fixed NLO, eq. (6.24), and with Debye mass resummation, eq. (6.49), respectively, but with the energy difference ΔE^p_n and $(\sigma_{\rm bsf}\, v_{\rm rel})^{\rm LO}_n(\boldsymbol{p})$ replaced by $\Delta E^n_{n'}$ and[26]

$$\Gamma^{n,\text{LO}}_{\text{de-ex.}} = \frac{4}{3}\alpha \sum_{n',E_{n'}<E_n} (\Delta E^n_{n'})^3 \, (1 + n_{\rm B}\,(\Delta E^n_{n'})) \, \left|\langle n'|\boldsymbol{r}|n\rangle\right|^2 , \tag{6.101}$$

respectively, where we have specified the quantum numbers, $n = (n, \ell, m)$, of the decaying bound state and the quantum numbers, $n' = (n', \ell', m')$, of the final bound state. A similar treatment can be done for the excitation process, where we can take the result for the bsd width at fixed NLO, eq. (6.90), and the one with Debye mass resummation, eq. (6.91), and replacing ΔE^p_n and $\int \frac{d^3p}{(2\pi)^3}\sigma^{n,\text{LO}}_{\rm bsd}(\boldsymbol{p})$ by $\Delta E^n_{n'}$, $\Gamma^{n,\text{LO}}_{\text{ex.}}$ and

$$\Gamma^{n,\text{LO}}_{\text{ex.}} = \frac{4}{3}\alpha \sum_{n',E_{n'}>E_n} (\Delta E^{n'}_n)^3 \, n_{\rm B}(\Delta E^{n'}_n) \, \left|\langle n'|\boldsymbol{r}|n\rangle\right|^2 , \tag{6.102}$$

[24] The energy of the incoming photon is not large enough to break the bound state into an unbound DM pair, thus the excitation process can be distinguished from the thermal break-up process by requiring the energy $E_\gamma + E_n$ to be negative.

[25] Since de-excitation transitions resemble the bound-state formation process, they may happen both in vacuum and in the thermal medium, although in the thermal medium they are enhanced by the stimulated emission. On the other hand, excitation transitions resemble the bound-state dissociation process, and hence the can happen only in a thermal bath.

[26] The dark photon carries an energy $\Delta E^n_{n'} = E_n - E_{n'} = (M\alpha^2/4)\left(1/n'^2 - 1/n^2\right)$ at leading order in the coupling and at zeroth order in the non-relativistic expansion of the total velocity, which is the energy difference $(\Delta E^n_{n'})_{\rm cm}$ in the center-of-mass frame.

respectively, where $\Gamma^{n,\mathrm{LO}}_{\mathrm{ex.}}$ is the leading-order result of the excitation width $\Gamma^n_{\text{de-ex.}} \equiv \sum_{n'>n} \Gamma^{n\to n'}_{\text{de-ex.}}$. Note that in eqs. (6.101) and (6.102) we have summed over the two polarizations of the dark photon either if the photon is emitted into or absorbed from the medium.

Instead for lower temperatures of the order of the ultrasoft scale or smaller, the NLO corrections are suppressed and the de-excitation width can be well approximated to be simply the leading order result (6.101). If we consider the motion of the center of mass $\boldsymbol{P}$ of the incoming bound state, then for the hierarchy (3.2) the total de-excitation width in the laboratory frame reads up to relative order T/M and $\Delta E^p_n/M$

$$\begin{aligned}(\Gamma^n_{\text{de-ex.}})_{\mathrm{lab}}(\boldsymbol{P}) &= \sum_{n',E_{n'}<E_n} (\Gamma^{n\to n'}_{\text{de-ex.}})_{\mathrm{lab}}(\boldsymbol{P}) \\ &= \frac{4}{3}\alpha \sum_{n',E_{n'}<E_n} (\Delta E^n_{n'})^3 \left(1+n_{\mathrm{B}}(\Delta E^n_{n'})\right) \\ &\quad \times \left(|\langle n'|\boldsymbol{r}|n\rangle_{\mathrm{lab}}|^2 F_1^{n'}(n,P) + \left|\langle n'|\boldsymbol{r}\cdot\frac{\boldsymbol{P}}{2M}|\boldsymbol{p}\rangle_{\mathrm{lab}}\right|^2 F_2^{n'}(n,P)\right), \end{aligned} \tag{6.103}$$

where the form factors $F_1^{n'}(n,P)$ and $F_2^{n'}(n,P)$ are defined as in eqs. (6.63) and (6.64), respectively, but with the energy difference ΔE^p_n replaced by $\Delta E^n_{n'}$. The total excitation width in the laboratory frame reads up to relative order T/M and $\Delta E^p_n/M$

$$\begin{aligned}(\Gamma^n_{\text{ex.}})_{\mathrm{lab}}(\boldsymbol{P}) &= \sum_{n',E_{n'}>E_n} (\Gamma^{n\to n'}_{\text{ex.}})_{\mathrm{lab}}(\boldsymbol{P}) \\ &= \frac{4}{3}\alpha \sum_{n',E_{n'}>E_n} (\Delta E^{n'}_n)^3\, n_{\mathrm{B}}(\Delta E^{n'}_n) \\ &\quad \times \left(|\langle n'|\boldsymbol{r}|n\rangle_{\mathrm{lab}}|^2 D_1^n(n',P) + \left|\langle n'|\boldsymbol{r}\cdot\frac{\boldsymbol{P}}{2M}|n\rangle_{\mathrm{lab}}\right|^2 D_2^n(n',P)\right), \end{aligned} \tag{6.104}$$

where the form factors $D_1^n(n',P)$ and $D_2^n(n',P)$ are defined as in eqs. (6.95) and (6.96), respectively, but with the energy difference ΔE^p_n replaced by $\Delta E^{n'}_n$. In the center-of-mass frame, where the bath is moving with velocity $-\boldsymbol{v}$, the de-excitation width, $(\Gamma^n_{\text{de-ex.}})_{\mathrm{cm}}(\boldsymbol{v})$, has the same expression as (6.103), but with $\boldsymbol{P}/(2M)$ replaced by $\boldsymbol{v}$ and form factors $\tilde{F}_1^{n'}(n,v)$ and $\tilde{F}_2^{n'}(n,v)$ defined as in eqs. (6.71) and (6.72), respectively, but in terms of $(\Delta E^n_{n'})_{\mathrm{cm}}$. The excitation width, $(\Gamma^n_{\text{ex.}})_{\mathrm{cm}}(\boldsymbol{v})$, has the same expression as (6.104), but with $\boldsymbol{P}/(2M)$ replaced by $\boldsymbol{v}$ and form factors $\tilde{D}_1^{n'}(n,v)$ and $\tilde{D}_2^{n'}(n,v)$ defined as in eqs. (6.98) and (6.99), respectively, but in terms of $(\Delta E^{n'}_n)_{\mathrm{cm}}$.

Upon using the Lorentz-transformation relation (A.23) and (A.33) for the energy difference between two bound states and the bound-state to bound-state matrix element,

respectively, which up to first order in $\boldsymbol{v}^2$ are

$$\begin{aligned}
&\left|\langle n|\boldsymbol{r}|n'\rangle_{\rm cm}\right|^2 \approx \left|\langle n|\boldsymbol{r}|n'\rangle_{\rm lab}\right|^2 + \left|\langle n|\boldsymbol{r}\cdot\boldsymbol{v}|n'\rangle_{\rm lab}\right|^2 ,\\
&\left|\langle n|\boldsymbol{r}\cdot\boldsymbol{v}|n'\rangle_{\rm cm}\right|^2 \approx \left|\langle n|\boldsymbol{r}\cdot\boldsymbol{v}|n'\rangle_{\rm lab}\right|^2 ,\\
&(\Delta E_n^{n'})_{\rm cm} = \gamma(\Delta E_n^{n'})_{\rm lab} \approx (\Delta E_n^{n'})_{\rm lab}\left(1+\frac{\boldsymbol{v}^2}{2}\right) ,
\end{aligned} \tag{6.105}$$

we can check that the behaviour of the (de-)excitation width under Lorentz boosts is the same as for the in-vacuum annihilation width, cf. (5.34), and for the thermal dissociation, cf. (6.100). We can visualize the recoil corrections for the bound-to-bound transitions between the ground state and the 2P state, by plotting in fig. 6.7 the ratios R_Γ of the (de-)excitation widths with recoil, thermally averaged according to (B.9), and the ones at leading order and without recoil, which can be computed from (6.101) and (6.102) and are[27]

$$\Gamma^{\rm 1S\to 2P}_{\rm ex.,LO} = \frac{2^7}{3^7}\frac{M\alpha^5}{e^{\frac{3M\alpha^2}{16T}}-1} , \tag{6.106}$$

$$\Gamma^{\rm 2P\to 1S}_{\rm de\text{-}ex.,LO} = \frac{2^7}{3^8}\frac{M\alpha^5}{1-e^{-\frac{3M\alpha^2}{16T}}} . \tag{6.107}$$

Comparing with the decay and bsd widths, we observe that the most significant recoil corrections are for the 1S $\leftrightarrow$ 2P transition widths at large temperatures (orange solid and dark green dashed lines), with a correction of about 25% for $T = M/10$. Hence, especially for bound-state to bound-state transitions the contribution from the motion of the center of mass should be taken into account whenever doing precision computations.

As for the NLO or resummation corrections, in figure 6.8, left, we plot the excitation width for the 1S $\to$ 2P process at leading order (black dashed line for $n_f = \{1, 2\}$), including next-to-leading order corrections (orange and black dotted lines for $n_f = 1$ and $n_f = 2$, respectively) and with Debye mass resummation (orange and black solid lines for $n_f = 1$ and $n_f = 2$, respectively). In the right panel, we plot the results for the de-excitation process 2P $\to$ 1S. We normalize by $M\alpha^5/2$, and choose $\alpha(2M) = 0.1$ which runs at one loop. The results are comparable to the ones for the bound-state dissociation in figure 6.6 left, i.e. at large temperatures we again observe an overestimation of the fixed NLO widths by a factor up to five as compared to the widths accounting for the resummation of the Debye mass scale.

6.4 Scattering-state to scattering-state transitions: bremsstrahlung, thermal absorption

Similarly to what happens for bound-state to bound-state transitions, scattering states can undergo processes of thermal emission, called *bremsstrahlung*, and thermal absorp-

[27] The widths in (6.106) and (6.107) have already been shown in fig. 6.2 right by the black solid and dashed lines, respectively, and can be checked to satisfy the detailed balance relation in (6.16). While in the limit $T \to 0$ the ground state cannot be excited, the 2P state can still deexcite.

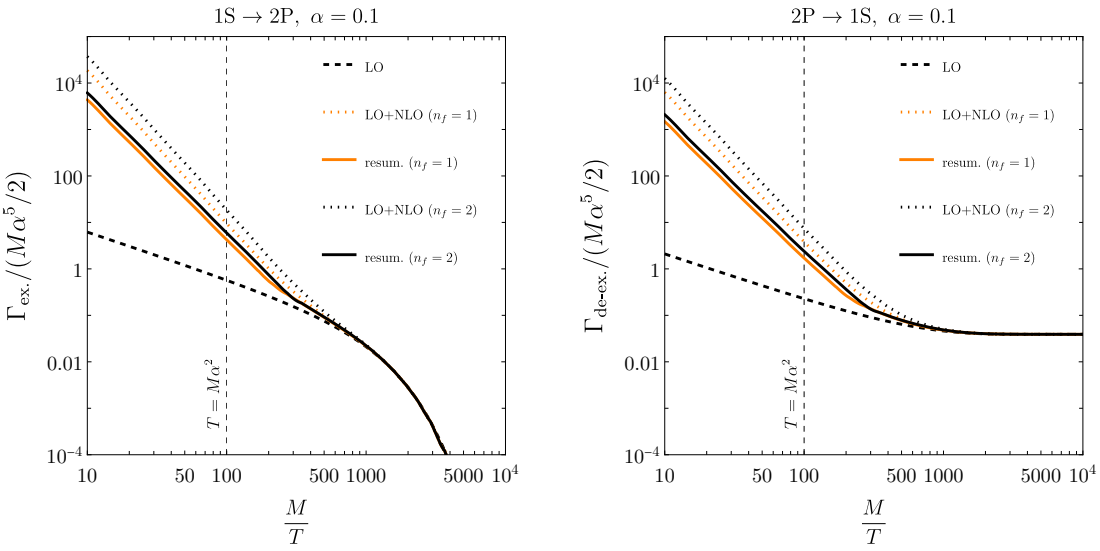

Figure 6.8: Excitation (left plot) and de-excitation (right plot) widths for the 1S $\leftrightarrow$ 2P process, at leading order (dashed lines), up to next-to-leading order (dotted lines) and with Debye mass resummation (solid lines), for $n_f = 1$ (orange lines), $n_f = 2$ (black lines), running coupling with $\alpha \equiv \alpha(2M) = 0.1$, normalized by $M\alpha^5/2$. The vertical dashed lines mark the position where $T = M\alpha^2$.

tion of an ultrasoft thermal photon. At large T, the Landau damping needs to be taken into account as well. The corresponding diagrams encompassing these scattering-to-scattering processes can be taken from figure 6.1, by just replacing the single solid lines in the loop with double solid lines. The recoil effect can be computed from the self-energy diagrams in fig. 6.4, again replacing the single with a double solid line. In the center-of-mass frame and at leading order in perturbation theory, the thermal absorption and emissions correspond to transitions from a scattering state of relative momentum $\boldsymbol{p}$ to a scattering state of relative momentum $\boldsymbol{p}'$ mediated by an electric-dipole vertex. For the differential cross section of the bremsstrahlung process, we obtain for $|\boldsymbol{p}'| < |\boldsymbol{p}|$

$$\frac{d(\sigma_{\rm emi} v_{\rm rel})(\boldsymbol{p}, \boldsymbol{p}')}{d^3 p'} = \frac{g^2}{24\pi^4} (E_p - E_{p'})^3 \left[1 + n_{\rm B}(E_p - E_{p'})\right] |\langle \boldsymbol{p}'|\boldsymbol{r}|\boldsymbol{p}\rangle|^2, \tag{6.108}$$

On the other hand, for the differential cross section of the thermal absorption process, we obtain for $|\boldsymbol{p}'| > |\boldsymbol{p}|$

$$\frac{d(\sigma_{\rm abs} v_{\rm rel})(\boldsymbol{p}, \boldsymbol{p}')}{d^3 p'} = \frac{1}{2} \frac{g^2}{24\pi^4} |E_p - E_{p'}|^3 n_{\rm B}(|E_p - E_{p'}|) |\langle \boldsymbol{p}'|\boldsymbol{r}|\boldsymbol{p}\rangle|^2, \tag{6.109}$$

where we have averaged over the polarizations of the incoming dark photon. The emission width follows from integrating $(\sigma_{\rm emi} v_{\rm rel})(\boldsymbol{p}, \boldsymbol{p}')$ over the momenta $\boldsymbol{p}$ and $\boldsymbol{p}'$. The absorption width follows from integrating $(\sigma_{\rm abs} v_{\rm rel})(\boldsymbol{p}, \boldsymbol{p}')$ over the momenta $\boldsymbol{p}$ and $\boldsymbol{p}'$,

and summing over the two photon polarizations. Notice that the absorption process cannot happen in vacuum. In particular, for an incoming S-wave we get

$$(\sigma_{\rm emi} v_{\rm rel})_{\ell=0}(\boldsymbol{p}) = \frac{4}{3}\alpha \int_{p'<p} dp'\,(p')^2 (p+p')^3 (p-p')^3 \left[1 + n_{\rm B}\left(\Delta E^p_{p'}\right)\right] |\langle \boldsymbol{p}' 1 | \boldsymbol{r} | \boldsymbol{p} 0\rangle|^2 \,, \tag{6.110}$$

$$(\sigma_{\rm abs} v_{\rm rel})_{\ell=0}(\boldsymbol{p}) = \frac{4}{3}\alpha \int_{p'>p} dp'\,(p')^2 (p+p')^3 (p-p')^3 \, n_{\rm B}\left(\Delta E^p_{p'}\right) |\langle \boldsymbol{p}' 1 | \boldsymbol{r} | \boldsymbol{p} 0\rangle|^2 \,, \tag{6.111}$$

which in principle can be integrated upon inserting the continuum dipole matrix element in eq. (C.32). The matrix element contains, however, a few divergences. They come from $p' \to 0$ (IR singularity) which is cured by the polynomial factors inside the integral in (6.110), from $p' \to \infty$ (UV singularity) which however vanishes due to the Bose–Einstein distribution function in (6.111), and $p' \to p$ (collinear singularity) which may pose a problem. We refer the reader to appendix C.3, which is devoted to the study of the collinear divergence, that can be extracted from the matrix element and is written in eqs. (C.57) and (C.58). One could introduce a cutoff $\delta \equiv p - p'$, and split the integrals in (6.110) and (6.111) into momentum regions close to the singularity, and regions far away. Performing the integrals numerically, the divergences between those two momentum regions should cancel out and the numerical results, that would depend on the cutoff parameter δ, should converge in the limit $\delta \to 0$. We expect the bremsstrahlung and thermal absorption processes, which count as elastic processes since the unbound heavy pairs remain in the scattering-state configuration throughout the reactions, to be responsible for keeping the dark fermion-antifermion pairs in kinetic equilibrium with the thermal bath. Hence the rates in (6.110)–(6.111) should dominate over the thermal rates that have been considered so far in the previous sections, which correspond to the bound-state formation and dissociation processes as well as the bound-to-bound transitions. However, since elastic collisions do not change the dark particle number n, they will not enter in the integrated coupled Boltzmann equations, which will be shown in the following chapter.

Chapter 7

Consequences for the dark matter energy density

In this chapter, we collect the numerical results obtained so far for the in-vacuum and thermal rates that enter in the evolution equations for the heavy dark matter and study their impact on the present DM relic abundance. Since the dark particles are assumed to be kinetically equilibrated during the thermal freeze-out, the evolution equations can be reduced to a network of coupled Boltzmann equations for the bound state number densities n_n^{para} and n_n^{ortho}, where the subscript n comprises the internal quantum numbers of a specific bound state, and the sum of the dark matter particle and antiparticle number densities $n = n_X + n_{\bar{X}} = 2n_X$ above threshold. The standard rate equation (2.6) for the single dark matter particle that is dictated by particle-antiparticle annihilations only, generalizes to a tower of semi-classical equations because of the near-threshold phenomena that allow for the formation of bound states before the particles annihilate. In the following, we are going to present the rate equations and study them from a phenomenological perspective, whereas in the subsequent chapters we aim to provide a derivation of these equations starting from the open quantum systems formalism, showing the several approximations that need to be done along the derivation and the corresponding limitations that are induced by them.

Although for Coulombic systems the maximum number of bound states is not limited as opposed to the spectrum of bound states for theories with massive-mediator interactions, the formation and dissociation rates are suppressed for higher excited states as we have shown in the previous chapter, see the numerical results in figure 6.2.[1] Hence for practical purposes we will consider only bound states up to $n = 2$.[2] If we include the Sommerfeld-enhanced annihilations and decays, as well as the thermal bound-state

[1] This is not quite true for the Debye-mass resummed rates at large temperatures, cf. the right plots in figure 6.5 for the bound-state formation cross section and figure 6.6 for the dissociation width, where the rates are larger for the excited states than the 1S. However, for most of the times after thermal freeze-out, where $T \lesssim M\alpha^2$, the contribution from the ground state dominates, cf. fig. 6.2.

[2] We remark that also the decay widths in eqs. (5.32) and (5.33) for the nS and nP discrete states are suppressed for large principal quantum number n, since $\Psi_n(\boldsymbol{r}) \sim n^{-3/2}$.

formation and bound-state dissociation rates and also the (de-)excitations among the bound states, then the evolution equations read[3]

$$(\partial_t + 3H)n = -\frac{1}{2}\langle\sigma_{\rm ann}\, v_{\rm M\o l}\rangle(n^2 - n_{\rm eq}^2) \\ -\frac{1}{2}\sum_{n=1,2}\langle\sigma^n_{\rm bsf} v_{\rm M\o l}\rangle n^2 + 2\sum_{n=1,2}\langle\Gamma^n_{\rm bsd}\rangle(n_n^{\rm para} + n_n^{\rm ortho})\,, \tag{7.1}$$

$$(\partial_t + 3H)n_n^{\rm para} = -\langle\Gamma^{n,{\rm para}}_{\rm ann}\rangle(n_n^{\rm para} - n^{\rm para}_{n,{\rm eq}}) - \langle\Gamma^n_{\rm bsd}\rangle n_n^{\rm para} + \frac{1}{16}\langle\sigma^n_{\rm bsf} v_{\rm M\o l}\rangle n^2 \\ -\left(\sum_{n'<n}\langle\Gamma^{n\to n'}_{\rm de\text{-}ex.}\rangle + \sum_{n'>n}\langle\Gamma^{n\to n'}_{\rm ex.}\rangle\right) n_n^{\rm para} + \left(\sum_{n'>n}\langle\Gamma^{n'\to n}_{\rm de\text{-}ex.}\rangle + \sum_{n'<n}\langle\Gamma^{n'\to n}_{\rm ex.}\rangle\right) n_{n'}^{\rm para}\,, \tag{7.2}$$

$$(\partial_t + 3H)n_n^{\rm ortho} = -\langle\Gamma^{n,{\rm ortho}}_{\rm ann}\rangle(n_n^{\rm ortho} - n^{\rm ortho}_{n,{\rm eq}}) - \langle\Gamma^n_{\rm bsd}\rangle n_n^{\rm ortho} + \frac{3}{16}\langle\sigma^n_{\rm bsf} v_{\rm M\o l}\rangle n^2\,, \\ -\left(\sum_{n'<n}\langle\Gamma^{n\to n'}_{\rm de\text{-}ex.}\rangle + \sum_{n'>n}\langle\Gamma^{n\to n'}_{\rm ex.}\rangle\right) n_n^{\rm ortho} + \left(\sum_{n'>n}\langle\Gamma^{n'\to n}_{\rm de\text{-}ex.}\rangle + \sum_{n'<n}\langle\Gamma^{n'\to n}_{\rm ex.}\rangle\right) n_{n'}^{\rm ortho}, \tag{7.3}$$

where eqs. (7.2) and (7.3) are for each bound state, i.e. $(n, n') \in \{1{\rm S}, 2{\rm S}, 2{\rm P}\}$. Since the Boltzmann equations (7.1)–(7.3) are frame-dependent, one needs to choose from beginning on a specific reference frame when computing the individual rates and their thermal averages, and solve the equations with respect to that reference frame. One typically considers the cosmic comoving frame where the thermal bath is at rest. Note that $\Gamma^{1{\rm S}\leftrightarrow 2{\rm S}} = \Gamma^{2{\rm S}\leftrightarrow 2{\rm P}} = 0$ at the dipole order and that $\Gamma^{2{\rm P}}_{\rm ann} = 0$ if we neglect the velocity corrections. Since we have already studied the impact of the relative velocity corrections to the Sommerfeld-enhanced annihilations and the present relic density, see fig. 5.3, we decide to drop from now on the corresponding four-fermion operators of dimension eight and keep only the dimension-six terms and the dimension-eight operators associated to the center-of-mass motion, corresponding to the terms in the fourth line of eq. (5.12).

We may use an approximation, first introduced in ref. [68] and commonly adopted in the literature, that is based on an effective treatment of dark matter bound states. In a typical cosmological setting, the annihilation and dissociation rate of bound states is pretty efficient, i.e. $\Gamma_{\rm ann}, \Gamma_{\rm bsd} \gg H$, so that they quickly adjust to their equilibrium number densities. Using the detailed balance conditions at equilibrium between bound-state formation and dissociation as well as excitations and de-excitations, cf. eqs. (6.15) and (6.16), respectively, one obtains a single Boltzmann equation that depends only on the density n of scattering states, and is governed by an effective cross section $\sigma_{\rm eff}$. The latter comprises the effects of dark matter annihilation via unbound pairs and bound states, but also bound-state formation cross sections, dissociation widths and bound-to-bound transition widths [41, 135]. The single effective rate equation reads

$$(\partial_t + 3H)n = -\frac{1}{2}\langle\sigma_{\rm eff}\, v_{\rm M\o l}\rangle(n^2 - n_{\rm eq}^2)\,, \tag{7.4}$$

[3]The dark matter number densities in thermal equilibrium for the para- and orthodarkonium are $n^{\rm para}_{n,{\rm eq}} = (2\ell+1)(MT/\pi)^{3/2}e^{-E_n/T}$ and $n^{\rm ortho}_{n,{\rm eq}} = 3n^{\rm para}_{n,{\rm eq}}$, respectively, and $n_{\rm eq}$ has been written in eq. (2.7).

where

$$\langle\sigma_{\rm eff}\, v_{\rm M\o l}\rangle = \langle\sigma_{\rm ann} v_{\rm M\o l}\rangle + \sum_n \left(\frac{1}{4}\langle\sigma^n_{\rm bsf}\, v_{\rm M\o l}\rangle\, \mathcal{R}^{\rm para}_n + \frac{3}{4}\langle\sigma^n_{\rm bsf}\, v_{\rm M\o l}\rangle\, \mathcal{R}^{\rm ortho}_n\right)$$
$$\approx \langle\sigma_{\rm ann} v_{\rm M\o l}\rangle + \sum_n \left(\frac{1}{4}\langle\sigma^n_{\rm bsf}\, v_{\rm M\o l}\rangle\, \frac{\langle\Gamma^{n,\rm para}_{\rm ann}\rangle}{\langle\Gamma^{n,\rm para}_{\rm ann}\rangle + \langle\Gamma^n_{\rm bsd}\rangle} + \frac{3}{4}\langle\sigma^n_{\rm bsf}\, v_{\rm M\o l}\rangle\, \frac{\langle\Gamma^{n,\rm ortho}_{\rm ann}\rangle}{\langle\Gamma^{n,\rm ortho}_{\rm ann}\rangle + \langle\Gamma^n_{\rm bsd}\rangle}\right), \tag{7.5}$$

where the result in the second line is valid if the bound-state to bound-state transitions are much smaller than $\Gamma^n_{\rm ann}$ and $\Gamma^n_{\rm bsd}$, also referred to as the no-transition limit [41]. The result in the first line of eq. (7.5) is, however, more general as it includes the information of the (de-)excitations, which, as was shown in ref. [51], strongly affect the numerical result of the Boltzmann equations and hence the DM relic abundance. From the right plot in figure 6.2 it can also be seen that at sufficiently small temperatures, the bound-state to bound-state transitions become as large as or larger than the dissociation widths. We will, therefore, not neglect the transitions among the 1S and 2P state when truncating the number of bound states at $n = 2$ as in (7.1)–(7.3). The general expression of $\mathcal{R}_n$ can be found in refs. [41, 135], which in our particular case reduces to

$$\mathcal{R}^{\rm para}_{\rm 1S} = 1 - \frac{\langle\Gamma^{\rm 1S}_{\rm bsd}\rangle - \sum\limits_{m=0,\pm1}\langle\Gamma^{\rm 1S\to 2P}_{\rm ex.}{}_m\rangle\langle\Gamma^{\rm 2P}_{\rm bsd}{}_m\rangle/\langle\Gamma^{\rm 2P}_{\rm para}{}_m\rangle}{\langle\Gamma^{\rm 1S}_{\rm para}\rangle - \sum\limits_{m=0,\pm1}\langle\Gamma^{\rm 1S\to 2P}_{\rm ex.}{}_m\rangle\langle\Gamma^{\rm 2P}_{\rm de\text{-}ex.}{}_m{}^{\to 1S}\rangle/\langle\Gamma^{\rm 2P}_{\rm para}{}_m\rangle}\,, \tag{7.6}$$

$$\mathcal{R}^{\rm para}_{\rm 2S} = \frac{1}{1 + \langle\Gamma^{\rm 2S}_{\rm bsd}\rangle/\langle\Gamma^{\rm 2S,para}_{\rm ann}\rangle} = \frac{\langle\Gamma^{\rm 2S,para}_{\rm ann}\rangle}{\langle\Gamma^{\rm 2S,para}_{\rm ann}\rangle + \langle\Gamma^{\rm 2S}_{\rm bsd}\rangle}\,, \tag{7.7}$$

$$\mathcal{R}^{\rm para}_{\rm 2P_0} = 1 + \frac{\langle\Gamma^{\rm 2P_0\to 1S}_{\rm de\text{-}ex.}\rangle}{\langle\Gamma^{\rm 2P_0}_{\rm para}\rangle}\left(1 - \mathcal{R}^{\rm para}_{\rm 1S}\right) - \frac{\langle\Gamma^{\rm 2P_0}_{\rm bsd}\rangle}{\langle\Gamma^{\rm 2P_0}_{\rm para}\rangle}\,, \tag{7.8}$$

$$\mathcal{R}^{\rm para}_{\rm 2P_{\pm1}} = 1 + \frac{\langle\Gamma^{\rm 2P_{\pm1}\to 1S}_{\rm de\text{-}ex.}\rangle}{\langle\Gamma^{\rm 2P_{\pm1}}_{\rm para}\rangle}\left(1 - \mathcal{R}^{\rm para}_{\rm 1S}\right) - \frac{\langle\Gamma^{\rm 2P_{\pm1}}_{\rm bsd}\rangle}{\langle\Gamma^{\rm 2P_{\pm1}}_{\rm para}\rangle}\,, \tag{7.9}$$

and similarly for $\mathcal{R}^{\rm ortho}_n$. In the eqs. (7.6)–(7.9) we have defined the total width of a bound state,

$$\Gamma^n_{\rm para/ortho} \equiv \Gamma^{n,\rm para/ortho}_{\rm ann} + \Gamma^n_{\rm bsd} + \sum_{n'}\Gamma^{n\to n'}\,. \tag{7.10}$$

We remark that at late times in the evolution of the universe, i.e. at temperatures such that the heavy dark particles are very diluted, DM particle interactions become negligible with respect to the universe expansion rate H that dominates the evolution equation (7.4). The effective Boltzmann equation (7.4) can be recast in terms of the yield $Y = n/s$ as in (2.9), and then be solved numerically.

The main advantage of the EFT framework is to allow for a rigorous derivation and a systematic inclusion of corrections to the relevant observables entering the thermally averaged effective cross section in (7.5). We refer to the scheme in figure 7.1 to pictorially illustrate the different corrections. As for the scattering states, which are integrated

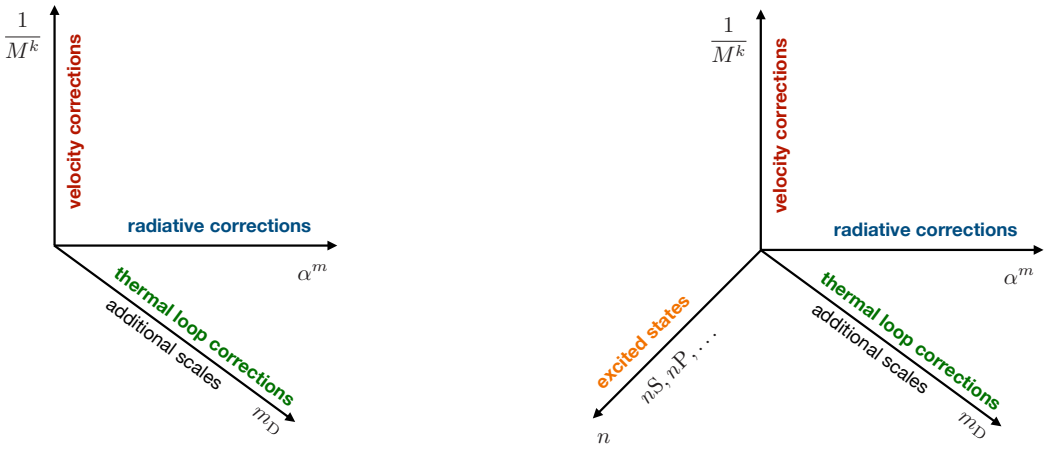

Figure 7.1: Schematic representation of the different corrections to the cross sections and widths considered in this work. The left plot is for scattering states, whereas the right plot is for bound states.

over all momenta, we can improve cross sections and widths by adding relativistic corrections. This amounts at including higher-dimensional operators in both NRQED_{DM} and $\text{pNRQED}_{\text{DM}}$. Furthermore, we can add radiative corrections to the matching coefficients of the effective field theories, as was done in chapter 5, but also to the dipole diagrams, cf. figure 6.1, which need to be resummed in the large temperature regime. As for the bound states, the situation is similar. Higher-dimensional operators account for higher-order relativistic corrections, which at the same time may open new decay channels through annihilations of heavy pairs of higher orbital quantum number. Radiative corrections at the hard scale improve the matching coefficients and at the ultrasoft scale they improve the near-threshold thermal rates. Moreover, we add a fourth dimension to the scheme that accounts for the number of bound states to be included in the analyses consistently with the other corrections. The inclusion of excited states can be seen as a further improvement towards an accurate description of the actual physical system, and hence a correction to the simplest possible situation, when only the ground state is considered. As explained above, in this work we include the first excited 2S and 2P states. In the following sections, we aim to assess the relative importance of the recoil and Debye-mass corrections on the effective cross section and eventually on the DM relic abundance.

7.1 Numerical results for the effective cross section

We would like to quantify the impact of the resummation of the Debye mass scale on the thermally averaged effective cross section, at zeroth order in the center-of-mass momentum. In figure 7.2 left, we plot the the effective cross section (7.5), thermally

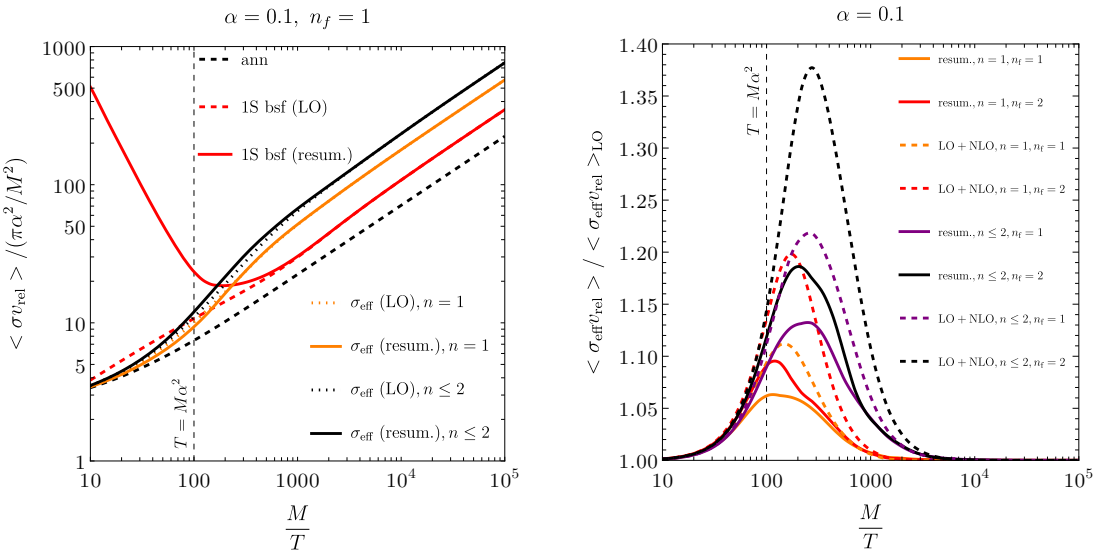

Figure 7.2: (Left) Thermally averaged annihilation (black dashed line), 1S bsf at LO (red dashed line) and $m_{\rm D}$-resummed 1S bsf (red solid line) cross sections, as well as the effective cross sections at LO (orange dotted line) and resummed (orange solid line) for the 1S state. The thermally averaged effective cross section for up to 2P states at LO and resummed is shown by the black dotted and black solid line, respectively. We normalize by $\pi\alpha^2/M^2$ and α runs at one loop with $\alpha(2M) = 0.1$ and $n_f = 1$. (Right) Ratios of the thermally averaged effective cross sections up to NLO (dashed lines) or with $m_{\rm D}$-resummation (solid lines), over the expression at LO. We consider both the $n_f = 1$ and $n_f = 2$ case.

averaged according to (B.15), for the ground state where the individual rates are either at leading order in the coupling or $m_{\rm D}$-resummed, and as a reference we plot also the 1S bound-state formation cross section (at LO and resummed), divided by $\pi\alpha^2/(2M)$, and the Sommerfeld annihilation factor, where α runs at one loop with one light fermion flavour and starting value $\alpha(2M) = 0.1$. In the next step, we include excited states up to 2P into the effective cross section. We observe that, although the resummation drastically increases the bsf cross section at $T \gg M\alpha^2$, the effective cross sections are not enhanced but close to the annihilation cross section at large temperatures. In order to extract quantitatively the corrections due to the resummation effect on the effective cross section, we plot in the right panel of fig. 7.2 the ratio of the resummed $\sigma_{\rm eff}$ over the expression obtained from the rates at LO (solid lines). As a comparison, we plot also the ratio when radiative corrections are not resummed but truncated at NLO (dashed lines). We see that for temperatures close to the freeze-out and far away, the ratios are close to one, reflecting the fact that in the $T \to 0$ limit the radiative corrections are suppressed, and that at large T one reaches the ionization-equilibrium regime, where the dipole processes, despite being large, balance each other, such that the net effect on the annihilations is small. The peak values for the deviations from the leading order effective

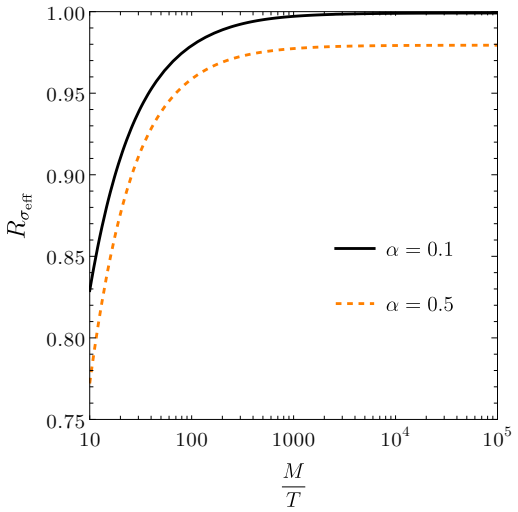

Figure 7.3: Ratios of thermally averaged effective cross section in the laboratory frame with recoil corrections, cf. (7.5), and the corresponding thermally averaged effective cross section without recoil corrections plotted as a function of M/T for couplings $\alpha = 0.1$ (black solid line) and $\alpha = 0.5$ (orange dashed line).

cross section are from about 5% to 20% at $T \approx M/200 - M/100$ for the resummed case, depending on n_f and the number of excited bound states in σ_{eff}. As a comparison, for the NLO case the correction is up to around 38% for $n_f = 2$ and excited states up to 2P. The treatment of thermal effects at fixed next-to-leading order results in an overestimation of the effective cross section, which originates from a systematic overestimation of the individual rates. At small temperatures, the solid and dashed lines eventually approach each other and stay constant at a value close to one. Here, the processes that involve a thermal incoming/outgoing dark photon are dominant and are fully accounted for by the individual rates at leading order. We summarize that, despite at large temperatures the Landau damping phenomenon leads to an enhancement of about two orders of magnitude for the bound-state formation cross section, the bound-state dissociation width and the (de-)excitation widths, at the level of the effective cross section we observe just a small enhancement due to the Debye-mass resummation that ranges only from 5% to 20%.

Next, we would like to make a comparison with the recoil corrections due to the thermal motion of the center of mass of the interacting heavy pairs in the thermal bath. In figure 7.3, we plot the ratio of (7.5), thermally averaged in the laboratory frame, with recoil corrections taken into account in the individual rates, and the corresponding effective cross section without recoil correction, which is thermally averaged according to (B.15). The ratio decreases with increasing temperature, and for large T there is a reduction in the thermally averaged effective cross section due to the recoil corrections by about 15-25% for both choices of coupling that we display. Hence, the contribution of the recoil corrections to the effective cross section, and, therefore, the Boltzmann equations, is significant for increasing T even for small couplings.

7.2 Boltzmann equations with recoil or Debye-mass effects

Finally, we quantify the recoil effect but also the corrections coming from the additional thermal processes, that are captured by the fixed NLO rates and the corresponding ones with a Debye mass resummation, to the dark matter relic density. We begin with the latter, i.e. analyze first the effect of the radiative corrections to $\Omega_{\rm DM}h^2$, while neglecting the center-of-mass motion of the heavy pairs.

In the left panel of figure 7.4, we show the energy density contours for $\Omega_{\rm DM}h^2 = 0.1200$ in the model parameter space (M, α), where $\alpha = \alpha(2M)$, and when considering bound states up to 2P. The orange lines correspond to an abelian model with only one light fermion, whilst the black lines are for $n_f = 2$ light fermion species. The black lines are systematically below the orange curves because of the additional annihilation channel into the second light fermionic particle. The dashed lines are always above the solid and dotted lines within each color, because the NLO corrections (dotted lines) or the $m_{\rm D}$-resummation corrections (solid lines) make the effective cross section in eq. (7.5) larger, so that the same energy density is reproduced for smaller α, and the dotted lines are below the solid lines due to the naive overestimation when truncating the radiative corrections two-loop order, cf. fig. 6.1 (see also the right plot in fig. 7.2, where the dashed lines are always above the solid lines for each color). The radiative corrections can be visualized more quantitatively if we plot the ratio of the DM energy densities at NLO or from $m_{\rm D}$-resummation, over $\Omega_{\rm DM}h^2$ as obtained from considering the near-threshold processes only at leading order. The corresponding plot, as a function of the coupling α at the hard scale $2M$ and for fixed dark matter mass $M = 1$ TeV, is shown on the right panel of figure 7.4. As we can see, if we vary the coupling from smaller to larger values up to 0.12, the ratio due to the resummation of the Debye mass scale (solid lines) decreases up to about 6.8% (8.7%) for $n_f = 1$ ($n_f = 1$) when adding bound states up to 2P, represented by the purple (black) solid line. If we consider only scattering states and the ground state 1S, then the corrections are up to 3.5% for $n_f = 1$ (orange solid line) or 4.7% for $n_f = 2$ (red solid line). If we, therefore, include more bound states to the network of coupled Boltzmann equations, then the radiative corrections deplete the present relic abundance to lower values for fixed coupling and DM mass,[4] which has a more drastic effect if we do not resum the thermal radiative contributions but stay at next-to-leading order (dotted lines). For instance, as can be seen in the right plot in fig. 7.4 for $n_f = 2$ and $\alpha(2M) = 0.12$, the correction increases from 8.7% to around 15% upon adding the 2S and 2P states to the ground state. Hence, a model with more light fermions which gives rise to the Landau damping phenomenon, together with inclusion of more excited states, allows even smaller values of α or larger values of the DM mass M to reproduce the observed energy density because of the additional channels for DM annihilations.

We now consider the recoil corrections with respect to the DM energy density. We remove the light fermions from the model, since they do not affect the study of the

[4]We checked explicitly, that in fact the corrections on the relic abundance stay almost constant when varying the dark matter mass from 0.1 TeV to 10 TeV. Here we choose $M = 1$ TeV.

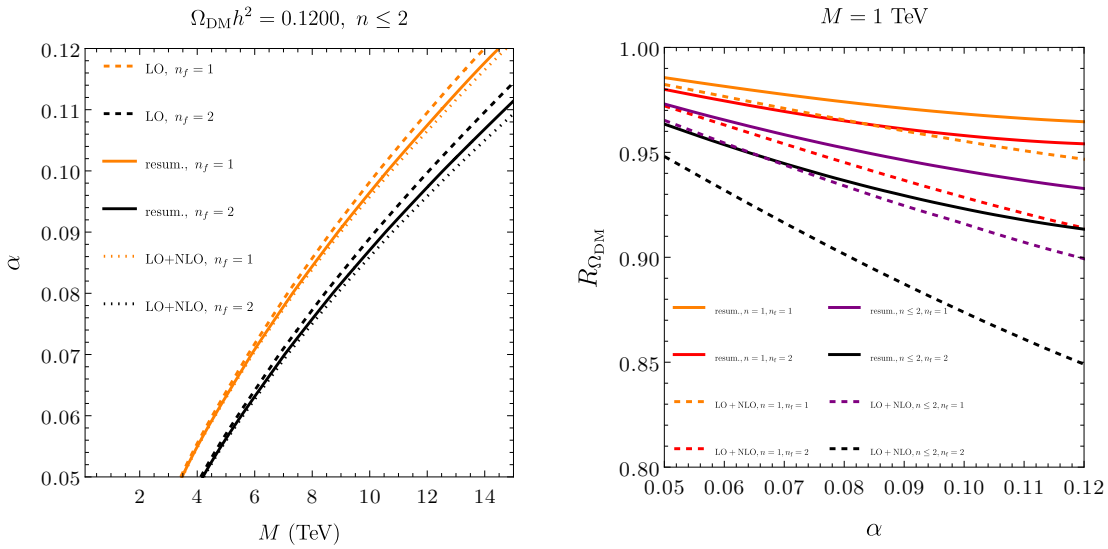

Figure 7.4: (Left) Contours in the parameter space (M, α) that correspond to the observed DM energy density obtained from different approximations of the effective cross section, when including bound states up to 2P. Orange lines are for $n_f = 1$, black lines for $n_f = 2$. (Right) Ratio of the present relic density with $m_{\rm D}$-resummed effective cross section (solid lines) or with $\sigma_{\rm eff}$ incl. radiative corrections at NLO (dashed lines), over $\Omega_{\rm DM}h^2$ as obtained from the near-threshold processes at leading order; plotted as a function of $\alpha \equiv \alpha(2M)$ that runs at one loop, and for fixed DM mass $M = 1$ TeV.

recoil for the hierarchy (3.2), where the Landau damping phenomenon is suppressed. Then we enlarge the range of parameter values for $\alpha(2M)$ up to 0.5, cf. footnote 8 in section 3.2 for more details. In the two panels of figure 7.5, we show the ratio of the present dark matter energy density, $R_{\Omega_{\rm DM}}$, obtained with center-of-mass recoil effects in the laboratory frame and the one obtained without recoil effects plotted as a function of α (left panel) and M (right panel). The left plot shows the ratio for a fixed dark matter mass of 1 TeV. For a wide range of couplings from 0.05 to 0.5, we observe that when considering the evolution of dark matter unbound pairs and only the ground state 1S, the ratio $R_{\Omega_{\rm DM}}$ (orange solid line) is larger than one, reflecting the fact that the dark matter relic abundance is less depleted in the laboratory frame due to the inclusion of center-of-mass recoil effects. For values of the coupling up to $\alpha = 0.2$, the recoil correction stays constant around 2.5%. For stronger couplings the recoil correction starts increasing, eventually reaching the maximal value of about 4.5% for $\alpha = 0.5$. Including the contribution from the first excited state 2S in the effective cross section (7.5), the ratio $R_{\Omega_{\rm DM}}$, now represented by the green dashed line, is nearly the same as the ratio obtained from only the 1S state. Finally, we add the excited state 2P and allow for transitions between 1S and 2P, represented by the black dash-dotted line in the left plot of fig. 7.5. The recoil correction amounts to an effect between 2.5% and 4.5%. The dark matter energy abundance is monotonically increasing with increasing α, since

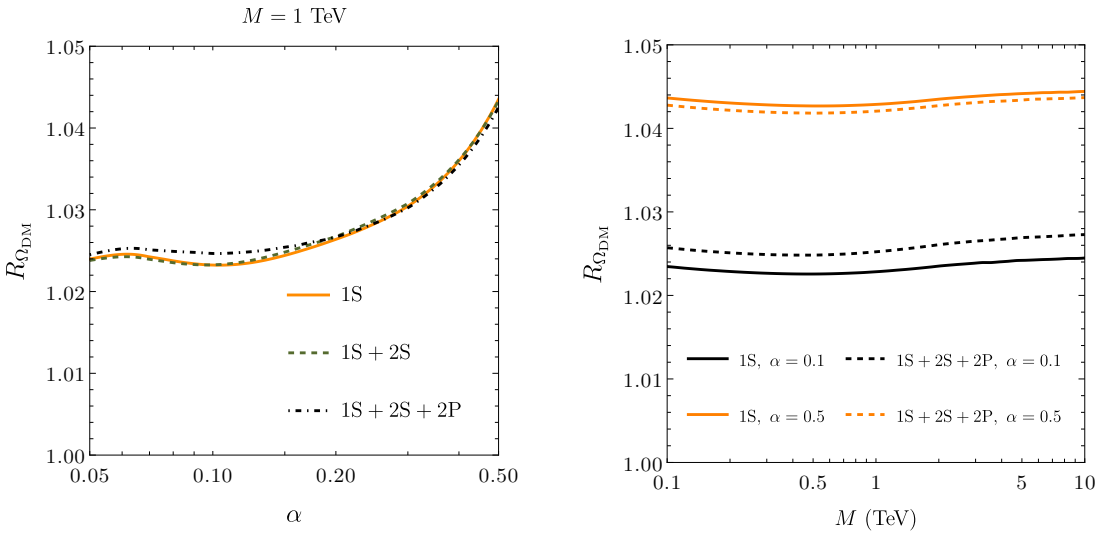

Figure 7.5: (Left) Ratio of the present dark matter relic abundance in $\mathrm{U}(1)_{\rm DM}$, where we put n_f to zero, as seen from the laboratory frame including center-of-mass recoil corrections and the relic abundance computed without recoil corrections plotted as a function of the coupling α for fixed dark matter mass $M = 1$ TeV. The orange solid line is for the ratio obtained by only considering the 1S bound state, the green dashed line by including the 2S state, the black dash-dotted line by including 2P states beyond the no-transition approximation. (Right) Ratio of the present dark matter relic abundance as a function of the dark matter mass for two benchmark values of the coupling α. Black solid and orange solid lines are for $\alpha = 0.1$ and $\alpha = 0.5$, respectively, and obtained by considering only the 1S state. Black dashed and orange dashed lines are for $\alpha = 0.1$ and $\alpha = 0.5$, respectively, and obtained by including the excited states 2S and 2P beyond the no-transition approximation.

the effective cross section (7.5) is a decreasing function with increasing coupling, see figure 7.3. Moreover, the recoil correction on the dark matter relic abundance seems to be independent of whether considering only the ground state or adding higher excited states and also transitions among them for the whole range of considered values for α. Hence, one can quantify the recoil correction on the relic energy density, to a good degree of precision, already including only the ground state in the evolution equations.

The right plot in figure 7.5 shows $R_{\Omega_{\rm DM}}$ for a wide range of dark matter masses from 0.1 TeV to 10 TeV. In the considered range, the recoil effect on the energy density is almost independent of the dark matter mass M. The black solid and orange solid lines include only the ground state contribution to the evolution equations for the specific values $\alpha = 0.1$ and $\alpha = 0.5$, respectively. The black dashed and orange dashed lines also include bound-state effects from the 2S and 2P states.

We conclude that the correction due to the motion of the center of mass of the heavy dark matter pairs is above the 1% accuracy of the present measurement of the dark

matter energy density, with values ranging between 2.5% and 4.5% for the considered values of α from 0.05 to 0.5. In the laboratory frame, the recoil leads to less depletion of the energy density due to a decreased effective cross section, and is independent of the particular value of the dark matter mass and the inclusion of bound-state effects from higher excited states. We obtain similar results for the recoil corrections to the dark matter relic abundance in the dark non-abelian model, which we are going to study in the next chapter. In the unbroken non-abelian gauge theories SU(2) and SU(3), for coupling $\alpha(2M) = 0.03$ and at one-loop running, we get a small correction to the relic density coming from recoil corrections of about 2%.

Finally we remind that, when T approaches $M\alpha$, the multipole expansion for thermal dark photons breaks down and one has to treat them at the level of $\mathrm{NRQED}_{\mathrm{DM}}$. However, for all the couplings considered in this work to compute the DM energy density, it holds that $T \ll M\alpha$ after freeze-out. The numerical results for the DM energy density presented in this section are based on the single effective Boltzmann equation (7.4). If instead we solve the coupled Boltzmann equations (7.1)–(7.2) numerically, we get results that differ at most by 1% from the ones presented here, and so are within the uncertainty of the measured DM relic abundance.

Part IV

Weakly-coupled non-abelian dark sector

Chapter 8

pNREFT$_{\rm DM}$, thermal scale hierarchies

The preceding sections were dedicated to a comprehensive dark matter study for the exemplary case of a heavy dark fermion species of mass M coupled to a dark abelian gauge field A_μ, where, in addition to the Lagrangian model studied in previous works [51, 52], also n_f light (practically massless) dark fermions of same charge where included into the model. The underlying theory of the dark sector was an abelian gauge theory, U(1)$_{\rm DM}$, as an equivalent version to the familiar QED. In this chapter, we work out the same step-by-step construction as for the abelian theory, however for a heavy DM fermion of mass M together with n_f massless dark fermions to be in the fundamental representation of a non-abelian dark SU(N) gauge group, SU(N)$_{\rm DM}$, with $N \geq 2$.[1]

We compute the cross sections and widths for particle-antiparticle heavy-pair annihilations in section 9.1, and discuss the dipole-transition processes for specific hierarchies of energy scales in section 9.2. Finally, in the follow-up chapter 10, we provide some numerical results from solving the Boltzmann equations, which aim to show the impact of bound-state effects as well as corrections due to the recoil on the DM energy density.

First of all, we begin by writing the dark-sector Lagrangian for a heavy Dirac fermion $X = X^a_\alpha$ ($\alpha = 1, \ldots, 4$ Dirac spinor index; $a = 1, \ldots, N$ color index in fundamental representation) and n_f light Dirac fermions f_i coupled to SU(N) gauge fields $A_\mu = T^A A^A_\mu$ in adjoint representation, where $A = 1, \ldots, N^2 - 1$:

$$\mathcal{L}_{\mathrm{SU}(N)_{\rm DM}} = \bar{X}(i\not{D} - M)X - \frac{1}{4} G^A_{\mu\nu} G^{A\,\mu\nu} + \sum_{i=1}^{n_f} \bar{f}_i (i\not{D} - m_i) f_i + \mathcal{L}_{\rm portal}\,, \tag{8.1}$$

where $D_\mu = \partial_\mu + igA^A_\mu T^A$, T^A are the group generators in the adjoint representation, $G^A_{\mu\nu} = \partial_\mu A^A_\nu - \partial_\nu A^A_\mu + g f^{ABC} A^B_\mu A^C_\nu$ the field strength tensor and f^{ABC} the totally antisymmetric fine structure constants of the underlying algebra; $\alpha \equiv g^2/(4\pi)$ is the dark fine structure constant, g the dark non-abelian gauge coupling. Moreover it holds

[1] Throughout this work, the notation SU(N) is meant to be the same as SU(N)$_{\rm DM}$, and denotes the dark non-abelian sector.

that $G^A_{\mu\nu} G^{A\,\mu\nu} = 2\ \mathrm{Tr}\,[G_{\mu\nu} G^{\mu\nu}]$, with $G_{\mu\nu} = (i/g)\,[D_\mu, D_\nu]$. As in the abelian case in the previous sections, we set $\mathcal{L}_{\rm portal} = 0$.[2]

Contrarily to the U(1) model, additional loop corrections due to gauge-field self-interactions (and couplings to the ghost fields in the path-integral formalism), lead to a significantly different running of the coupling compared to the abelian equivalent in eq. (3.3), where the first coefficient of the beta function at leading order now reads

$$\beta_0 = \frac{11}{3} N - \frac{4}{3} T_F n_f \,, \tag{8.2}$$

where $T_F = 1/2$ is the Dynkin index ($T_F = 1$ in U(1)). Since β_0 is positive for all different kinds of numerical combinations between $N = \{2, 3, 4\}$ and $n_f = \{1, 2\}$ used in this work, asymptotic freedom is approached at high energies or temperatures, like in the QCD gauge theory, whereas perturbation theory is spoiled in the low-energy/temperature limit due to antiscreening effects of the gauge fields. The non-perturbative scale, at which the weak-coupling expansion in α breaks down, is denoted by Λ and can be computed by solving the renormalization equation for α,

$$\frac{d\alpha}{d\log\mu} = \alpha\beta(\alpha) = -\frac{\alpha^2}{2\pi}\beta_0 + \mathcal{O}(\alpha^3) \,, \tag{8.3}$$

which at one-loop accuracy and for the boundary condition $\alpha(\Lambda) = \infty$ reads

$$\Lambda = \exp\left[-\frac{2\pi}{\beta_0 \alpha(\mu)}\right]\mu \,. \tag{8.4}$$

While in QCD, which corresponds to the SU(3) case and is relevant to describe the effects of a moving quark-gluon plasma on quarkonium formation and dissociation in heavy-ion collisions [131, 140], the scale Λ is about 200 MeV and hence of the order of the pion masses, in our dark non-abelian $\mathrm{SU}(N)_{\rm DM}$ model we would like to keep the value for the coupling sufficiently small in order not to endanger the weak-coupling expansion in the lowest temperature region, $T \approx 10^{-5} M$, that is considered in this work. This temperature regime sets the magnitude of the ultrasoft scale. Hence, if we require that the coupling at the ultrasoft scale is weak, then we need to require that, in particular, $\alpha(10^{-5} M) < 1$. This condition is fulfilled for the SU(4) theory at one-loop running if we choose $\alpha(2M) \lesssim 0.03$ at the hard scale of non-relativistic heavy-pair annihilations, $2M$, and by somewhat larger values of $\alpha(2M)$ for smaller gauge groups: $\alpha(2M) \lesssim 0.04$ for the SU(3) theory and $\alpha(2M) \lesssim 0.06$ for the SU(2) theory.[3] For these values of the

[2] We remark that, at variance with the abelian model, for $\mathrm{SU}(N)_{\rm DM}$ a portal interaction via kinetic mixing with the Standard Model is not viable because of gauge invariance. A possible workaround can be achieved by including non-renormalizable operators [136–138], a Higgs portal [139], or introducing vector-like fermions [137]. We assume these portal interactions to keep the dark sector at the same temperature as the Standard Model and, at the same time, the portal couplings to be much weaker than the dark gauge coupling g, such that effects from $\mathcal{L}_{\rm portal}$ can be practically ignored with respect to the freeze-out process within the dark sector.

[3] These benchmark values for $\alpha(2M)$ represent only approximate upper numbers, since the coupling depends also on the number n_f of massless fermions that run in the loop.

gauge couplings, the absolute value of the binding energy of the dark fermion-antifermion bound states, $|E_1^b|$, is smaller than the freeze-out temperature $T_\mathrm{F} \sim M/25$. Hence, it is not possible to satisfy $\Lambda < M/10^5$ and $T_\mathrm{F} \lesssim |E_1^b|$ at the same time; the latter condition would require stronger couplings $\alpha(2M) \sim 0.1$ that we, however, avoid.[4]

We are interested in very similar temperature regimes as the ones discussed in chapter 3, but now extended by the additional non-perturbative scale Λ taken to be the lowest energy scale, and we consider again two different arrangements for the temperature T: The hierarchy corresponding to later times in the universe expansion,

$$M \gg M\alpha \gtrsim \sqrt{MT} \gg M\alpha^2 \gtrsim T \gg m_\mathrm{D} \gg \Lambda\,, \tag{8.5}$$

and the hierarchy related at earlier times close to the thermal freeze-out of the dark matter,

$$M \gg \sqrt{MT} \gg M\alpha \gg T \gg m_\mathrm{D}, M\alpha^2 \gg \Lambda\,. \tag{8.6}$$

The Debye mass, $m_\mathrm{D} \sim gT \ll T$ is not only generated by the massless dark fermions running in the loop, but also by the self-interactions of the gauge fields. More details will be shown in section 9.2. Both of these two choices of hierarchies for the energy scales in eqs. (8.5) and (8.6) allow us, like in the abelian case, to integrate out modes associated with the hard and soft scale by setting to zero the temperature characterizing the thermal distribution of the dark gauge fields. Moreover, computations at the hard, soft and ultrasoft energy scale may be done in weak-coupling perturbation theory, since we choose the coupling at the hard scale to be sufficiently small, $\alpha(2M) < 0.05$. The ultimate effective field theory is a pNRQCD-like EFT [92, 94] for DM fermion-antifermion bilocal fields and an SU(N) dark gauge group.[5] We dub it pNREFT$_\mathrm{DM}$.[6] The Lagrangian

[4] In the abelian case, where numerical values up to $\alpha(2M) = 0.5$ have been considered, for such large values it turns out that the freeze-out temperature is below the ultrasoft scale. Physics at thermal freeze-out can therefore be described fully within pNRQED, cf. sections 3.1–3.2. On the other hand, for the non-abelian theory it may be, in dependence of the coupling and the particular model, that also the soft scale becomes smaller than or of the same order as the freeze-out temperature, which signals the break down of the multipole expansion for thermal gauge fields at freeze out. This happens for the SU(2), SU(3) and SU(4) theories considered here at $\alpha(2M) \lesssim 0.03$, where the freeze-out temperature $M/25$ is slightly larger than the soft scale $M\alpha$. We will not account for this issue in this work, where we assume that the multipole expansion holds also at freeze-out.

[5] One can make a one-to-one correspondence between the pNREFT$_\mathrm{DM}$ model, that will be scrutinized in the following sections, and pNRQCD. In pNRQCD, the non-relativistic degrees of freedom of mass M are the heavy quarks and antiquarks like the bottom or the top, and a fermion-antifermion bound-state of heavy quarks of the same flavor is called *quarkonium* in analogy to positronium [141–143]. Those bosonic states, that are frequently observed in collider experiments, are charmonium (charm-anticharm pair) and bottomonium (bottom-antibottom pair). The latter is known as the Y(1S)-meson, if it is in the lowest energy configuration with a mass of around $2M_b \approx 9.5$ GeV [144]. Its Bohr momentum is about $Mv_\mathrm{rel} \approx 1.5$ GeV and the ultrasoft scale about $Mv_\mathrm{rel}^2 \approx 0.5$ GeV, that is the typical splitting between the binding energies of the two lowest bound states. Hence the relative velocity of the bottom-antibottom meson, $v_\mathrm{rel}^2 \approx 0.1$, can be safely considered to be non-relativistic, while for charmionium with $v_\mathrm{rel}^2 \approx 1/3$, a non-relativistic expansion in the velocities may be less secure [101]. The coupling in QCD, with $\alpha(M_b) \approx 0.2$, is by an order of magnitude larger than the values for the dark coupling constant that we consider in this work.

[6] The reason for not calling the non-relativistic EFT, emerging from the SU(N)$_\mathrm{DM}$ model considered

at order r in the multipole expansion reads[7]

$$\begin{aligned}\mathcal{L}_{\text{pNREFT}_{\text{DM}}} = \int d^3r \Bigg\{ & \operatorname{Tr}\left[\mathrm{S}^\dagger \left(i\partial_0 - H_s\right)\mathrm{S} + \mathrm{O}^\dagger \left(iD_0 - H_o\right)\mathrm{O}\right] \\ & + \operatorname{Tr}\left[V_A(r) g(\mathrm{S}^\dagger \boldsymbol{r}\cdot\boldsymbol{E}\mathrm{O} + \mathrm{O}^\dagger \boldsymbol{r}\cdot\boldsymbol{E}\mathrm{S}) + \frac{V_B(r)}{2} g(\mathrm{O}^\dagger \boldsymbol{r}\cdot\boldsymbol{E}\mathrm{O} + \mathrm{O}^\dagger\mathrm{O}\boldsymbol{r}\cdot\boldsymbol{E})\right]\Bigg\} \\ & - \frac{1}{4} G^A_{\mu\nu} G^{A\,\mu\nu} + \sum_{i=1}^{n_f} \bar{f}_i i \not{D} f_i \,,\end{aligned} \tag{8.7}$$

where the trace is over color indices. The field $\mathrm{S} = S\mathbb{1}_{N\times N}/\sqrt{N}$ is an SU(N) singlet field made of a dark fermion and antifermion and $\mathrm{O} = O^a T^a/\sqrt{T_F}$ is the corresponding SU(N) adjoint field; they depend on time t, the relative coordinate $\boldsymbol{r}$ and the center of mass coordinate $\boldsymbol{R}$. The non-abelian electric field $E_i = T^A E_i^A = \partial_i A_0 - \partial_0 A_i + g f^{ABC} T^A A_i^B A_0^C$ depends only on t and $\boldsymbol{R}$. The temporal covariant derivative acting on the adjoint field is $D_0\mathrm{O} = \partial_0\mathrm{O} + ig[A_0, \mathrm{O}]$. The Hamiltonians, H_s and H_o, can be written as in (4.3) and (4.4) with the leading order potentials given respectively by[8]

$$V_s^{(0)} = -C_F \frac{\alpha}{r}\,, \qquad\qquad V_o^{(0)} = \frac{\alpha}{2Nr}\,. \tag{8.8}$$

The Casimir of the fundamental representation is $C_F = (N^2-1)/(2N)$. The adjoint field O is a color octet field for $N = 3$, which is the QCD case. The Lagrangian term for the n_f massless dark fermions remains unchanged.

The electric dipole terms in the second line of eq. (8.7), with the associated matching coefficients $V_A(r) = V_B(r) = 1$ at leading order, allow for transitions between an unbound adjoint dark fermion-antifermion pair and a bound or unbound singlet pair. Such transitions are responsible for bound-state formation and dissociation. Moreover, they allow for scattering-state to scattering-state transitions among dark fermion-antifermion pairs in the SU(N) adjoint representation. A crucial difference with respect to the abelian model is that color-singlet transitions in SU(N), either involving bound states or scattering states, cannot happen in this model because of the SU(N) charge conservation. The electric-dipole vertex between a color-singlet bound state and an color-adjoint state resembles the abelian electric-dipole vertex, cf. figure 4.1 left, except that an additional factor $\sqrt{T_F/N}\delta^{AB}$ needs to be taken into account, where the indices A and B connect the vertex with the electric correlator and color-adjoint propagator, respectively. The

in this chapter, simply pNRQCD$_{\text{DM}}$, is because we do not restrict to only $N = 3$, like in QCD, but keep N variable in this work.

[7]Like in the abelian case, additional interactions involving the Röntgen terms appear at leading order in r and in the center-of-mass momentum P, which we do not write explicitly in (8.7). They are of the same form as the electric-dipole terms in the second line, one just needs to replace the operator $\boldsymbol{r}\cdot\boldsymbol{E}$ by $\boldsymbol{r}/(4M)\cdot\{\boldsymbol{P}\times, \boldsymbol{B}\}$, involving the dark non-abelian magnetic field $B_i = T^A B_i^A = -\epsilon_{ijk} G_{jk}/2$, in every single term.

[8]Notice that, due to the positive sign of the potential $V_o^{(0)}$ and hence its repulsive nature, color-adjoint bound states cannot exist.

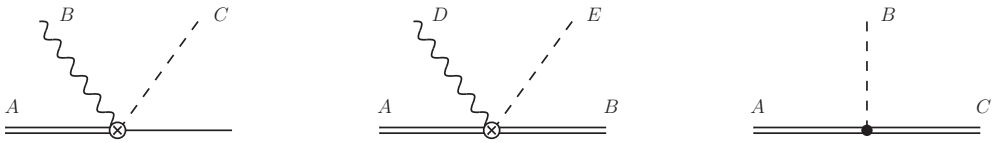

Figure 8.1: The first two vertices are exclusive in non-abelian theories: The vertex on the left connects a color-singlet heavy pair (solid line) with a color-adjoint heavy pair (double solid line), the vertex in the middle of the figure connects two heavy adjoint pairs. The vertex on the right comes from the covariant derivative D_0 that acts only on the adjoint field $\mathrm{O}(t, \boldsymbol{R})$. Dashed (wavy) lines represent the longitudinal (transversal) gauge fields, whereas the latin capital letters denote the color indices. More vertices can be found in ref. [141].

constant factor comes from taking the color trace of the generators in (8.7). There is an additional electric-dipole vertex connecting two color-adjoint propagators, with a factor $gd^{ABC}/2$, but also three more vertices that are depicted in figure 8.1.[9] From left to right, they read $ig^2\sqrt{T_F/N}f^{ABC}\boldsymbol{r}$, $ig^2 d^{ABC}f^{CDE}\boldsymbol{r}/2$ and $-igf^{abc}$.[10] When including interactions at leading order in the center-of-mass momentum $\boldsymbol{P}$, then there are more vertices compared to the one shown on the right in fig. 4.1 in the abelian case, that come from the self-interacting term in the dark non-abelian magnetic field within the Röntgen dipole interaction. Diagrams involving such interaction vertices of order g^2 are disregarded in this work, because we stay at leading order in the coupling when computing the leading recoil corrections to the dipole processes in section 9.2.

We can replace the temporal covariant derivative D_0 by the partial time derivative ∂_0 in the pNREFT$_{\mathrm{DM}}$ Lagrangian (8.7), if we make the following substitutions for the adjoint field,

$$\tilde{\mathrm{O}}(\boldsymbol{r}, \boldsymbol{R}, t) = \mathcal{W}_{[(\boldsymbol{R},t),(\boldsymbol{R},t_0)]}\, \mathrm{O}(\boldsymbol{r}, \boldsymbol{R}, t)\, \mathcal{W}_{[(\boldsymbol{R},t_0),(\boldsymbol{R},t)]}\,, \tag{8.9}$$

and for the dark electric field,

$$\tilde{E}^i(\boldsymbol{R}, t) = \mathcal{W}_{[(\boldsymbol{R},t),(\boldsymbol{R},t_0)]}\, E^i(\boldsymbol{R}, t)\, \mathcal{W}_{[(\boldsymbol{R},t_0),(\boldsymbol{R},t)]}\,, \tag{8.10}$$

where now the new fields are *dressed* by the temporal Wilson line

$$\mathcal{W}_{[(\boldsymbol{R},t),(\boldsymbol{R},t_0)]} = \mathcal{P}\left[e^{ig\int_{t_0}^{t} dt'\ A_0(\boldsymbol{R},t')}\right], \tag{8.11}$$

where $\mathcal{P}$ denotes path-ordering, which for fixed $\boldsymbol{R}$ can be replaced by the time ordering operator $\mathcal{T}$. The initial time t_0 can be chosen arbitrarily, since it cancels out in concrete

[9] The first two vertices stem from the self-interacting term in the non-abelian electric field, whereas the vertex on the right in fig. 8.1 comes from the covariant derivative D_0.

[10] The totally symmetric tensor d^{ABC} is defined by the anticommutator $\{T^A, T^B\} = \delta^{AB}/N + d^{ABC}T^C$.

calculations. The Lagrangian in terms of these new fields now reads[11]

$$\begin{aligned}\mathcal{L}_{\mathrm{pNREFT_{DM}}} \supset \int d^3r \Bigg\{ &\mathrm{Tr}\left[\mathrm{S}^\dagger \left(i\partial_0 - H_s\right) \mathrm{S} + \tilde{\mathrm{O}}^\dagger \left(i\partial_0 - H_o\right) \tilde{\mathrm{O}}\right] \\ &+ g\mathrm{Tr}\left[(\mathrm{S}^\dagger \boldsymbol{r}\cdot\tilde{\boldsymbol{E}}\tilde{\mathrm{O}} + \mathrm{h.c.}) + \frac{1}{2}(\tilde{\mathrm{O}}^\dagger \boldsymbol{r}\cdot\tilde{\boldsymbol{E}}\tilde{\mathrm{O}} + \tilde{\mathrm{O}}^\dagger\tilde{\mathrm{O}}\boldsymbol{r}\cdot\tilde{\boldsymbol{E}})\right]\Bigg\},\end{aligned} \tag{8.12}$$

which implies that the interaction term in the covariant derivative D_0 has now been resummed. The Lagrangians (8.7) and (8.12) will generate the same diagrams in perturbation theory, once we expand the exponential in (8.11) up to the desired order in the coupling.

Due to the running of the coupling constant, cf. equation (8.3), α will certainly approach different numerical values when computing processes occurring at the hard, soft and ultrasoft scale. We typically renormalize the gauge coupling at the hard scale $2M$ in annihilation processes, at a soft scale of order $M\alpha$ in the wavefunction and at a scale of order $M\alpha^2$ or T when considering gauge bosons at the ultrasoft scale. A further scale, $|\boldsymbol{p}| = Mv_{\mathrm{rel}}/2$, can be associated to the coupling of gauge bosons with non-relativistic scattering states.[12] Because of asymptotic freedom, it follows for the coupling constant that $\alpha(2M) \ll \alpha(M\alpha), \alpha(Mv_{\mathrm{rel}}) \ll \alpha(M\alpha^2)$. Finally, we briefly remark that the scale $\sqrt{MT}$, generated by the thermal motion of the heavy dark matter particles, may give possible non-vanishing thermal contributions to the color-singlet and color-adjoint potentials if $\sqrt{MT} \gg M\alpha$, which is the case for the particular hierarchy written in eq. (8.6). Like in the abelian case, we do not address those specific thermal corrections in this work.

[11] The equality between (8.7) and (8.12) can be straightforwardly verified by inserting (8.9) and (8.10) into eq. (8.12), then using the Leibniz integral rule whenever ∂_0 acts on the Wilson line, and the cyclicity property of the trace.

[12] The coupling constant α in the potentials (8.8) as well as in the color-singlet and color-adjoint wavefunctions typically runs at a soft scale of the order of the inverse Bohr radius $1/a_0$.

Chapter 9

Thermal rates in $\mathrm{SU}(N)_{\mathrm{DM}}$

9.1 Color-singlet and color-adjoint pair annihilations

Similarly to U(1), also in SU(N) the heavy DM particles can annihilate into the dark light degrees of freedom, i.e. the gauge fields and the massless fermions. In the non-abelian theory, however, there are two more four-fermion dimension six operators contributing to fermion-antifermion annihilations than in the abelian case due to the SU(N) adjoint configurations, such that the four contact-interaction terms responsible for S-wave annihilations read

$$\begin{aligned}\delta\mathcal{L}_{\mathrm{NREFT_{DM}}} = &\frac{f_{[\mathbb{1}]}(^1S_0))}{M^2}\psi^\dagger\chi\,\chi^\dagger\psi + \frac{f_{[\mathbb{1}]}(^3S_1))}{M^2}\psi^\dagger\boldsymbol{\sigma}\chi\cdot\chi^\dagger\boldsymbol{\sigma}\psi \\ &+ \frac{f_{[\mathbf{adj}]}(^1S_0))}{M^2}\psi^\dagger T^a\chi\,\chi^\dagger T^a\psi + \frac{f_{[\mathbf{adj}]}(^3S_1))}{M^2}\psi^\dagger T^a\boldsymbol{\sigma}\chi\cdot\chi^\dagger T^a\boldsymbol{\sigma}\psi\,.\end{aligned} \tag{9.1}$$

The dimension eight operators, that will depend on the heavy-particle momenta and incorporate the P-wave as well as the first relativistic corrections to the S-wave annihilations, can be viewed in refs. [141, 145]. Then for the effective field theory at lower energies, the four-fermion dimension six operators in (9.1) are inherited in the local potentials in the pNREFT$_{\mathrm{DM}}$ Lagrangian, where its imaginary parts capture the annihilation processes of heavy fermion-antifermion pairs [116]:

$$\begin{aligned}&\delta\mathcal{L}^{\mathrm{ann}}_{\mathrm{pNREFT_{DM}}} = \\ &\frac{i}{M^2}\int d^3r\,\mathrm{Tr}\Big\{\mathrm{S}^\dagger\delta^3(\boldsymbol{r})\,N\left[2\mathrm{Im}\left[f_{[\mathbb{1}]}(^1S_0)\right] - \boldsymbol{S}^2\left(\mathrm{Im}\left[f_{[\mathbb{1}]}(^1S_0)\right] - \mathrm{Im}\left[f_{[\mathbb{1}]}(^3S_1)\right]\right)\right]\mathrm{S} \\ &\quad + \mathrm{O}^\dagger\delta^3(\boldsymbol{r})\,T_F\left[2\mathrm{Im}\left[f_{[\mathbf{adj}]}(^1S_0)\right] - \boldsymbol{S}^2\left(\mathrm{Im}\left[f_{[\mathbf{adj}]}(^1S_0)\right] - \mathrm{Im}\left[f_{[\mathbf{adj}]}(^3S_1)\right]\right)\right]\mathrm{O}\Big\}\,.\end{aligned} \tag{9.2}$$

At order α^3, the imaginary parts of the singlet matching coefficients read [100, 102]:[1]

$$\begin{aligned}\mathrm{Im}\left[\mathrm{f}_{[\mathbb{1}]}({}^1\mathrm{S}_0)\right] &= \frac{\mathrm{N}^2-1}{4\mathrm{N}^2}\pi\,\alpha(2\mathrm{M})^2 \\ &\quad\times\left\{1+\frac{\alpha}{\pi}\left[\frac{1}{2N}\left(5-\frac{\pi^2}{4}\right)+N\left(\frac{77}{9}-\frac{5}{12}\pi^2\right)-\frac{8}{9}n_f\right]\right\}, \qquad (9.3)\\ \mathrm{Im}\left[\mathrm{f}_{[\mathbb{1}]}({}^3\mathrm{S}_1)\right] &= \frac{2}{9}(\pi^2-9)\frac{(\mathrm{N}^2-1)(\mathrm{N}^2-4)}{8\mathrm{N}^3}\alpha^3+\mathrm{n}_f\pi\,\alpha(2\mathrm{M})^2\left(1-\frac{\alpha}{\pi}\mathrm{C}_F\frac{13}{4}\right), \qquad (9.4)\end{aligned}$$

and the imaginary parts of the SU(N) adjoint matching coefficients are [100, 102, 146]:[2]

$$\begin{aligned}\mathrm{Im}\left[\mathrm{f}_{[\mathbf{adj}]}({}^1\mathrm{S}_0)\right] &= \frac{\mathrm{N}^2-4}{4\mathrm{N}}\pi\,\alpha(2\mathrm{M})^2 \\ &\quad\times\left\{1+\frac{\alpha}{\pi}\left[\frac{1}{2N}\left(5-\frac{\pi^2}{4}\right)+N\left(\frac{199}{18}-\frac{7}{12}\pi^2\right)-\frac{8}{9}n_f\right]\right\}, \qquad (9.5)\\ \mathrm{Im}\left[\mathrm{f}_{[\mathbf{adj}]}({}^3\mathrm{S}_1)\right] &= \frac{\mathrm{n}_f}{6}\pi\,\alpha(2\mathrm{M})^2\Bigg\{1+\frac{\alpha}{\pi}\left[\frac{13}{8\mathrm{N}}\right. \\ &\quad\left.+N\left(\frac{415}{72}+\frac{2}{3}\log 2-\frac{\pi^2}{4}\right)-\frac{5}{9}n_f+\left(-\frac{73}{4}+\frac{67}{36}\pi^2\right)\frac{5}{n_f}\right]\Bigg\}. \qquad (9.6)\end{aligned}$$

At order α^2, taking the matching coefficients from eqs. (9.3) and (9.4), and the SU(N) equivalent of eq. (5.25), it follows that the Sommerfeld-enhanced SU(N)-singlet annihilation cross section, at leading order in the coupling, reads

$$(\sigma^{\mathrm{NR}}_{\mathrm{ann}}v_{\mathrm{rel}})^{[\mathbb{1}]}_{\mathrm{LO}}(\boldsymbol{p}) = (\sigma^{\mathrm{NR}}_{\mathrm{ann}}v_{\mathrm{rel}})^{[\mathbb{1}]}_{\mathrm{LO}}\,|\Psi^{[\mathbb{1}]}_{\boldsymbol{p}}(\mathbf{0})|^2\,, \qquad (9.7)$$

with the free annihilation cross section at leading order in the gauge coupling given by

$$(\sigma^{\mathrm{NR}}_{\mathrm{ann}}v_{\mathrm{rel}})^{[\mathbb{1}]}_{\mathrm{LO}} = \left(\frac{C_F}{2}+3Nn_f\right)\frac{\pi\alpha(2M)^2}{M^2}\,. \qquad (9.8)$$

The Sommerfeld factor for the color-singlet scattering-state wavefunction at leading order is

$$|\Psi^{[\mathbb{1}]}_{\boldsymbol{p}}(\mathbf{0})|^2 = \frac{2\pi C_F\zeta}{1-e^{-2\pi C_F\zeta}}\,, \qquad \zeta=\frac{\alpha(\mu_{\mathrm{s}})}{v_{\mathrm{rel}}}\,. \qquad (9.9)$$

Similarly, for the annihilation cross section of a pair in the adjoint representation we find

$$(\sigma^{\mathrm{NR}}_{\mathrm{ann}}v_{\mathrm{rel}})^{[\mathbf{adj}]}_{\mathrm{LO}}(\boldsymbol{p}) = (\sigma^{\mathrm{NR}}_{\mathrm{ann}}v_{\mathrm{rel}})^{[\mathbf{adj}]}_{\mathrm{LO}}\,|\Psi^{[\mathbf{adj}]}_{\boldsymbol{p}}(\mathbf{0})|^2\,, \qquad (9.10)$$

[1] The matching coefficients $\mathrm{Im}(\mathrm{f}_{[\mathbb{1}]}({}^3\mathrm{S}_1))$ reported in [100] and [102] agree for $N=3$, however they do not for $N\neq 3$, as the factor 1/54 in [100] reads $1/(18N)$ in [102]. Equation (9.4) is the one that can be found in [102].

[2] Contrarily to the SU(N) model considered in refs. [51, 52], the matching coefficient $\mathrm{Im}(\mathrm{f}_{[\mathbf{adj}]}({}^3\mathrm{S}_1))$ does not vanish at order α^2 because now the gauge bosons in (8.1) couple to the dark light fermions. At order α^3, the expression in (9.6) is the one reported in ref. [146], while the expression in ref. [102] is three times larger.

where

$$(\sigma^{\rm NR}_{\rm ann} v_{\rm rel})^{[\mathbf{adj}]}_{\rm LO} = \left(\frac{N^2-4}{8N} + \frac{n_f}{4}\right) \frac{\pi\alpha(2M)^2}{M^2}\,, \tag{9.11}$$

and we have averaged over the N^2-1 configurations of the incoming dark fermion-antifermion pair in the adjoint representation of SU(N). The Sommerfeld factor is[3]

$$|\Psi^{[\mathbf{adj}]}_{\boldsymbol{p}}(\mathbf{0})|^2 = \frac{\pi\zeta/N}{e^{\pi\zeta/N}-1}\,, \tag{9.12}$$

with ζ defined as in (9.9). The total Sommerfeld-corrected cross section reads

$$(\sigma^{\rm NR}_{\rm ann} v_{\rm rel})_{\rm LO}(\boldsymbol{p}) = \frac{(\sigma^{\rm NR}_{\rm ann} v_{\rm rel})^{[\mathbb{1}]}_{\rm LO}(\boldsymbol{p}) + (N^2-1)(\sigma^{\rm NR}_{\rm ann} v_{\rm rel})^{[\mathbf{adj}]}_{\rm LO}(\boldsymbol{p})}{N^2}\,, \tag{9.13}$$

whereas the free total annihilation cross section, at order α^2, is

$$\begin{aligned}(\sigma^{\rm NR}_{\rm ann} v_{\rm rel})_{\rm LO} &= \frac{(\sigma^{\rm NR}_{\rm ann} v_{\rm rel})^{[\mathbb{1}]}_{\rm LO} + (N^2-1)(\sigma^{\rm NR}_{\rm ann} v_{\rm rel})^{[\mathbf{adj}]}_{\rm LO}}{N^2} \\ &= \left[\frac{3n_f}{N} + \frac{C_F}{4N^2}(N^2-2+2Nn_f)\right]\frac{\pi\alpha(2M)^2}{M^2}\,. \end{aligned} \tag{9.14}$$

The Sommerfeld factor has a different impact on the cross sections. For the attractive singlet channel, the Sommerfeld factor (9.9) is larger than one and increases the cross section, whereas for the adjoint repulsive channel, the Sommerfeld factor (9.12) is smaller than one and consequently decreases the cross section. At $\mathcal{O}(\alpha^2)$ our results in eqs. (9.8) and (9.11) agree with those in ref. [147], once the cross sections in ref. [147] are expanded in $v_{\rm rel}$.

Bound states are sustained only by the SU(N)-singlet configuration. The annihilation width of a spin- and SU(N)-singlet pair in an nS wave reads at LO in $\mathrm{Im}(\mathrm{f}_{[\mathbb{1}]}(^1\mathrm{S}_0))$

$$\Gamma^{n\mathrm{S,para}}_{\rm ann,LO} = C_F^4 \frac{M\alpha(\mu_{\rm s})^3\alpha(2M)^2}{4n^3}\,, \tag{9.15}$$

where we distinguish between the coupling coming from the four-fermion matching coefficient, which is renormalized at the scale $2M$, and the coupling coming from the wavefunction, which is renormalized at a scale $\mu_{\rm s}$ of the order of the soft scale. The decay width (9.15) neither includes relativistic corrections to the bound-state wavefunction nor radiative corrections to the matching coefficients, where the former corrections, as we have remarked, may be as much important as or more important than the $\mathcal{O}(\alpha^3)$

[3]The expressions (9.9) and (9.12) for the Sommerfeld factors do not include relativistic corrections to the wavefunctions. It is important to realize that in a non-abelian theory these corrections may eventually turn out to be more important than considering corrections at next-to-leading order in α to the free annihilation cross section, as the first ones are governed by the coupling at the soft scale, whereas the latter ones are governed by the coupling at the hard scale $2M$.

corrections to the four-fermion matching coefficient.[4] At leading order, the decay width of a spin-triplet SU(N)-singlet pair in an nS wave reads

$$\Gamma_{\text{ann,LO}}^{n\text{S,ortho}} = \frac{Nn_f}{2n^3} C_F^3 M\alpha(\mu_\text{s})^3\alpha(2M)^2\,, \tag{9.16}$$

which vanishes for all nS bound states upon removing the dark light fermions from the model, i.e. $n_f = 0$. We considered such a theory without thermal light Dirac particles in refs. [51,52], and computed the annihilation cross sections of color-singlet and adjoint unbound pairs, as well as the para- and orthodarkonium decay widths up to next-to-leading order in the matching coefficients.

The results for the annihilation rates, that we obtained so far in this section, are valid in both the laboratory and in the center-of-mass frame of the annihilating pair, because we neglected the center-of-mass momentum-dependent dimension eight contact terms in (9.1) as well as in (9.2). Once we include them, we can compute the spin- and color-averaged annihilation cross section in the laboratory frame up to second order in the center-of-mass momentum of the annihilating pair, which is given by

$$\begin{aligned}(\sigma_\text{ann}^\text{NR}\, v_\text{Møl})_\text{lab}(\boldsymbol{p},\boldsymbol{P}) &= \frac{1}{N^2}\Big[(\sigma_\text{ann}^\text{NR} v_\text{rel}^{(0)})^{[\mathbb{1}]}\,\Big(|\Psi_{\boldsymbol{p}}^{[\mathbb{1}]}(\mathbf{0})|^2\Big)_\text{lab}(\boldsymbol{P}) \\ &\quad + (N^2-1)(\sigma_\text{ann}^\text{NR} v_\text{rel}^{(0)})^{[\mathbf{adj}]}\,\Big(|\Psi_{\boldsymbol{p}}^{[\mathbf{adj}]}(\mathbf{0})|^2\Big)_\text{lab}(\boldsymbol{P})\Big]\left(1-\frac{\boldsymbol{P}^2}{4M^2}\right) \\ &= (\sigma_\text{ann}^\text{NR}\, v_\text{Møl})_\text{cm}(\boldsymbol{p})\left(1-\frac{\boldsymbol{P}^2}{4M^2}\right),\end{aligned} \tag{9.17}$$

where we remind the reader that on the left hand side of eq. (9.17) the Møller velocity appears instead of the relative velocity. In the last line of (9.17) we have replaced the squared SU(N)-singlet and SU(N)-adjoint scattering wavefunctions at the origin in the laboratory frame with the ones in the center-of-mass frame using the Lorentz transformations derived in appendix A.2 in analogy to the abelian case. Eq. (9.17) holds also at higher order in the radiative corrections. Furthermore, the decay widths for para- and orthodarkonia in the laboratory frame can be inferred from the annihilation widths in the center-of-mass frame using the Lorentz contraction formula (5.34), which is independent of the underlying gauge symmetry, here U(1) or SU(N).

9.2 Dipole transitions in SU(N)$_\text{DM}$

In this section, we compute the formation and dissociation of bound states at leading order in the multipole expansion, i.e. in the dipole limit, where the vertices are depicted in fig. 4.1, but now augmented with appropriate color factors. In addition, there are two new vertices, the left and right one in fig. 8.1, that would need to be taken into

[4] A simple analytic expression, that approximates the NLO correction to the bound-state wavefunction, can be found in ref. [148]. In ref. [51], we provide an analytic result for the paradarkonium decay width up to order α^3 in the matching coefficients, with $n_f = 0$, and the wavefunction correction from [148].

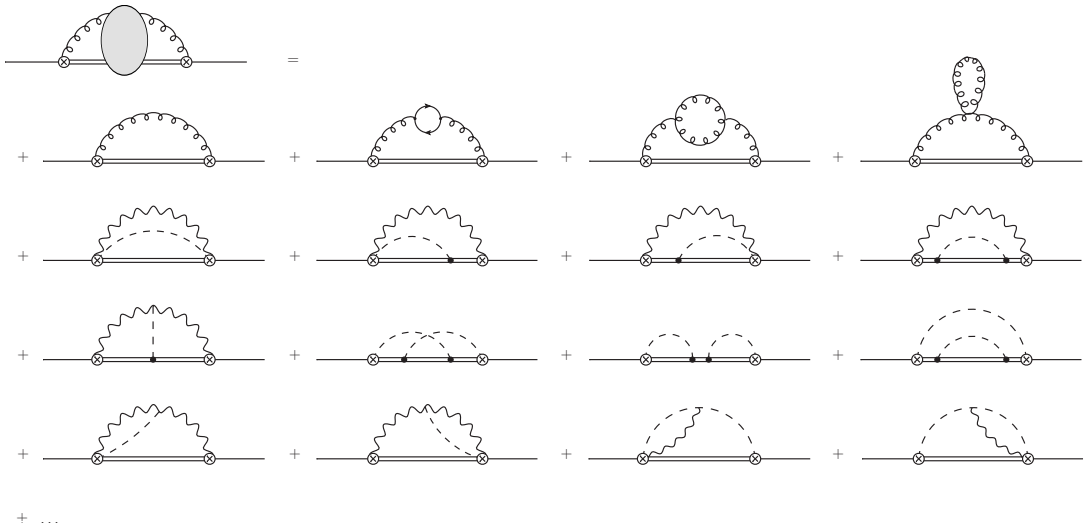

Figure 9.1: Self-energy diagram of the bound state at dipole order r^2 and at zeroth order in velocity expansion (left-hand side). In the weakly coupled SU(N) theory, it is expanded up to NLO in the coupling, where the first diagram in the second line is of order α and the rest of the depicted diagrams is of order α^2. The external solid lines represent the color-singlet bound state, the double solid lines the color-adjoint state. The wavy (dashed) lines denote transversal (longitudinal) gauge fields, whereas the curly lines the full (transverse + longitudinal) gauge field propagator.

account; the left vertex, however, is of higher order in the coupling. Similarly as in the abelian case, we first neglect the center-of-mass motion of the interacting heavy DM pair, and draw the diagrams at order r^2 and up to NLO in α. In figure 9.1, we show the sum of the self-energy diagrams of the bound state up to the desired accuracy, where its imaginary part comprises all kind of processes that lead to the dissociation of that heavy singlet bound pair into a color-adjoint unbound state. One can draw similar diagrams for the self-energy of the adjoint pair, whose imaginary part contains the reverse process, namely the formation of a singlet bound state.[5]

At leading order in perturbation theory, we have to compute only the first electric-dipole diagram in the second line in fig. 9.1. Switching the single solid with the double solid line and using the optical theorem as in the abelian case, we obtain for the cross section accounting for bound-state formation via on-shell gauge-field emission

$$(\sigma_{\rm bsf} v_{\rm rel})^{[\mathbf{adj}]}_{\rm LO}(\boldsymbol{p}) = \frac{2}{3N}\,\alpha(\mu_{\rm us}) \sum_{n,\ell,m} \left[1 + n_{\rm B}(\Delta E^p_n)\right] \left|\langle n\ell m|\boldsymbol{r}|\boldsymbol{p}\rangle^{[\mathbf{adj}]}\right|^2 (\Delta E^p_n)^3\,, \qquad (9.18)$$

where $|n\ell m\rangle$ is the eigenstate of the Hamiltonian H_s describing a bound state with quantum numbers n, ℓ and m, $|\boldsymbol{p}\rangle^{[\mathbf{adj}]}$ is the eigenstate of the Hamiltonian H_o labeled

[5]Hereby one just needs to switch the solid with the double solid lines, and keep in mind that the dashed lines cannot connect with the single solid lines representing the bound state.

by the relative momentum $\boldsymbol{p} = M\boldsymbol{v}_{\rm rel}/2$ of the unbound dark fermion-antifermion pair, and we have averaged over the N^2-1 configurations of the incoming dark fermion-antifermion pair in the adjoint representation of SU(N). Although the result is at LO in α, we have made explicit in eq. (9.18) that the natural renormalization scale of the electric-dipole coupling in such a process is a scale $\mu_{\rm us}$ of the order of the ultrasoft scale. The formation of a bound state out of an unbound singlet state by emission of a gauge boson is not possible in a non-abelian theory due to the SU(N) charge conservation, i.e. $(\sigma_{\rm bsf}v_{\rm rel})^{[\mathbb{1}]}(\boldsymbol{p}) = 0$. The total bound-state formation cross section $(\sigma_{\rm bsf}v_{\rm rel})(\boldsymbol{p}) = \sum\limits_n (\sigma^n_{\rm bsf}v_{\rm rel})(\boldsymbol{p})$, defined similarly to eq. (9.13), is then just $(N^2-1)/N^2$ times $(\sigma_{\rm bsf}v_{\rm rel})^{[\mathbf{adj}]}(\boldsymbol{p})$. It is the total bound-state formation cross section that can be found in the literature [21, 41].

For the reverse process, namely bound-state dissociation via absorption of an incoming thermal gauge field, the thermal dissociation width of a bound pair with quantum numbers $n = (n, \ell, m)$ is given by

$$\begin{aligned}\Gamma^{n,\rm LO}_{\rm bsd} &= 2(N^2-1)\int \frac{d^3p}{(2\pi)^3}\sigma^{n,\rm LO}_{\rm bsd}(\boldsymbol{p}) \\ &= 2(N^2-1)\int_{|\boldsymbol{k}|\geq|E^b_n|}\frac{d^3k}{(2\pi)^3}\,n_{\rm B}(|\boldsymbol{k}|)\,\sigma^{n,\rm LO}_{\rm ion}(\boldsymbol{k})\,,\end{aligned} \tag{9.19}$$

where $\sigma^{n,\rm LO}_{\rm bsd}(\boldsymbol{p})$ is the temperature-dependent dissociation cross section defined similarly as in eq. (6.78) for the abelian case, $E^b_n = -M(C_F\alpha)^2/(4n^2)$ is the binding energy and the in-vacuum ionization cross section is

$$\sigma^{n,\rm LO}_{\rm ion}(\boldsymbol{k}) = \frac{1}{3N}\,\alpha(\mu_{\rm us})\,\frac{M^{\frac{3}{2}}}{2}|\boldsymbol{k}|\sqrt{|\boldsymbol{k}|+E^b_n}\,\Big|\langle n\ell m|\boldsymbol{r}|\boldsymbol{p}\rangle^{[\mathbf{adj}]}\Big|^2\Big|_{|\boldsymbol{p}|=\sqrt{M(|\boldsymbol{k}|+E^b_n)}}. \tag{9.20}$$

In the ionization cross section we have averaged over the N^2-1 degrees of freedom of the incoming dark gauge field.

As for the abelian model, the remaining computational effort is in the electric dipole matrix element, where we can take the general analytic result in the center-of-mass frame given in appendix C.2. For the particular case of the ground state, the electric dipole matrix element is given in (C.42), which we insert into (9.18) and (9.19) to compute the formation of the ground state and its dissociation into an unbound SU(N) adjoint pair.

The total bsf cross section for the ground state, at leading order in the electric dipole coupling $\alpha(\mu_{\rm us})$, is

$$\begin{aligned}(\sigma^{\rm 1S}_{\rm bsf}v_{\rm rel})^{\rm LO}(\boldsymbol{p}) &= \frac{4C_F}{3N^2}\,\alpha(\mu_{\rm us})\,[1+n_{\rm B}(\Delta E^p_1)]\,\Big|\langle 1{\rm S}|\boldsymbol{r}|\boldsymbol{p}\rangle^{[\mathbf{adj}]}\Big|^2\,(\Delta E^p_1)^3 \\ &= \alpha(\mu_{\rm us})\frac{2^7\pi^2\alpha^6}{3\,M^2\,v^5_{\rm rel}}\frac{C_F^4}{N^3}\,(2C_F+N)^2\,\frac{1+\left(\frac{\alpha}{2Nv_{\rm rel}}\right)^2}{\left[1+\left(\frac{C_F\alpha}{v_{\rm rel}}\right)^2\right]^3}\,\frac{e^{\frac{2\alpha}{Nv_{\rm rel}}\,{\rm arccot}\frac{C_F\alpha}{v_{\rm rel}}}}{e^{\frac{\pi}{N}\frac{\alpha}{v_{\rm rel}}}-1}\,[1+n_{\rm B}(\Delta E^p_1)]\,,\end{aligned} \tag{9.21}$$

with $p = Mv_{\rm rel}/2$ the incoming relative momentum of the adjoint pair, and

$$\Delta E_1^p = \frac{Mv_{\rm rel}^2}{4}\left[1+\left(\frac{C_F\alpha}{v_{\rm rel}}\right)^2\right]. \tag{9.22}$$

Our result agrees with the outcome of ref. [21].[6]

Like in the abelian case, we thermally average the bsf cross section over the incoming momenta of the adjoint pair following the Maxwell–Boltzmann distribution (B.15). In the left panel of figure 9.2, we plot the thermally averaged leading-order annihilation and bsf cross section for the particular case of $N = 2$ (i.e. dark SU(2) gauge theory), normalized by the thermally averaged free annihilation cross section at LO of an unbound pair, cf. equation (9.14), as a function of M/T. We show the behaviour of the cross sections with running coupling at one loop with one massless dark fermion (dashed lines) and two massless fermions (solid lines). The benchmark value $\alpha(2M) = 0.03$ is taken at the hard scale, and it runs down to the smaller soft and ultrasoft scales, where one finds $\alpha(2M) < \alpha(\mu_{\rm s}) < \alpha(\mu_{\rm us})$ for typical non-relativistic velocities. We take $\mu_{\rm s} = Mv_{\rm rel}/2$ and $\mu_{\rm us} = Mv_{\rm rel}^2/4$. We plot the annihilation of the singlet pair (orange lines), adjoint pair (red lines) and the total annihilation cross section (brown lines). Comparing with the abelian case in figure 6.2 left, we see that the annihilation processes for the pair in a color singlet show a similar behaviour, namely a Sommerfeld enhancement that increases for smaller temperatures. However, the contribution for the adjoint pair annihilations is suppressed by a Sommerfeld factor smaller than unity. This is due to the repulsive potential experienced by the adjoint pair, which becomes more relevant for smaller T, and thus lower velocities. The Sommerfeld effect, however, leads to an overall increase of the total annihilation cross section (brown lines). The effect of a repulsive potential appears also clearly in the bsf process (black lines). At variance with the abelian case, the rising of the bsf cross section is saturated by the repulsive potential at small temperatures, and the bsf process becomes progressively less likely. This is signaled by the fact that for small $v_{\rm rel}$, whereas the right-hand side of eq. (6.11) goes like $1/v_{\rm rel}$, the right-hand side of eq. (9.21) is exponentially suppressed. The running coupling with $n_f = 2$ light fermions decreases the bsf cross section by a factor two with respect to a running with only one light fermion for the full range of M/T shown in the plot. Instead for annihilations there is almost no effect of whether α is running with only one or two fermions, because the dependence of α on n_f becomes more significant only at lower energies than the soft scale, at which the Sommerfeld factors (9.9) and (9.12) are evaluated. We obtain similar results for SU(N) with $N > 2$.

The dissociation width of an SU(N)-singlet ground state into an unbound adjoint state is

$$\Gamma_{\rm bsd}^{\rm 1S,LO} = 2(N^2-1)\int_{|\boldsymbol{k}|\geq|E_1^b|}\frac{d^3k}{(2\pi)^3}\,n_{\rm B}(|\boldsymbol{k}|)\,\sigma_{\rm ion}^{\rm 1S,LO}(|\boldsymbol{k}|)\,, \tag{9.23}$$

[6] In ref. [21], the authors distinguish between the coupling coming from the bound-state wavefunction, renormalized at a soft scale of order $M\alpha$, and the coupling coming from the scattering-state wavefunction, renormalized at a soft scale of order $Mv_{\rm rel}$. In this work, however, we do not make a distinction between these two soft scales at the level of the running of α, but we keep track of the ultrasoft scale in the electric dipole coupling.

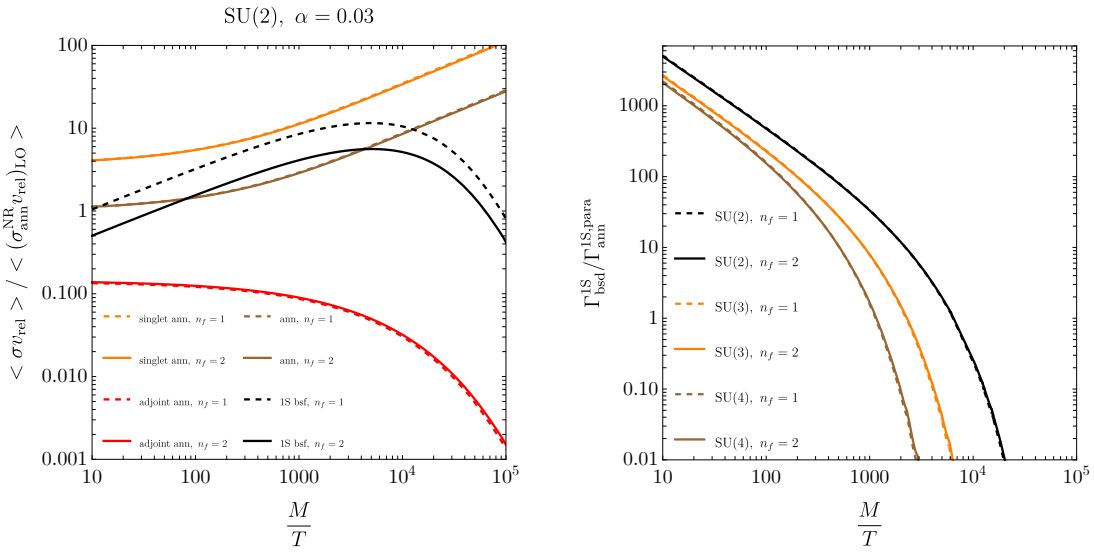

Figure 9.2: (Left) Ratios of the thermally averaged cross sections at leading order over the free LO annihilation cross section (9.14) in the dark non-abelian model SU(2). The orange (red) lines denote the ratio for the color-singlet (-adjoint) annihilation, the brown lines for the total annihilation and the black lines for the 1S bsf. (Right) Thermal dissociation widths over the 1S paradarkonium decay width at LO in the dark SU(2) (black lines), SU(3) (orange lines) and SU(4) (brown lines) theory. Solid lines depict the ratios for running coupling α, starting from $\alpha(2M) = 0.03$, with $n_f = 2$; dashed lines for $n_f = 1$.

where the ionization cross section, averaged over the incoming SU(N) gauge fields, is

$$\sigma^{\rm 1S,LO}_{\rm ion}(|\boldsymbol{k}|) = \alpha(\mu_{\rm us}) \frac{2^3\pi^2}{3} \frac{|E_1^b|^4}{M|\boldsymbol{k}|^5} \frac{(2C_F+N)^2}{N^4 C_F^5} \left[1 + (2NC_F w_1(|\boldsymbol{k}|))^2\right] \frac{e^{\frac{2\arctan(w_1(|\boldsymbol{k}|))}{NC_F w_1(|\boldsymbol{k}|)}}}{e^{\frac{\pi}{NC_F w_1(|\boldsymbol{k}|)}} - 1}\,, \tag{9.24}$$

with $w_1(|\boldsymbol{k}|) \equiv \sqrt{|\boldsymbol{k}|/|E_1^b| - 1}$. The expression is in agreement with the result of ref. [50]. The right panel of figure 9.2 shows the behaviour of the dissociation width, normalized to the paradarkonium decay width at LO for the ground state, $\Gamma^{\rm 1S,para}_{\rm ann} = C_F^4 M\alpha(\mu_{\rm s})^3\alpha(2M)^2/4$ with $\mu_{\rm s} = M\alpha/2$ and $\mu_{\rm us} = M\alpha^2/4$, as a function of M/T for different non-abelian models. Compared to the temperature-independent decay width, the thermal bsd width falls off exponentially with decreasing T due to the dependence on the Bose–Einstein distribution in eq. (9.23). Contrarily to the bsf cross section, varying the flavor number n_f has a negligible impact on the bsd width.

At next-to-leading order in the electric dipole coupling, we would need to compute the self-energy diagrams at two loops, which corresponds to calculating all the subsequent diagrams in figure 9.1. We do not show the derivation in this work, but refer the reader to the ref. [149], where the authors computed all diagrams contributing to the non-abelian electric-electric correlator up to NLO in the real-time formalism. In the abelian

model only one diagram shows up at next-to-leading order, corresponding to the second diagram on the right-hand side in fig. 6.1, whose imaginary part captures the on-shell dark photon emission, the bath-particle scattering and the one-to-three off-shell decay process that has been extensively scrutinized in the sections 6.1.1.1 and 6.1.1.2. In SU(N), this diagram, which matches with the second diagram in the second row in fig. 9.1, gets augmented by the other two diagrams on the right. Hence from now on, by a *bath particle* we understand the n_f light fermions together with the dark gauge fields that can self-interact. In this work, we disregard the diagrams depicted in the third, fourth and fifth row in fig. 9.1. We compute the imaginary part of the diagrams in the second row with single solid and double solid lines interchanged, following closely the computational steps done for the abelian case in sec. 6.1.1.1. Then from the optical theorem we obtain for the total bound-state formation cross section

$$
\begin{aligned}
&(\sigma_{\rm bsf}\, v_{\rm rel})^{\rm LO+NLO^*}(\boldsymbol{p}) = \frac{N^2-1}{N^2}\sum_n (\sigma^n_{\rm bsf} v_{\rm rel})^{[\mathbf{adj}]}_{\rm LO+NLO^*}(\boldsymbol{p}) \\
&= \sum_n (\sigma^n_{\rm bsf}\, v_{\rm rel})^{\rm LO}(\boldsymbol{p}) \Bigg\{ 1 - \frac{\beta_0}{4\pi}\alpha(\mu_{\rm us}) \log\left(\frac{4(\Delta E^p_n)^2}{\mu^2_{\rm us}}\right) + \frac{\alpha(\mu_{\rm us})}{\pi}\left[\left(\frac{149}{36}+\frac{\pi^2}{3}\right)N - \frac{5}{9}n_f\right] \\
&\qquad + \frac{\alpha(\mu_{\rm us})}{\pi}\left[n_f \mathcal{X}^f_{\rm th}\left(\frac{\Delta E^p_n}{T}\right) + N\mathcal{X}^b_{\rm th}\left(\frac{\Delta E^p_n}{T}\right)\right]\Bigg\}, \qquad (9.25)
\end{aligned}
$$

where the α-suppressed terms in the second line survive at $T=0$, and the terms in the third line correspond the thermal contributions. The function $\mathcal{X}^f_{\rm th}$, that stems from the massless thermal fermions in the loop, equals the $\mathcal{X}_{\rm th}$-function derived in the abelian case, cf. eq. (6.25). The term $\mathcal{X}^b_{\rm th}$, that does not appear in the dark U(1) model, originates from the contributions of the gauge bosons in the loop, i.e. the last two diagrams in the first line in fig. 9.1, with single solid and double solid lines exchanged. It can be written, similarly as $\mathcal{X}^f_{\rm th}$, as an integral over a dimensionless variable $t \equiv |\boldsymbol{k}|/T$, and reads

$$
\mathcal{X}^b_{\rm th}(x) = \frac{2}{x^3}\int_0^\infty \frac{dt}{e^t-1}\left[(t^2+x^2)\log\left|\frac{t+x}{t-x}\right| + tx\log\left|\frac{t^2-x^2}{x^2}\right| - 2xt\right]. \qquad (9.26)
$$

By the subscript NLO* we recall that the result in (9.25) does not contain the complete next-to-leading order corrections in α, since the two-loop diagrams in the third to fifth row in fig. 9.1 have been discarded. Hence, the index NLO* means that we consider only a subset of the NLO self-energy diagrams, which encapsulates the Landau damping phenomenon and the on-shell gauge field emission process.

The bound-state dissociation width at NLO* can be computed in a very similar way, and the result is

$$
\begin{aligned}
&\Gamma^{n,\rm LO+NLO^*}_{\rm bsd} = 2(N^2-1)\int \frac{d^3p}{(2\pi)^3}\sigma^{n,\rm LO}_{\rm bsd}(\boldsymbol{p})\Bigg\{1 - \frac{\beta_0}{4\pi}\alpha(\mu_{\rm us})\log\left(\frac{4(\Delta E^p_n)^2}{\mu^2_{\rm us}}\right) \\
&+\frac{\alpha(\mu_{\rm us})}{\pi}\left[\left(\frac{149}{36}+\frac{\pi^2}{3}\right)N - \frac{5}{9}n_f\right] + \frac{\alpha(\mu_{\rm us})}{\pi}\left[n_f\mathcal{X}^f_{\rm th}\left(\frac{\Delta E^p_n}{T}\right) + N\mathcal{X}^b_{\rm th}\left(\frac{\Delta E^p_n}{T}\right)\right]\Bigg\}. \qquad (9.27)
\end{aligned}
$$

Like in the abelian theory, we observe that the higher-order terms in eqs. (9.25) and (9.27) remain suppressed for the particular hierarchy of energy scales given in eq. (8.5), where $T \lesssim M\alpha^2$. However, despite the fact that the vacuum correction term is always suppressed by a factor of α irrespective of the value of the temperature, the thermal corrections increase with increasing T, and as soon as the scale hierarchy (8.6) is realized, perturbation theory breaks down signaling that the thermal parts of the diagrams in the second row of fig. 9.1 need to be resummed, as it was done in the U(1) model. The contribution from the scale T to the self-energy of the heavy pair can be inferred from refs. [129, 130, 150]. Hence, the imaginary part of the heavy-pair self-energy reads

$$\mathrm{Im}\left[\Sigma^{11}_{(T)}\right] = C_F\frac{\alpha}{6}\boldsymbol{r}^2 T m_{\mathrm{D}}^2\left[\frac{1}{\epsilon}+\gamma_{\mathrm{E}}+\frac{2}{3}-2\frac{\zeta'(2)}{\zeta(2)}-\log\left(\frac{(4T)^2}{\pi\mu^2}\right)+\frac{2N\log 2}{N+T_F n_f}\right], \quad (9.28)$$

which shares the same infrared divergence with the abelian analogue in (6.30). Eq. (9.28) contains a constant, given by the last term in the square bracket, that appears only in non-abelian theories and is zero in the U(1) model. In order to get the contributions from the scales $m_{\mathrm{D}} \sim \Delta E$, we follow closely the analysis done in section 6.1.1.2 for the abelian case, and obtain

$$\begin{aligned}\mathrm{Im}\left[\Sigma^{11}_{(m_{\mathrm{D}}\sim\Delta E)}(\Delta E)\right] &= -C_F\frac{\alpha}{6}T m_{\mathrm{D}}^2 r^i \\ &\times\left[\frac{1}{\epsilon}-\gamma_{\mathrm{E}}+\frac{8}{3}-\log\left(\frac{(\Delta E)^2}{\pi\mu^2}\right)+2\mathcal{Y}^{\mathrm{long}}_{\mathrm{th}}\left(\frac{\Delta E}{m_{\mathrm{D}}}\right)+2\mathcal{Y}^{\mathrm{trans}}_{\mathrm{th}}\left(\frac{\Delta E}{m_{\mathrm{D}}}\right)\right] r^i\,, \quad (9.29)\end{aligned}$$

where the closed expressions for the dimensionless functions $\mathcal{Y}^{\mathrm{long}}_{\mathrm{th}}$ and $\mathcal{Y}^{\mathrm{trans}}_{\mathrm{th}}$ can be taken from eqs. (6.38) and (6.45), respectively. Eq. (9.30) is ultraviolet divergence. It cancels the IR divergence in (9.28) once we sum up the results (9.28) and (9.30), i.e.

$$\begin{aligned}&\mathrm{Im}\left[\Sigma^{11}(\Delta E)\right] = C_F\frac{\alpha}{3}T m_{\mathrm{D}}^2 r^i \\ &\times\left[\gamma_{\mathrm{E}}-1-\frac{\zeta'(2)}{\zeta(2)}+\log\left(\frac{\Delta E}{4T}\right)+\frac{N\log 2}{N+T_F n_f}-\mathcal{Y}^{\mathrm{long}}_{\mathrm{th}}\left(\frac{\Delta E}{m_{\mathrm{D}}}\right)-\mathcal{Y}^{\mathrm{trans}}_{\mathrm{th}}\left(\frac{\Delta E}{m_{\mathrm{D}}}\right)\right] r^i\,. \quad (9.30)\end{aligned}$$

The Debye mass, that enters in (9.30), is not the same as the one in the abelian model, cf. eq. (D.39). Because of the gauge boson self-interactions, in SU(N) now reads

$$m_{\mathrm{D}} = \sqrt{\frac{4\pi}{3}(N+T_F n_f)\alpha}\; T\,. \quad (9.31)$$

For the hierarchy given in (8.6), employing the optical theorem we eventually extract the Debye-mass resummed bound-state formation cross section

$$\begin{aligned}(\sigma_{\mathrm{bsf}}\, v_{\mathrm{rel}})_{\mathrm{resum.}}(\boldsymbol{p}) &= \sum_n (\sigma^n_{\mathrm{bsf}}\, v_{\mathrm{rel}})^{\mathrm{LO}}(\boldsymbol{p})\Big|_{T\gg\Delta E^p_n} \\ &\times\left\{-\frac{\beta_0}{4\pi}\alpha(\mu_{\mathrm{us}})\log\left(\frac{4(\Delta E^p_n)^2}{\mu^2_{\mathrm{us}}}\right)+\frac{\alpha(\mu_{\mathrm{us}})}{\pi}\left[\left(\frac{149}{36}+\frac{\pi^2}{3}\right)N-\frac{5}{9}n_f\right]\right. \\ &\left.+\frac{1}{2}\left(\frac{m_{\mathrm{D}}}{\Delta E^p_n}\right)^2\left[1-\gamma_{\mathrm{E}}+\frac{\zeta'(2)}{\zeta(2)}-\log\left(\frac{\Delta E^p_n}{4T}\right)+\mathcal{Y}^{\mathrm{long}}_{\mathrm{th}}\left(\frac{\Delta E^p_n}{m_{\mathrm{D}}}\right)+\mathcal{Y}^{\mathrm{trans}}_{\mathrm{th}}\left(\frac{\Delta E^p_n}{m_{\mathrm{D}}}\right)\right]\right\}, \quad (9.32)\end{aligned}$$

and the Debye-mass resummed bound-state dissociation width

$$
\begin{aligned}
(\Gamma^n_{\rm bsd})_{\rm resum.} &= 2(N^2-1)\int \frac{d^3p}{(2\pi)^3}\sigma^{n,\rm LO}_{\rm bsd}(\boldsymbol{p})\Big|_{T\gg\Delta E^p_n} \\
&\times\Bigg\{-\frac{\beta_0}{4\pi}\alpha(\mu_{\rm us})\log\left(\frac{4(\Delta E^p_n)^2}{\mu^2_{\rm us}}\right)+\frac{\alpha(\mu_{\rm us})}{\pi}\left[\left(\frac{149}{36}+\frac{\pi^2}{3}\right)N-\frac{5}{9}n_f\right] \\
&\quad+\frac{1}{2}\left(\frac{m_{\rm D}}{\Delta E^p_n}\right)^2\left[1-\gamma_{\rm E}+\frac{\zeta'(2)}{\zeta(2)}-\log\left(\frac{\Delta E^p_n}{4T}\right)+\mathcal{Y}^{\rm long}_{\rm th}\left(\frac{\Delta E^p_n}{m_{\rm D}}\right)+\mathcal{Y}^{\rm trans}_{\rm th}\left(\frac{\Delta E^p_n}{m_{\rm D}}\right)\right]\Bigg\},
\end{aligned}
\tag{9.33}
$$

where the thermal factors $[1+n_{\rm B}(\Delta E^p_n)]$ and $n_{\rm B}(\Delta E^p_n)$, that enter in the expressions $(\sigma^n_{\rm bsf}\,v_{\rm rel})_{\rm LO}(\boldsymbol{p})\big|_{T\gg\Delta E^p_n}$ and $\sigma^{n,\rm LO}_{\rm bsd}(\boldsymbol{p})\big|_{T\gg\Delta E^p_n}$, respectively, are approximated to leading order in $(\Delta E^p_n)/T$, which is $T/(\Delta E^p_n)$ in both cases.

We neglect the suppressed T-independent corrections, do the dimensionless integrations in $\mathcal{X}^f_{\rm th}$, $\mathcal{X}^b_{\rm th}$, $\mathcal{Y}^{\rm long}_{\rm th}$ and $\mathcal{Y}^{\rm trans}_{\rm th}$ numerically, and plot the total 1S bound-state formation cross sections for the exemplary SU(2) model, thermally averaged according to (B.15), at LO (dashed lines), up to NLO* (dotted lines) and with Debye-mass resummation (solid lines) in the left panel of figure 9.3. The observables are normalized by the free annihilation cross section at leading order, cf. eq. (9.14). Orange lines are for the particular case of one massless dark fermion in the model, black lines for two massless fermions. The coupling runs at one loop, with $\alpha(2M)=0.03$. On the right panel we show the results for the dissociation widths of the ground state, normalized by the 1S paradarkonium decay width at LO in eq. (9.15), with the same line properties and colors as in the left panel. The rates share the same behaviour as the ones in the abelian theory, cf. figures 6.3 and 6.6: At low temperatures of the order of the ultrasoft energy scale, the lines approach each other, because the bath-particle scatterings become insignificant compared to the on-shell thermal gauge-boson dissociation/absorption processes. The bsf cross sections decrease due to the repulsive potential taking its effect at low particle momenta. The bsd widths fall off due to the exponential decrease of the Bose–Einstein distribution for $T\ll\Delta E^p_n$. At earlier times close to the freeze-out, however, the bath-particle scatterings become the dominating process, which increases both the bsf cross section and bsd width by several orders of magnitude compared to the processes induced via on-shell light-like gauge boson emissions or absorptions. As in U(1)$_{\rm DM}$, if we treat the Landau screening processes only up to fixed NLO* instead of resumming them properly, we notably overestimate the rates. Moreover, including more massless dark fermions to the model leads to a decrease in the ratios of the observables depicted in fig. 9.3 over the full temperature range down to $10^{-5}M$, in our case going from one to two fermion species corresponds to a reduction by a factor between 1.5 and 2. We obtain very similar results in the non-abelian gauge models SU(3)$_{\rm DM}$, which resembles the QCD subgroup of the Standard Model in the weakly-coupled regime at sufficiently large temperatures $T\lesssim 500$ MeV of the QGP, and SU(4)$_{\rm DM}$.

We remind the reader, that we did not consider the two-loop diagrams in the third to fifth row in fig. 9.1, which seem to have a particularly different structurial form compared to the diagrams in the first row due to the additional vertex interactions

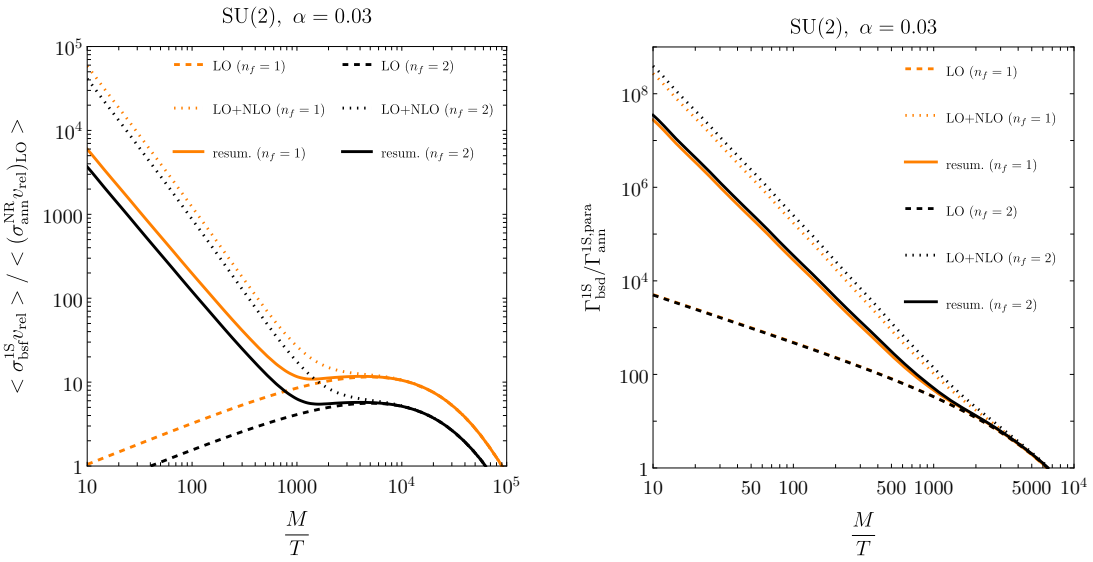

Figure 9.3: (Left) Thermally averaged total bound-state formation cross sections for the 1S state at LO (dashed lines, cf. (9.21)), up to NLO≡NLO* (dotted lines, cf. (9.25)) and with Debye mass resummation (solid lines, cf. (9.32)), plotted over M/T for $n_f = 1$ (orange lines) and $n_f = 2$ (black lines) and running coupling with starting value $\alpha \equiv \alpha(2M) = 0.03$; normalized by the free LO annihilation cross section (9.14). (Right) 1S bound-state dissociation widths, normalized by the leading-order 1S paradarkonium decay width (9.15). Both panels depict the rates for the particular SU(2) theory.

shown in figure 8.1. Despite the fact that the computation of the remaining diagrams has been completed in ref. [149] and thus we could in principle add the contributions to the thermal rates in eqs. (9.25) and (9.27) and in this way write down the results up to full next-to-leading order, we did not study so far if any of these terms may become large for large T in a similar way as the three two-loop diagrams in the second row in fig. 9.1. Hence, it remains to check if any of these diagrams needs to be resummed as well, and if it shares any similarities with the familiar physical understanding behind the Debye mass resummation.

We have neglected the non-relativistic motion of the center of mass of the heavy pair so far. We would like to study quantitatively impact of the leading recoil corrections on the bsf cross section (9.21) and bsd width (9.23) for the ground state. At leading order in perturbation theory, the total bound-state formation cross section in the laboratory frame from dark heavy fermion-antifermion pairs charged under an SU(N) gauge group is given up to relative order $\boldsymbol{P}^2/M^2 \sim T/M$ and $\Delta E^p_n/M$ by

$$(\sigma_{\text{bsf}}\, v_{\text{Møl}})^{\text{LO}}_{\text{lab}}(\boldsymbol{p}, \boldsymbol{P}) = \frac{4C_F}{3N^2}\,\alpha(\mu_{\text{us}}) \sum_n (\Delta E^p_n)^3\,(1 + n_{\text{B}}(\Delta E^p_n)) \times \left(\left| \langle n|\boldsymbol{r}|\boldsymbol{p}\rangle^{[\mathbf{adj}]}_{\text{lab}} \right|^2 F^n_1(p,P) + \left| \langle n|\boldsymbol{r}\cdot\frac{\boldsymbol{P}}{2M}|\boldsymbol{p}\rangle^{[\mathbf{adj}]}_{\text{lab}} \right|^2 F^n_2(p,P) \right). \quad (9.34)$$

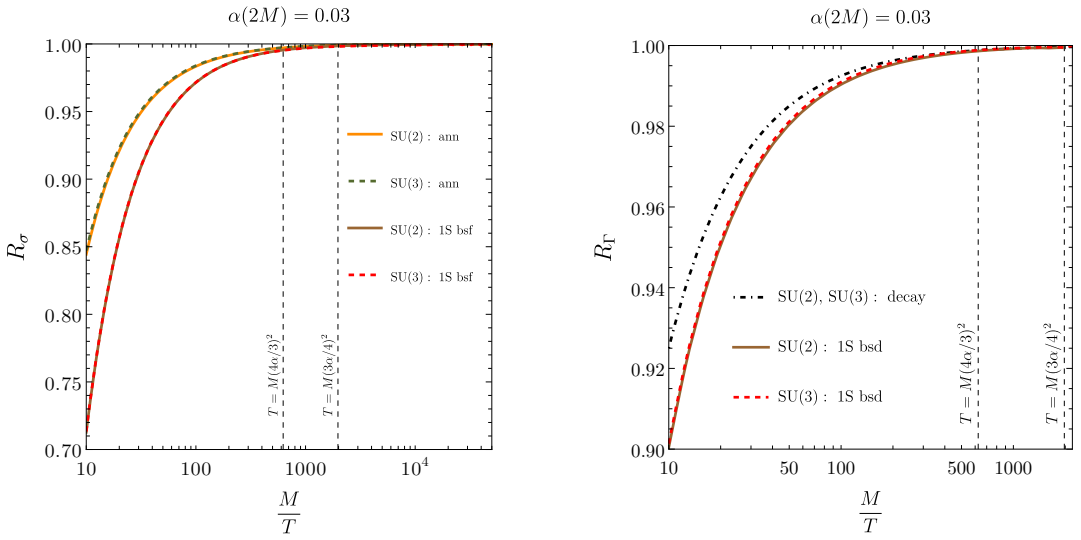

Figure 9.4: (Left) Ratios of thermally averaged cross sections in the laboratory frame with recoil corrections and the corresponding thermally averaged cross sections without recoil corrections plotted as a function of M/T for the non-abelian model (8.1). The orange solid and green dashed lines denote the ratios when taking the thermal average of (9.13) in SU(2) and SU(3), respectively, the brown solid and red dashed lines when taking the thermal average of (9.34) for the 1S state in SU(2) and SU(3), respectively. (Right) Ratios of thermally averaged widths in the laboratory frame with recoil corrections and the corresponding thermally averaged widths without recoil corrections plotted as a function of M/T for the non-abelian model (8.1). The black dash-dotted line is for the para- and orthodarkonium decay width, which is valid in any SU(N) model, the brown solid and red dashed lines are for taking the thermal average of (9.35) for the 1S state in SU(2) and SU(3), respectively. The coupling runs at one loop, starting from $\alpha(2M) = 0.03$. The vertical lines mark the positions where $T = M(C_F\alpha)^2$.

The functions $F_1^n(p,P)$ and $F_2^n(p,P)$ are defined in (6.63) and (6.64), respectively.

Similarly, the thermal bound-state dissociation width in the laboratory frame is given up to relative order $\boldsymbol{P}^2/M^2 \sim T/M$ and $\Delta E_n^p/M$ by

$$(\Gamma_{\rm bsd}^n)_{\rm lab}^{\rm LO}(\boldsymbol{P}) = \frac{4}{3} C_F \alpha(\mu_{\rm us}) \int \frac{d^3p}{(2\pi)^3} \, (\Delta E_n^p)^3 \, n_{\rm B}(\Delta E_n^p) \times \left(\left| \langle n | \boldsymbol{r} | \boldsymbol{p} \rangle_{\rm lab}^{[\mathbf{adj}]} \right|^2 D_1^n(p,P) + \left| \langle n | \boldsymbol{r} \cdot \frac{\boldsymbol{P}}{2M} | \boldsymbol{p} \rangle_{\rm lab}^{[\mathbf{adj}]} \right|^2 D_2^n(p,P) \right). \quad (9.35)$$

The functions $D_1^n(p,P)$, $D_2^n(p,P)$ are defined in (6.95) and (6.96), respectively. Now in order to quantify the effect of the recoil corrections on the annihilation cross section and bound-state formation cross section as well as on the decay width and bound-state dissociation width, we follow the same procedure as in the abelian case and divide those observables obtained in the laboratory frame with c.m. momentum dependence

(thermally averaged according to (B.1) or (B.9)), for instance (9.17) or (9.34), by the corresponding ones that have been obtained at leading order in the coupling without center-of-mass motion (thermally averaged according to (B.15)), e.g. (9.13) or (9.21). As for the cross sections, we show the ratios in the left panel of figure 9.4, and the ratios for the bound-state annihilation and dissociation width in the right panel of figure 9.4. The coupling is taken to be $\alpha = 0.03$ at the hard scale $2M$ and runs down to the lower energy scales at one loop, and we choose $n_f = 1$. We observe that the size of the recoil corrections does not change much from SU(2) to SU(3). At high temperatures, the relative effect of the recoil corrections is largest for the bound-state formation cross section. Nevertheless, we observe that the radiative corrections, generating the Landau damping effect at large T, have a much bigger impact on each of the thermal dipole rates than the center-of-mass recoil corrections.

We have completed the study of the color-singlet bound-state to color-adjoint transitions at the dipole order in $\mathrm{SU}(N)_{\mathrm{DM}}$. As for color-adjoint to color-adjoint as well as color-singlet scattering-state to color-adjoint transitions, that generate the continuum dipole processes such as thermal emissions and absorptions, the corresponding cross sections resemble those written in (6.108)–(6.111) in the abelian model. The only differences lie in the different color prefactors and in the different quantum-mechanical dipole matrix elements, where the analytic expressions are collected in appendix C.

Chapter 10

Bound-state effects on the dark matter relic density

In the following, we aim to solve the coupled Boltzmann equations for the dark SU(N) theory. Differently from the abelian case, the number density of scattering states comprises now the unbound pairs in both the SU(N) singlet and adjoint configurations. We consider the simple case where we include the ground state only. The coupled equations can be traded with a single effective Boltzmann equation in the form of eq. (7.4) for unbound pairs. Since bound-state to bound-state transitions are zero in the SU(N) models under study, the thermally averaged effective cross section (7.5) does not get modified by them. We work in the laboratory frame, where the thermal medium is at rest, but do not account for the thermal motion of the center of mass of the heavy pairs, because we checked that, as in the abelian case, the corrections on the dark matter relic density due to the recoil are small, i.e. at the level of a few percent. At variance with the relic-density study in ref. [51],[1] we consider annihilations and decays at order α^2 in the coupling. We use for the annihilation cross section the thermal average of eq. (9.13) and for the bsf cross section the thermal average of eq. (9.21) if we stay at LO, eq. (9.25) if we work up to NLO* or eq. (9.32) if we do the resummation of the Debye mass scale $m_{\rm D}$. We do it likewise for the dissociation widths at LO, cf. (9.23), up to NLO*, cf. (9.27), or with resummed $m_{\rm D}$-scale, cf. (9.33).[2] For the annihilation widths we take eqs. (9.15) and (9.16). We recall that the widths do not depend on any momentum, and therefore they do not need to be thermally averaged.

In figure 10.1, we plot the thermally averaged, Debye-mass resummed effective cross section normalized to (9.14) for the SU(2) (black solid line), SU(3) (orange solid line)

[1] In ref. [51], we did not add light dark fermions to the model, but instead we analyzed the contribution from the spin-triplet annihilation channel on the DM relic abundance by considering the annihilation matching coefficients at $\mathcal{O}(\alpha^3)$, such that the orthodarkonia can still annihilate, although with an α-suppressed rate compared to the spin-singlet bound states.

[2] In the special case of $N = 3$, eq. (9.33) can be associated with the dissociation width for heavy quarkonium in pNRQCD, and in each of the two limits $m_{\rm D} \gg \Delta E$ and $\Delta E \gg m_{\rm D}$ it agrees with the analytic expressions for the inelastic-parton scattering processes obtained in refs. [129,150]. On the other hand, eq. (9.23) matches with the gluo-dissociation width in ref. [151].

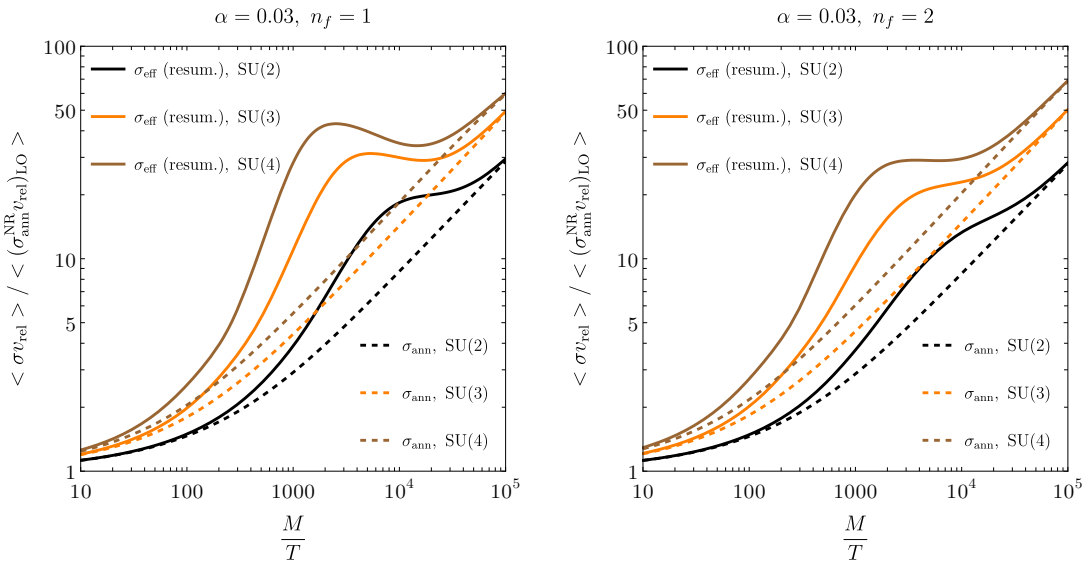

Figure 10.1: Thermally averaged effective cross sections over (9.14) in the SU(2), SU(3) and SU(4) theory (black, orange and brown solid lines, respectively). The coupling, with $\alpha \equiv \alpha(2M) = 0.03$, runs at one loop. Dashed lines represent the Sommerfeld-enhanced annihilations in the three gauge models. The left panel is for $n_f = 1$, the right panel for $n_f = 2$ massless fermions.

and SU(4) (brown solid line) theory. Dashed lines correspond to the thermally averaged, Sommerfeld-enhanced annihilation cross section (9.13) divided by (9.14). The coupling runs at one loop, with $\alpha(2M) = 0.03$. The left panel shows the ratios for $n_f = 1$, the right panel for $n_f = 2$. The bell shape originates from the bound-state formation and decay contribution, $\langle \sigma^{\rm 1S}_{\rm bsf} v_{\rm rel} \rangle \, \Gamma^{\rm 1S}_{\rm ann} / (\Gamma^{\rm 1S}_{\rm ann} + \Gamma^{\rm 1S}_{\rm bsd})$, being dominant with respect to the annihilation term, $\langle \sigma_{\rm ann} v_{\rm rel} \rangle$, for some N-dependent temperature regions. The solid lines approach the dashed lines in the low-T limit, because of the repulsive interaction between the color-charged heavy DM fermion and antifermion that starts to dominate at very small velocities, hence avoiding the heavy pair to form a bound state. Note that the curves for $n_f = 1$ (left panel) are above the curves for $n_f = 2$ (right panel) in the temperature region around the bell shape, i.e. increasing the number of light fermions in the model decreases the ratio of the thermally averaged effective cross section over the free annihilation cross section. The decrease in $\langle \sigma_{\rm eff} v_{\rm rel} \rangle / \langle \sigma_{\rm ann} v_{\rm rel} \rangle$ is, however, significantly smaller than for the individual bsf and bsd rates, cf. the orange and black lines in the left and right plots in fig. 9.3. We do not show the plots for the effective cross section at leading order or up to NLO*, because they barely deviate from the Debye-mass resummed curves in fig. 10.1. We checked that, like in the abelian case, the correction on the dark matter relic density coming from the Landau damping processes indeed turns out to be only of order of a few percent, despite the fact that these processes increase the dipole rates by several orders of magnitude at high temperatures, cf. fig.

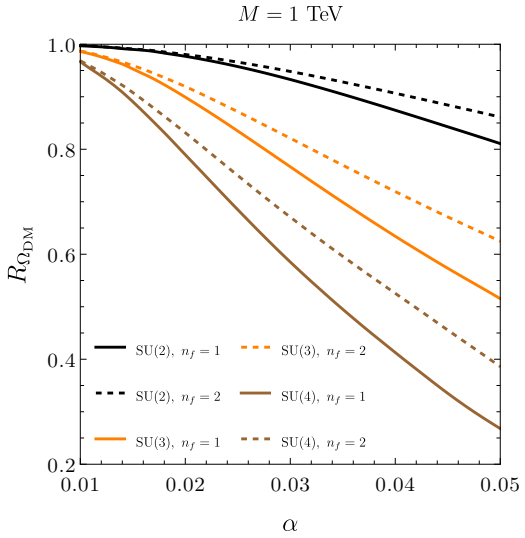

Figure 10.2: Ratio of the DM energy density obtained from the effective cross section incl. the ground state 1S, cf. eq. (7.5), over the density obtained from only the Sommerfeld-enhanced annihilations, cf. eq. (9.13); in SU(2) (black lines), SU(3) (orange lines) and in SU(4) (brown lines). $R_{\Omega_{\rm DM}}$ is plotted as a function over $\alpha \equiv \alpha(2M)$ for fixed DM mass $M = 1$ TeV and $n_f = 1$ (solid lines) or $n_f = 2$ (dashed lines) massless DM fermions.

9.3. The reason is that at large T the dipole rates are in ionization equilibrium. Hence, the net effect on the relic density is quite small, with corrections of order of a few percent, i.e. of similar magnitude as the corrections coming from the center-of-mass recoil effect. Therefore, from now on, we approximate the bound-state formation cross section and bound-state dissociation width for the 1S state by the analytic expressions at LO, i.e. (9.13) and (9.23), respectively.

We would like to quantify the numerical impact on the DM energy density $\Omega_{\rm DM}h^2$ when including bound-state effects from the 1S state, compared to the energy density as a result of considering only the Sommerfeld-enhanced annihilation cross section (9.13) in the effective Boltzmann equation (7.4). In figure 10.2, we plot the ratio of the present energy density with bound-state formation and dissociation processes for the ground state over the the one where only annihilations are taken into consideration. We plot the ratio $R_{\Omega_{\rm DM}}$ as a function of $\alpha \equiv \alpha(2M)$ for fixed DM mass $M = 1$ TeV in SU(2) (black lines), SU(3) (orange lines) and in SU(4) (brown lines).[3] We observe that the bound-state effects are more significant in SU(N) models with increasing N, and that $R_{\Omega_{\rm DM}}$ decreases approximately linear with increasing $\alpha(2M)$. For the largest considered value $\alpha(2M) = 0.05$ and only one dark massless fermion species included in the theory, the present DM energy density is reduced, due to the presence of the ground state 1S, down to about 27% with respect to the value it would have if the 1S would have been

[3]We checked numerically, that the ratio stays almost constant when varying the DM mass for fixed coupling and $N = (2, 3, 4)$.

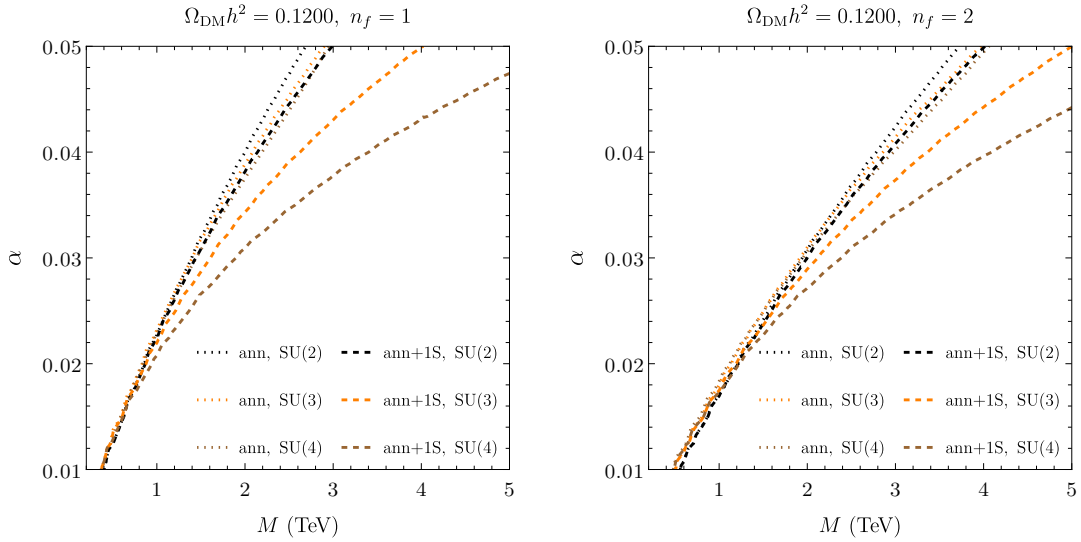

Figure 10.3: Contours in the parameter space (M, α), with $\alpha = \alpha(2M)$, that correspond to the observed DM energy density obtained from Sommerfeld-enhanced annihilations only (dotted lines), or upon including the bound-state formation effect of the 1S ground state (dashed lines). The left panel is for $n_f = 1$, the right panel for $n_f = 2$. The black, orange and brown lines are for the SU(2), SU(3) and SU(4) model, respectively.

removed entirely from the effective Boltzmann equation.[4] As a comparison, in SU(2) and SU(3) the value of $\Omega_{\rm DM}h^2$ is scaled down to about 81% and 52%, respectively. Since, by comparing the solid lines on the left panel in fig. 10.1 with the curves (with same color) on the right panel, the ratio $\langle\sigma_{\rm eff}v_{\rm rel}\rangle/\langle\sigma_{\rm ann}v_{\rm rel}\rangle$ decreases with increasing number of dark massless fermion flavors in the temperature region around $10^{-2}M - 10^{-4}M$. As a consequence, the present relic-abundance ratio $R_{\Omega_{\rm DM}}$ increases, which can be seen in fig. 10.2, where the dashed lines for $n_f = 2$ are always above the corresponding solid lines ($n_f = 1$). For $\alpha(2M) = 0.05$, the increase is about 5–10% depending on N.

Despite the fact that $R_{\Omega_{\rm DM}}$ increases with increasing n_f, the present energy density does not. On the contrary: if we increase the number n_f of light fermions, the heavy DM particles will annihilate more likely because of the additional annihilation channels into these light particles, which can be seen the two plots in fig. 10.3. We perform an entire parameter scan for α and M, see the left panel in fig. 10.3 for $n_f = 1$ and the right panel for $n_f = 2$, for which the numerical value of $\Omega_{\rm DM}h^2$, obtained from solving the Boltzmann equations up to the present time, equals 0.12, namely the measured relic abundance. Upon increasing the number of light dark particle species, from fig. 10.3 we deduce, by comparing the contour lines on the left panel ($n_f = 1$) with the ones on

[4] As a cross check for the validity of the numerical results obtained by solving the single effective Boltzmann equation, we numerically evaluate also the coupled evolution equations. We observe a $\lesssim 1\%$ difference to the obtained energy density in the SU(2), SU(3) and SU(4) model, which is within the uncertainty of the measured relic density.

the right panel ($n_f = 2$), that for a fixed value of the coupling, let us pick for instance $\alpha(2M) = 0.05$, one needs a larger DM mass in order to secure that $\Omega_{\rm DM}h^2 = 0.12$, e.g. $M = 5$ TeV instead of $M = 4$ TeV in SU(3). In the opposite parametric case we come to the following conclusion: For fixed DM mass, one needs a smaller value for the coupling in order to maintain $\Omega_{\rm DM}h^2 = 0.12$ constant.[5]. We therefore understand that increasing the particle number n_f increases (decreases) the effective cross section (the ratio $\langle\sigma_{\rm eff}v_{\rm rel}\rangle/\langle\sigma_{\rm ann}v_{\rm rel}\rangle$, cf. fig. 10.1) and hence decreases (increases) the present relic density $\Omega_{\rm DM}h^2$ (the ratio $R_{\Omega_{\rm DM}}$, cf. fig. 10.2).[6]

[5]As an example: For $M = 5$ TeV, one requires $\alpha(2M) \approx 0.048$ for $n_f = 1$ and $\alpha(2M) \approx 0.044$ for $n_f = 2$ in the SU(4) theory.

[6]The reason why the observable $\sigma_{\rm eff}$, and hence $\Omega_{\rm DM}h^2$, behaves oppositely to the corresponding ratio $\langle\sigma_{\rm eff}v_{\rm rel}\rangle/\langle\sigma_{\rm ann}v_{\rm rel}\rangle$, and hence $R_{\Omega_{\rm DM}}$, with increasing n_f, is because the (Sommerfeld-enhanced) annihilation cross section in ((9.13)) (9.14) increases more strongly than the bound-state formation cross section with growing number of light fermions, such that in overall the ratio $\langle\sigma_{\rm eff}v_{\rm rel}\rangle/\langle\sigma_{\rm ann}v_{\rm rel}\rangle$ decreases. If we would decide to normalize the effective cross section by $\pi\alpha^2/M^2$, as in the abelian case, then the ratio would increase instead.

Part V

Open quantum system approach

Chapter 11

Dark matter viewed as a reduced open system

In this chapter, we discuss the interpretation of the heavy DM particles, in particular the fermion-antifermion pairs, in a thermal bath as an *open quantum system* (OQS). Our aim is to pursue a time-dependent out-of-equilibrium treatment to describe the dynamics of the dark bound and scattering states during the freeze-out in the early universe. As we have shown in the preceding chapters, many reactions near threshold induce a quite complicated dynamics. On the one hand darkonium can dissociate via interactions with the thermal medium, due to on-shell photo-absorption or due to bath-particle scatterings, on the other hand the bound state may form e.g. through emission of a dark gauge field at leading order in α. De-excitations of excited bound states can also populate the lower-lying states, and together with the reverse process, i.e. the thermally induced excitations, these transitions redistribute the relative abundance of bound states within the thermal bath. All of these close-to-threshold transitions give rise to a network of rate equations that are coupled, cf. eqs. (7.1)–(7.3). The dipole reactions conserve the number of heavy particles, as can be seen upon summing up the eqs. (7.1)–(7.3). Conversely at the hard scale, heavy-pair annihilations into highly energetic light degrees of freedom effectively deplete the dark matter particles.

We stress that, so far, the numerical analysis of bound-state effects, center-of-mass recoil and Debye-mass resummation corrections on the DM energy density in the chapters 7 and 10 for the dark U(1) and SU(N) model, respectively, relied on the semi-classical Boltzmann equations stated in eqs. (7.1)–(7.3), where kinetic equilibrium was taken for granted and bound states were implemented from beginning on as on-shell degrees of freedom. One may, however, question if these assumptions are reliable because bound states do not exist as probes "*injected*" in the medium. It may take some time for the dark fermions and antifermions to form a bound state configuration and, hence, inserting bound states as on-shell degrees of freedom in a network of Boltzmann equations can lead to an inaccurate description. We stress that the results based on spectral function calculations and classical kinetic approaches leading to Boltzmann equations put the emphasis on static and stationary aspects. Also, extracting the spectral functions from

equilibrium correlators and using them for late-time out-of-equilibrium annihilations can be questionable [23].

In general terms, an open system can be understood as a quantum system that is coupled to another quantum system much larger in size, the latter representing the thermal bath. Hence, the open quantum system is just a subsystem of the combined total system (which most of the time is assumed to be closed and hence it follows a Hamiltonian unitary dynamics). The state or density operator of the open quantum system evolves due to its internal dynamics as well as the interactions with the surroundings; the latter may lead to certain system-environment correlations so that the corresponding changes in time of the open system cannot be represented, in general, with a unitary dynamics. Sometimes the open system is referred to as the *reduced* system, or simply system as in the following sections. It is one of the main aims of the OQS theory to derive the evolution equation for the density operator of the reduced system, denoted as the *reduced density operator*, which is then called a *quantum master equation*. Once the density of states of the system is known, one is able to extract all observables of interest that indeed refer to the system only. It is then said that the environment has been *traced out* and its initial correlation effects are encoded in the non-unitary evolution of the system, that manifests through decoherence effects and dissipation.

We shall build on recent developments in heavy-ion phenomenology, where the time evolution for the heavy-quarkonium number density has been recast in an OQS framework [99, 152, 153]. Here the system is made of heavy quark-antiquark pairs, either in a color-singlet or color-octet configuration, and the quark-gluon plasma represents the environment. We follow, in particular, the derivation in pNRQCD given in refs. [152, 153], and adapt it to the dark abelian model (3.1).[1] For the problem at hand in this work, the early universe plasma plays the role of the environment, whereas the DM pairs correspond to the reduced system. A critical aspect will however be treated differently in the present case. We have to consider the dark fermion-antifermion annihilations, at variance with the evolution of quark-antiquark pairs in the QGP. Since the hot QCD medium lives for typical time scales smaller than the inverse annihilation rate, it follows that heavy-quarkonium annihilations are practically irrelevant for the number density evolution.[2] In the dark SU(N) model, however, annihilation processes need to be taken into account since the primordial thermal universe is sustained at much longer time scales. But the analysis that we are going to develop in the following sections for the $\mathrm{U}(1)_{\mathrm{DM}}$ model, can be straightforwardly generalized to the weakly-coupled dark non-abelian theory (8.1).[3]

[1] As for the weakly-coupled $\mathrm{SU}(N)_{\mathrm{DM}}$ model (8.1) and its EFTs developed in chapter 8, one can directly adopt the results from refs. [99, 152, 153].

[2] The typical life-time of the thermal medium established in heavy-ion collisions is about 10-20 fm^{-1}, which is much shorter than the typical time scale set by heavy quark-antiquark annihilations, e.g. by at least a factor of 100 for the Y(1S)-meson.

[3] One has to be more cautious here, since this statement is only true if we consider in $\mathrm{SU}(N)_{\mathrm{DM}}$ only the subset of diagrams at next-to-leading order associated to the bath-particle scatterings, which correspond to the two-loop diagrams in the second row in fig. 9.1. If, however, we study the dynamics at lower temperatures such that the hierarchy (3.2) is realized, then the statement is correct to a good

Of primary importance are the time scales that characterize the environment, the system and the system-environment correlations. Such scales and their relative size are at the base of the approximations that lead to tractable quantum master equations. We recall from the chapters 1–3, that the temperature scale T (or πT, see the discussion in chapter 3, footnote 6) characterizes the thermal medium, whereas the binding and kinetic energies $M\alpha^2$ and Mv_X^2, respectively, define the energy scale of the dark matter system.[4] The intrinsic time scales of the system and environment are accordingly estimated as $\tau_S \sim \{1/(Mv^2), 1/(M\alpha^2)\}$ and $\tau_E \sim 1/T$, respectively. Finally, the relaxation time τ_R defines the time-scale of the system evolution under the influence of the environment. In analogy with the heavy-quarkonium case, the relaxation time is proportional to the inverse self-energy of a heavy fermion-antifermion pair, that is driven by the electric-dipole transitions as the dominant force in the dipole limit. Hence for $T \lesssim M\alpha^2$ (cf. hierarchy in (3.2)), which is realized for most of the time after the thermal freeze-out, we can estimate it by $\tau_R^{\rm dip} \sim 1/(\alpha a_0^2 T^3)$, where a_0 is the Bohr radius.[5] In addition, bound state annihilations proceed with $\tau_R^{\rm ann,b} \sim 1/\Gamma_{\rm ann} \sim M^2 a_0^3/\alpha^2$ (see also sec. 5.2.2, footnote 14). We typically find $\tau_R^{\rm ann,b} \gg \tau_R^{\rm dip}$, meaning that bound-state formation and dissociation processes happen much faster than heavy-pair annihilations.[6]

In the following, we are going to consider the dynamics of the dark heavy-pair system at temperatures of the order of or smaller than the ultrasoft scale, such that the hierarchy of energy scales written in (3.2) is certainly fulfilled,[7] and we will include annihilations and the thermal motion of the center of mass, in this way extending the analysis done in ref. [152, 153].

11.1 Warm-up: Lindblad equation for annihilations exclusively

Let us focus for the moment only on the dark fermion-antifermion annihilation reactions and exclude the dipole transitions such as the formation of bound states. According to the refs. [154, 155], non-relativistic annihilation processes can be incorporated into a quantum master equation for the reduced density operator ρ of the annihilating dark matter, that takes the form of a *Lindblad* equation [156, 157],

$$\frac{d\rho}{dt} = -i[H_{\rm eff}, \rho] + \sum_n \left(C_n \rho\, C_n^\dagger - \frac{1}{2}\left\{ C_n^\dagger C_n, \rho \right\} \right) , \tag{11.1}$$

degree of accuracy.

[4] If the dark matter system is in kinetic equilibrium with the thermal bath, which we always assumed in this work so far, then the kinetic energy Mv_X^2 of the heavy dark fermion is of order T.

[5] We can infer the estimate of $\tau_R^{\rm dip}$ from the bsf cross section at LO in (6.9), where the squared dipole matrix element is of order a_0^2 and $\Delta E_n^p \sim T$ for the hierarchy of energy scales given in (3.2).

[6] At late times the situation changes for the dissociations, which are then exponentially suppressed and hence $\Gamma_{\rm bsd}^n \ll \Gamma_{\rm ann}^n$, see the right plot in fig. 6.2.

[7] Since for the hierarchy (3.2) the interesting dynamics for the dark particles occurs when they are non-relativistic, their abundance can be assumed to be diluted in the thermal plasma due to $e^{-M/T} \ll 1$.

where H_{eff} is a hermitian operator,[8] and the collapse operators C_n, also referred to as the Lindblad operators, are responsible for the non-unitary evolution of the open system.[9] Eq. (11.1), where the right-hand side is called the Lindblad superoperator that is only valid for an evolution in positive-time direction, is a linear Markovian differential equation in ρ and fulfills the fundamental properties of a density operator: hermiticity ($\rho = \rho^\dagger$), conserved probability ($\text{Tr}[\dot{\rho}] = 0$) and positivity ($\langle\phi|\rho|\phi\rangle \geq 0 \; \forall \phi \in \mathcal{H}$, where $\mathcal{H}$ denotes the Hilbert space of the reduced system).

The Lindblad equation has been applied to a single heavy-particle decay, for instance an unstable muon, but also to deeply inelastic processes in ultracold atom systems [158]. In the latter example, the corresponding Lindblad equation reads [155]

$$i\frac{d}{dt}\rho_\psi = [H_{\text{eff}}, \rho_\psi] - i\frac{\Gamma}{2}\int d^3x \left[\psi^{\dagger 2}(\boldsymbol{x})\psi^2(\boldsymbol{x})\rho_\psi + \rho_\psi\psi^{\dagger 2}(\boldsymbol{x})\psi^2(\boldsymbol{x}) - 2\,\psi^2(\boldsymbol{x})\rho_\psi\psi^{\dagger 2}(\boldsymbol{x})\right] , \tag{11.2}$$

where the field ψ annihilates a non-relativistic atom in the specific hyperfine state $|\psi\rangle$. Equation (11.2) describes the evolution for the reduced density operator ρ_ψ of the heavy cold atoms that trap to form a molecule, and the highly energetic degrees of freedom ϕ produced in the process, which escape the system after the deep-inelastic collision $\psi\psi \to \phi\phi$, have been integrated out.[10]

From the Lindblad equation (11.2) we can derive the rate of change of the probability $P_n(t)$ for finding n cold atoms ψ in the system,

$$P_n(t) \equiv \sum_{\lambda_n} \langle\lambda_n|\rho_\psi(t)|\lambda_n\rangle \, , \tag{11.3}$$

that equals the partial trace of ρ_ψ over the multiparticle states $|\lambda_n\rangle$, where λ_n comprises the quantum numbers, for the n heavy atoms. We do the same for the terms on the right-hand side of eq. (11.2), for instance one of the anticommutator terms becomes

$$\begin{aligned}\int d^3x \, \langle\lambda_n|\rho_\psi \, \psi^\dagger(\boldsymbol{x})\psi^\dagger(\boldsymbol{x}) \, \psi(\boldsymbol{x})\psi(\boldsymbol{x})|\lambda_n\rangle &= \frac{\sqrt{n(n-1)}}{V}\int d^3x \, \langle\lambda_n|\rho_\psi \, \psi^\dagger(\boldsymbol{x})\psi^\dagger(\boldsymbol{x})|\lambda_{n-2}\rangle \\ &= \frac{n(n-1)}{V^2}\int d^3x \, \langle\lambda_n|\rho_\psi|\lambda_n\rangle = \frac{n(n-1)}{V}\langle\lambda_n|\rho_\psi|\lambda_n\rangle \, , \end{aligned} \tag{11.4}$$

where in the first and second equality we used the properties of the creation and annihilation operators. We get the same result for the other anticommutator term. The Lindblad term becomes

$$\int d^3x \, \langle\lambda_n|\psi^2(\boldsymbol{x})\rho_\psi\psi^{\dagger 2}(\boldsymbol{x})|\lambda_n\rangle = \frac{(n+1)(n+2)}{V}\langle\lambda_{n+2}|\rho_\psi|\lambda_{n+2}\rangle \, , \tag{11.5}$$

[8] The *effective* Hamiltonian H_{eff} usually consists of the internal Hamiltonian H of the reduced system, augmented by an induced mass shift from the thermal medium.

[9] As can be seen, for $C_n \ll H_{\text{eff}}$, the Lindblad equation reduces to $\dot{\rho} \approx -i[H_{\text{eff}}, \rho]$ and hence describes an effective unitary evolution of the open quantum system, see also footnote 1 in appendix D.

[10] Note that the dimension of the continuous Lindblad operator $C(\boldsymbol{x}) \equiv \psi(\boldsymbol{x})^2$ is three, hence the width Γ has to scale as $1/M^2$ accordingly, which has the dimension of a cross section, i.e. indeed the pair-annihilation cross section.

where again one factor of volume survives. The commutator term vanishes. The rate equation for $P_n(t)$ therefore is

$$\frac{d}{dt}P_n(t) = -\frac{\Gamma}{V}\left[n(n-1)P_n(t) - (n+1)(n+2)P_{n+2}(t)\right] . \tag{11.6}$$

We define the number operator

$$\hat{N}_\psi = \int d^3x\, \psi^\dagger(\boldsymbol{x})\psi(\boldsymbol{x})\,, \tag{11.7}$$

and the normal ordered squared number operator

$$:\hat{N}_\psi^2: = \int d^3x \int d^3y\, \psi^\dagger(\boldsymbol{x})\psi^\dagger(\boldsymbol{y})\psi(\boldsymbol{y})\psi(\boldsymbol{x})\,. \tag{11.8}$$

The number of cold atoms N_ψ can be written in terms of the probability as

$$\begin{aligned} N_\psi = \mathrm{Tr}\left[\hat{N}_\psi\,\rho_\psi\right] &= \sum_n \sum_{\lambda_n} \langle\lambda_n| \int d^3x\, \psi^\dagger(\boldsymbol{x})\psi(\boldsymbol{x})\,\rho_\psi\,|\lambda_n\rangle \\ &= \sum_n n \sum_{\lambda_n} \langle\lambda_n|\rho_\psi\,|\lambda_n\rangle = \sum_n nP_n(t)\,, \end{aligned} \tag{11.9}$$

and hence the rate equation for N_ψ reads

$$\begin{aligned} \frac{d}{dt}N_\psi = \sum_n n\frac{d}{dt}P_n(t) &= -\frac{\Gamma}{V}\sum_{n=0}^{\infty} n\left[n(n-1)P_n(t) - (n+1)(n+2)P_{n+2}(t)\right] \\ &= -\frac{\Gamma}{V}\left[\sum_{n=0}^{\infty} n^2(n-1)P_n(t) - \sum_{n=2}^{\infty}(n-2)(n-1)nP_n(t)\right] \\ &= -\frac{\Gamma}{V}\left[\sum_{n=0}^{\infty} n^2(n-1)P_n(t) - \sum_{n=0}^{\infty}(n-2)(n-1)nP_n(t)\right] \\ &= -\frac{2\Gamma}{V}\sum_n n(n-1)P_n(t)\,, \end{aligned} \tag{11.10}$$

where in the first line we inserted eq. (11.6), and in the second line we shifted the sum of the second term. On the other hand, for the number squared N_ψ^2 we obtain

$$\begin{aligned} N_\psi^2 = \mathrm{Tr}\left[:\hat{N}_\psi^2:\,\rho_\psi\right] &= \sum_n \sum_{\lambda_n} \langle\lambda_n| \int d^3x \int d^3y\, \psi^\dagger(\boldsymbol{x})\psi^\dagger(\boldsymbol{y})\psi(\boldsymbol{y})\psi(\boldsymbol{x})\,\rho_\psi\,|\lambda_n\rangle \\ &= \sum_n n(n-1) \sum_{\lambda_n} \langle\lambda_n|\rho_\psi|\lambda_n\rangle = \sum_n n(n-1)P_n(t)\,. \end{aligned} \tag{11.11}$$

Combining eqs. (11.10) and (11.11) we end up with

$$\frac{d}{dt}N_\psi = -2\frac{\Gamma}{V}N_\psi^2\,, \tag{11.12}$$

or in terms of the number density, $n_\psi = N_\psi/V$, eq. (11.12) becomes

$$\frac{d}{dt} n_\psi = -2\Gamma n_\psi^2 \,. \tag{11.13}$$

Defining the total number density $n = 2n_\psi$ of two atoms that are lost in the process, we finally get[11]

$$\frac{d}{dt} n = -\Gamma n^2 \,, \tag{11.14}$$

which resembles the standard Boltzmann equation (2.6) for particle-antiparticle annihilation, since Γ is related to the annihilation cross section due to a dimensional analysis, cf. footnote 10 in this section.[12]

We now consider the case of heavy dark fermion-antifermion free annihilation processes in NRQED_{DM}, and apply similar methods we learned so far from the study of inelastic collisions of ultracold atoms. If we neglect the dark light fermions, then annihilations proceed via $\psi\chi \to \gamma\gamma$ at leading order in the coupling. Hence the imaginary part of the matching coefficient d_s of the dimension-six four-fermion operator in (4.1) provides the anti-hermitian part of the Lagrangian, that will be connected to the Lindblad operators as we shall see in a moment. At variance with the previous situation, we now have a system with two types of states: the particle ψ and the antiparticle χ. Accordingly, we have two subsystems for the heavy dark matter species, namely S_ψ for the ψ-sector and S_χ for the χ-sector. To be more precise, we define the tensor-product state vector $|X_n Y_m\rangle = \sum_{\psi,\chi} \lambda^\psi \lambda^\chi |\psi_n\, \chi_m\rangle = \sum_\psi \lambda^\psi |\psi_n\rangle \otimes \sum_\chi \lambda^\chi |\chi_m\rangle$ of the tensor-product space $\mathcal{H} = \mathcal{H}_\psi \otimes \mathcal{H}_\chi$ of the two independent subsystems S_ψ and S_χ, where $\{|\psi_n\rangle\}$ and $\{|\chi_n\rangle\}$ form an orthonormalbasis for $\mathcal{H}_\psi$ and $\mathcal{H}_\chi$, respectively, and $\langle \psi'_{n'}\, \chi'_{m'} | \psi_n\, \chi_m\rangle = \delta_{n,n'}\delta_{m,m'}\delta(\psi'-\psi)\delta(\chi'-\chi)$, where the eigenvalues ψ, χ shall comprise the continuous as well as discrete quantum numbers like the momentum and the spin, respectively, and n (m) denotes the number of (anti-)fermions in the state $|\psi_n\rangle$ ($|\chi_m\rangle$). The Lindblad evolution equation for the density operator of the composite system can be written in a matrix form,

$$\begin{aligned} i\frac{d}{dt}\begin{pmatrix} \rho_{\psi\psi} & \rho_{\psi\chi} \\ \rho_{\chi\psi} & \rho_{\chi\chi} \end{pmatrix} &= \begin{pmatrix} [H_\psi, \rho_{\psi\psi}] & 0 \\ 0 & [H_\chi, \rho_{\chi\chi}] \end{pmatrix} - \frac{i}{2}\Gamma \begin{pmatrix} 0 & \{K_{\psi\chi}, \rho_{\psi\chi}\} \\ \{K_{\chi\psi}, \rho_{\chi\psi}\} & 0 \end{pmatrix} \\ &\quad + i\Gamma \begin{pmatrix} 0 & \int_{\boldsymbol{x}} \chi^\dagger\psi\, \rho_{\psi\chi}\, \psi^\dagger\chi \\ \int_{\boldsymbol{x}} \chi^\dagger\psi\, \rho_{\chi\psi}\, \psi^\dagger\chi & 0 \end{pmatrix} , \end{aligned} \tag{11.15}$$

where H_ψ and H_χ are the effective Hamiltonians, comprising the bilinear terms from the first and second line of (4.1), respectively, $\Gamma \sim \text{Im}[d_s]_{\text{LO}}/M^2$ and the anti-hermitian

[11] We remark that in an annihilation process the particle number can change only if the two annihilating particles approach the same location point in space, thus the rate of change is proportional to the squared of the number density, n^2, instead of a single n_ψ in the case of a decaying particle.

[12] The Boltzmann equation (2.6) contains the recombination term on the right-hand side, which is absent in eq. (11.14) because heavy-pair creation processes have been excluded and hence do not appear in the Lindblad equation (11.2).

term reads

$$K_{\psi\chi} = \int_{\boldsymbol{x}} \psi^\dagger \chi \, \chi^\dagger \psi \,, \tag{11.16}$$

where we abbreviate $\int_{\boldsymbol{x}} \equiv \int d^3x$. We notice the following differences to the pair-annihilation process of two cold atoms $\psi\psi \to \phi\phi$ considered in the previous case taken from refs. [155, 158]. First, we find four different combinations for the relevant heavy-particle sector

$$\langle X_n Y_m | \rho_{\psi\psi} | X_n Y_m \rangle \,, \quad \langle X_n Y_m | \rho_{\psi\chi} | X_n Y_m \rangle \,, \tag{11.17}$$

$$\langle X_n Y_m | \rho_{\chi\psi} | X_n Y_m \rangle \,, \quad \langle X_n Y_m | \rho_{\chi\chi} | X_n Y_m \rangle \,, \tag{11.18}$$

where the state $|X_n Y_m\rangle$ contains n particles and m antiparticles. Then, because in $\mathrm{U}(1)_{\mathrm{DM}}$ there is no operator, and hence an associated process, that allows for particle-particle or antiparticle-antiparticle annihilations, the corresponding entries in eq. (11.15) are zero. It means that $\rho_{\psi\psi}$ and $\rho_{\chi\chi}$ evolve in time according to the unitary evolution, where the number of heavy species does not deplete through processes that annihilate two particles (or two-antiparticles) at the same time. Instead, the number of the heavy species changes because of particle-antiparticle annihilations. One particle is removed only if one antiparticle is also removed at the same time, and hence the process is incorporated through the off-diagonal elements in eq. (11.15).

We now proceed with the evaluation of the terms in the evolution equation for $\rho_{\psi\chi}$ in (11.15). Recalling that $\chi^\dagger$ is the field operator that annihilates an antiparticle, namely $\chi^\dagger |X_n Y_m\rangle = \sqrt{\frac{m}{V}} |X_n Y_{m-1}\rangle$, we obtain

$$\Gamma \langle X_n Y_m | \{ K_{\psi\chi}, \rho_{\psi\chi} \} | X_n Y_m \rangle = 2 \frac{\Gamma}{V} \, nm \langle X_n Y_m | \rho_{\psi\chi} | X_n Y_m \rangle \,, \tag{11.19}$$

whereas from the Lindblad term one finds

$$\Gamma \langle X_n Y_m | \int_{\boldsymbol{x}} \chi^\dagger \psi \, \rho_{\psi\chi} \, \psi^\dagger \chi | X_n Y_m \rangle = \frac{\Gamma}{V} (n+1)(m+1) \langle X_{n+1} Y_{n+1} | \rho_{\psi\chi} | X_{n+1} Y_{n+1} \rangle \,. \tag{11.20}$$

We define the joint probability to find n fermions and m antifermions similarly as in eq. (11.3),

$$P_{n,m}(t) = \sum_{X_n} \sum_{Y_m} \langle X_n Y_m | \rho_{\psi\chi} | X_n Y_m \rangle \,. \tag{11.21}$$

Then from the 12-matrix element of the Lindblad equation (11.15) it follows that

$$\frac{d}{dt} P_{n,m}(t) = -\frac{\Gamma}{V} \left[nm \, P_{n,m} - (n+1)(m+1) P_{n+1,m+1} \right] \,. \tag{11.22}$$

We define the normal ordered number operator for a particle-antiparticle pair similarly as in eq. (11.8). Then for the number of heavy fermion-antifermion pairs we get

$$\begin{aligned} N_{\psi\chi} = \mathrm{Tr} \left[: \hat{N}_{\psi\chi} : \, \rho_{\psi\chi} \right] &= \sum_{n,m} \sum_{X_n, Y_m} \langle X_n Y_m | \int_{\boldsymbol{x}} \int_{\boldsymbol{y}} \psi^\dagger(\boldsymbol{x}) \chi(\boldsymbol{y}) \chi^\dagger(\boldsymbol{y}) \psi(\boldsymbol{x}) \rho_{\psi\chi} | X_n Y_m \rangle \\ &= \sum_{n,m} nm \, P_{n,m}(t) \,. \end{aligned} \tag{11.23}$$

In the next step, we compute the number of fermions N_ψ and of antifermions N_χ in a similar way. For the particle sector we obtain

$$\begin{aligned} N_\psi = \mathrm{Tr}\left[\hat{N}_\psi\,\rho_{\psi\chi}\right] &= \sum_{n,m}\sum_{X_n,Y_m}\langle X_nY_m|\int_{\boldsymbol{x}}\psi^\dagger(\boldsymbol{x})\psi(\boldsymbol{x})\rho_{\psi\chi}|X_nY_m\rangle \\ &= \sum_n\sum_{X_n}\langle X_n|\int_{\boldsymbol{x}}\psi^\dagger(\boldsymbol{x})\psi(\boldsymbol{x})\rho_\psi|X_n\rangle \\ &= \sum_n n\sum_{X_n}\langle X_n|\rho_\psi|X_n\rangle = \sum_n n\,P_n(t)\,, \end{aligned} \tag{11.24}$$

where in the second line we recognize the partial trace

$$\rho_\psi = \sum_m\sum_{Y_m}\langle Y_m|\rho_{\psi\chi}|Y_m\rangle\,, \tag{11.25}$$

and in the last line the particle probability

$$P_n(t) = \sum_{X_n}\langle X_n|\rho_\psi|X_n\rangle\,. \tag{11.26}$$

For the antiparticle sector we obtain analogously

$$\begin{aligned} N_\chi = \mathrm{Tr}\left[\hat{N}_\chi\,\rho_{\psi\chi}\right] &= \sum_{n,m}\sum_{X_n,Y_m}\langle X_nY_m|\int_{\boldsymbol{x}}\chi(\boldsymbol{x})\chi^\dagger(\boldsymbol{x})\rho_{\psi\chi}|X_nY_m\rangle \\ &= \sum_m\sum_{Y_m}\langle Y_m|\int_{\boldsymbol{x}}\chi(\boldsymbol{x})\chi^\dagger(\boldsymbol{x})\rho_\chi|Y_m\rangle \\ &= \sum_m m\sum_{Y_m}\langle Y_m|\rho_\chi|Y_m\rangle = \sum_m m\,P_m(t)\,, \end{aligned} \tag{11.27}$$

where the partial trace over the particles gives

$$\rho_\chi = \sum_n\sum_{X_n}\langle X_n|\rho_{\psi\chi}|X_n\rangle\,, \tag{11.28}$$

and the antiparticle probability is

$$P_m(t) = \sum_{Y_m}\langle Y_m|\rho_\chi|Y_m\rangle\,. \tag{11.29}$$

We remark that the definitions above are consistent with the general notion of marginal probabilities $P_n = \sum_m P_{n,m}$ and $P_m = \sum_n P_{n,m}$, since

$$\sum_m P_{n,m} = \sum_m\sum_{X_n}\sum_{Y_m}\langle X_nY_m|\rho_{\psi\chi}|X_nY_m\rangle = \sum_{X_n}\langle X_n|\rho_\psi|X_n\rangle = P_n\,, \tag{11.30}$$

$$\sum_n P_{n,m} = \sum_n\sum_{X_n}\sum_{Y_m}\langle X_nY_m|\rho_{\psi\chi}|X_nY_m\rangle = \sum_{Y_m}\langle Y_m|\rho_\chi|Y_m\rangle = P_m\,, \tag{11.31}$$

where we used eqs. (11.21), (11.25) and (11.28). Then from the rate equation (11.22) for the joint probability, upon summing over m and using relation (11.30), it follows

$$\sum_m \frac{d}{dt} P_{n,m} = \frac{d}{dt} P_n = -\frac{\Gamma}{V} \sum_m \left[nm\, P_{n,m} - (n+1)(m+1) P_{n+1,m+1} \right] , \tag{11.32}$$

and if we multiply by $\sum_n n$, we then have

$$\begin{aligned} \frac{d}{dt} \sum_n nP_n &= -\frac{\Gamma}{V} \sum_{n,m} \left[n^2 m\, P_{n,m} - n(n+1)(m+1) P_{n+1,m+1} \right] \\ &= -\frac{\Gamma}{V} \sum_{n,m} n\, m\, P_{n,m} , \end{aligned} \tag{11.33}$$

where we have shifted the indices n and m in order to obtain the expression in the second line. Plugging eqs. (11.23) and (11.24) into (11.33), we eventually get the rate equation for the fermion particle number N_ψ,

$$\frac{d}{dt} N_\psi = -\frac{\Gamma}{V} N_{\psi\chi} . \tag{11.34}$$

We obtain the evolution equation for the antiparticles in a similar way, by summing eq. (11.22) over n and using (11.31),

$$\sum_n \frac{d}{dt} P_{n,m} = \frac{d}{dt} P_m = -\frac{\Gamma}{V} \sum_n \left[nm\, P_{n,m} - (n+1)(m+1) P_{n+1,m+1} \right] , \tag{11.35}$$

and multiplying by $\sum_m m$, which gives

$$\begin{aligned} \frac{d}{dt} \sum_m mP_m &= -\frac{\Gamma}{V} \sum_{n,m} \left[nm^2\, P_{n,m} - (n+1)m(m+1) P_{n+1,m+1} \right] \\ &= -\frac{\Gamma}{V} \sum_{n,m} n\, m\, P_{n,m} . \end{aligned} \tag{11.36}$$

If we insert (11.23) and (11.27) into (11.36), we finally get

$$\frac{d}{dt} N_\chi = -\frac{\Gamma}{V} N_{\psi\chi} . \tag{11.37}$$

We conclude with the following observation. As we already anticipated, the number of particles N_ψ (antiparticles N_χ) can change only by pair-annihilation with antiparticles (particles). Hence, as we can read-off from eqs. (11.34) and (11.37), the rate of change for N_ψ and N_χ depends on the fermion-antifermion number $N_{\psi\chi}$. The abundance for the particles (antiparticles) depends on the number of particle-antiparticle pairs $N_{\psi\chi}$.

Summing eqs. (11.34) and (11.37) and dividing by the volume, we eventually obtain the rate equation for the fermion-antifermion number density $n = (N_\psi + N_\chi)/V$,

$$\frac{d}{dt}n = -2\frac{\Gamma}{V^2}N_{\psi\chi} = -2\Gamma\, n_\psi n_\chi = -\frac{1}{2}\Gamma n^2\,, \tag{11.38}$$

where in the second equality we factorized $N_{\psi\chi} = N_\psi N_\chi$, since we consider the fermion and antifermion as free scatters and hence independent from each other prior to their annihilation. In the last step we assumed an absence of asymmetry between the particles and antiparticles, thus $n_\psi = n_\chi = n/2$. The rate equation (11.38) can be compared with the Boltzmann equation in (2.6).

The study so far applies to free S-wave heavy-pair annihilations at leading order within NRQED_{DM}. It can be straightforwardly extended to annihilations of higher order in the coupling, but also in the non-relativistic expansion by including four-fermion operators of higher order than six. We did not consider soft Coulombic photon exchanges that, as explained in the previous chapters, are of paramount importance when studying the dark matter dynamics precisely at and after the thermal freeze-out. Instead of implementing the analysis we gained so far within the $\text{pNRQED}_{\text{DM}}$ theory, which then accounts for the Sommerfeld enhancement effect, we rather pursue a different method via a diagrammatic reformulation of the annihilations, together with the dipole processes, within the real-time formalism in the next chapter. We aim to derive the comple quantum master equations for the dark matter density operator, that encompass the in-vacuum annihilations but also all the near-threshold processes at finite temperature at one time.

Chapter 12

Diagrammatic derivation of the master equations

In this chapter, we aim to establish a diagrammatic out-of-equilibrium derivation of the quantum master equations for the dark matter dynamics at times after the DM thermal freeze-out according to the hierarchy given in (3.2), extending the formalism developed in ref. [153] by accounting for the leading recoil effect in the laboratory frame, but also by including the heavy-pair annihilation process.

The central object for the practical calculation is the reduced density operator of the dark matter fermion-antifermion pairs, that can be either in a continuous scattering-state or discrete bound-state configuration. It can be defined in terms of the corresponding fields of pNRQED$_{\rm DM}$, cf. eq. (4.2), in the real-time formalism. The doubling of the degrees of freedom, giving rise to quantum fields of type-two on the lower time branch, cf. appendix D for more details on the closed-time-path contour, is essential to build the relevant correlator representing the reduced density matrix, which for a single dark heavy pair is given by [152, 153]

$$\langle \phi_1(t', \boldsymbol{r}', \boldsymbol{R}') \phi_2^\dagger(t, \boldsymbol{r}, \boldsymbol{R}) \rangle \equiv \langle \boldsymbol{r}', \boldsymbol{R}' | \rho(t'; t) | \boldsymbol{r}, \boldsymbol{R} \rangle \,, \tag{12.1}$$

where we do not consider mixed terms of bound and scattering states of the form $\phi_b^\dagger \phi_s$, but only diagonal ones in eq. (12.1). In eq. (12.1), the density operator ρ has been projected into position space in terms of center-of-mass coordinates, but one can also project ρ on any state of interest, for instance on momentum states, where the correlator on the left-hand side would then be with respect to the momentum space.

The main advantage of the present approach is to allow for a diagrammatic derivation of the relevant in-vacuum and thermal processes: annihilations and decays, bound-state formation and dissociation, excitations and deexcitations of bound heavy pairs as well as thermal emissions and absorptions of unbound DM pairs. The diagrams can be organized over exploiting the power counting of the operators in pNRQED$_{\rm DM}$, namely as an expansion in $1/M$, multipole expansion in r and in the coupling constant α. In particular for the evolution of the bound-state density operator $\rho_b(t'; t)$, in the dipole limit and at leading order in the center-of-mass momentum $\boldsymbol{P}$ and coupling α, the

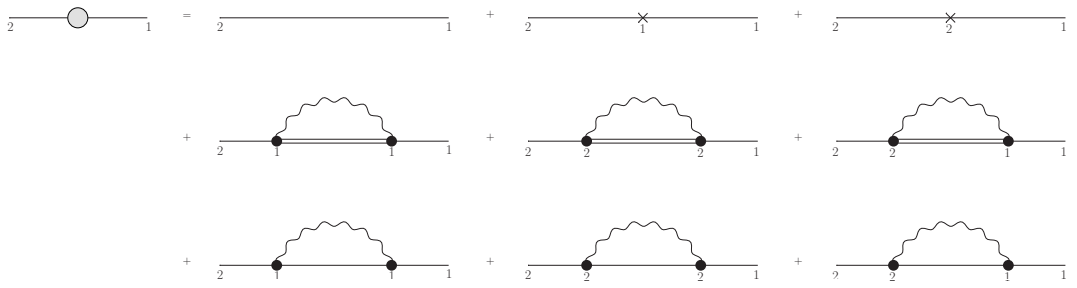

Figure 12.1: Diagrammatic expression of the evolution equation for the reduced bound-state density operator ρ_b in the real-time formalism, that corresponds to the propagator $\langle \phi_1^b(t', \boldsymbol{r}', \boldsymbol{R}') \phi_2^{b,\dagger}(t, \boldsymbol{r}, \boldsymbol{R}) \rangle$ in position space. It is expanded up to $\mathcal{O}(\boldsymbol{r}^2, \boldsymbol{P}^2/M^2)$, and consists of the diagrams on the right-hand side with electric-electric, magnetic-magnetic, electric-magnetic and magnetic-electric correlators at leading order in α. Single solid lines represent the bound-state propagator, double solid lines the scattering-state propagator. The local vertex coming from the dimension-six four-fermion operators, denoted by a cross in the last two diagrams of the first line, has an imaginary part that encompasses the decay of the bound pair into the dark light degrees of freedom. The black-dot vertices in the self-energy diagrams in the second and third line denote one of the two dipole vertices in fig. 4.1. The numbers 1 or 2 near the vertices stand for insertions of fields from the upper or lower branches of the closed-time path, respectively.

relevant diagrams are shown in figure 12.1. We will consider only the dominant S-wave annihilations and hence exclude the four-fermion operators of higher dimension than six. We will take the imaginary parts of the matching coefficients d_s and d_v at leading order in α, cf. eqs. (5.1), which are represented by the local cross vertex in the last two diagrams of the first line in fig. 12.1. The bound-state dissociation process and bound-state to bound-state transitions are inherited in the self-energy diagrams in the second and third row, respectively, where the black-dot vertex comprises the electric-dipole and Röntgen vertex, cf. fig. 4.1. As for the evolution equation for the scattering-state density operator ρ_s, one obtains the very similar structure of diagrams, by just replacing the single solid lines by double solid lines in fig. 12.1.

At order $1/M^0$ and r^0, the only relevant diagram is the tree-level diagram

$$\underset{2 \qquad\qquad 1}{\text{———}} \;=\; e^{-iH(t-t_0)} \rho_b(t_0; t_0) e^{iH(t-t_0)} \,, \tag{12.2}$$

and similarly for ρ_s, where $H = 2M + \boldsymbol{p}^2/M + \boldsymbol{P}^2/(4M)$ is the Hamiltonian of the reduced dark matter system at leading order in the laboratory frame, cf. eq. (4.3). The expression in (12.2) indeed defines the reduced density matrix $\rho_b(t,t) = e^{-iH(t-t_0)} \rho_b(t_0; t_0) e^{iH(t-t_0)}$ at leading order in the OQS formalism.[1] Our ultimate goal is to obtain a quantum

[1] Whenever there is no need for distinguishing two different time arguments, we will abbreviate $\rho(t,t) \equiv \rho(t)$ for any time t.

master equation for the system of the form[2]

$$\frac{\partial\rho(t)}{\partial t} = -i[H_{\text{eff}}, \rho(t)] + \mathcal{F}(t, \rho(t))\,, \tag{12.3}$$

where the first term on the right-hand side describes the usual unitary evolution, whereas the non-unitary dynamics is comprised in the second term. The density matrix ρ contains both bound and scattering states, and we take it in a diagonal form $\rho = \text{diag}(\rho_b, \rho_s)$. The effective Hamiltonian H_{eff} is in general different from H due to interactions with the thermal environment. We shall obtain in the next sections the explicit form of H_{eff} and $\mathcal{F}(t, \rho(t))$, by including the effects of bound- and scattering-state annihilations and the dipole transitions. In order to have a more simple and transparent overview, we treat the reaction processes once at a time according to the power counting in pNRQED$_{\text{DM}}$, and combine them into the quantum master equation (12.3) comprising all interactions at the end of this chapter.

12.1 Annihilations in a diluted system

As elaborated in chapter 2, the freeze-out dynamics is induced by the interplay between the universe expansion rate and the pair-annihilation rate. The DM particles are in equilibrium at high temperatures $T \gg M$ at some initial stage of the universe evolution. Then, the expanding universe cools down and the heavy dark particles depart from equilibrium once $T \lesssim M/25$.[3] The Sommerfeld- and bound-state effects enlarge the annihilation rate with decreasing T and hence smaller DM velocities, but eventually at late times all reactions fall out of equilibrium with respect to the expanding medium and, although annihilations may still occur, they are almost inefficient.

In the diagrammatic framework, the annihilation of heavy pairs is implemented via the last two diagrams in the first row of fig. 12.1 for bound states, and similarly for scattering states (by replacing single solid with double solid lines). We sum the contributions from ρ_b and ρ_s into $\rho = \text{diag}(\rho_b, \rho_s)$. The 211-type diagram reads

$$\int_{t_0}^{t} dt_1\, e^{-iH(t-t_1)}\,(-i\delta V^{\text{ann}})\, e^{-iH(t_1-t_0)}\rho(t_0)e^{iH(t-t_0)}\,, \tag{12.4}$$

whereas the 221-type diagram is the complex conjugate, i.e.

$$\int_{t_0}^{t} dt_1\, e^{-iH(t-t_0)}\rho(t_0)e^{iH(t_1-t_0)}\,(-i\delta V^{\text{ann}})^{\dagger}\, e^{iH(t-t_1)}\,, \tag{12.5}$$

[2]Notice that if no interactions with the thermal environment are present, the master equation (12.3) for the reduced system reduces to the von-Neumann equation for a standard closed quantum system, cf. footnote 1 in appendix D.

[3]We can compare again the situation with heavy quarkonium in a quark-gluon plasma. Bottomonium states in heavy-ion collisions will never experience a thermal freeze-out due to the short lifetime of the QGP. Indeed, if we approximate the hadronization temperature of the hot QCD medium and the bottom quark mass by $T_c \approx 200$ MeV and $M_b \approx 5$ GeV, respectively, then the smallest temperature-over-mass ratio is $T_c/M_b \approx 1/25$, and hence T_c is of the same order as the freeze-out temperature $T_F \approx M/25$. However, the thermal QGP itself ceases to exists at this point.

where the imaginary part of the local potential $\delta V^{\rm ann}$ can be read-off from eq. (5.19). If we inspect only S-wave annihilations at order $1/M^2$, $\delta V^{\rm ann} = -\frac{\delta^3(\boldsymbol{r})}{M^2}\big[2d_s - \boldsymbol{S}^2\,(d_s - d_v)\big]$. Taking into account the free diagram (12.2) and taking the time derivative according to the Leibniz integral rule, we find

$$\begin{aligned}\frac{d\rho(t)}{dt} &= -i\,[H,\rho(t)] \\ &\quad + (-i\delta V^{\rm ann})\,e^{-iH(t-t_0)}\rho(t_0)e^{iH(t-t_0)} + e^{-iH(t-t_0)}\rho(t_0)e^{iH(t-t_0)}\,(-i\delta V^{\rm ann})^\dagger\ . \end{aligned} \tag{12.6}$$

If we make the replacement $e^{-iH(t-t_0)}\rho(t_0;t_0)e^{iH(t-t_0)} \to \rho(t;t)$ as in ref. [153],[4] and split the local potential into its real and imaginary part, we obtain

$$\frac{d\rho(t)}{dt} = -i\,[H + {\rm Re}[\delta V^{\rm ann}],\rho(t)] + \{{\rm Im}[\delta V^{\rm ann}],\rho(t)\}\ , \tag{12.7}$$

which can already be compared with the Lindblad equation written in (11.1). Some comments are in order. First, the Hamiltonian H gets augmented by the real part of the local potential, giving rise to an effective Hamiltonian $H_{\rm eff}$ as already anticipated in the previous chapter. Hence ${\rm Re}[\delta V^{\rm ann}]$ contributes only to the unitary evolution of the reduced system. Second, the anticommutator term in (12.7), which can be compared with the anticommutator term in the Lindblad equation (11.1), implements the annihilation of the heavy pairs and induces a non-hermitian evolution as opposed to the commutator term. We will see in the subsequent chapter 13 that it indeed will correspond to the loss term of DM heavy-pair states. The anticommutator term $\{{\rm Im}[\delta V^{\rm ann}],\rho(t)\}$ contributes to $\mathcal{F}(t,\rho(t))$ in eq. (12.3). There is, however, a caveat in (12.7), because the right-hand side violates the conservation of probability of the single heavy-pair state, i.e. ${\rm Tr}[\dot\rho] = 0$ is not consistent with eq. (12.7). A proper quantum master equation should be compatible with the basic properties of the density operator and its probabilistic interpretation.

In order to circumvent this issue, we consider multi-pair density operators. In this way one can follow the probability flow between sectors with different number of dark matter pairs. In the context of NREFTs, a similar discussion can be found in refs. [155, 158]. In this work, we give a diagrammatic interpretation to multi-particle states and the associated density operator within pNRQED$_{\rm DM}$. The key observation is that the annihilation vertex in (5.18), as applied to a two-pair state, still generates one-pair states.[5] We consider a composite density matrix $\rho_{\rm I+II}$ made of two one-pair density matrices $\rho_{\rm I}$ and $\rho_{\rm II}$, each of them of the form $\rho_{\rm I(II)} = {\rm diag}(\rho_{b,{\rm I}(b,{\rm II})},\rho_{s,{\rm I}(s,{\rm II})})$ in the reduced one-particle systems I and II respectively. Generalizing the definition in eq. (12.1), we write for the density of a two-pair state $\rho_{\rm I+II} = \rho_{\rm I}\otimes\rho_{\rm II}$

$$\begin{aligned}&\langle\phi_{{\rm I},1}(t_1',\boldsymbol{r}_1',\boldsymbol{R}_1')\,\phi_{{\rm II},1}(t_2',\boldsymbol{r}_2',\boldsymbol{R}_2')\,\phi^\dagger_{{\rm I},2}(t_1,\boldsymbol{r}_1,\boldsymbol{R}_1)\phi^\dagger_{{\rm II},2}(t_2,\boldsymbol{r}_2,\boldsymbol{R}_2)\rangle \\ &\equiv \langle\boldsymbol{r}_1',\boldsymbol{R}_1';\boldsymbol{r}_2',\boldsymbol{R}_2'|\rho_{\rm I+II}(t',t)|\boldsymbol{r}_1,\boldsymbol{R}_1;\boldsymbol{r}_2,\boldsymbol{R}_2\rangle\ ,\end{aligned} \tag{12.8}$$

[4] We can approximate $e^{-iH(t-t_0)}\rho(t_0;t_0)e^{iH(t-t_0)} \approx \rho(t;t)$, since corrections are of higher order than $1/M^2$.

[5] The simultaneous annihilation of two heavy pairs would be an effect of order $1/M^4$ that we do not consider in this work.

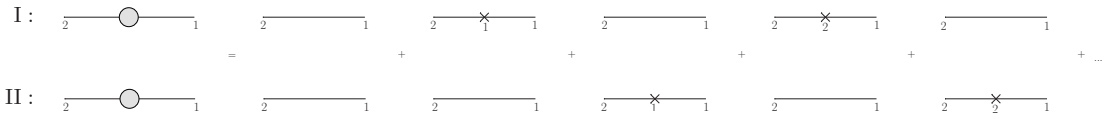

Figure 12.2: Diagrams at order r^0 in the multiple expansion and $\mathcal{O}(1/M^2)$ in the local potential, contributing to the two-pair density operator $\rho_{\rm I+II} = \rho_{\rm I} \otimes \rho_{\rm II}$.

where in the last line we define $t_1 = t_2 \equiv t$ and $t_1' = t_2' \equiv t'$. Diagrammatically, we have two disconnected graphs which are shown in fig. 12.2 at order r^0 and $1/M^2$. We have considered just one insertion at a time for the annihilation vertex, because two insertions would give a suppressed correction of order $1/M^4$. Moreover, we work at order r^0 and do not include dipole diagrams in this section, since dipole transitions will be treated in the subsequent section. The resulting evolution equation, that generalizes the one given in eq. (12.6) to a two-pair state, reads

$$\frac{d}{dt}\rho_{\rm I+II}(t) = \left\{-i\left[H_{\rm I}, \rho_{\rm I}(t)\right] + (-i\delta V_{\rm I}^{\rm ann})\,\rho_{\rm I}(t) + \rho_{\rm I}(t)\,(-i\delta V_{\rm I}^{\rm ann})^\dagger\right\} \otimes \rho_{\rm II}(t) + \rho_{\rm I}(t) \otimes \left\{-i\left[H_{\rm II}, \rho_{\rm II}(t)\right] + (-i\delta V_{\rm II}^{\rm ann})\,\rho_{\rm II}(t) + \rho_{\rm II}(t)\,(-i\delta V_{\rm II}^{\rm ann})^\dagger\right\} . \quad (12.9)$$

Our goal is to arrive at an evolution equation for a one-pair density matrix. We take the system I as the dark matter heavy-pair system of interest, but clearly the treatment at this stage is symmetric with respect to system II. We perform the trace of equation (12.9) over system II and get

$$\frac{d\rho_{\rm I}(t)}{dt} = -i\left[H_{\rm I} + {\rm Re}[\delta V_{\rm I}^{\rm ann}], \rho_{\rm I}(t)\right] + \{{\rm Im}[\delta V_{\rm I}^{\rm ann}], \rho_{\rm I}(t)\} + \rho_{\rm I}(t){\rm Tr}_{\rm II}\left[\{{\rm Im}[\delta V_{\rm II}^{\rm ann}], \rho_{\rm II}(t)\}\right] , \quad (12.10)$$

where ${\rm Tr}_{\rm II}\left[\rho_{\rm II}(t)\right] = 1$, and the commutator vanishes under the trace. Tracing instead (12.9) over system I, which leads to a quite similar evolution equation for $\rho_{\rm II}$, solving for the anticommutator $\{{\rm Im}[\delta V_{\rm II}^{\rm ann}], \rho_{\rm II}(t)\}$ and substituting it in (12.10), leads to

$$\frac{d\rho_{\rm I}(t)}{dt} = -i\left[H_{\rm I} + {\rm Re}[\delta V_{\rm I}^{\rm ann}], \rho_{\rm I}(t)\right] + \{{\rm Im}[\delta V_{\rm I}^{\rm ann}], \rho_{\rm I}(t)\} - 2\rho_{\rm I}(t)\,{\rm Tr}_{\rm I}\left[{\rm Im}[\delta V_{\rm I}^{\rm ann}]\,\rho_{\rm I}(t)\right] , \quad (12.11)$$

and the equation for system I is now uncoupled from system II. The physical meaning of the last term in eq. (12.11) can be understood as a *feed down* of the composite two-pair state into the one-pair sector due to the annihilation of a single heavy pair at order $1/M^2$. In other words, it injects a probability flow from a higher multi-pair state to a state with lower DM pairs. The trace in (12.11) implies that one has to sum over all possible annihilations of a one-pair system, namely for both bound and scattering states. As a crucial consistency check, we can perform the trace over system I of the right-hand side of eq. (12.11), and observe that it vanishes (at variance with eq. (12.7)). The evolution equation (12.11) is, therefore, consistent with the probabilistic interpretation of the one-pair density matrix. There is, however, an essential difference between (12.11)

and the Lindblad equation in (11.1), the latter being a linear differential equation in ρ. The third term on the right-hand side of eq. (12.11) is indeed quadratic in the one-pair density matrix. The master equation (12.11) does not acquire a Lindblad form, and, hence, is not linear in the density operator.

There is a fundamental physical reasoning behind the difference between the evolution equations (12.11) and (11.1). First of all, the single closed Lindblad equation accounts for the evolution of a general reduced density operator of the full multi-pair state in the reduced heavy dark matter system, which in principle consists of an ensemble of N dark heavy pairs. Instead, if we want to extract the time evolution of the one-pair density operator, whose knowledge may be sufficient in order to calculate certain observables like the number density (that in turn is related to the DM relic abundance) or the pressure of the heavy pairs in the thermal bath, by marginalizing/integrating over the $N-1$ heavy pairs, one would encounter a network of coupled equations: the evolution of the one-pair density is given by a self-term plus a sum over two-pair terms, the evolution of the two-pair density is given by a self-term plus a sum over three-pair terms, and so on, which in classical kinetic theory is known as the Bogoliubov-Born-Green-Kirkwood-Yvon (BBGKY) hierarchy [159–162].[6]

Second, in this work we have truncated the number of heavy pairs to only two, and assumed the two-pair density operator $\rho_{\mathrm{I+II}}$ to be decomposable into a direct product of two one-pair densities ρ_{I} and ρ_{II}, which we expect to be adequate for diluted dark matter.[7] Our procedure is closely related to the molecular chaos approximation in kinetic theory,[8] but built in from the start at the diagrammatic level, cf. fig. 12.2, by the separation of the two mutually non-interacting systems I and II, where the reduced Hilbert space of the composite system I+II is a tensor product space $\mathcal{H}_{\mathrm{I+II}} = \mathcal{H}_{\mathrm{I}} \otimes \mathcal{H}_{\mathrm{II}}$, such that for a pure state we can indeed write $\rho = |\phi_{\mathrm{I}}\phi_{\mathrm{II}}\rangle\langle\phi_{\mathrm{I}}\phi_{\mathrm{II}}| = |\phi_{\mathrm{I}}\rangle\langle\phi_{\mathrm{I}}| \otimes |\phi_{\mathrm{II}}\rangle\langle\phi_{\mathrm{II}}| = \rho_{\mathrm{I}} \otimes \rho_{\mathrm{II}}$.

Since the quantum master equation (12.11) is a closed evolution equation for a single annihilating heavy dark matter pair, we will drop from now on the index I for the ease of notation.

[6] We remark that the BBGKY hierarchy for the one-body, two-body, ..., distribution functions, that one recovers by marginalizing the Liouville equation for the multiparticle joint phase-space distribution function, is usually done for a closed system. In our case, the starting point would not be the von-Neumann equation, but instead the Lindblad equation since the thermal environment has already been traced out. But we expect there to be a, yet to be checked, consistency between the hierarchy obtained in a closed quantum system and in an open quantum system.

[7] We assume a diluted system for the heavy dark matter pair evolution around freeze-out, and hence expect the individual non-relativistic pairs to be localized at regions sufficiently far apart from each other, such that their mutual wavefunctions do not overlap and hence any exchange density vanishes. There is, therefore, no need to symmetrize the spatial wavefunctions and the bosonic quantum nature of the fermion-antifermion pairs becomes irrelevant. The systems I and II, each representing a heavy DM pair, are then distinguishable and obey a classical statistical behaviour.

[8] The assumption of *molecular chaos* is based on the hypothesis that the incoming velocities of colliding particles are uncorrelated, and eventually allows to reduce the open network of linear evolution equations, i.e. the BBGKY hiearchy, to a closed set of non-linear Boltzmann equations, in turns of loosing the time-reversibility of the evolving system.

12.2 Contributions from the dipole transitions

We focus now on the dipole interactions shown in the second and third row of fig. 12.1, that are generated by the dipole vertices depicted in fig. 4.1, and we recall that they give rise to several reactions, that conserve the number of heavy pairs, and govern the dynamics of the transitions between scattering and bound states. In other words, they determine the relative populations of above- and below-threshold states. The self-energy diagrams, that will contribute to the dissociation of the bound pairs within the bound-state density evolution, are shown in figure 12.3. As for bound-state to bound-state transitions, we take into account the same diagrams upon replacing the double solid lines in the loops by single solid lines. We do not display explicitly the one-loop self-energy diagrams inheriting the bound-state formation as well as the continuum dipole transitions that enter the evolution equation for ρ_s, since they can be straightforwardly obtained by replacing single with double solid lines in each of the self-energy diagrams for the density ρ_b.

In close analogy with the analysis carried out in refs. [152,153], the full set of one-loop dipole diagrams implement the following near-threshold observables that are dominant for the hierarchy of energy scales in (3.2): (i) a thermal decay width of bound states into scattering states by photo-dissociation; (ii) a correction to the mass of the bound as well as scattering states; (iii) the generation of bound states through the emission of dark photons from an above threshold scattering state. In addition, we include the bound-to-bound transitions and the analogue process for the scattering states as well as the recoil effect due to the relative motion of the center of mass of the heavy pairs with respect to the thermal bath. Our derivation of the evolution equations follows closely the steps given in ref. [153]. However, some differences hold that need to be clarified. In ref. [153], the dynamics via electric-dipole transitions involves color-singlet and colored-octet quarkonia, that are described by different potentials, written in (8.8) at leading order, and hence different Hamiltonians. In the abelian case that is considered in this chapter, there is no such distinction since bound and scattering states are both included in the spectrum of the very same Hamiltonian. Only when projecting the operators onto the Hilbert space of interest, i.e. either on bound or scattering states, the corresponding self-energies, which are formally the same, acquire a clear meaning for each of the two distinct parts of the heavy-pair energy spectrum. The projection of the density operators on the Hilbert states of the dark matter pairs will be the subject of the subsequent chapter 13.

In the following, we shall label the self-energy diagrams in such a way that one can still appreciate at this stage the processes for the bound- and scattering-state configurations of a single heavy dark matter pair. Moreover, if we include a second heavy-pair system II in analogy to the preceding section, we observe that it will not play a role for the dipole transitions, i.e. the system II decouples entirely once we integrate it out, as opposed to the annihilation processes. We will elaborate on this important point at the end of this section. In the case of the dipole transitions, bound and scattering states can turn into each other. For this reason we find it more convenient to directly start with

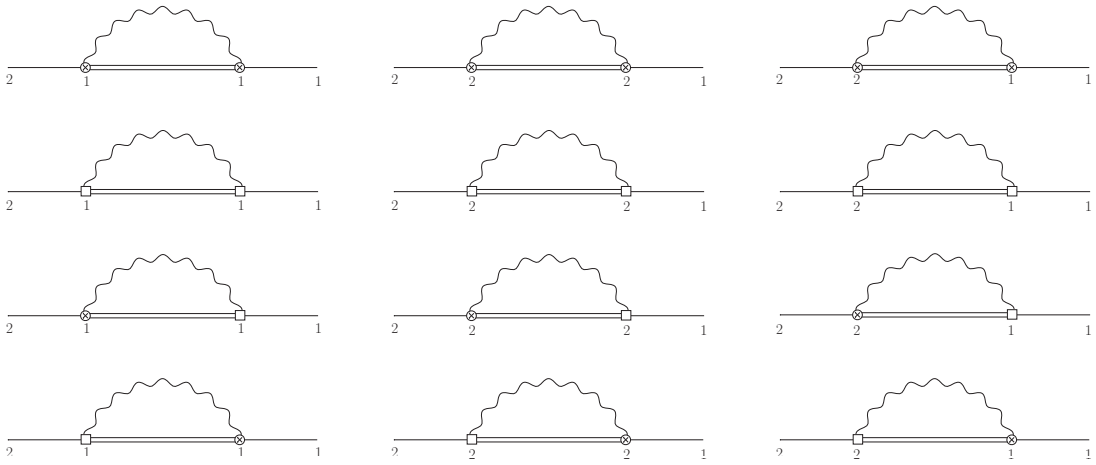

Figure 12.3: One-loop self-energy diagrams contributing at order $\boldsymbol{r}^2$ and $\boldsymbol{P}^2/M^2$ to the reduced bound-state density operator ρ_b. In addition, there is a second set of diagrams involving only single solid lines, that inherit the transitions among bound states, which we do not display explicitily though. The tree-level diagrams have been already included in fig. 12.2.

two separate equations for the corresponding reduced density operators, and we give the result for the evolution equations for ρ_b and ρ_s as follows:[9]

$$\begin{aligned}\frac{d\rho_b(t)}{dt} &= -i\,[H,\rho_b(t)] \\ &\quad + (-i\Sigma_{bs} - i\Sigma_{bb})\rho_b(t) + \rho_b(t)(-i\Sigma_{bs} - i\Sigma_{bb})^\dagger + \Xi_{bs}(\rho_s(t),t) + \Xi_{bb}(\rho_b(t),t)\,,\end{aligned} \tag{12.12}$$

for the bound-state density evolution, and

$$\begin{aligned}\frac{d\rho_s(t)}{dt} &= -i\,[H,\rho_s(t)] \\ &\quad + (-i\Sigma_{sb} - i\Sigma_{ss})\rho_s(t) + \rho_s(t)(-i\Sigma_{sb} - i\Sigma_{ss})^\dagger + \Xi_{sb}(\rho_b(t),t) + \Xi_{ss}(\rho_s(t),t)\,,\end{aligned} \tag{12.13}$$

for the scattering-state density evolution, where each of the self-energies Σ_{bs}, Σ_{bb}, Σ_{sb}, Σ_{ss} and Ξ_{bs}, Ξ_{bb}, Ξ_{sb}, Ξ_{ss} comprises several diagrams, namely[10]

$$\Sigma = \Sigma^{ee} + \Sigma^{mm} + \Sigma^{em} + \Sigma^{me}\,, \tag{12.14}$$

[9] We remark that the leading order term, i.e. the first diagram on the right-hand side of fig. 12.1, has been already included in the preceding section when dealing with the annihilations. We add it also to the eqs. (12.12) and (12.13) to make the unitary commutator term noticeable. Later on, when summing up the contributions from annihilations and dipole transitions, we take it into account only once.

[10] We remind that the four Σ's are all equal before we project on either bound or scattering states; similarly for the Ξ's.

$$\Xi = \Xi^{ee} + \Xi^{mm} + \Xi^{em} + \Xi^{me}\,, \tag{12.15}$$

where we use the index notation in analogy to the self-energy expressions written in section 6.1.2, cf. eqs. (6.56)–(6.59). The self-energies read[11]

$$-i\Sigma^{ee}(t) = (ig)^2 \int_{t_0}^{t} dt_2\, r^i E^i(t,\boldsymbol{R}) e^{-iH(t-t_2)} r^j E^j(t_2,\boldsymbol{R}') e^{iH(t-t_2)}\,, \tag{12.16}$$

$$-i\Sigma^{mm}(t) = \frac{(ig)^2}{(4M)^2} \int_{t_0}^{t} dt_2\, \boldsymbol{r}\cdot\{\boldsymbol{P}\times,\boldsymbol{B}(t,\boldsymbol{R})\} e^{-iH(t-t_2)} \boldsymbol{r}\cdot\{\boldsymbol{P}\times,\boldsymbol{B}(t_2,\boldsymbol{R}')\} e^{iH(t-t_2)}\,, \tag{12.17}$$

$$-i\Sigma^{em}(t) = \frac{(ig)^2}{4M} \int_{t_0}^{t} dt_2\, \boldsymbol{r}\cdot\{\boldsymbol{P}\times,\boldsymbol{B}(t,\boldsymbol{R})\} e^{-iH(t-t_2)} \boldsymbol{r}\cdot\boldsymbol{E}(t_2,\boldsymbol{R}') e^{iH(t-t_2)}\,, \tag{12.18}$$

$$-i\Sigma^{me}(t) = \frac{(ig)^2}{4M} \int_{t_0}^{t} dt_2\, \boldsymbol{r}\cdot\boldsymbol{E}(t,\boldsymbol{R}) e^{-iH(t-t_2)} \boldsymbol{r}\cdot\{\boldsymbol{P}\times,\boldsymbol{B}(t_2,\boldsymbol{R}')\} e^{iH(t-t_2)}\,, \tag{12.19}$$

$$\Xi^{ee}(t) = ig(-ig) \int_{t_0}^{t} dt_2 \left[r^i E^i(t_2,\boldsymbol{R}')\rho(t) e^{-iH(t-t_2)} r^j E^j(t,\boldsymbol{R}) e^{iH(t-t_2)} + \text{h.c.} \right], \tag{12.20}$$

$$\Xi^{mm}(t) = \frac{ig(-ig)}{(4M)^2} \int_{t_0}^{t} dt_2 \Big[\boldsymbol{r}\cdot\{\boldsymbol{P}\times,\boldsymbol{B}(t_2,\boldsymbol{R}')\}\rho(t) e^{-iH(t-t_2)} \boldsymbol{r}\cdot\{\boldsymbol{P}\times,\boldsymbol{B}(t,\boldsymbol{R})\} e^{iH(t-t_2)} + \text{h.c.} \Big]\,, \tag{12.21}$$

$$\Xi^{em}(t) = \frac{ig(-ig)}{4M} \int_{t_0}^{t} dt_2 \left[\boldsymbol{r}\cdot\{\boldsymbol{P}\times,\boldsymbol{B}(t_2,\boldsymbol{R}')\}\rho(t) e^{-iH(t-t_2)} \boldsymbol{r}\cdot\boldsymbol{E}(t,\boldsymbol{R}) e^{iH(t-t_2)} + \text{h.c.} \right], \tag{12.22}$$

$$\Xi^{me}(t) = \frac{ig(-ig)}{4M} \int_{t_0}^{t} dt_2 \left[\boldsymbol{r}\cdot\boldsymbol{E}(t_2,\boldsymbol{R}')\rho(t) e^{-iH(t-t_2)} \boldsymbol{r}\cdot\{\boldsymbol{P}\times,\boldsymbol{B}(t,\boldsymbol{R})\} e^{iH(t-t_2)} + \text{h.c.} \right]. \tag{12.23}$$

The physical interpretation of the expressions above, its real and imaginary parts respectively, is a thermal mass shift to the heavy pair mass on the one hand, a thermal width and a thermal cross section on the other hand. When considering the self-energy diagrams that involve both bound and scattering states, the imaginary parts implement the photo-dissociation of a bound state into an unbound pair, whereas the loss of a scattering state can be interpreted as a bound state forming together with the emission of a dark photon. Excitations and de-excitations together with bremsstrahlung processes correspond to Σ_{bb} and Σ_{ss} respectively. For example, Ξ_{bs} implements the reverse process of the one induced by the imaginary part of Σ_{bs}, namely the formation of a bound-state and a dark photon from a "decaying" scattering state. An explicit one-to-one correspondence between the operators (12.16)–(12.23) appearing in the evolution equations (12.12)–(12.13) and the thermal dipole rates will be shown in the next chapter.

Owing to the conservation of the probability for the sum of bound and scattering states (in this section we exclude processes that annihilate away the heavy pairs), one

[11] In order to obtain the evolution eqs. (12.12) and (12.13), we have used the Leibniz integral rule, followed by the replacement $e^{-iH(t-t_0)}\rho(t_0;t_0)e^{iH(t-t_0)} \approx \rho(t;t)$ as in ref. [153].

can find two relations among the various Σ's and Ξ's. Summing up eqs. (12.12) and (12.13), and taking the trace we obtain

$$\mathrm{Tr}\left[\rho_b(-i\Sigma_{bs}+(-i\Sigma_{bs})^\dagger - i\Sigma_{bb}+(-i\Sigma_{bb})^\dagger)\right] = \mathrm{Tr}\left\{\Xi_{sb}(\rho_b(t,t),t)+\Xi_{bb}(\rho_b(t,t),t)\right\}\,, \tag{12.24}$$

$$\mathrm{Tr}\left[\rho_s(-i\Sigma_{sb}+(-i\Sigma_{sb})^\dagger - i\Sigma_{ss}+(-i\Sigma_{ss})^\dagger)\right] = \mathrm{Tr}\left\{\Xi_{bs}(\rho_s(t,t),t)+\Xi_{ss}(\rho_s(t,t),t)\right\}\,. \tag{12.25}$$

Such conditions reflect the optical theorem, which will manifest once we project them onto either bound or scattering states in the subsequent chapter.

Since we invoked a second system II to derive a consistent master equation when treating diagrammatically the annihilation process in the previous section, it comes natural to ask whether the inclusion of the second system alters the derivation of the evolution equation from the dipole diagrams. In fact, one finds that this is not the case. Since we are working at order $\boldsymbol{r}^2$, there are two different sets of diagrams to be discussed. The first set involves the dark photon to be always attached on either the heavy pair in system I or the one in system II. Hence, the systems I and II are diagrammatically disconnected. The second set corresponds to diagrams where the dark photon connects the heavy pair in system I with the one in system II. For the first set of diagrams it can be straightforwardly shown that, when tracing over the system II and reducing the evolution equation for the composite density operator $\rho_{\mathrm{I+II}}$ to ρ_{I} for a single heavy-pair state, one finds exactly the relations in eq. (12.24) and (12.25) for the system II. This guarantees the first set of disjoint self-energy diagrams to vanish. As for the second set of diagramms, where a dark photon connects the two single heavy-pair states, which we call the *dipole exchange* diagrams (cf. fig. E.1 where we display only the electric-transition exchange diagrams between the systems I and II), we also find them to vanish when tracing over the system II, see the detailed derivation in appendix E. A more intuitive argument is that this latter set of diagrams does not introduce any imaginary part, and therefore does not induce a contribution to the non-unitary evolution of the density operators.

12.3 Summary: quantum master equations

So far we have treated separately the processes that govern the evolution of the heavy dark matter pairs at order r^0, i.e. the annihilations, and at order r^2, i.e. the dipole transitions, in section 12.1 and 12.2, respectively. We combine now the individual results into the overall evolution equations for the scattering- and bound-state density operators ρ_s and ρ_b, respectively. They read in a compact form as follows:

$$\frac{d\rho_b(t)}{dt} = -i\left[H_{b,\mathrm{eff}},\rho_b(t)\right]+\mathcal{F}_b(\rho_b(t),\rho_s(t))\,, \tag{12.26}$$

$$\frac{d\rho_s(t)}{dt} = -i\left[H_{s,\mathrm{eff}},\rho_s(t)\right]+\mathcal{F}_s(\rho_b(t),\rho_s(t))\,, \tag{12.27}$$

where the effective Hamiltonians are

$$H_{b,\text{eff}} = H_b + \text{Re}[\delta V_b^{\text{ann}}] + \text{Re}[\Sigma_{bs}] + \text{Re}[\Sigma_{bb}]\,, \tag{12.28}$$

$$H_{s,\text{eff}} = H_s + \text{Re}[\delta V_s^{\text{ann}}] + \text{Re}[\Sigma_{sb}] + \text{Re}[\Sigma_{ss}]\,, \tag{12.29}$$

and the non-unitary evolution is dictated by $\mathcal{F}_b \equiv \mathcal{F}_b^{\text{ann}} + \mathcal{F}_b^{\text{dip}}$, with

$$\mathcal{F}_b^{\text{ann}}(\rho_b(t), \rho_s(t)) = \{\text{Im}[\delta V_b^{\text{ann}}], \rho_b(t)\} - 2\rho_b(t)\,\text{Tr}\,[\text{Im}[\delta V^{\text{ann}}]\,\rho(t)]\,, \tag{12.30}$$

$$\mathcal{F}_b^{\text{dip}}(\rho_b(t), \rho_s(t)) = \{\text{Im}[\Sigma_{bs}], \rho_b\} + \{\text{Im}[\Sigma_{bb}], \rho_b\} + \Xi_{bs}(\rho_s) + \Xi_{bb}(\rho_b)\,, \tag{12.31}$$

for the bound-state density operator, and similar expressions hold for the scattering-state density operator as well, with $\mathcal{F}_s \equiv \mathcal{F}_s^{\text{ann}} + \mathcal{F}_s^{\text{dip}}$,

$$\mathcal{F}_s^{\text{ann}}(\rho_b(t), \rho_s(t)) = \{\text{Im}[\delta V_s^{\text{ann}}], \rho_s(t)\} - 2\rho_s(t)\,\text{Tr}\,[\text{Im}[\delta V^{\text{ann}}]\,\rho(t)]\,, \tag{12.32}$$

$$\mathcal{F}_s^{\text{dip}}(\rho_b(t), \rho_s(t)) = \{\text{Im}[\Sigma_{sb}], \rho_s\} + \{\text{Im}[\Sigma_{ss}], \rho_s\} + \Xi_{sb}(\rho_b) + \Xi_{ss}(\rho_s)\,. \tag{12.33}$$

The quantum master equations (12.26) and (12.27) do not look like a Lindblad equation, cf. eq. (11.1). However, following the derivation in ref. [152], it can be shown that in the limit $T \gg M\alpha^2$ the terms implementing the dipole transitions may be brought into a Lindblad form, by extracting explicitly the expressions of the collapse operators from the Σ's and Ξ's. In this chapter we consider, however, the hierarchy (3.2), where the temperature is ultrasoft and supposed to be related to most of the times after the DM freeze-out. We neither pursue to match the master equations to a Lindbladian form nor we aim to solve them directly in this work. Instead we want to determine the coupled rate equations in the Boltzmann limit out of the equations of motion in (12.26) and (12.27) for the reduced density operators ρ_b and ρ_s, respectively, in this way justifying the raison d'être of the Boltzmann equations that have been used in the previous chapters in order to calculate the dark matter relic abundance.

Chapter 13

Semi-classical limit: reduction to Boltzmann-like equations

We would like to understand how the rate equations (7.1)–(7.3) together with the various thermally averaged observables in the laboratory frame that have been computed in this work, such as the bound-state formation cross section in (6.62), the bound-state dissociation width (6.94), the transitions between different bound states (cf. (6.103) and (6.104)), but also the annihilation cross section (5.28) and decay widths (5.30)–(5.31) emerge from the quantum master equations (12.26) and (12.27). In particular, we shall highlight under which approximations the semi-classical limit in terms of the Boltzmann transport equations can be approached.

A similar derivation has been put forward for heavy quarkonia in a hot QCD medium, see e.g. refs. [99, 163–165]. We shall derive the evolution equations for the Wigner-Weyl transform of the density matrix, known as the Wigner distribution function [166].[1] This is an object that generalizes the classical Boltzmann distribution function to the quantum realm. The Wigner function is often dubbed a *quasi-probability* distribution, most notably by the fact that it can take negative or even complex values due to the uncertainty principle [171, 172],[2] however only on compact regions of size $\hbar$ in phase space. It is entirely positive semi-definite in the classical limit $\hbar \to 0$, or at regions in phase space much larger than $\hbar$ (i.e. the semi-classical limit, where the phase space is coarsered). We Wigner-transform the quantum master equations (12.26) and (12.27) between a bra and a ket with the same discrete quantum numbers. Whenever it is

[1] The mapping between density operators and semi-classical distribution functions, which allows to present the quantum nature of the system as a statistical theory on a classical phase space, is not unique [167]. In fact, besides the Wigner distribution, common choices for the quasi-probability distribution, arising because of different possibilities of operator orderings, involve the Glauber–Sudarshan (cf. refs. [168, 169]) or Husimi functions (cf. ref. [170]) frequently used e.g. in the field of quantum optics. These functions are related to each other in terms of Weierstrass transforms.

[2] To be more rigorous in terms of the notion of pseudo-differential operators, the Wigner function corresponds to the symbol of the density operator (similarly to as $H(\boldsymbol{x}, \boldsymbol{p})$ denotes the Weyl-symbol of the Hamiltonian operator $\hat{H}(\hat{\boldsymbol{x}}, \hat{\boldsymbol{p}})$ in ordinary quantum mechanics), while the classical phase space distribution function is the principal symbol.

possible, we adopt the abbreviation $(n, \ell, m) \equiv n$ and $(S, m_S) \equiv S$. The quasi-probability distribution function of a bound state with internal quantum numbers (n, S) is[3,4]

$$f^b_{n,S}(t, \boldsymbol{P}, \boldsymbol{R}) \equiv \int_{\boldsymbol{P}'} e^{i\boldsymbol{P}'\cdot\boldsymbol{R}} \langle \boldsymbol{P} + \boldsymbol{P}'/2; n; S|\rho_b|\boldsymbol{P} - \boldsymbol{P}'/2; n; S\rangle \,, \tag{13.1}$$

and similarly for a scattering state, i.e.

$$f^s_S(t, \boldsymbol{P}, \boldsymbol{R}, \boldsymbol{p}, \boldsymbol{r}) \equiv \int_{\boldsymbol{p}'} e^{i\boldsymbol{p}'\cdot\boldsymbol{r}} \int_{\boldsymbol{P}'} e^{i\boldsymbol{P}'\cdot\boldsymbol{R}} \langle \boldsymbol{P} + \boldsymbol{P}'/2; \boldsymbol{p} + \boldsymbol{p}'/2; S|\rho_s|\boldsymbol{P} - \boldsymbol{P}'/2; \boldsymbol{p} - \boldsymbol{p}'/2; S\rangle \,. \tag{13.2}$$

In case the quantum numbers in the bra and ket are not the same, we will note them in the subscript of the Wigner functions (e.g. $f^b_{nn',SS'}$). Moreover, on the left-hand side of eq. (13.1), the subscript n has to be understood comprising the orbital and magnetic quantum numbers, and the index S includes the total spin quantum number S and the magnetic spin quantum number m_S of the heavy-pair system. Next, we define the Wigner transformation of a generic operator as

$$\hat{\mathcal{O}}\Big|_{\rm WT} \equiv \int_{\boldsymbol{P}'} e^{i\boldsymbol{P}'\cdot\boldsymbol{R}} \langle \boldsymbol{P} + \boldsymbol{P}'/2; n; S|\hat{\mathcal{O}}|\boldsymbol{P} - \boldsymbol{P}'/2; n'; S'\rangle \,, \tag{13.3}$$

(and analogously for a projection onto scattering states) that we will use in the following. It is important to note that the state vectors used in the definition of the Wigner transforms (13.1)–(13.2) represent time-independent eigenstates of the Hamiltonian H, cf. eq. (4.3) at leading order. In the following calculations, we will project the energy eigenstates into position space in order to create the wave functions of bound and scattering states. For instance in the case of a para- or orthodarkonium, the projection gives at leading order

$$\langle \boldsymbol{R}, \boldsymbol{r}|\boldsymbol{P}; n; S\rangle = e^{i\boldsymbol{P}\cdot\boldsymbol{R}} \Psi_n(\boldsymbol{r})|S\rangle \,, \tag{13.4}$$

where the residual ket refers to the spin. Moreover, we will use the completeness relations for the position eigenstates and the bound and scattering states:

$$\mathbb{1} = \int_{\boldsymbol{r}} \int_{\boldsymbol{R}} |\boldsymbol{r}; \boldsymbol{R}\rangle\langle \boldsymbol{r}; \boldsymbol{R}| \,, \tag{13.5}$$

$$\mathbb{1} = \sum_S \int_{\boldsymbol{P}} \left[\sum_n |\boldsymbol{P}; n; S\rangle\langle \boldsymbol{P}; n; S| + \int_{\boldsymbol{p}} |\boldsymbol{P}; \boldsymbol{p}; S\rangle\langle \boldsymbol{P}; \boldsymbol{p}; S| \right] . \tag{13.6}$$

[3]Note that the Wigner distribution functions are dimensionless. Since $[\rho_b] = [\rho_s] = 0$, $[|\boldsymbol{P}; n; S\rangle] = -3/2$, $[|\boldsymbol{P}; \boldsymbol{p}; S\rangle] = -3$, it follows that $[f^b_{n,S}] = [f^s_S] = 0$. Integrating the Wigner functions, then $n_b(\boldsymbol{R}, t) = \sum_{n,S} n^S_n = \sum_{n,S} \int_{\boldsymbol{P}} f^b_{n,S}$ corresponds to the bound-state number density, while $n_s(\boldsymbol{r}, \boldsymbol{R}, t) = \sum_S \int_{\boldsymbol{p}} \int_{\boldsymbol{P}} f^s_S$ is the scattering-state number density. Then $N_b(t) = \int_{\boldsymbol{R}} n_b$ and $N_s(t) = \int_{\boldsymbol{r}} \int_{\boldsymbol{R}} n_s$ count the numbers of bound and unbound pairs, respectively.

[4]From now on we abbreviate $\int_{\boldsymbol{x}} \equiv \int d^3x$ for position-space integrals and $\int_{\boldsymbol{p}} \equiv \int \frac{d^3p}{(2\pi)^3}$ for integrals in momentum space.

We perform the Wigner transformations like in (13.1) and (13.2) on the equations of motion (12.26) and (12.27), respectively. The left-hand sides can be transformed straightforwardly, whereas

$$
\begin{aligned}
&-i\int_{\boldsymbol{P}'} e^{i\boldsymbol{P}'\cdot\boldsymbol{R}}\langle \boldsymbol{P}+\frac{\boldsymbol{P}'}{2};n;S|\left[H_b,\rho_b(t)\right]|\boldsymbol{P}-\frac{\boldsymbol{P}'}{2};n;S\rangle\\
&\quad=-i\int_{\boldsymbol{P}'} e^{i\boldsymbol{P}'\cdot\boldsymbol{R}}\left(E_n^{P+P'/2}-E_n^{P-P'/2}\right)\langle \boldsymbol{P}+\frac{\boldsymbol{P}'}{2};n;S|\rho_b(t)|\boldsymbol{P}-\frac{\boldsymbol{P}'}{2};n;S\rangle\\
&\quad=-i\frac{\boldsymbol{P}}{2M}\cdot\int_{\boldsymbol{P}'}\boldsymbol{P}' e^{i\boldsymbol{P}'\cdot\boldsymbol{R}}\langle \boldsymbol{P}+\frac{\boldsymbol{P}'}{2};n;S|\rho_b(t)|\boldsymbol{P}-\frac{\boldsymbol{P}'}{2};n;S\rangle\\
&\quad=-\frac{\boldsymbol{P}\cdot\boldsymbol{\nabla}_{\boldsymbol{R}}}{2M}\int_{\boldsymbol{P}'} e^{i\boldsymbol{P}'\cdot\boldsymbol{R}}\langle \boldsymbol{P}+\frac{\boldsymbol{P}'}{2};n;S|\rho_b(t)|\boldsymbol{P}-\frac{\boldsymbol{P}'}{2};n;S\rangle\\
&\quad=-\frac{\boldsymbol{P}}{2M}\cdot\boldsymbol{\nabla}_{\boldsymbol{R}} f^b_{n,S}(t,\boldsymbol{P},\boldsymbol{R})\,,
\end{aligned}
\tag{13.7}
$$

and similarly

$$
\begin{aligned}
&-i\int_{\boldsymbol{p}'} e^{i\boldsymbol{p}'\cdot\boldsymbol{r}}\int_{\boldsymbol{P}'} e^{i\boldsymbol{P}'\cdot\boldsymbol{R}}\langle \boldsymbol{P}+\frac{\boldsymbol{P}'}{2};\boldsymbol{p}+\frac{\boldsymbol{p}'}{2};S|\left[H_s,\rho_s(t)\right]|\boldsymbol{P}-\frac{\boldsymbol{P}'}{2};\boldsymbol{p}-\frac{\boldsymbol{p}'}{2};S\rangle\\
&\quad=-\left(\frac{\boldsymbol{P}}{2M}\cdot\boldsymbol{\nabla}_{\boldsymbol{R}}+2\frac{\boldsymbol{p}}{M}\cdot\boldsymbol{\nabla}_{\boldsymbol{r}}\right) f^s_S(t,\boldsymbol{P},\boldsymbol{R},\boldsymbol{p},\boldsymbol{r})\,.
\end{aligned}
\tag{13.8}
$$

On the other hand, the commutator term $-i\left[\mathrm{Re}[\delta V^{\mathrm{ann}}],\rho\right]$ transforms in case of the bound state with annihilation operators at order $1/M^2$ as follows:

$$
\begin{aligned}
&-i\int_{\boldsymbol{P}'} e^{i\boldsymbol{P}'\cdot\boldsymbol{R}}\langle \boldsymbol{P}+\frac{\boldsymbol{P}'}{2};n;S|\left[\mathrm{Re}[\delta V_b^{\mathrm{ann}}],\rho_b(t)\right]|\boldsymbol{P}-\frac{\boldsymbol{P}'}{2};n;S\rangle\\
&\quad=\frac{i}{M^2}\left[2\mathrm{Re}[d_s]-S(S+1)(\mathrm{Re}[d_s]-\mathrm{Re}[d_v])\right]\\
&\qquad\times\int_{\boldsymbol{P}'} e^{i\boldsymbol{P}'\cdot\boldsymbol{R}}\langle \boldsymbol{P}+\frac{\boldsymbol{P}'}{2};n;S|\left(\delta^3(\boldsymbol{r})\rho_b(t)-\rho_b(t)\delta^3(\boldsymbol{r})\right)|\boldsymbol{P}-\frac{\boldsymbol{P}'}{2};n;S\rangle\\
&\quad=\frac{i}{M^2}\left[2\mathrm{Re}[d_s]-S(S+1)(\mathrm{Re}[d_s]-\mathrm{Re}[d_v])\right]\\
&\qquad\times\sum_{n_1}\int_{\boldsymbol{P}'} e^{i\boldsymbol{P}'\cdot\boldsymbol{R}}\Bigg(\Psi^*_n(\boldsymbol{0})\Psi_{n_1}(\boldsymbol{0})\,\langle \boldsymbol{P}+\frac{\boldsymbol{P}'}{2};n_1;S|\rho_b(t)|\boldsymbol{P}-\frac{\boldsymbol{P}'}{2};n;S\rangle\\
&\qquad\qquad-\Psi^*_{n_1}(\boldsymbol{0})\Psi_n(\boldsymbol{0})\,\langle \boldsymbol{P}+\frac{\boldsymbol{P}'}{2};n;S|\rho_b(t)|\boldsymbol{P}-\frac{\boldsymbol{P}'}{2};n_1;S\rangle\Bigg)\\
&\quad=\frac{i}{M^2}\left[2\mathrm{Re}[d_s]-S(S+1)(\mathrm{Re}[d_s]-\mathrm{Re}[d_v])\right]\\
&\qquad\times\sum_{n_1}\left(\Psi^*_n(\boldsymbol{0})\Psi_{n_1}(\boldsymbol{0})f^b_{n_1n,S}(t,\boldsymbol{P},\boldsymbol{R})-\Psi^*_{n_1}(\boldsymbol{0})\Psi_n(\boldsymbol{0})f^b_{nn_1,S}(t,\boldsymbol{P},\boldsymbol{R})\right)\,,
\end{aligned}
\tag{13.9}
$$

where in the first equality we used $\boldsymbol{S}^2|S\rangle=S(S+1)|S\rangle$, in the second equality we inserted the complete sets (13.5) and (13.6), where $\langle\boldsymbol{p}|\rho_b|n\rangle=0$, and subsequently applied the

identity $\int_{\boldsymbol{R}} e^{i\boldsymbol{R}\cdot\boldsymbol{P}} = (2\pi)^3\delta^3(\boldsymbol{P})$, which then cancels the momentum integral from the completeness relation.

We may understand the semi-classical limit to be approached at late times. Hence, in order to grasp the connection with the semi-classical transport equations, we write

$$\begin{aligned}
&\langle \boldsymbol{P}+\frac{\boldsymbol{P}'}{2}; n; S|\rho_b(t)|\boldsymbol{P}-\frac{\boldsymbol{P}'}{2}; n'; S\rangle \\
&\simeq \langle \boldsymbol{P}+\frac{\boldsymbol{P}'}{2}; n; S|e^{-iHt}\rho_b(0)e^{iHt}|\boldsymbol{P}-\frac{\boldsymbol{P}'}{2}; n'; S\rangle \\
&\simeq e^{-i\Delta Et}\langle \boldsymbol{P}+\frac{\boldsymbol{P}'}{2}; n; S|\rho_b(0)|\boldsymbol{P}-\frac{\boldsymbol{P}'}{2}; n'; S\rangle\,,
\end{aligned} \tag{13.10}$$

where in the second line we used the approximation already discussed in the previous chapter, cf. footnote 4, and in the last line we extracted the phase involving $\Delta E \equiv E_n^{P+P'/2} - E_{n'}^{P-P'/2} = \frac{M\alpha^2}{4}\left(n'^2-n^2\right) + \frac{\boldsymbol{P}\cdot\boldsymbol{P}'}{2M}$ at leading order. The exponential factor can be understood of the form e^{-it/τ_S}, where the time scale of the bound-state system is indeed $\tau_S \sim 1/(M\alpha^2)$. If we follow the system evolution for times $t \gg \tau_S$, the exponential phase oscillates very fast except for the case $n' = n$ and $|\boldsymbol{P}'| \ll |\boldsymbol{P}|$. This is close in spirit to the *rotating-wave* approximation, and we call it the *diagonal limit* of the density operator and evolution equation.[5] Hence, in the diagonal limit, upon setting $n_1 = n$ in (13.9), we observe that the Wigner transform of the commutator involving $\mathrm{Re}[\delta V_b^{\mathrm{ann}}]$ vanishes. In fact, the cancellation between the two terms in the commutator happens also when including higher dimensional annihilation operators in $1/M$ as well as for $-i[\mathrm{Re}[\Sigma],\rho]$. As for scattering states, the diagonal limit implies $|\boldsymbol{p}'| \ll |\boldsymbol{p}|$ and $|\boldsymbol{P}'| \ll |\boldsymbol{P}|$. Thus the master equations (12.26) and (12.27), upon applying the Wigner transformations, reduce in the diagonal limit to

$$\left(\frac{\partial}{\partial t} + \frac{\boldsymbol{P}}{2M}\cdot\boldsymbol{\nabla}_{\boldsymbol{R}}\right) f^b_{n,S}(t,\boldsymbol{P},\boldsymbol{R}) = \mathcal{F}_b(\rho_b,\rho_s)\Big|_{\mathrm{WT}}\,, \tag{13.11}$$

$$\left(\frac{\partial}{\partial t} + \frac{\boldsymbol{P}}{2M}\cdot\boldsymbol{\nabla}_{\boldsymbol{R}} + 2\frac{\boldsymbol{p}}{M}\cdot\boldsymbol{\nabla}_{\boldsymbol{r}}\right) f^s_S(t,\boldsymbol{P},\boldsymbol{R},\boldsymbol{p},\boldsymbol{r}) = \mathcal{F}_s(\rho_b,\rho_s)\Big|_{\mathrm{WT}}\,, \tag{13.12}$$

where on the left-hand sides we recover the familiar free-streaming terms that implement the unitary evolution part, manifesting as a total time derivative acting on the distributions, and since we omit higher-order center-of-mass dependent terms in H except the leading-order kinetic energy $\boldsymbol{P}^2/(4M)$, there is no diffusion term proportional to the gradient $\boldsymbol{\nabla}_{\boldsymbol{P}}$.

We now focus on the non-unitary evolution part, and compute the right-hand side of (13.11) that may be superficially understood as a kind of collision term. We consider first the dipole transitions and Wigner-transform the dipole term $(-i\Sigma_{bs} - i\Sigma_{bb})\rho_b(t) +$

[5] One may understand the diagonal limit by looking at the solution of the evolution equation, $\langle\dot\rho(t)\rangle \sim e^{-i\Delta Et}\langle\rho(0)\rangle$, at late times: $\langle\rho(t\to\infty)\rangle \sim \int_0^{t\to\infty} dt\, e^{-i\Delta Et}\langle\rho(0)\rangle = \langle\rho(0)\rangle\int_{-\infty}^{\infty} dt\,\Theta(t)e^{-i\Delta Et} = \langle\rho(0)\rangle(\pi\delta(\Delta E) - i/\Delta E)$, which has a non-vanishing real part only for $\Delta E = 0$. Rotating-wave or secular approximations are frequently used when solving Lindblad equations, see ref. [173] for a more pedagogical introduction.

$\rho_b(t)(-i\Sigma_{bs} - i\Sigma_{bb})^\dagger$ in (12.12), which for the electric-dipole self-energy (12.16), after inserting the completeness relations (13.5)–(13.6) and performing some manipulations together with the Markov approximation and the kinetic equilibrium assumption for the dark photons, results in[6,7]

$$
\begin{aligned}
&-g^2 \int_{\boldsymbol{P}'} e^{i\boldsymbol{P}'\cdot\boldsymbol{R}} \int \frac{d^4k}{(2\pi)^4} \left[k_0^2 D_{11}^{ij}(k) + k^i k^j D_{11}^{00}(k)\right] \\
&\quad \times \Bigg\{ \sum_{n_1,n_2} \Bigg(\frac{i}{\Delta E_{n_1}^{n_2} + \frac{2(\boldsymbol{P}+\boldsymbol{P}'/2)\cdot\boldsymbol{k}-\boldsymbol{k}^2}{4M} - k_0 + i\epsilon} \langle n|r^i|n_1\rangle\langle n_1|r^j|n_2\rangle \\
&\qquad\qquad \times \langle \boldsymbol{P} + \frac{\boldsymbol{P}'}{2}; n_2; S|\rho_b(t)|\boldsymbol{P} - \frac{\boldsymbol{P}'}{2}; n; S\rangle \\
&\qquad - \frac{i}{\Delta E_{n_1}^{n_2} + \frac{2(\boldsymbol{P}-\boldsymbol{P}'/2)\cdot\boldsymbol{k}-\boldsymbol{k}^2}{4M} - k_0 - i\epsilon} \langle n_1|r^j|n_2\rangle\langle n_2|r^i|n\rangle \\
&\qquad\qquad \times \langle \boldsymbol{P} + \frac{\boldsymbol{P}'}{2}; n; S|\rho_b(t)|\boldsymbol{P} - \frac{\boldsymbol{P}'}{2}; n_1; S\rangle \Bigg) \\
&\quad + \int_{\boldsymbol{p}} \sum_{n_1} \Bigg(\frac{i}{\Delta E_{p}^{n_1} + \frac{2(\boldsymbol{P}+\boldsymbol{P}'/2)\cdot\boldsymbol{k}-\boldsymbol{k}^2}{4M} - k_0 + i\epsilon} \langle n|r^i|\boldsymbol{p}\rangle\langle \boldsymbol{p}|r^j|n_1\rangle \\
&\qquad\qquad \times \langle \boldsymbol{P} + \frac{\boldsymbol{P}'}{2}; n_1; S|\rho_b(t)|\boldsymbol{P} - \frac{\boldsymbol{P}'}{2}; n; S\rangle \\
&\qquad - \frac{i}{\Delta E_{p}^{n_1} + \frac{2(\boldsymbol{P}-\boldsymbol{P}'/2)\cdot\boldsymbol{k}-\boldsymbol{k}^2}{4M} - k_0 - i\epsilon} \langle n_1|r^j|\boldsymbol{p}\rangle\langle \boldsymbol{p}|r^i|n\rangle \\
&\qquad\qquad \times \langle \boldsymbol{P} + \frac{\boldsymbol{P}'}{2}; n; S|\rho_b(t)|\boldsymbol{P} - \frac{\boldsymbol{P}'}{2}; n_1; S\rangle \Bigg) \Bigg\} .
\end{aligned}
\tag{13.13}
$$

The expression above simplifies further in the diagonal limit, where we set either $n_1 = n$

[6]The Markov approximation has been implemented via the variable substitution $s \equiv t - t_2$ in (12.16), followed by the assumption that the time difference $t - t_0$ is much larger than any other time scale, such that $\int_{t_0}^{t} dt_2 f(t_2) \approx \int_0^\infty ds f(t-s)$ [153]. Moreover, in chapter 2 we have clarified that, although the expanding universe evolves in overall as an out-of-equilibrium system, the time dependency of the temperature is rather mild at late times, and we can assume the thermal bath to be quasistatic to a good degree of accuracy. Then we may approximate the time-ordered electric-field correlator as follows:

$$
\langle E^i(\boldsymbol{R}_1, t) E^j(\boldsymbol{R}_2, t-s)\rangle \approx \int \frac{d^4k}{(2\pi)^4} e^{-ik_0 s} e^{i\boldsymbol{k}\cdot(\boldsymbol{R}_1 - \boldsymbol{R}_2)} \left[k_0^2 D_{11}^{ij}(k) + k^i k^j D_{11}^{00}(k)\right] .
$$

[7]The heavy-pair propagators in (13.13) appear once we perform the integration over time, for instance

$$
\begin{aligned}
&\int_0^\infty ds\, \exp\left[-i\left(E_{n_1}^{P+P'/2-k} - E_{n_2}^{P+P'/2} + k_0\right)s\right] \\
&= \lim_{\epsilon\to 0^+} \int_0^\infty ds\, \exp\left[-i\left(E_{n_1}^{P+P'/2-k} - E_{n_2}^{P+P'/2} + k_0 - i\epsilon\right)s\right] = \frac{i}{E_{n_2}^{P+P'/2} - E_{n_1}^{P+P'/2-k} - k_0 + i\epsilon} .
\end{aligned}
$$

or $n_2 = n$, such that the density matrices factorize, i.e.

$$
\begin{aligned}
&-g^2 \int_{\boldsymbol{P}'} e^{i\boldsymbol{P}'\cdot\boldsymbol{R}} \langle \boldsymbol{P} + \frac{\boldsymbol{P}'}{2}; n; S|\rho_b(t)|\boldsymbol{P} - \frac{\boldsymbol{P}'}{2}; n; S\rangle \int \frac{d^4k}{(2\pi)^4} \left[k_0^2 D_{11}^{ij}(k) + k^i k^j D_{11}^{00}(k)\right] \\
&\quad \times \Bigg\{ \sum_{n'} \langle n|r^j|n'\rangle\langle n'|r^i|n\rangle \\
&\qquad \times \left(\frac{i}{\Delta E_{n'}^n + \frac{2(\boldsymbol{P}+\boldsymbol{P}'/2)\cdot\boldsymbol{k}-\boldsymbol{k}^2}{4M} - k_0 + i\epsilon} - \frac{i}{\Delta E_{n'}^n + \frac{2(\boldsymbol{P}-\boldsymbol{P}'/2)\cdot\boldsymbol{k}-\boldsymbol{k}^2}{4M} - k_0 - i\epsilon} \right) \\
&\quad + \int_{\boldsymbol{p}} \langle n|r^j|\boldsymbol{p}\rangle\langle \boldsymbol{p}|r^i|n\rangle \\
&\qquad \times \left(\frac{i}{\Delta E_{p}^n + \frac{2(\boldsymbol{P}+\boldsymbol{P}'/2)\cdot\boldsymbol{k}-\boldsymbol{k}^2}{4M} - k_0 + i\epsilon} - \frac{i}{\Delta E_{p}^n + \frac{2(\boldsymbol{P}-\boldsymbol{P}'/2)\cdot\boldsymbol{k}-\boldsymbol{k}^2}{4M} - k_0 - i\epsilon} \right) \Bigg\},
\end{aligned}
\tag{13.14}
$$

and expand the heavy-pair propagators up to zeroth order in $|\boldsymbol{P}'|/M$, resulting in

$$
\begin{aligned}
&-ig^2 f_{n,S}^b(t,\boldsymbol{P},\boldsymbol{R}) \int \frac{d^4k}{(2\pi)^4} \left[k_0^2 D_{11}^{ij}(k) + k^i k^j D_{11}^{00}(k)\right] \\
&\qquad \times \Bigg\{ \sum_{n'} \langle n|r^j|n'\rangle\langle n'|r^i|n\rangle \, 2i\,\mathrm{Im}\left[\frac{1}{\Delta E_{n'}^n + \frac{2\boldsymbol{P}\cdot\boldsymbol{k}-\boldsymbol{k}^2}{4M} - k_0 + i\epsilon} \right] \\
&\qquad\quad + \int_{\boldsymbol{p}} \langle n|r^j|\boldsymbol{p}\rangle\langle \boldsymbol{p}|r^i|n\rangle \, 2i\,\mathrm{Im}\left[\frac{1}{\Delta E_{p}^n + \frac{2\boldsymbol{P}\cdot\boldsymbol{k}-\boldsymbol{k}^2}{4M} - k_0 + i\epsilon} \right] \Bigg\}.
\end{aligned}
\tag{13.15}
$$

Since in the diagonal limit the off-diagonal matrix elements of the density operator are discarded, we loose the information of quantum superposition or quantum coherence of the open dark matter system. At this stage, the Wigner distribution has been entirely factorized out and we can compute the remaining terms in (13.15). Upon inserting the time-ordered dark photon propagator at leading order, cf. eqs. (D.4)–(D.5), we recognize the terms in eq. (13.15) to resemble the self-energy expressions we have already encountered in chapter 6, where we aimed to compute the individual thermal dipole rates. We expand the recoil term in the propagators in eq. (13.15) according to (6.60), and evaluate the integrals analytically up to order $\boldsymbol{P}^2/M^2$ and $\Delta E_n^p/M$ in the recoil corrections as in chapter 6. The other self-energy expressions involving the dark magnetic-magnetic, electric-magnetic and magnetic-electric correlators (cf. eqs. (12.17)–(12.19), respectively) can be computed in the very same way. Summing up all contributions, we eventually obtain

$$
\begin{aligned}
&\Big[(-i\Sigma_{bs} - i\Sigma_{bb})\rho_b(t) + \rho_b(t)(-i\Sigma_{bs} - i\Sigma_{bb})^\dagger\Big]\Big|_{\mathrm{WT}} \\
&\quad = -\left[(\Gamma_{\mathrm{bsd}}^n)_{\mathrm{lab}}(\boldsymbol{P}) + (\Gamma_{\mathrm{de\text{-}ex.}}^n)_{\mathrm{lab}}(\boldsymbol{P}) + (\Gamma_{\mathrm{ex.}}^n)_{\mathrm{lab}}(\boldsymbol{P})\right] f_{n,S}^b(t,\boldsymbol{P},\boldsymbol{R}),
\end{aligned}
\tag{13.16}
$$

where the bound-state dissociation width, de-excitation width and excitation width can be read-off from the eqs. (6.94), (6.103) and (6.104), respectively. We can call the Σ's altogether as the depletion term as it leads to a loss of the bound state (n, S).

Next, we Wigner-transform $\Xi_{bs}(\rho_s(t), t)$ in eq. (12.12), which for the electric-electric part (cf. eq. (12.20)), upon applying the same approximations and manipulations as for the Σ's, reads

$$
\begin{aligned}
& g^2 \int_{\boldsymbol{P}'} e^{i\boldsymbol{P}'\cdot\boldsymbol{R}} \int \frac{d^4k}{(2\pi)^4} \int_{\boldsymbol{p}_1}\int_{\boldsymbol{p}_2} \Bigg\{ \left[k_0^2 D_{11}^{ij}(k) + k^i k^j D_{11}^{00}(k)\right] \langle n|r^j|\boldsymbol{p}_1\rangle\langle \boldsymbol{p}_2|r^i|n\rangle \\
& \times \frac{i}{\Delta E_n^{p_1} + \frac{2(\boldsymbol{P}+\boldsymbol{P}'/2)\cdot\boldsymbol{k}-\boldsymbol{k}^2}{4M} - k_0 + i\epsilon} \langle \boldsymbol{P}+\boldsymbol{k}+\frac{\boldsymbol{P}'}{2}; \boldsymbol{p}_1; S|\rho_s(t)|\boldsymbol{P}+\boldsymbol{k}-\frac{\boldsymbol{P}'}{2}; \boldsymbol{p}_2; S\rangle + \text{h.c.} \Bigg\} \\
& \approx g^2 \int_{\boldsymbol{r}} e^{-i(\boldsymbol{p}_1-\boldsymbol{p}_2)\cdot\boldsymbol{r}} \int \frac{d^4k}{(2\pi)^4} \int_{\boldsymbol{p}_1}\int_{\boldsymbol{p}_2} \Bigg\{ \left[k_0^2 D_{11}^{ij}(k) + k^i k^j D_{11}^{00}(k)\right] \langle n|r^j|\boldsymbol{p}_1\rangle\langle \boldsymbol{p}_2|r^i|n\rangle \\
& \qquad \times \frac{i}{\Delta E_n^{p_1} + \frac{2\boldsymbol{P}\cdot\boldsymbol{k}-\boldsymbol{k}^2}{4M} - k_0 + i\epsilon} f_S^s\left(t, \boldsymbol{P}+\boldsymbol{k}, \boldsymbol{R}, \frac{\boldsymbol{p}_1+\boldsymbol{p}_2}{2}, \boldsymbol{r}\right) + \text{h.c.} \Bigg\}, \qquad (13.17)
\end{aligned}
$$

where we first expanded the heavy-pair propagator to zeroth order in $|\boldsymbol{P}'|/M$ and then used the following relation [163]:[8]

$$
\int_{\boldsymbol{P}'} e^{i\boldsymbol{P}'\cdot\boldsymbol{R}} \langle \boldsymbol{P}+\frac{\boldsymbol{P}'}{2}; \boldsymbol{p}_1; S|\rho_s(t)|\boldsymbol{P}-\frac{\boldsymbol{P}'}{2}; \boldsymbol{p}_2; S\rangle = \int_{\boldsymbol{r}} e^{-i(\boldsymbol{p}_1-\boldsymbol{p}_2)\cdot\boldsymbol{r}} f_S^s\left(t, \boldsymbol{P}, \boldsymbol{R}, \frac{\boldsymbol{p}_1+\boldsymbol{p}_2}{2}, \boldsymbol{r}\right). \qquad (13.18)
$$

In the next step, we expand the scattering-state Wigner function around $\boldsymbol{r}_0$ and in $|\boldsymbol{k}| \ll |\boldsymbol{P}|$, i.e.[9]

$$
\begin{aligned}
& f_S^s\left(t, \boldsymbol{P}+\boldsymbol{k}, \boldsymbol{R}, \frac{\boldsymbol{p}_1+\boldsymbol{p}_2}{2}, \boldsymbol{r}\right) \approx f_S^s\left(t, \boldsymbol{P}, \boldsymbol{R}, \frac{\boldsymbol{p}_1+\boldsymbol{p}_2}{2}, \boldsymbol{r}_0\right) \\
& \quad + (\boldsymbol{r}-\boldsymbol{r}_0)\cdot\boldsymbol{\nabla}_{\boldsymbol{r}_0} f_S^s\left(t, \boldsymbol{P}, \boldsymbol{R}, \frac{\boldsymbol{p}_1+\boldsymbol{p}_2}{2}, \boldsymbol{r}_0\right) + \boldsymbol{k}\cdot\boldsymbol{\nabla}_{\boldsymbol{k}} f_S^s\left(t, \boldsymbol{P}, \boldsymbol{R}, \frac{\boldsymbol{p}_1+\boldsymbol{p}_2}{2}, \boldsymbol{r}_0\right) + \ldots, \qquad (13.19)
\end{aligned}
$$

and keep only the zeroth order term from now on. This simplifies the expression (13.17) significantly, since $\int_{\boldsymbol{r}} e^{-i(\boldsymbol{p}_1-\boldsymbol{p}_2)\cdot\boldsymbol{r}} = (2\pi)^3\delta^3(\boldsymbol{p}_1-\boldsymbol{p}_2)$, hence $\boldsymbol{p}_2 = \boldsymbol{p}_1 \equiv \boldsymbol{p}$, and eq. (13.17)

[8] The relation (13.18) can be straightforwardly proven by rewriting the Wigner function on the right-hand side of (13.18) according to (13.2), integrating over $\boldsymbol{r}$, which in turn generates a delta function that puts a constraint on the integral over the relative momentum.

[9] Truncating the Taylor-expanded distribution function in (13.19), known as the *gradient* expansion, works if f^s varies slowly on distances of the order of the Bohr radius a_0 of the heavy DM pair, i.e. if the diffusion length $\sqrt{D\tau} \gg a_0$. On distances $\boldsymbol{r}$ much larger than the typical size of the fermion-antifermion pair, the dipole matrix elements are quite suppressed due to a small overlap integral between bound- and scattering-state wavefunctions. Moreover, we can expand in $|\boldsymbol{k}| \ll |\boldsymbol{P}|$ since recoil corrections are small for non-relativistic dark matter.

becomes

$$
\begin{aligned}
g^2 \int \frac{d^4k}{(2\pi)^4} \int_{\boldsymbol{p}} \left[k_0^2 D_{11}^{ij}(k) + k^i k^j D_{11}^{00}(k)\right] \langle n|r^j|\boldsymbol{p}\rangle\langle \boldsymbol{p}|r^i|n\rangle \, f_S^s\left(t, \boldsymbol{P}, \boldsymbol{R}, \boldsymbol{p}, \boldsymbol{r}_0\right) \\
\times \left(\frac{i}{\Delta E_n^p + \frac{2\boldsymbol{P}\cdot\boldsymbol{k} - \boldsymbol{k}^2}{4M} - k_0 + i\epsilon} - \frac{i}{\Delta E_n^p + \frac{2\boldsymbol{P}\cdot\boldsymbol{k} - \boldsymbol{k}^2}{4M} - k_0 - i\epsilon} \right) \\
= -2 \int_{\boldsymbol{p}} \mathrm{Im}\left[\left(\Sigma_{ee}^{11}\right)(\boldsymbol{p}, \boldsymbol{P})\right] f_S^s\left(t, \boldsymbol{P}, \boldsymbol{R}, \boldsymbol{p}, \boldsymbol{r}_0\right) ,
\end{aligned}
\tag{13.20}
$$

and adding up the Wigner transforms of (12.21)–(12.23), we obtain

$$
\begin{aligned}
\Xi_{bs}(\rho_s(t), t)\Big|_{\mathrm{WT}} &= -2 \int_{\boldsymbol{p}} \Big(\mathrm{Im}\left[\left(\Sigma_{ee}^{11}\right)(\boldsymbol{p}, \boldsymbol{P})\right] + \mathrm{Im}\left[\left(\Sigma_{mm}^{11}\right)(\boldsymbol{p}, \boldsymbol{P})\right] \\
&\qquad + \mathrm{Im}\left[\left(\Sigma_{em}^{11}\right)(\boldsymbol{p}, \boldsymbol{P})\right] + \mathrm{Im}\left[\left(\Sigma_{me}^{11}\right)(\boldsymbol{p}, \boldsymbol{P})\right] \Big) f_S^s\left(t, \boldsymbol{P}, \boldsymbol{R}, \boldsymbol{p}, \boldsymbol{r}_0\right) \\
&= \int_{\boldsymbol{p}} (\sigma_{\mathrm{bsf}}\, v_{\mathrm{M\o l}})_{\mathrm{lab}}(\boldsymbol{p}, \boldsymbol{P}) f_S^s\left(t, \boldsymbol{P}, \boldsymbol{R}, \boldsymbol{p}, \boldsymbol{r}_0\right) ,
\end{aligned}
\tag{13.21}
$$

where the bound-state formation cross section can be read-off from (6.62). An analogous computation gives

$$
\Xi_{bb}(\rho_b(t), t)\Big|_{\mathrm{WT}} = \left[\sum_{n'>n} (\Gamma_{\text{de-ex.}}^{n'\to n})_{\mathrm{lab}}(\boldsymbol{P}) + \sum_{n'<n} (\Gamma_{\text{ex.}}^{n'\to n})_{\mathrm{lab}}(\boldsymbol{P}) \right] f_{n',S}^b(t, \boldsymbol{P}, \boldsymbol{R}) \,. \tag{13.22}
$$

We can call the Ξ's altogether as the recombination term, since it creates a bound state (n, S) out of a scattering state or via (de-)excitation of another bound state (n', S), and we sum over all of them. We have worked out all contributions from the dipole transitions, so that in total we get

$$
\begin{aligned}
\mathcal{F}_b^{\mathrm{dip}}(\rho_b(t), \rho_s(t))\Big|_{\mathrm{WT}} &= -\left[(\Gamma_{\mathrm{bsd}}^n)_{\mathrm{lab}}(\boldsymbol{P}) + (\Gamma_{\text{de-ex.}}^n)_{\mathrm{lab}}(\boldsymbol{P}) + (\Gamma_{\text{ex.}}^n)_{\mathrm{lab}}(\boldsymbol{P})\right] f_{n,S}^b(t, \boldsymbol{P}, \boldsymbol{R}) \\
&\quad + \int_{\boldsymbol{p}} (\sigma_{\mathrm{bsf}}\, v_{\mathrm{M\o l}})_{\mathrm{lab}}(\boldsymbol{p}, \boldsymbol{P}) f_S^s\left(t, \boldsymbol{P}, \boldsymbol{R}, \boldsymbol{p}, \boldsymbol{r}_0\right) \\
&\quad + \left[\sum_{n'>n} (\Gamma_{\text{de-ex.}}^{n'\to n})_{\mathrm{lab}}(\boldsymbol{P}) + \sum_{n'<n} (\Gamma_{\text{ex.}}^{n'\to n})_{\mathrm{lab}}(\boldsymbol{P}) \right] f_{n',S}^b(t, \boldsymbol{P}, \boldsymbol{R}) \,.
\end{aligned}
\tag{13.23}
$$

Indeed, the non-unitary evolution of a specific bound state of interest, with quantum numbers (n, S), is governed by all processes at order r^2, and we have already calculated all individual interaction rates in chapter 6. On the one hand, in the first line of eq. (13.23) one sees the processes that deplete the bound state: photo-dissociation and excitations or de-excitations. On the other hand, in the second and third line, the processes responsible for the regeneration of the bound state are the bound-state formation from a scattering state and excitations as well as de-excitations into the bound state of reference. The two classes of processes determine the loss and gain term in a Boltzmann-like

semi-classical transport equation, respectively. We now consider the annihilation terms in eq. (12.30). An important difference with respect to the dipole transitions is that annihilation processes are sensitive to the total spin S of the heavy DM pair. We perform the same steps as outlined so far for a generic spin state S, and the Wigner transform of the anticommutator $\{\mathrm{Im}[\delta V_b^{\mathrm{ann}}], \rho_b(t)\}$, with

$$\begin{aligned}\mathrm{Im}\,[\delta V^{\mathrm{ann}}] &= -\frac{\delta^3(\boldsymbol{r})}{M^2}\left[2\mathrm{Im}\,[d_s] - \boldsymbol{S}^2\left(\mathrm{Im}\,[d_s] - \mathrm{Im}\,[d_v]\right)\right] \\ &\quad + \frac{\delta^3(\boldsymbol{r})}{M^4}\nabla^i_{\boldsymbol{R}}\nabla^j_{\boldsymbol{R}}\left[2\,\mathrm{Im}\,[g_{\mathrm{c\,cm}}]\,\delta_{ij} - \boldsymbol{S}^2\left(\mathrm{Im}\,[g_{\mathrm{c\,cm}}] - \mathrm{Im}\,[g_{\mathrm{a\,cm}}]\right)\delta_{ij} + S^iS^j\,\mathrm{Im}\,[g_{\mathrm{b\,cm}}]\right] \\ &= -\frac{\delta^3(\boldsymbol{r})}{M^2}\left[2\mathrm{Im}\,[d_s] - \boldsymbol{S}^2\left(\mathrm{Im}\,[d_s] - \mathrm{Im}\,[d_v]\right)\right]\left(1 + \frac{\Delta_{\boldsymbol{R}}}{4M^2}\right), \end{aligned} \tag{13.24}$$

where in the second equality we used the relations (5.15) from reparametrization invariance, becomes

$$\begin{aligned}&-\frac{1}{M^2}\left[2\mathrm{Im}[d_s] - S(S+1)(\mathrm{Im}[d_s] - \mathrm{Im}[d_v])\right] \\ &\times\sum_{n_1}\int_{\boldsymbol{P'}} e^{i\boldsymbol{P'}\cdot\boldsymbol{R}}\left(\psi_n^*(\boldsymbol{0})\psi_{n_1}(\boldsymbol{0})\left[1 - \frac{\left(\boldsymbol{P} + \frac{\boldsymbol{P'}}{2}\right)^2}{4M^2}\right]\langle \boldsymbol{P} + \frac{\boldsymbol{P'}}{2}; n_1; S|\rho_b(t)|\boldsymbol{P} - \frac{\boldsymbol{P'}}{2}; n; S\rangle\right. \\ &\qquad\left. + \psi_{n_1}^*(\boldsymbol{0})\psi_n(\boldsymbol{0})\left[1 - \frac{\left(\boldsymbol{P} - \frac{\boldsymbol{P'}}{2}\right)^2}{4M^2}\right]\langle \boldsymbol{P} + \frac{\boldsymbol{P'}}{2}; n; S|\rho_b(t)|\boldsymbol{P} - \frac{\boldsymbol{P'}}{2}; n_1; S\rangle\right). \end{aligned} \tag{13.25}$$

In the diagonal limit, where we single out the bound state contribution with $n_1 = n$ and expand the factors to zeroth order in $\boldsymbol{P'}$, the density matrix factorizes (and so does the Wigner distribution function), and we obtain

$$\begin{aligned}\{\mathrm{Im}[\delta V_b^{\mathrm{ann}}], \rho_b(t)\}\Big|_{\mathrm{WT}} &= -\frac{2}{M^2}\left[2\mathrm{Im}[d_s] - S(S+1)(\mathrm{Im}[d_s] - \mathrm{Im}[d_v])\right] \\ &\qquad\times\left(1 - \frac{\boldsymbol{P}^2}{4M^2}\right)|\psi_n(\boldsymbol{0})|^2 f^b_{n,S}(t, \boldsymbol{P}, \boldsymbol{R}) \\ &= -\left(\Gamma^{n,S}_{\mathrm{ann}}\right)_{\mathrm{lab}}(\boldsymbol{P})\, f^b_{n,S}(t, \boldsymbol{P}, \boldsymbol{R}), \end{aligned} \tag{13.26}$$

where the decay width corresponds either to the para- or orthodarkonium decay width for $S = 0$ or $S = 1$, respectively (cf. first lines in (5.30) and (5.31), respectively). Hence, the anticommutator term leads to a depletion of the bound state (n, S), in agreement with the general behaviour of the anticommutator term in the Lindblad equation (11.1).

We finally Wigner-transform the trace term $-2\rho_b(t)\,\mathrm{Tr}\,[\mathrm{Im}[\delta V^{\mathrm{ann}}]\,\rho(t)]$ in eq. (12.30), where we recall that $\rho(t) = \mathrm{diag}(\rho_b(t), \rho_s(t))$, and get

$$-2\rho_b(t)\,\mathrm{Tr}\,[\mathrm{Im}[\delta V^{\mathrm{ann}}]\,\rho(t)]\Big|_{\mathrm{WT}} = -2f^b_{n,S}(t, \boldsymbol{P}, \boldsymbol{R})\,\mathrm{Tr}\,[\mathrm{Im}[\delta V^{\mathrm{ann}}]\,\rho(t)]\,. \tag{13.27}$$

Splitting the trace as $\mathrm{Tr}[\mathcal{O}] = \sum_S \int_{\boldsymbol{P}} \left(\sum_n \langle \boldsymbol{P}; n; S|\mathcal{O}|\boldsymbol{P}; n; S\rangle + \int_{\boldsymbol{p}} \langle \boldsymbol{P}; \boldsymbol{p}; S|\mathcal{O}|\boldsymbol{P}; \boldsymbol{p}; S\rangle \right)$, plugging in (13.24) and inserting complete sets (13.5)–(13.6), we obtain after some manipulations

$$
\begin{aligned}
-2\rho_b(t)\,\mathrm{Tr}\left[\mathrm{Im}[\delta V^{\mathrm{ann}}]\,\rho(t)\right]\Big|_{\mathrm{WT}} &= 2f^b_{n,S}(t,\boldsymbol{P},\boldsymbol{R}) \\
&\times \sum_{S_1} \frac{1}{M^2}\left[2\mathrm{Im}[d_s] - S_1(S_1+1)(\mathrm{Im}[d_s]-\mathrm{Im}[d_v])\right] \int_{\boldsymbol{P}_1} \left(1 - \frac{\boldsymbol{P}_1^2}{4M^2}\right) \\
&\times \Bigg\{ \sum_{n_1,n_2} \Psi^*_{n_1}(\boldsymbol{0})\Psi_{n_2}(\boldsymbol{0}) \langle \boldsymbol{P}_1; n_2; S_1|\rho_b(t)|\boldsymbol{P}_1; n_1; S_1\rangle \\
&\quad + \int_{\boldsymbol{p}_1}\int_{\boldsymbol{p}_2} \Psi^*_{\boldsymbol{p}_1}(\boldsymbol{0})\Psi_{\boldsymbol{p}_2}(\boldsymbol{0}) \langle \boldsymbol{P}_1; \boldsymbol{p}_2; S_1|\rho_s(t)|\boldsymbol{P}_1; \boldsymbol{p}_1; S_1\rangle \Bigg\}. \qquad (13.28)
\end{aligned}
$$

In the next step, we insert, similarly as in ref. [99], the identity $1 = \int_{\boldsymbol{P}'}(2\pi)^3\delta^3(\boldsymbol{P}') = \int_{\boldsymbol{P}'}\int_{\boldsymbol{R}'} e^{i\boldsymbol{P}'\cdot\boldsymbol{R}'}$ into (13.28) and shift the ket and the bra by the momentum $\boldsymbol{P}'/2$, i.e. $|\boldsymbol{P}_1 - \boldsymbol{P}'/2\rangle$ and $\langle \boldsymbol{P}_1 + \boldsymbol{P}'/2|$ in order to make the density matrices appear as in the definition of the Wigner distributions, cf. eqs. (13.1)–(13.2). Using the relation (13.18) for the scattering-state density matrix, eq. (13.28) becomes

$$
\begin{aligned}
-2\rho_b(t)\,\mathrm{Tr}\left[\mathrm{Im}[\delta V^{\mathrm{ann}}]\,\rho(t)\right]\Big|_{\mathrm{WT}} &= 2f^b_{n,S}(t,\boldsymbol{P},\boldsymbol{R}) \\
&\times \sum_{S_1} \frac{1}{M^2}\left[2\mathrm{Im}[d_s] - S_1(S_1+1)(\mathrm{Im}[d_s]-\mathrm{Im}[d_v])\right] \int_{\boldsymbol{P}_1} \left(1 - \frac{\boldsymbol{P}_1^2}{4M^2}\right) \\
&\times \Bigg\{ \int_{\boldsymbol{P}'}\int_{\boldsymbol{R}'} e^{i\boldsymbol{P}'\cdot\boldsymbol{R}'} \sum_{n_1,n_2} \Psi^*_{n_1}(\boldsymbol{0})\Psi_{n_2}(\boldsymbol{0}) \langle \boldsymbol{P}_1 + \frac{\boldsymbol{P}'}{2}; n_2; S_1|\rho_b(t)|\boldsymbol{P}_1 - \frac{\boldsymbol{P}'}{2}; n_1; S_1\rangle \\
&\quad + \int_{\boldsymbol{R}'}\int_{\boldsymbol{p}_1}\int_{\boldsymbol{p}_2} \Psi^*_{\boldsymbol{p}_1}(\boldsymbol{0})\Psi_{\boldsymbol{p}_2}(\boldsymbol{0}) \int_{\boldsymbol{r}'} e^{-i(\boldsymbol{p}_2-\boldsymbol{p}_1)\cdot\boldsymbol{r}'} f^s_{S_1}\left(t, \boldsymbol{P}_1, \boldsymbol{R}', \frac{\boldsymbol{p}_1+\boldsymbol{p}_2}{2}, \boldsymbol{r}'\right) \Bigg\}. \qquad (13.29)
\end{aligned}
$$

We take the diagonal limit by setting $n_2 = n_1$ and perform the gradient expansion of the Wigner distribution of the scattering state up to zeroth order in $\boldsymbol{r}'$ around some value $\boldsymbol{r}_0$ (cf. eq. (13.19)), which enables us to do the $\boldsymbol{r}'$ integration straightforwardly, yielding the constraint $\boldsymbol{p}_2 = \boldsymbol{p}_1$. Renaming $\boldsymbol{R}' = \boldsymbol{R}_1$, we end up with

$$
\begin{aligned}
-2\rho_b(t)\,\mathrm{Tr}\left[\mathrm{Im}[\delta V^{\mathrm{ann}}]\,\rho(t)\right]\Big|_{\mathrm{WT}} &= f^b_{n,S}(t,\boldsymbol{P},\boldsymbol{R}) \\
&\times \sum_{S_1} \int_{\boldsymbol{P}_1}\int_{\boldsymbol{R}_1} \Bigg\{ \sum_{n_1} \left(\Gamma^{n_1,S_1}_{\mathrm{ann}}\right)_{\mathrm{lab}}(\boldsymbol{P}_1)\, f^b_{n_1,S_1}(t,\boldsymbol{P}_1,\boldsymbol{R}_1) \\
&\quad + 4\int_{\boldsymbol{p}_1} \left(\sigma_{\mathrm{ann}} v_{\mathrm{M\o l}}\right)^{S_1}_{\mathrm{lab}}(\boldsymbol{p}_1,\boldsymbol{P}_1)\, f^s_{S_1}(t,\boldsymbol{P}_1,\boldsymbol{R}_1,\boldsymbol{p}_1,\boldsymbol{r}_0) \Bigg\}, \qquad (13.30)
\end{aligned}
$$

where the superscript S_1 in the spin-averaged annihilation cross section, cf. eq. (5.28), denotes that we pick up only the S_1 spin state. Together with the contribution from the anticommutator in (13.26), the non-unitary collision operator, induced by dark fermion-antifermion annihilations, reads

$$\begin{aligned}\mathcal{F}_b^{\text{ann}}(\rho_b(t),\rho_s(t))\Big|_{\text{WT}} &= -\left(\Gamma_{\text{ann}}^{n,S}\right)_{\text{lab}}(\boldsymbol{P})\, f_{n,S}^b(t,\boldsymbol{P},\boldsymbol{R}) \\ &+ f_{n,S}^b(t,\boldsymbol{P},\boldsymbol{R})\sum_{S_1}\int_{\boldsymbol{P}_1}\int_{\boldsymbol{R}_1}\Bigg\{\sum_{n_1}\left(\Gamma_{\text{ann}}^{n_1,S_1}\right)_{\text{lab}}(\boldsymbol{P}_1)\, f_{n_1,S_1}^b(t,\boldsymbol{P}_1,\boldsymbol{R}_1) \\ &\qquad + 4\int_{\boldsymbol{p}_1}(\sigma_{\text{ann}}v_{\text{Møl}})_{\text{lab}}^{S_1}(\boldsymbol{p}_1,\boldsymbol{P}_1)\, f_{S_1}^s(t,\boldsymbol{P}_1,\boldsymbol{R}_1,\boldsymbol{p}_1,\boldsymbol{r}_0)\Bigg\}.\end{aligned} \tag{13.31}$$

As can be seen, the first line implements a depletion of the bound state (n,S), whereas the second and third line correspond to the feed-down from the heavy two-pair states, which come from both bound- and scattering-state configurations. Our initial assumption for a composite density operator $\rho_{\text{I+II}}$ of a two heavy-pair system to be decomposable into a direct product $\rho_{\text{I}}\otimes\rho_{\text{II}}$, translates into factorized Wigner distribution functions in eq. (13.31), i.e. $f_{n,S}^b f_{n_1,S_1}^b$ and $f_{n,S}^b f_{S_1}^s$. However, in case of a more general, entangled density operator $\rho_{\text{I+II}}\neq\rho_{\text{I}}\otimes\rho_{\text{II}}$, we would expect an outcome involving a two heavy-pair distribution function like $f(t,\boldsymbol{P},\boldsymbol{R},\boldsymbol{P}_1,\boldsymbol{R}_1)$ to appear, that is not separable in general. It would make an attempt to solve the Boltzmann transport equations tremendously difficult, since the coupled equations are not closed, i.e. we would need an additional equation of motion for the two-pair distribution, which in turn depends on a three-pair distribution, and so on. Instead, the outcomes in (13.23) and (13.31) result in a set of coupled but closed Boltzmann equations, which, upon plugging them into (13.11), eventually leads to the following bound-state evolution equation:

$$\begin{aligned}&\left(\frac{\partial}{\partial t}+\frac{\boldsymbol{P}}{2M}\cdot\boldsymbol{\nabla}_{\boldsymbol{R}}\right)f_{n,S}^b(t,\boldsymbol{P},\boldsymbol{R}) \\ &\quad= -\left[\left(\Gamma_{\text{ann}}^{n,S}\right)_{\text{lab}}(\boldsymbol{P})+(\Gamma_{\text{bsd}}^{n})_{\text{lab}}(\boldsymbol{P})+(\Gamma_{\text{de-ex.}}^{n})_{\text{lab}}(\boldsymbol{P})+(\Gamma_{\text{ex.}}^{n})_{\text{lab}}(\boldsymbol{P})\right]f_{n,S}^b(t,\boldsymbol{P},\boldsymbol{R}) \\ &\qquad+ f_{n,S}^b(t,\boldsymbol{P},\boldsymbol{R})\sum_{S_1}\int_{\boldsymbol{P}_1}\int_{\boldsymbol{R}_1}\Bigg\{\sum_{n_1}\left(\Gamma_{\text{ann}}^{n_1,S_1}\right)_{\text{lab}}(\boldsymbol{P}_1)\, f_{n_1,S_1}^b(t,\boldsymbol{P}_1,\boldsymbol{R}_1) \\ &\qquad\qquad+ 4\int_{\boldsymbol{p}_1}(\sigma_{\text{ann}}v_{\text{Møl}})_{\text{lab}}^{S_1}(\boldsymbol{p}_1,\boldsymbol{P}_1)\, f_{S_1}^s(t,\boldsymbol{P}_1,\boldsymbol{R}_1,\boldsymbol{p}_1,\boldsymbol{r}_0)\Bigg\} \\ &\qquad+\int_{\boldsymbol{p}}(\sigma_{\text{bsf}}\,v_{\text{Møl}})_{\text{lab}}(\boldsymbol{p},\boldsymbol{P})f_S^s(t,\boldsymbol{P},\boldsymbol{R},\boldsymbol{p},\boldsymbol{r}_0) \\ &\qquad+\left[\sum_{n'>n}(\Gamma_{\text{de-ex.}}^{n'\to n})_{\text{lab}}(\boldsymbol{P})+\sum_{n'<n}(\Gamma_{\text{ex.}}^{n'\to n})_{\text{lab}}(\boldsymbol{P})\right]f_{n',S}^b(t,\boldsymbol{P},\boldsymbol{R}),\end{aligned} \tag{13.32}$$

which is a partial integro-differential equation, and, hence, still difficult to solve in general. Besides the dipole approximation, we recall the various approximations that have

been made along the reduction from the full quantum master equation (12.26) to the semi-classical transport equation (13.32): (i) In the dilute limit we truncate the system to only two heavy dark matter pairs, i.e. systems I and II, and consider only diagrams at leading order in the density operator, cf. fig. 12.1. (ii) We discard quantum entanglement by decomposing $\rho_{\mathrm{I+II}} = \rho_{\mathrm{I}} \otimes \rho_{\mathrm{II}}$, known as molecular chaos approximation. (iii) We implement the Markov approximation in order to pass from a two-times dependence in the Σ's and Ξ's in eqs. (12.16)–(12.23) to a single time variable. (iv) In the rotating-wave approximation, we omit the off-diagonal density-matrix elements, enabling us to factorize the distribution function from the interaction rates in return of loosing the quantum superposition property of the DM system. It is closely connected to the gradient expansion and to what we have called as the diagonal limit. In order to relate (13.32) to the familiar integrated Boltzmann equation for the bound-state number density, cf. eqs. (7.2)–(7.3), three additional assumptions are required: (v) Another molecular chaos approximation, where $f_S^s\,(t, \boldsymbol{P}, \boldsymbol{R}, \boldsymbol{p}, \boldsymbol{r}_0) = f_X(t, \boldsymbol{p}_1, \boldsymbol{r}_1) f_{\bar{X}}(t, \boldsymbol{p}_2, \boldsymbol{r}_2)$. (vi) Isotropy of the thermal bath, i.e. neglect the $\boldsymbol{r}$, $\boldsymbol{R}$ dependence in the distribution. (vii) Assume the dark matter pairs to be kinetically equilibrated with the thermal bath, such that

$$f^b_{n,S}(t, \boldsymbol{P}) = \frac{f^{b,\mathrm{eq}}_{n,S}(|\boldsymbol{P}|)}{n^S_{n,\mathrm{eq}}} n^S_n(t)\,, \quad f_X(t, \boldsymbol{p}_1) = \frac{f^{\mathrm{eq}}_X(|\boldsymbol{p}_1|)}{n_{X,\mathrm{eq}}} n_X(t)\,, \tag{13.33}$$

with $n(t) = n_X(t) + n_{\bar{X}}(t) = 2n_X(t)$, and where the bound-state number densities in equilibrium, $n^S_{n,\mathrm{eq}}$, have been written chapter 7, footnote 3 (see also the definition of n^S_n in footnote 3 at the beginning of this chapter), and the particle number density in equilibrium, n_{eq}, can be read-off from eq. (2.7). Taking into account all those approximations and the expansion rate of the universe, integrating the bound-state transport equation (13.32) over the total momentum $\boldsymbol{P}$ and summing over the total spin $S = \{0, 1\}$, where we recognize the thermal-average expressions of the observables in the laboratory frame, we end up with

$$\begin{aligned}
&(\partial_t + 3H) n_n(t) \\
&\quad = -\langle \Big[(\Gamma^{n,\mathrm{para}}_{\mathrm{ann}})_{\mathrm{lab}} + (\Gamma^{n,\mathrm{ortho}}_{\mathrm{ann}})_{\mathrm{lab}} + (\Gamma^{n}_{\mathrm{bsd}})_{\mathrm{lab}} + (\Gamma^{n}_{\text{de-ex.}})_{\mathrm{lab}} + (\Gamma^{n}_{\text{ex.}})_{\mathrm{lab}} \Big] \rangle_{\mathrm{lab}}\, n_n(t) \\
&\qquad + \frac{1}{4} \langle (\sigma_{\mathrm{bsf}}\, v_{\mathrm{Møl}})_{\mathrm{lab}} \rangle_{\mathrm{lab}}\, n^2(t) + \left[\sum_{n'>n} \langle (\Gamma^{n' \to n}_{\text{de-ex.}})_{\mathrm{lab}} \rangle_{\mathrm{lab}} + \sum_{n'<n} \langle (\Gamma^{n' \to n}_{\text{ex.}})_{\mathrm{lab}} \rangle_{\mathrm{lab}} \right] n_{n'}(t)\,,
\end{aligned} \tag{13.34}$$

where we have dropped the recombination term with respect to annihilations, since it is quadratic in the distribution function and hence suppressed. We finally recover the rate equation for the bound pair, upon summing eqs. (7.2) and (7.3), that we have used throughout this work whenever we were interested in the computation of the dark matter relic abundance.[10]

[10] In the familiar Boltzmann equations (7.2)–(7.3) there are additional terms $\langle \Gamma^{n,S}_{\mathrm{ann}} \rangle n^S_{n,\mathrm{eq}}$, which do not appear in eq. (13.34). The reason is that such a recombination term corresponds to the creation of a heavy dark fermion-antifermion pair out of the light degrees of freedom, but those reversed processes to the annihilations have not been included in the present treatment.

So far we have derived explicitly and step-by-step the Boltzmann transport equation for the Wigner distribution function of a dark matter bound state. We will not reiterate the calculation, but in a very similar way and under the same approximations one may compute the transport equation for the Wigner distribution of a scattering state, to which eq. (13.34) is ultimately coupled. Hence, in the semi-classical limit one may recover the Boltzmann equation (7.1) that has been extensively used in this work in order to obtain a numerical solution for the present dark matter energy density. However, since we identified and elaborated thoroughly all the underlying approximations, it would be desirable to examine quantitatively the order of uncertainty on $\Omega_{\rm DM}h^2$ induced by these simplifications, in this way establishing a better control of the full accuracy from the theoretical side on the precise value of the DM relic abundance.

Part VI

Summary and conclusions

Unveiling the dark matter identity from the hidden sector, which so far manifests only through its gravitational effects on large scales such as galaxies or galaxy clusters, has been one of the essential ambitions in astrophysics, cosmology and particle physics since over several decades. Because the dark sector contributes to the total abundance of the universe by a factor of five compared to the visible sector, it is indispensable to uncover the fundamental DM properties in order to have a more profound understanding of the cosmos. A viable and well motivated possibility consists of extending the Standard Model of particle physics by additional novel particles that are not charged with respect to the SM gauge group, which qualifies them as *dark* degrees of freedom, but imposing a new dark gauge symmetry to which they couple. As prototypical dark matter models, we have considered a QED-like dark sector made of dark Dirac fermions and dark photons, dubbed as $\mathrm{QED}_{\mathrm{DM}}$ or $\mathrm{U}(1)_{\mathrm{DM}}$ in this work, and the corresponding non-abelian version featuring an $\mathrm{SU}(N)_{\mathrm{DM}}$ gauge group. We allow for several dark fermion flavors, where, however, one of the species is assumed to be much heavier than the others. Hence it accounts for most of the mass within the dark sector and dominates the present DM relic abundance, which is set by the *thermal freeze-out* of the heavy particle during the early expanding universe. Since $\mathrm{U}(1)_{\mathrm{DM}}$ or $\mathrm{SU}(N)_{\mathrm{DM}}$ resemble strongly the gauge symmetries within the SM, there has been a considerable effort in transferring and extending known techniques adopted in atomic and heavy-quarkonium physics to dark matter models in the recent years, both at zero and finite temperature. Indeed, whenever the massive dark particles experience self-interactions through a massless or light vector mediator, the dark particle dynamics shares some similarities with the one of positronium in QED, or even heavy quarkonium in a quark gluon plasma. In fact, the generation of bound states of dark fermion-antifermion pairs, that we call *darkonia* to make a close connection to e.g. positronia or bottomonia, turns out to have a strong impact on the DM relic density evolution. It is therefore of paramount importance to determine the relevant processes and the associated reaction rates at a precise level as well as to keep possible theoretical uncertainties under systematic control.

In the context of the freeze-out mechanism, the relevant interactions, that determine the non-equilibrium dynamics of the non-relativistic dark matter particles, and the relative strengths among them are mainly dictated according to the hierarchy of energy scales, where we find two distinct scale arrangements given in (3.2) and (3.4). In particular, in $\mathrm{U}(1)_{\mathrm{DM}}$ and $\mathrm{SU}(N)_{\mathrm{DM}}$ the DM number-changing processes are induced by particle-antiparticle annihilations and decays, augmented by the bound-state effects such as the formation and dissociation of bound states, dubbed *bsf* and *bsd*, respectively, as well as the transitions among the bound states; the latter only realized in $\mathrm{U}(1)_{\mathrm{DM}}$. Since the thermal and internal energy scales are hierarchically ordered for each arrangements in (3.2) and (3.4), we can systematically replace the full relativistic theories $\mathrm{U}(1)_{\mathrm{DM}}$ and $\mathrm{SU}(N)_{\mathrm{DM}}$, with all the scales intertwined resulting in a pretty cumbersome computation of corresponding physical quantities, by a tower of simpler non-relativistic effective field theories for the effective degrees of freedom that describe the physics of interest at the Lagrangian level, where long- and short-range contributions are factorized for any observable and hence the contribution from each scale becomes transparent. In

this way one can systematically improve the accuracy of the physical observables by including radiative corrections in the coupling and relativistic corrections in the particle momenta, cf. fig. 7.1, guided by the power counting of the effective theory. In this work, we have scrutinized the implementation of non-relativistic effective field theories at finite temperature, i.e. abelian and non-abelian (p)NREFTs$_{\rm DM}$, cf. chapters 4 and 8, respectively, in order to address the dynamics of heavy dark matter in the thermal environment provided by the dark sector of the early expanding universe. The main aim has been to provide a detailed step-by-step computation of the aforementioned relevant reactions. We refer to part III for the study of the abelian model, and to part IV for the non-abelian case. We have emphasized the differences between the two theories, the corresponding processes and results in the associated sections.

We have accounted for the multiple soft photon exchanges that lead to the Sommerfeld enhancement affecting the soft dynamics prior to the annihilation process, and calculated the corrections to the S-wave annihilation in the particle momenta at next-to-leading order and, together with the annihilation of P-waves at LO, we contrasted the momentum-corrections to the radiative corrections at NLO inherited in the Wilson coefficients of the dimension-six four-fermion operators, cf. chapter 5. Moreover, we have computed the leading recoil corrections and higher-order radiative effects to the near-threshold processes induced by the dipole operators (the corresponding vertices are depicted in fig. 4.1), cf. chapter 6. Since under certain circumstances the radiative corrections may not be suppressed, they need to be resummed. We have correctly accounted for the HTL resummation of the Debye mass scale $m_{\rm D}$ in the temperature regime above the ultrasoft scale, and studied its impact on the present relic abundance, cf. chapter 7 for the abelian case. Although the resummation effect has a strong dependence on the individual thermal dipole rates, it reduces the DM energy density only by a few percentage, and it diminishes even more when taking into account the recoil effect due to the relative motion between the thermal plasma and the center-of-mass of the dark matter pairs. In addition, we have studied the recoil effect on the thermal rates with respect to two different reference frames, where we have chosen the laboratory and the center-of-mass frame of the heavy pair, and verified explicitly the Lorentz-boost transformation behaviour of cross sections and widths up to first order in the non-relativistic expansion, thereby proving that Lorentz-boost symmetry is not spoiled due to the presence of the thermal bath.

Among the differences between abelian and non-abelian models, we remark that, while in an abelian model a small value of the coupling at the hard scale is enough to guarantee a weak-coupling treatment for threshold observables, in a non-abelian dark matter model a weak-coupling treatment requires that the coupling remains small also at the ultrasoft scale. If we take the ultrasoft scale to be of the order of the temperature, then the smallest scale considered in this work is $T \approx 10^{-5} M$. At one-loop running, $\alpha(2M)$ needs to be quite small to keep $\alpha(T) < 1$. For instance, in the SU(3) non-abelian model the weak-coupling condition requires $\alpha(2M) \lesssim 0.04$. This should caution about computing at weak coupling the bound-state formation cross section and dissociation width entering the network of Boltzmann equations for the extraction of the DM en-

ergy density, whenever dealing with QCD-like charged particles in coannihilation dark matter scenarios. Nevertheless, the EFT framework holds also if the ultrasoft scale is strongly coupled, which is a situation familiar to QCD [11,174], as long as the multipole expansion is not spoiled, that is if the thermal wavelength $\sim 1/T$ of the gauge fields is sufficiently larger than the typical size of the fermion-antifermion pair. Consequently, at large temperatures, $T \sim M\alpha$, the multipole expansion breaks down. Estimating DM formation and dissociation in this situation requires computing thermal effects in $\mathrm{NREFT}_{\mathrm{DM}}$ and matching to a version of $\mathrm{pNREFT}_{\mathrm{DM}}$ that does not contain thermal gauge fields as dynamical degrees of freedom, but encodes them in a temperature dependent potential. Similar situations have been examined in QED [49,82] and QCD [48,84]. A quantitative assessment of such scenarios may be needed in order to solve the Boltzmann equations over a range of couplings that include values making $M\alpha$ smaller than the freeze-out temperature, i.e. $\alpha \lesssim 0.04$. This range encompasses coupling values typical of the electroweak SM sector, which may be relevant for genuine WIMP dark matter particles, with or without coannihilating partners, e.g. supersymmetric model realizations [16,113,122,175–177] and the inert doublet model [178–181].

Bound-state formation and dissociation rates are routinely used in the network of Boltzmann equations in order to extract the dark matter energy density, where however the thermal rates are just ingredients to be computed independently to fix the dynamics of the rate equations. A more accurate treatment of the out-of-equilibrium evolution for dark matter particles from non-relativistic effective field theories can be realized within the framework of open quantum systems. As for similar systems in the SM or the QCD theory, where Lindblad-like equations [99,152,153,155,182–184] were derived, we aim to obtain the quantum master equations for the reduced dark density operator, whose solution provides the present relic energy density of dark matter. The final part V in this work has been devoted to the out-of-equilibrium treatment of the heavy dark matter evolving as an open quantum system, where we present the quantum master equations in the abelian case, which we eventually reduce to the set of coupled Boltzmann equations in the semi-classical limit, that have finally been solved numerically in the preceding chapter 7. The results can be straightforwardly adopted to dark matter charged under $\mathrm{SU}(N)_{\mathrm{DM}}$. Along the Boltzmann reduction of the evolution equations, several approximations have been made which are required in order to approach the familiar coupled rate equations for the DM particle densities. A main drawback of the semi-classical rate equations, though phenomenologically useful since numerically solvable and hence of practical purpose, is that several pure quantum physical phenomena have been discarded due to the underlying approximations. It would be desirable to examine possible consequences on the dark matter relic abundance due to the ignored quantum effects such as the coherence and decoherence of states along the quantum evolution. Moreover, the integrated Boltzmann equations inherit the notion of kinetic equilibrium throughout the entire time evolution, but it may be interesting to study how and when thermalization is approached, if at all possible.

A possible approach to track the full quantum evolution of the reduced dark matter system, which requires solving the master equations directly, could consist for instance

in using the quantum trajectories algorithm QTraj, which has been developed in recent years in order to find a numerical solution to the Lindblad equations for heavy quarkonium in a hot thermal bath, cf. refs. [185–187]. The QTraj method enables one to evolve a large set of independently sampled quantum evolutions of the heavy-pair wave function. The corresponding observables, like the dark matter particle density, may then be computed along each sampled quantum trajectory, and upon averaging them over the many quantum paths, one can eventually make predictions for the time evolution of the particular observable [188].

Acknowledgments, Appendices and References

Acknowledgments

First of all, I want to thank my supervisors Prof. Dr. Nora Brambilla and Prof. Dr. Antonio Vairo that have offered me a position to be part of their scientific research group T30f (*Theoretical Particle and Nuclear Physics*), and to make this PhD thesis possible. I am very grateful for their guidance, encouragement and patience over the last years. I thank both of you for opening my mind on effective field theories and, owing to your outstanding knowledge, for giving me indispensable advice on how to think and work in an innovative and responsible way. Moreover, I am deeply grateful that I have had the opportunity to attend many conferences and workshops all over the world, to present my work and have insightful conversations with lots of experts in the field. I would like to express my deepest appreciation to my collaborator Dr. Simone Biondini, for helping me in any situation and taking time on many occasions for enlightening discussions. I am grateful for his constant availability which helped me a lot to keep myself thinking clearly about technical aspects of my PhD work, and for his kind invitations and hospitality at the University of Basel. Then of course many thanks to the other colleagues in the group, especially Abhishek, Xiangpeng, Julian, Tommaso, Tom, Panayiotis, but also to Wai Kin, Saga, Peter, Sebastian, Viljami, Stefan and Tobias for uncountable fruitful discussions in the office, during coffee breaks and on evenings downtown. Heartful thanks to Susanne Tillich for the great support on administrative issues. Moreover, I acknowledge the support from the DFG (Deutsche Forschungsgemeinschaft, German Research Foundation) cluster of excellence "ORIGINS" under Germany's Excellence Strategy - EXC-2094-390783311. Finally, I want to thank my parents and siblings for their continuous motivating words and great support, but also my roommates, friends and especially Janin Pätzold for the encouragement to successfully complete my PhD.

Appendix A

Lorentz boost transformations

A.1 Coordinates, momenta and internal energies

Let $\boldsymbol{r}_1$ and $\boldsymbol{r}_2$, $\boldsymbol{p}_1$ and $\boldsymbol{p}_2$, and $E_1 = \sqrt{M^2 + \boldsymbol{p}_1^2}$ and $E_2 = \sqrt{M^2 + \boldsymbol{p}_2^2}$ be the positions, momenta and energies, respectively, of two particles 1 and 2 with equal mass M in a reference frame S, and $\boldsymbol{r}_1'$ and $\boldsymbol{r}_2'$, $\boldsymbol{p}_1'$ and $\boldsymbol{p}_2'$, and $E_1' = \sqrt{M^2 + \boldsymbol{p}_1'^2}$ and $E_2' = \sqrt{M^2 + \boldsymbol{p}_2'^2}$ the positions, momenta and energies, respectively, of the two particles in a reference frame S' moving with respect to S with velocity $\boldsymbol{v}$. We can define the center-of-mass coordinates and momenta in the two reference frames. In the following, we consider the special case where the reference frame S' is the center-of-mass frame (cm) of the two particles. We call then S the laboratory frame (lab), see figure A.1 for a pictorial illustration. In general, the relative distances are defined as

$$\boldsymbol{r} \equiv \boldsymbol{r}_1 - \boldsymbol{r}_2\,, \qquad\qquad \boldsymbol{r}' \equiv \boldsymbol{r}_1' - \boldsymbol{r}_2'\,, \tag{A.1}$$

whereas the position vectors of the center-of-mass in the reference frames S and S' are

$$\boldsymbol{R} \equiv \frac{\boldsymbol{r}_1 + \boldsymbol{r}_2}{2}\,, \qquad\qquad \boldsymbol{R}' \equiv \frac{\boldsymbol{r}_1' + \boldsymbol{r}_2'}{2}\,. \tag{A.2}$$

The relative momenta of the pairs in the two reference frames are defined as

$$\boldsymbol{p} \equiv \frac{\boldsymbol{p}_1 - \boldsymbol{p}_2}{2}\,, \qquad\qquad \boldsymbol{p}' \equiv \frac{\boldsymbol{p}_1' - \boldsymbol{p}_2'}{2}\,, \tag{A.3}$$

and the total momenta as

$$\boldsymbol{P} \equiv \boldsymbol{p}_1 + \boldsymbol{p}_2\,, \qquad\qquad \boldsymbol{P}' \equiv \boldsymbol{p}_1' + \boldsymbol{p}_2'\,. \tag{A.4}$$

The Lorentz transformations relating momenta and energies in the two reference frames are

$$\boldsymbol{p}_1' = \boldsymbol{p}_1 + (\gamma - 1)(\boldsymbol{p}_1 \cdot \boldsymbol{v})\frac{\boldsymbol{v}}{\boldsymbol{v}^2} - \gamma E_1 \boldsymbol{v}\,, \tag{A.5}$$

$$\boldsymbol{p}_2' = \boldsymbol{p}_2 + (\gamma - 1)(\boldsymbol{p}_2 \cdot \boldsymbol{v})\frac{\boldsymbol{v}}{\boldsymbol{v}^2} - \gamma E_2 \boldsymbol{v}\,, \tag{A.6}$$

$$E_1' = \gamma(E_1 - \boldsymbol{p}_1 \cdot \boldsymbol{v})\,, \tag{A.7}$$

$$E_2' = \gamma(E_2 - \boldsymbol{p}_2 \cdot \boldsymbol{v})\,, \tag{A.8}$$

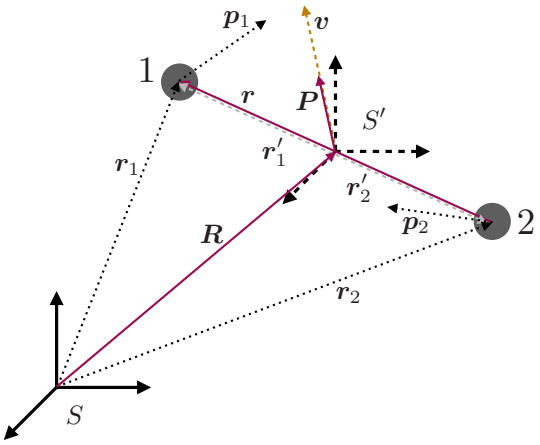

Figure A.1: Positions and momenta of two particles, dubbed 1 and 2, with respect to the reference frames S and S'. S' is moving with velocity $\boldsymbol{v}$ with respect to S. S' coincides with the center-of-mass frame, whereas S is the laboratory frame.

where $\gamma = 1/\sqrt{1-\boldsymbol{v}^2}$ is the Lorentz factor. Then from (A.3) and (A.4) it follows that the Lorentz transformations relating the relative and center-of-mass momenta between S and S' read

$$\boldsymbol{p}' = \boldsymbol{p} + (\gamma-1)(\boldsymbol{p}\cdot\boldsymbol{v})\frac{\boldsymbol{v}}{\boldsymbol{v}^2} - \frac{\gamma}{2}(E_1 - E_2)\boldsymbol{v}\,, \tag{A.9}$$

and

$$\boldsymbol{P}' = \boldsymbol{P} + (\gamma-1)(\boldsymbol{P}\cdot\boldsymbol{v})\frac{\boldsymbol{v}}{\boldsymbol{v}^2} - \gamma(E_1 + E_2)\boldsymbol{v}\,. \tag{A.10}$$

Now in our case, where S is the lab frame and S' the cm frame, the total momentum in S is

$$\boldsymbol{P}_{\rm lab} = (\boldsymbol{p}_1)_{\rm lab} + (\boldsymbol{p}_2)_{\rm lab}\,, \tag{A.11}$$

whereas in the center-of-mass frame it is, by definition,

$$\boldsymbol{P}_{\rm cm} = (\boldsymbol{p}_1)_{\rm cm} + (\boldsymbol{p}_2)_{\rm cm} = \boldsymbol{0}\,. \tag{A.12}$$

Using eq. (A.10) in (A.12), we get

$$\boldsymbol{0} = \boldsymbol{P}_{\rm cm} = \boldsymbol{P}_{\rm lab} + (\gamma-1)(\boldsymbol{P}_{\rm lab}\cdot\boldsymbol{v})\frac{\boldsymbol{v}}{\boldsymbol{v}^2} - \gamma((E_1)_{\rm lab} + (E_2)_{\rm lab})\boldsymbol{v}\,. \tag{A.13}$$

This equality fixes $\boldsymbol{v}$ as a function of the center-of-mass momentum and energy of the pair in the laboratory frame. Its solution reads

$$\boldsymbol{v} = \frac{\boldsymbol{P}_{\rm lab}}{(E_1)_{\rm lab} + (E_2)_{\rm lab}}\,. \tag{A.14}$$

If the two particles are non relativistic, which implies $E_1 \approx M$ and $E_2 \approx M$, then we get $\boldsymbol{v} \approx \boldsymbol{P}_{\rm lab}/(2M)$. This is the value of $\boldsymbol{v}$ used in the main body of the paper to compute the leading relativistic corrections to the various observables.

Furthermore, the condition (A.12) fixes the energies of the two particles in the center-of-mass frame to be equal:

$$(E_1)_{\rm cm} = (E_2)_{\rm cm}. \tag{A.15}$$

Using eqs. (A.7) and (A.8) in (A.15), we obtain a relation between the relative momentum in the laboratory frame, $\boldsymbol{p}_{\rm lab}$, the velocity $\boldsymbol{v}$ and the energy difference in the laboratory frame $(E_1)_{\rm lab} - (E_2)_{\rm lab}$, i.e.

$$\boldsymbol{p}_{\rm lab} \cdot \boldsymbol{v} = \frac{(E_1)_{\rm lab} - (E_2)_{\rm lab}}{2}\,. \tag{A.16}$$

Then, by trading $(E_1)_{\rm lab} - (E_2)_{\rm lab}$ for $2\,\boldsymbol{p}_{\rm lab} \cdot \boldsymbol{v}$, the Lorentz transformation (A.9) can be rewritten as

$$\boldsymbol{p}_{\rm cm} = \boldsymbol{p}_{\rm lab} + \frac{1-\gamma}{\gamma\,\boldsymbol{v}^2}(\boldsymbol{p}_{\rm lab} \cdot \boldsymbol{v})\boldsymbol{v}\,. \tag{A.17}$$

Selecting the component of the relative momentum along the direction of $\boldsymbol{v}$, eq. (A.17) implies

$$\boldsymbol{p}_{\rm lab} \cdot \boldsymbol{v} = \gamma\,\boldsymbol{p}_{\rm cm} \cdot \boldsymbol{v}\,, \tag{A.18}$$

which shows that the relative momentum component parallel to $\boldsymbol{v}$ gets larger by a factor γ in the laboratory frame with respect to the center-of-mass frame. Only the momentum component along $\boldsymbol{v}$ gets modified. This can be made explicit by decomposing the momentum $\boldsymbol{p}$ into a component parallel to $\boldsymbol{v}$, $\boldsymbol{p}_\parallel \equiv (\boldsymbol{p} \cdot \boldsymbol{v})\boldsymbol{v}/\boldsymbol{v}^2$, and a component orthogonal to it, $\boldsymbol{p}_\perp \equiv \boldsymbol{p} - \boldsymbol{p}_\parallel$, and rewriting eq. (A.17) accordingly:

$$\boldsymbol{p}_{\rm cm} = (\boldsymbol{p}_\perp)_{\rm lab} + \frac{(\boldsymbol{p}_\parallel)_{\rm lab}}{\gamma}\,. \tag{A.19}$$

The square of the relative momentum changes from one frame to the other as

$$|\boldsymbol{p}_{\rm cm}|^2 = |(\boldsymbol{p}_\perp)_{\rm lab}|^2 + \frac{|(\boldsymbol{p}_\parallel)_{\rm lab}|^2}{\gamma^2}\,. \tag{A.20}$$

From eq. (A.19) it follows that the momentum volume element gets also larger by a factor γ in the laboratory frame with respect to the center-of-mass frame:

$$d^3 p_{\rm cm} = \frac{d^3 p_{\rm lab}}{\gamma}\,. \tag{A.21}$$

Next we derive the Lorentz boost relations for the total energy of the two particles, $E_{\rm cm} \equiv (E_1)_{\rm cm} + (E_2)_{\rm cm}$ in the center-of-mass frame and $E_{\rm lab} \equiv (E_1)_{\rm lab} + (E_2)_{\rm lab}$ in the laboratory frame. From (A.7) and (A.8) it follows that

$$E_{\rm cm} = \gamma(E_{\rm lab} - \boldsymbol{P}_{\rm lab} \cdot \boldsymbol{v}) = \frac{E_{\rm lab}}{\gamma}\,, \tag{A.22}$$

where in the last equality we have used eq. (A.14), i.e. $\boldsymbol{v} = \boldsymbol{P}_{\rm lab}/E_{\rm lab}$, which implies $1/\gamma^2 = 1 - (\boldsymbol{P}_{\rm lab}/E_{\rm lab})^2$. While the center-of-mass energy increases by a factor γ in the laboratory frame with respect to the center-of-mass frame, the opposite happens to the energy difference of two two-particle states, ΔE, for a suitable choice of the center-of-mass frame. The reason is that the Lorentz factor γ depends on the total energy of the pair and therefore it changes by $\Delta\gamma = -\gamma^3\, \boldsymbol{P}_{\rm lab}^2\, (\Delta E)_{\rm lab}/E_{\rm lab}^3$ from one state to the other. Fixing the center-of-mass frame to be just the center-of-mass frame of one chosen state, and computing the relative velocity $\boldsymbol{v}$ and the Lorentz factor with respect to it, we get

$$(\Delta E)_{\rm cm} = \gamma (\Delta E)_{\rm lab}\,. \tag{A.23}$$

Since ΔE may be understood as a frequency, the above relation expresses the Lorentz dilation of the time intervals measured from transition frequencies in the laboratory frame with respect to the center-of-mass frame.

Similarly to the relative momentum, we may decompose the relative distance, $\boldsymbol{r}$, between the two particles into a component parallel to $\boldsymbol{v}$, $\boldsymbol{r}_\parallel \equiv (\boldsymbol{r}\cdot\boldsymbol{v})\boldsymbol{v}/\boldsymbol{v}^2$, and a component orthogonal to it, $\boldsymbol{r}_\perp \equiv \boldsymbol{r} - \boldsymbol{r}_\parallel$. The Lorentz transformation of $\boldsymbol{r}$ reads

$$\boldsymbol{r}_{\rm cm} = \boldsymbol{r}_{\rm lab} + \frac{\gamma-1}{\boldsymbol{v}^2}(\boldsymbol{r}_{\rm lab}\cdot\boldsymbol{v})\boldsymbol{v} = (\boldsymbol{r}_\perp)_{\rm lab} + \gamma(\boldsymbol{r}_\parallel)_{\rm lab}\,, \tag{A.24}$$

where we understand $\boldsymbol{r}_{\rm lab}$ as determined from the coordinates of the two particles taken at the same time in the laboratory frame.[1] The square of the relative distance changes from one frame to the other as

$$|\boldsymbol{r}_{\rm cm}|^2 = |(\boldsymbol{r}_\perp)_{\rm lab}|^2 + \gamma^2 |(\boldsymbol{r}_\parallel)_{\rm lab}|^2\,. \tag{A.25}$$

From eq. (A.24) it also follows that the volume element gets contracted by a factor $1/\gamma$ in the laboratory frame with respect to the center-of-mass frame:

$$d^3 r_{\rm cm} = \gamma\, d^3 r_{\rm lab}\,. \tag{A.26}$$

A.2 Wavefunctions and matrix elements

In quantum mechanics a Lorentz transformation may be represented by a unitary transformation $U(\boldsymbol{v})$, with $U(\boldsymbol{v})^\dagger = U(\boldsymbol{v})^{-1}$. The explicit form of the transformation is not relevant here, but its action on a generic discrete energy eigenstate $|n\rangle$, scattering energy eigenstate $|\boldsymbol{p}\rangle$, and on the relative distance operator $\boldsymbol{r}$ is

$$U^\dagger(\boldsymbol{v})\,|n\rangle_{\rm cm} = |n\rangle_{\rm lab}\,, \tag{A.27}$$

$$U^\dagger(\boldsymbol{v})\,|\boldsymbol{p}\rangle_{\rm cm} = N(\boldsymbol{v})\,|\boldsymbol{p}\rangle_{\rm lab}\,, \qquad |N(\boldsymbol{v})|^2 = \gamma\,, \tag{A.28}$$

$$U^\dagger(\boldsymbol{v})\,\boldsymbol{r}_{\rm cm}\,U(\boldsymbol{v}) = \boldsymbol{r}_{\rm lab} + \frac{\gamma-1}{\boldsymbol{v}^2}(\boldsymbol{r}_{\rm lab}\cdot\boldsymbol{v})\boldsymbol{v}\,. \tag{A.29}$$

[1] The difference between this condition and eq. (A.15) is at the origin of the contraction of the distance along the motion direction in the laboratory frame in eq. (A.24) and the dilation of the relative momentum along the motion direction in the laboratory frame in eq. (A.19).

Equation (A.27) follows from the invariance of the normalization of discrete states under Lorentz transformations: $\langle n|m\rangle_{\rm lab} = \langle n|m\rangle_{\rm cm} = \delta_{nm}$. In the following, the notation $\langle n|A|m\rangle_{\rm lab}$ ($\langle n|A|m\rangle_{\rm cm}$) means that the observable A as well as the bra and the ket are in the laboratory (center-of-mass) frame; the same notation applies to scattering states. Equation (A.28) follows from the fact that the non-relativistic normalization of scattering states is not Lorentz invariant. The normalization factor $N(\boldsymbol{v})$ is then necessary to keep both $|\boldsymbol{p}\rangle_{\rm cm}$ and $|\boldsymbol{p}\rangle_{\rm lab}$ non-relativistically normalized: $\langle \boldsymbol{p}|\boldsymbol{q}\rangle_{\rm lab} = \delta^3(\boldsymbol{p}_{\rm lab} - \boldsymbol{q}_{\rm lab})$ and $\langle \boldsymbol{p}|\boldsymbol{q}\rangle_{\rm cm} = \delta^3(\boldsymbol{p}_{\rm cm} - \boldsymbol{q}_{\rm cm})$. It can be computed from

$$\begin{aligned}
|N(\boldsymbol{v})|^2 \langle \boldsymbol{p}|\boldsymbol{q}\rangle_{\rm lab} &= \langle \boldsymbol{p}|\boldsymbol{q}\rangle_{\rm cm} = \delta^3(\boldsymbol{p}_{\rm cm} - \boldsymbol{q}_{\rm cm}) \\
&= \delta^3\left(\boldsymbol{p}_{\rm lab} - \boldsymbol{q}_{\rm lab} + \frac{1-\gamma}{\gamma\,\boldsymbol{v}^2}((\boldsymbol{p}_{\rm lab} - \boldsymbol{q}_{\rm lab})\cdot\boldsymbol{v})\boldsymbol{v}\right) \\
&= \sum_{n=0}^{\infty}\frac{1}{n!}\left(\frac{1-\gamma}{\gamma\,\boldsymbol{v}^2}((\boldsymbol{p}_{\rm lab} - \boldsymbol{q}_{\rm lab})\cdot\boldsymbol{v})(\boldsymbol{v}\cdot\boldsymbol{\nabla}_{\boldsymbol{p}_{\rm lab}})\right)^n \delta^3(\boldsymbol{p}_{\rm lab} - \boldsymbol{q}_{\rm lab}) \\
&= \sum_{n=0}^{\infty}\frac{1}{n!}\left(\frac{1-\gamma}{\gamma\,\boldsymbol{v}^2}\right)^n n!\,(\boldsymbol{v}^2)^n\,(-1)^n\,\delta^3(\boldsymbol{p}_{\rm lab} - \boldsymbol{q}_{\rm lab}) \\
&= \frac{1}{1-(\gamma-1)/\gamma}\delta^3(\boldsymbol{p}_{\rm lab} - \boldsymbol{q}_{\rm lab}) = \gamma\,\delta^3(\boldsymbol{p}_{\rm lab} - \boldsymbol{q}_{\rm lab})\,, \qquad \text{(A.30)}
\end{aligned}$$

where we used eq. (A.17) in the second line, performed the Taylor expansion of the Dirac delta function in the third line and recognized the geometric series in the last line.[2] From eq. (A.30), it follows $|N(\boldsymbol{v})|^2 = \gamma$. Equation (A.29) expresses at the operator level the transformation (A.24).

The relevant quantum-mechanical matrix elements appearing in this work may be boosted in the different reference frames using eqs. (A.27)–(A.29). Let us first consider the bound-state wavefunction at the origin:

$$\begin{aligned}
\left(|\Psi_{n\ell m}(\boldsymbol{0})|^2\right)_{\rm cm} &= \langle n\ell m|\delta^3(\boldsymbol{r})|n\ell m\rangle_{\rm cm} = \langle n\ell m|U(\boldsymbol{v})\,U^\dagger(\boldsymbol{v})\delta^3(\boldsymbol{r})U(\boldsymbol{v})\,U^\dagger(\boldsymbol{v})|n\ell m\rangle_{\rm cm} \\
&= \langle n\ell m|\delta^3\left(\boldsymbol{r} + (\gamma-1)(\boldsymbol{r}\cdot\boldsymbol{v})\boldsymbol{v}/\boldsymbol{v}^2\right)|n\ell m\rangle_{\rm lab} \\
&= \int d^3r_{\rm lab}\,\delta^3\left(\boldsymbol{r}_{\rm lab} + (\gamma-1)(\boldsymbol{r}_{\rm lab}\cdot\boldsymbol{v})\boldsymbol{v}/\boldsymbol{v}^2\right)\,\left(|\Psi_{n\ell m}(\boldsymbol{r}_{\rm lab})|^2\right)_{\rm lab} \\
&= \int d^3r_{\rm lab}\,\frac{1}{\gamma}\delta^3\left(\boldsymbol{r}_{\rm lab}\right)\,\left(|\Psi_{n\ell m}(\boldsymbol{r}_{\rm lab})|^2\right)_{\rm lab} = \frac{\left(|\Psi_{n\ell m}(\boldsymbol{0})|^2\right)_{\rm lab}}{\gamma}\,, \qquad \text{(A.31)}
\end{aligned}$$

where we have specified the principal, orbital and magnetic quantum numbers. In the last line, we have rewritten the delta function using an argument similar to the one in (A.30). Instead, due to the different normalization, for the scattering state wavefunction

[2] In the fourth line, the property $x^n\delta^{(n)}(x) = (-1)^n n!\,\delta(x)$, which can straightforwardly be generalized to higher dimensions, has been used to evaluate the gradients. $\delta^{(n)}(x)$ denotes the nth derivative acting on the delta function.

at the origin, we obtain

$$\begin{aligned}
\left(|\Psi_{\boldsymbol{p}\ell}(\boldsymbol{0})|^2\right)_{\rm cm} &= \langle \boldsymbol{p}\ell|\delta^3(\boldsymbol{r})|\boldsymbol{p}\ell\rangle_{\rm cm} = \langle \boldsymbol{p}\ell|U(\boldsymbol{v})\,U^\dagger(\boldsymbol{v})\delta^3(\boldsymbol{r})U(\boldsymbol{v})\,U^\dagger(\boldsymbol{v})|\boldsymbol{p}\ell\rangle_{\rm cm} \\
&= |N(\boldsymbol{v})|^2\langle \boldsymbol{p}\ell|\delta^3\left(\boldsymbol{r}+(\gamma-1)(\boldsymbol{r}\cdot\boldsymbol{v})\boldsymbol{v}/\boldsymbol{v}^2\right)|\boldsymbol{p}\ell\rangle_{\rm lab} \\
&= \gamma\int d^3r_{\rm lab}\,\delta^3\left(\boldsymbol{r}_{\rm lab}+(\gamma-1)(\boldsymbol{r}_{\rm lab}\cdot\boldsymbol{v})\boldsymbol{v}/\boldsymbol{v}^2\right)\,\left(|\Psi_{\boldsymbol{p}\ell}(\boldsymbol{r}_{\rm lab})|^2\right)_{\rm lab} \\
&= \gamma\int d^3r_{\rm lab}\,\frac{1}{\gamma}\delta^3\left(\boldsymbol{r}_{\rm lab}\right)\,\left(|\Psi_{\boldsymbol{p}\ell}(\boldsymbol{r}_{\rm lab})|^2\right)_{\rm lab} = \left(|\Psi_{\boldsymbol{p}\ell}(\boldsymbol{0})|^2\right)_{\rm lab}\,. \quad \text{(A.32)}
\end{aligned}$$

Dipole matrix elements between generic bound states are related in the different reference frames by

$$\begin{aligned}
\langle n|\boldsymbol{r}|m\rangle_{\rm cm} &= \langle n|U(\boldsymbol{v})\,U^\dagger(\boldsymbol{v})\boldsymbol{r}U(\boldsymbol{v})\,U^\dagger(\boldsymbol{v})|m\rangle_{\rm cm} \\
&= \langle n|\boldsymbol{r}+(\gamma-1)(\boldsymbol{r}\cdot\boldsymbol{v})\boldsymbol{v}/\boldsymbol{v}^2|m\rangle_{\rm lab} \\
&= \langle n|\boldsymbol{r}|m\rangle_{\rm lab}+\frac{\gamma-1}{\boldsymbol{v}^2}\langle n|(\boldsymbol{r}\cdot\boldsymbol{v})\boldsymbol{v}|m\rangle_{\rm lab} \\
&\approx \langle n|\boldsymbol{r}|m\rangle_{\rm lab}+\frac{1}{2}\langle n|(\boldsymbol{r}\cdot\boldsymbol{v})\boldsymbol{v}|m\rangle_{\rm lab}\,, \quad \text{(A.33)}
\end{aligned}$$

where in the last line we have expanded the Lorentz boost factor up to quadratic order in small $\boldsymbol{v}$, i.e. $\gamma\approx 1+\boldsymbol{v}^2/2$. Finally, dipole matrix elements between a generic bound and scattering state in different reference frames are related by

$$\begin{aligned}
\langle n|\boldsymbol{r}|\boldsymbol{p}\rangle_{\rm cm} &= \langle n|U(\boldsymbol{v})\,U^\dagger(\boldsymbol{v})\boldsymbol{r}U(\boldsymbol{v})\,U^\dagger(\boldsymbol{v})|\boldsymbol{p}\rangle_{\rm cm} \\
&= N(\boldsymbol{v})\langle n|\boldsymbol{r}+(\gamma-1)(\boldsymbol{r}\cdot\boldsymbol{v})\boldsymbol{v}/\boldsymbol{v}^2|\boldsymbol{p}\rangle_{\rm lab} \\
&= N(\boldsymbol{v})\langle n|\boldsymbol{r}|\boldsymbol{p}\rangle_{\rm lab}+N(\boldsymbol{v})\frac{\gamma-1}{\boldsymbol{v}^2}\langle n|(\boldsymbol{r}\cdot\boldsymbol{v})\boldsymbol{v}|\boldsymbol{p}\rangle_{\rm lab} \\
&\approx \left(1+\frac{\boldsymbol{v}^2}{4}\right)\langle n|\boldsymbol{r}|\boldsymbol{p}\rangle_{\rm lab}+\frac{1}{2}\langle n|(\boldsymbol{r}\cdot\boldsymbol{v})\boldsymbol{v}|\boldsymbol{p}\rangle_{\rm lab}\,, \quad \text{(A.34)}
\end{aligned}$$

where in the last line we have expanded in $\boldsymbol{v}$ up to order $\boldsymbol{v}^2$, with $N(\boldsymbol{v})=\sqrt{\gamma}\approx 1+\boldsymbol{v}^2/4$.

Appendix B

Thermal averages in different reference frames

Along this work we dealt with different kinds of scattering processes like annihilations or the formation of bound states, involving the computation of the corresponding cross sections and widths in two particularly different frames, the lab and the cm frame. However, for the sake of determining its impact on the dark matter relic abundance, it is necessary to compute the thermally averaged versions of those observables that eventually enter the coupled evolution equations, taking the statistical average over the incoming momenta of the dark matter particles and antiparticles with respect to the chosen reference frame. Hence let us consider a generic cross section involving the scattering of two incoming particles with center-of-mass momentum $\boldsymbol{P}_{\rm lab} = (\boldsymbol{p}_1)_{\rm lab} + (\boldsymbol{p}_2)_{\rm lab}$ and relative momentum $\boldsymbol{p}_{\rm lab} = ((\boldsymbol{p}_1)_{\rm lab} - (\boldsymbol{p}_2)_{\rm lab})/2$ times Møller velocity in the laboratory frame, $(\sigma\, v_{\rm Møl})_{\rm lab}(\boldsymbol{p}_{\rm lab}, \boldsymbol{P}_{\rm lab})$. The *thermal average in the laboratory frame* is defined as

$$\langle(\sigma\, v_{\rm Møl})_{\rm lab}\rangle_{\rm lab} = \frac{\displaystyle\int \frac{d^3(p_1)_{\rm lab}}{(2\pi)^3}\,\frac{d^3(p_2)_{\rm lab}}{(2\pi)^3}\, e^{-\frac{(E_1)_{\rm lab}}{T}}\, e^{-\frac{(E_2)_{\rm lab}}{T}}\,(\sigma\, v_{\rm Møl})_{\rm lab}(\boldsymbol{p}_{\rm lab}, \boldsymbol{P}_{\rm lab})}{\displaystyle\int \frac{d^3(p_1)_{\rm lab}}{(2\pi)^3}\,\frac{d^3(p_2)_{\rm lab}}{(2\pi)^3}\, e^{-\frac{(E_1)_{\rm lab}}{T}}\, e^{-\frac{(E_2)_{\rm lab}}{T}}}\,, \quad \text{(B.1)}$$

where $e^{-(E_1)_{\rm lab}/T}$ and $e^{-(E_2)_{\rm lab}/T}$ are the Maxwell–Boltzmann distributions of the incoming particles in the laboratory frame, i.e. the frame where the bath is at rest, and $((E_1)_{\rm lab}, (\boldsymbol{p}_1)_{\rm lab})$, $((E_2)_{\rm lab}, (\boldsymbol{p}_2)_{\rm lab})$ are the four-momenta of the two incoming particles. For unbound particles of mass M on mass shell, $(E_1)_{\rm lab} = \sqrt{(\boldsymbol{p}_1)^2_{\rm lab} + M^2}$ and $(E_2)_{\rm lab} = \sqrt{(\boldsymbol{p}_2)^2_{\rm lab} + M^2}$. We average over Maxwell–Boltzmann distributions because we assume $M/T \gg 1$, which is certainly fulfilled for all times at and after the thermal DM freeze-out.

The numerator on the right-hand side of (B.1),

$$\int \frac{d^3(p_1)_{\rm lab}}{(2\pi)^3}\,\frac{d^3(p_2)_{\rm lab}}{(2\pi)^3}\, e^{-\frac{(E_1)_{\rm lab}}{T}}\, e^{-\frac{(E_2)_{\rm lab}}{T}}\,(\sigma\, v_{\rm Møl})_{\rm lab}(\boldsymbol{p}_{\rm lab}, \boldsymbol{P}_{\rm lab})\,, \quad \text{(B.2)}$$

is Lorentz invariant [57], which is the reason for the use of the Møller velocity. For each pair of momenta $\boldsymbol{p}_{\rm lab}$ and $\boldsymbol{P}_{\rm lab}$ in the laboratory frame, we may identify a center-of-mass frame such that with respect to it the particles move with relative momentum $\boldsymbol{p}_{\rm cm}$, center-of-mass momentum $\boldsymbol{P}_{\rm cm} = \boldsymbol{0}$, and the laboratory frame moves with relative velocity $-\boldsymbol{v}$. From eqs. (A.9) and (A.10), it follows that the two pairs of kinematical variables are related by the Lorentz transformations

$$\begin{aligned} \boldsymbol{p}_{\rm lab} &= \boldsymbol{p}_{\rm cm} + (\gamma - 1)(\boldsymbol{p}_{\rm cm} \cdot \boldsymbol{v})\frac{\boldsymbol{v}}{\boldsymbol{v}^2}\,, \\ \boldsymbol{P}_{\rm lab} &= \gamma E_{\rm cm}\boldsymbol{v}\,, \end{aligned} \tag{B.3}$$

where $E_{\rm cm} = ((E_1)_{\rm lab}+(E_2)_{\rm lab})/\gamma = 2\sqrt{\boldsymbol{p}_{\rm cm}^2 + M^2}$ is the total energy of the two particles in the center-of-mass frame. The Jacobian of the transformation from the kinematical variables $(\boldsymbol{p})_{\rm lab}$ and $(\boldsymbol{P})_{\rm lab}$ to $\boldsymbol{p}_{\rm cm}$ and $\boldsymbol{v}$ is

$$\gamma^6 E_{\rm cm}^3 \left(1 - \frac{(\boldsymbol{p}_{\rm cm} \cdot \boldsymbol{v})^2}{(E_{\rm cm}/2)^2}\right). \tag{B.4}$$

The factor $\gamma^2 \left(1 - \dfrac{(\boldsymbol{p}_{\rm cm} \cdot \boldsymbol{v})^2}{(E_{\rm cm}/2)^2}\right)$ cancels against the transformation factor of the Møller velocity, see eq. (5.17), so that the integral (B.2) can be eventually written in terms of the center-of-mass kinematical variables $\boldsymbol{p}_{\rm cm}$ and $\boldsymbol{v}$ as

$$\frac{1}{(2\pi)^3}\int_{|\boldsymbol{v}|\leq 1} d^3v\, \frac{d^3p_{\rm cm}}{(2\pi)^3}\, \gamma^4 E_{\rm cm}^3\, e^{-\frac{\gamma E_{\rm cm}}{T}}\, (\sigma\, v_{\rm M\o l})_{\rm cm}(\boldsymbol{p}_{\rm cm}, \boldsymbol{v})\,. \tag{B.5}$$

The result agrees with an analogous expression that can be found in ref. [189]. Note that $e^{-\gamma E_{\rm cm}/T}$ may be also rewritten as $e^{-|(p_1)^\mu_{\rm cm} u_\mu|/T} e^{-|(p_2)^\mu_{\rm cm} u_\mu|/T}$, where $e^{-|p^\mu u_\mu|/T}$ is the small T limit of the particle distribution in the moving thermal bath defined in (6.65).

The *thermal average in the center-of-mass frame* is defined as

$$\langle(\sigma\, v_{\rm M\o l})_{\rm cm}\rangle_{\rm cm} = \frac{\displaystyle\int_{|\boldsymbol{v}|\leq 1} d^3v\, \frac{d^3p_{\rm cm}}{(2\pi)^3}\, \gamma^4 E_{\rm cm}^3\, e^{-\frac{\gamma E_{\rm cm}}{T}}\, (\sigma\, v_{\rm M\o l})_{\rm cm}(\boldsymbol{p}_{\rm cm}, \boldsymbol{v})}{\displaystyle\int_{|\boldsymbol{v}|\leq 1} d^3v\, \frac{d^3p_{\rm cm}}{(2\pi)^3}\, \gamma^4 E_{\rm cm}^3\, e^{-\frac{\gamma E_{\rm cm}}{T}}}\,. \tag{B.6}$$

While the numerators in the right-hand sides of eqs. (B.1) and (B.6) are Lorentz invariant, the denominators, which are up to a degeneracy factor the products of the particle number densities at equilibrium, $n_{1,\rm eq}$ and $n_{2,\rm eq}$, are not. Hence the conversion factor from $\langle(\sigma\, v_{\rm M\o l})_{\rm lab}\rangle_{\rm lab}$ to $\langle(\sigma\, v_{\rm M\o l})_{\rm cm}\rangle_{\rm cm}$ is given by the ratio of the particle number densities at equilibrium in the two frames. An explicit calculation gives

$$\begin{aligned} \langle(\sigma\, v_{\rm M\o l})_{\rm lab}\rangle_{\rm lab} &= \frac{n_{1,\rm eq}^{\rm cm} n_{2,\rm eq}^{\rm cm}}{n_{1,\rm eq}^{\rm lab} n_{2,\rm eq}^{\rm lab}}\, \langle(\sigma\, v_{\rm M\o l})_{\rm cm}\rangle_{\rm cm} \\ &= \frac{1}{2}\left(1 + \frac{K_1^2(M/T)}{K_2^2(M/T)}\right) \langle(\sigma\, v_{\rm M\o l})_{\rm cm}\rangle_{\rm cm}\,, \end{aligned} \tag{B.7}$$

where K_i are modified Bessel functions of the second kind. The above expression was first derived in ref. [57].

As an application, we consider the thermal average of the annihilation cross section derived in eq. (5.16). In the laboratory frame at order T/M, it reads

$$\begin{aligned}\langle(\sigma_{\rm ann}v_{\rm M\o l})_{\rm lab}\rangle_{\rm lab} &= \left[1-\frac{8\pi^3}{(MT)^3}\int\frac{d^3p_{\rm lab}}{(2\pi)^3}\,\frac{d^3P_{\rm lab}}{(2\pi)^3}e^{-\frac{\boldsymbol{p}_{\rm lab}^2}{MT}}e^{-\frac{\boldsymbol{P}_{\rm lab}^2}{4MT}}\,\frac{\boldsymbol{P}_{\rm lab}^2}{4M^2}\right]\sigma_{\rm ann}^{\rm NR}v_{\rm rel}^{(0)}\\ &= \left(1-\frac{3T}{2M}\right)\sigma_{\rm ann}^{\rm NR}v_{\rm rel}^{(0)}\,,\end{aligned}\tag{B.8}$$

where we have expanded $(E_1)_{\rm lab}+(E_2)_{\rm lab}=2M+\boldsymbol{p}_{\rm lab}^2/M+\boldsymbol{P}_{\rm lab}^2/(4M)+\dots$. The result is consistent with eq. (B.7) in the limit $M\gg T$, as a consequence of $\sigma_{\rm ann}^{\rm NR}v_{\rm rel}^{(0)}$ being independent of the momenta. Concerning the absolute accuracy of the thermal average in (B.8) and the other thermal averages considered in this work, we remark that corrections proportional to the center-of-mass momentum $\boldsymbol{P}$ due to the motion of the dark fermion-antifermion pair in the laboratory frame, or equivalently corrections due to the motion of the thermal bath in the center-of-mass reference frame, give corrections to the thermal averages of relative order T/M at low temperatures. These are of the same order as the corrections due to the relative momentum $\boldsymbol{p}$ that are of relative order $\boldsymbol{p}^2/M^2$, which have not been considered here.

Similarly, the thermal average of a bound-state decay width in the laboratory frame is defined as

$$\langle(\Gamma)_{\rm lab}\rangle_{\rm lab}=\frac{\displaystyle\int\frac{d^3P_{\rm lab}}{(2\pi)^3}\,e^{-\frac{(E_n)_{\rm lab}}{T}}\,(\Gamma)_{\rm lab}(\boldsymbol{P}_{\rm lab})}{\displaystyle\int\frac{d^3P_{\rm lab}}{(2\pi)^3}\,e^{-\frac{(E_n)_{\rm lab}}{T}}}\,,\tag{B.9}$$

and related to the thermal average of the decay width in the center-of-mass frame through

$$\langle(\Gamma)_{\rm lab}\rangle_{\rm lab}=\frac{\displaystyle\int_{|\boldsymbol{v}|\le1}d^3v\,\gamma^5\,e^{-\frac{\gamma(E_n)_{\rm cm}}{T}}\,\frac{(\Gamma)_{\rm cm}(\boldsymbol{v})}{\gamma}}{\displaystyle\int_{|\boldsymbol{v}|\le1}d^3v\,\gamma^5\,e^{-\frac{\gamma(E_n)_{\rm cm}}{T}}}=\left\langle\frac{(\Gamma)_{\rm cm}}{\gamma}\right\rangle_{\rm cm}\,,\tag{B.10}$$

where E_n is the energy of the bound state. In the center-of-mass frame, it is given in eq. (4.7). In the laboratory frame, it may be computed either from $\gamma(E_n)_{\rm cm}$, which amounts at boosting the energy from the center-of-mass frame, or directly from the bound-state potentials and kinetic energy corrections listed in section 4.2, footnote 4. The result is the same and reads

$$(E_n)_{\rm lab}=2M-\frac{M\alpha^2}{4n^2}+\frac{\boldsymbol{P}_{\rm lab}^2}{4M}+\frac{M\alpha^2}{4n^2}\frac{\boldsymbol{P}_{\rm lab}^2}{8M^2}-\frac{\boldsymbol{P}_{\rm lab}^4}{64M^3}\,.\tag{B.11}$$

The first two terms drop out in the thermal average, as they do not depend on the momentum; the last two terms are suppressed with respect to $\boldsymbol{P}_{\rm lab}^2/(4M)$ by E/M or T/M. The first equality in eq. (B.10) follows from the Lorentz transformation $\boldsymbol{P}_{\rm lab}=$

$\gamma(E_n)_{\rm cm}\boldsymbol{v}$, whose Jacobian is $\gamma^5(E_n)^3_{\rm cm}$, from $(E_n)_{\rm lab} = \gamma(E_n)_{\rm cm}$ and $(\Gamma)_{\rm lab}(\boldsymbol{P}_{\rm lab}) = (\Gamma)_{\rm cm}(\boldsymbol{v})/\gamma$. Note that $(E_n)_{\rm cm}$ is a constant that does not depend on the integration variables.

As an application, we consider the thermal average of the annihilation widths computed in eq. (5.29) and following. If we neglect thermal corrections affecting the annihilation width in the center-of-mass frame (cf. chapter 6, footnote 16), then $(\Gamma_{\rm ann})_{\rm cm}$ is $\boldsymbol{v}$ independent and factorizes outside the integral, leading to

$$\begin{aligned}\langle(\Gamma_{\rm ann})_{\rm lab}\rangle_{\rm lab} &= \frac{\displaystyle\int_{|\boldsymbol{v}|\le 1} d^3v\,\gamma^4\,e^{-\frac{\gamma(E_n)_{\rm cm}}{T}}}{\displaystyle\int_{|\boldsymbol{v}|\le 1} d^3v\,\gamma^5\,e^{-\frac{\gamma(E_n)_{\rm cm}}{T}}}\,(\Gamma_{\rm ann})_{\rm cm} = \frac{K_1((E_n)_{\rm cm}/T)}{K_2((E_n)_{\rm cm}/T)}\,(\Gamma_{\rm ann})_{\rm cm} \\ &\approx \left(1-\frac{3T}{2(E_n)_{\rm cm}}\right)(\Gamma_{\rm ann})_{\rm cm}\,. \end{aligned} \tag{B.12}$$

Finally, we summarize the steps that we followed in this work to compute consistently thermal averages in the laboratory frame at first order in the center-of-mass momentum.

(i) Thermal averages of cross sections and decay widths in the laboratory frame are defined as in eqs. (B.1) and (B.9), respectively.

(ii) Since matrix elements are most easily computed in the center-of-mass frame, see for instance ref. [51], they are first boosted in the center-of-mass frame according to the transformation formulas derived in appendix A.2. Then the relative momentum in the center-of-mass frame is re-expressed in terms of the momentum in the laboratory frame by means of the Lorentz transformation (A.19), as this is our integration variable. We may follow the same procedure with the energy differences, or compute them directly in the laboratory frame.

(iii) All expressions inside the thermal average integrals are expanded in powers of $\boldsymbol{P}$ in accordance with the power counting. In particular, the Maxwell–Boltzmann distributions for scattering states entering the cross section thermal averages are expanded as

$$e^{-\frac{(E_1)_{\rm lab}}{T}}\,e^{-\frac{(E_2)_{\rm lab}}{T}} = e^{-\frac{2M}{T}}\,e^{-\frac{\boldsymbol{p}^2_{\rm lab}}{MT}}\,e^{-\frac{\boldsymbol{P}^2_{\rm lab}}{4MT}}\left(1+\frac{\boldsymbol{P}^2_{\rm lab}\boldsymbol{p}^2_{\rm lab}}{8M^3T}+\frac{\boldsymbol{P}^4_{\rm lab}}{64M^3T}+\frac{(\boldsymbol{P}_{\rm lab}\cdot\boldsymbol{p}_{\rm lab})^2}{4M^3T}+\dots\right), \tag{B.13}$$

and the Maxwell–Boltzmann distribution for bound states entering the decay width thermal averages is expanded as

$$e^{-\frac{(E_n)_{\rm lab}}{T}} = e^{-\frac{2M}{T}}\,e^{\frac{M\alpha^2}{4n^2T}}\,e^{-\frac{\boldsymbol{P}^2_{\rm lab}}{4MT}}\left(1-\frac{M\alpha^2}{4n^2}\frac{\boldsymbol{P}^2_{\rm lab}}{8M^2T}+\frac{\boldsymbol{P}^4_{\rm lab}}{64M^3T}+\dots\right), \tag{B.14}$$

where we display only the relevant terms, i.e. those that depend on the center-of-mass momentum and contribute to the thermal average at order T/M or E/M according to the power counting $P_{\rm lab}\sim p_{\rm lab}\sim\sqrt{MT}$. Constant factors, like $e^{-2M/T}$ and $e^{M\alpha^2/(4n^2T)}$, drop out in the thermal averages. Also the number densities in the denominators of the thermal averages are expanded in powers of T/M or E/M up to first order.

The integrals in (B.1) and (B.9) simplify a lot if we neglect the center-of-mass momentum $\boldsymbol{P}$ in the integrands, and similarly omit the velocity dependence $\boldsymbol{v}$ in the observables in (B.6) and (B.10). Then the cross sections times Møller velocities and widths, together with their corresponding thermal averages, become equal in the two reference frames, since the laboratory frame coincides with the center-of-mass frame for $\boldsymbol{P} = \boldsymbol{0} = \boldsymbol{v}$. In this case there is no need to thermally average the widths, since they do not depend on any momentum and thus can be pulled out of the integrals. The result of those integrals cancels between the numerator and denominator in each of the eqs. (B.9) and (B.10). If we neglect $\boldsymbol{P}$ in the laboratory frame, or equivalently $\boldsymbol{v}$ in the center-of-mass frame, then it follows that $(v_{\text{Møl}})_{\text{lab}} = (v_{\text{Møl}})_{\text{cm}} \equiv v_{\text{rel}} \approx 2|\boldsymbol{p}|/M$. Hence, in the thermal average the integral over $\boldsymbol{P}$ factorizes and cancels against the normalization. We are left with

$$\begin{aligned} \langle \sigma v_{\text{rel}} \rangle &= 8 \left(\frac{\pi}{MT} \right)^{\frac{3}{2}} \int \frac{d^3p}{(2\pi)^3} e^{-\frac{\boldsymbol{p}^2}{MT}} \sigma v_{\text{rel}}(\boldsymbol{p}) \\ &= \sqrt{\frac{2}{\pi}} \left(\frac{M}{2T} \right)^{\frac{3}{2}} \int_0^\infty dv_{\text{rel}}\, v_{\text{rel}}^2\, e^{-\frac{M}{4T} v_{\text{rel}}^2}\, \sigma v_{\text{rel}}(v_{\text{rel}})\,, \end{aligned} \tag{B.15}$$

where the last line applies only to rotationally invariant cross sections.

Appendix C

General dipole matrix elements

C.1 General expressions in $\mathrm{U}(1)_{\mathrm{DM}}$

The analytic expression for the dipole matrix element $\langle n|\boldsymbol{r}|\boldsymbol{p}\rangle$ in a (non-)abelian model derived in ref. [51] in the center-of-mass frame holds for a coordinate system in which the relative momentum $\boldsymbol{p}$ of the dark matter unbound pair is chosen along the z-direction. In this work, we put the center-of-mass momentum $\boldsymbol{P}$ in the laboratory frame (or equivalently the thermal bath velocity $\boldsymbol{v}$ in the center-of-mass frame) along the z-direction, $\boldsymbol{P} = P\boldsymbol{e}_z$. The relative distance and momentum in spherical coordinates are given by $\boldsymbol{r} = (\cos\phi\sin\theta, \sin\phi\sin\theta, \cos\theta)r$ and $\boldsymbol{p} = (\cos\phi_p\sin\theta_p, \sin\phi_p\sin\theta_p, \cos\theta_p)p$, respectively. Moreover $p = Mv_{\mathrm{rel}}^{(0)}/2$ and $a_0 = 2/(M\alpha)$, such that $\alpha/v_{\mathrm{rel}}^{(0)} = (a_0 p)^{-1}$.

The Coulomb wavefunction for a dark matter bound state $|n\rangle \equiv |n\ell m\rangle$ in $\mathrm{U}(1)_{\mathrm{DM}}$, with quantum numbers n, ℓ and m, reads

$$\Psi_{n\ell m}(\boldsymbol{r}) = \langle \boldsymbol{r}|n\ell m\rangle = R_{n\ell}(r)Y_\ell^m(\Omega_{\boldsymbol{r}})\,, \tag{C.1}$$

with $Y_\ell^m(\Omega_{\boldsymbol{r}})$ being the spherical harmonics

$$Y_\ell^m(\theta,\phi) = (-1)^m\sqrt{\frac{2\ell+1}{4\pi}\frac{(\ell-m)!}{(\ell+m)!}}P_\ell^m(\cos\theta)e^{im\phi}\,, \tag{C.2}$$

$P_\ell^m(x) = (1-x^2)^{m/2}\frac{d^m}{dx^m}P_\ell(x)$ the associated Legendre polynomials and the radial functions given by

$$\begin{aligned} R_{n\ell}(r) \;=\; & \frac{1}{(2\ell+1)!}\sqrt{\left(\frac{2}{na_0}\right)^3\frac{(n+\ell)!}{2n(n-\ell-1)!}} \\ & \times\left(\frac{2r}{na_0}\right)^\ell e^{-\frac{r}{na_0}}\;{}_1F_1\left(\ell+1-n, 2\ell+2, \frac{2r}{na_0}\right)\,. \end{aligned} \tag{C.3}$$

The scattering wavefunction for a dark matter unbound state $|\boldsymbol{p}\rangle$ in $\mathrm{U}(1)_{\mathrm{DM}}$, where $\boldsymbol{p}$ points into an arbitrary direction, can be expanded into partial waves $\Psi_{\boldsymbol{p}\ell}(\boldsymbol{r}) = \langle \boldsymbol{r}|\boldsymbol{p}\ell\rangle$

as

$$\Psi_{\boldsymbol{p}}(\boldsymbol{r}) = \sum_{\ell=0}^{\infty} \Psi_{\boldsymbol{p}\ell}(\boldsymbol{r}) \;=\; \sqrt{\frac{2\pi/(a_0 p)}{1-e^{-2\pi/(a_0 p)}}} \sum_{\ell=0}^{\infty} i^{\ell} \frac{(2pr)^{\ell}}{(2\ell)!} P_{\ell}(\boldsymbol{e}_r \cdot \boldsymbol{e}_p) e^{ipr}$$
$$\times\, {}_1F_1\left(\ell+1-\frac{i}{a_0 p}, 2\ell+2, -2ipr\right) \prod_{\kappa=1}^{\ell} \sqrt{\kappa^2+(a_0 p)^{-2}}\ , \quad \text{(C.4)}$$

where $\boldsymbol{e}_r = \hat{\boldsymbol{r}} = \boldsymbol{r}/r$ and $\boldsymbol{e}_p = \hat{\boldsymbol{p}} = \boldsymbol{p}/p$ are the radial unit vectors in spherical coordinates, ${}_1F_1\,(a,b,c)$ is the confluent hypergeometric function and $P_\ell(x)$ are the Legendre polynomials. It holds that

$$P_{\ell}(\boldsymbol{e}_r \cdot \boldsymbol{e}_p) \;=\; \frac{4\pi}{2\ell+1} \sum_{m=-\ell}^{\ell} Y_{\ell}^{m}(\boldsymbol{e}_r) Y_{\ell}^{m,*}(\boldsymbol{e}_p)$$
$$= P_{\ell}(\cos\theta) P_{\ell}(\cos\theta_p) + \; 2\sum_{m=1}^{\ell} \frac{(\ell-m)!}{(\ell+m)!} P_{\ell}^{m}(\cos\theta) P_{\ell}^{m}(\cos\theta_p) \cos\left(m(\phi-\phi_p)\right). \quad \text{(C.5)}$$

The computation of the electric dipole matrix element $\langle n\ell m|\boldsymbol{r}|\boldsymbol{p}\rangle$ in the center-of-mass frame, based on previous works in refs. [190, 191], results in

$$\langle n\ell m|\boldsymbol{r}|\boldsymbol{p}\rangle = \sum_{\ell'=\ell\pm1,\ell'\geq 0} \int d^3r\, \boldsymbol{r}\, \Psi^{*}_{n\ell m}(\boldsymbol{r}) \Psi_{\boldsymbol{p}\ell'}(\boldsymbol{r})$$
$$= N_{n\ell m}(p) X^{1}_{n\ell}(p) G^{1}_{n\ell}(p)$$
$$\times \Bigg\{ (\ell+1) P_{\ell+1}(\cos\theta_p) \left[\ell \left(\delta_{m,1} - \frac{\delta_{m,-1}}{\ell(\ell+1)} \right) \boldsymbol{e}_x - i\ell \left(\delta_{m,1} + \frac{\delta_{m,-1}}{\ell(\ell+1)} \right) \boldsymbol{e}_y + 2\delta_{m,0} \boldsymbol{e}_z \right]$$
$$+ \sum_{m'=1}^{\ell+1} (\ell-m'+1) P^{m'}_{\ell+1}(\cos\theta_p) \left[(\ell-m')(C^{x}_{\ell m m'} \boldsymbol{e}_x - i C^{y}_{\ell m m'} \boldsymbol{e}_y) + 2C^{z}_{\ell m m'} \boldsymbol{e}_z \right]$$
$$- \sum_{m'=1}^{\ell+1} P^{m'}_{\ell+1}(\cos\theta_p) \left[\tilde{C}^{x}_{\ell m m'} \boldsymbol{e}_x + i \tilde{C}^{y}_{\ell m m'} \boldsymbol{e}_y \right] \Bigg\}$$
$$+ N_{n\ell m}(p) X^{2}_{n\ell}(p) G^{2}_{n\ell}(p) \times \Bigg\{ \ell P_{\ell-1}(\cos\theta_p)$$
$$\times \left[-(\ell+1) \left(\delta_{m,1} - \frac{\delta_{m,-1}}{\ell(\ell+1)} \right) \boldsymbol{e}_x + i(\ell+1) \left(\delta_{m,1} + \frac{\delta_{m,-1}}{\ell(\ell+1)} \right) \boldsymbol{e}_y + 2\delta_{m,0} \boldsymbol{e}_z \right]$$
$$+ \sum_{m'=1}^{\ell-1} (\ell+m') P^{m'}_{\ell-1}(\cos\theta_p) \left[(\ell+m'+1)(-C^{x}_{\ell m m'} \boldsymbol{e}_x + i C^{y}_{\ell m m'} \boldsymbol{e}_y) + 2C^{z}_{\ell m m'} \boldsymbol{e}_z \right]$$
$$+ \sum_{m'=1}^{\ell-1} P^{m'}_{\ell-1}(\cos\theta_p) \left[\tilde{C}^{x}_{\ell m m'} \boldsymbol{e}_x + i \tilde{C}^{y}_{\ell m m'} \boldsymbol{e}_y \right] \Bigg\}, \quad \text{(C.6)}$$

where $\boldsymbol{e}_x$, $\boldsymbol{e}_y$ and $\boldsymbol{e}_z$ are the unit vectors in Cartesian coordinates. Due to the selection rule for electric-dipole transitions, only the partial waves $\ell' = \ell \pm 1$ give a non-vanishing

contribution. In (C.6), we have defined the following prefactors

$$N_{n\ell m}(p) = \frac{i^{\ell+3}2^{\ell}(-1)^{n-\ell+m}}{(2\ell+1)!}\sqrt{\left(\frac{2}{na_0}\right)^3\frac{(n+\ell)!}{2n(n-\ell-1)!}}\left(\frac{2}{na_0}\right)^{\ell}\sqrt{\frac{2\pi/(a_0p)}{1-e^{-2\pi/(a_0p)}}} \times\sqrt{\frac{\pi}{2\ell+1}\frac{(\ell-m)!}{(\ell+m)!}}\frac{e^{-\frac{2}{a_0p}(1+i(\ell+1-n)a_0p)\arctan(na_0p)}}{p^{\ell}\left(1+(na_0p)^{-2}\right)^{\ell}}\,, \tag{C.7}$$

$$X^1_{n\ell}(p) = \frac{ie^{-2i\arctan(na_0p)}}{p^4\left(1+(na_0p)^{-2}\right)^2}\prod_{\kappa=1}^{\ell+1}\sqrt{\kappa^2+(a_0p)^{-2}}\,, \tag{C.8}$$

$$X^2_{n\ell}(p) = \frac{a_0n\ell(2\ell+1)}{2p^3\left(1+(na_0p)^{-2}\right)}\prod_{\kappa=1}^{\ell-1}\sqrt{\kappa^2+(a_0p)^{-2}}\,, \tag{C.9}$$

whereas $G^1_{n\ell}(p)$ and $G^2_{n\ell}(p)$ are combinations of hypergeometric functions, ${}_2F_1\left(a,b,c,d\right)$,

$$\begin{aligned} G^1_{n\ell}(p) = {}& {}_2F_1\left(\ell+2-\frac{i}{a_0p},\ell+1-n,2\ell+2,\frac{4ina_0p}{(1+ina_0p)^2}\right) \\ & - e^{4i\arctan(na_0p)}\,{}_2F_1\left(\ell-\frac{i}{a_0p},\ell+1-n,2\ell+2,\frac{4ina_0p}{(1+ina_0p)^2}\right)\,, \end{aligned} \tag{C.10}$$

$$\begin{aligned} G^2_{n\ell}(p) = {}& {}_2F_1\left(\ell-\frac{i}{a_0p},\ell+1-n,2\ell,\frac{4ina_0p}{(1+ina_0p)^2}\right) \\ & - e^{4i\arctan(na_0p)}\,{}_2F_1\left(\ell-\frac{i}{a_0p},\ell-1-n,2\ell,\frac{4ina_0p}{(1+ina_0p)^2}\right)\,. \end{aligned} \tag{C.11}$$

The constants $C^{x/y/z}_{\ell mm'}$, $\tilde{C}^{x/y}_{\ell mm'}$ in (C.6) are defined as:

$$C^x_{\ell mm'} = e^{-im'\phi_p}\delta_{m',m-1} + e^{im'\phi_p}\delta_{m',-(m+1)}(-1)^{m'+1}\frac{(\ell-m'-1)!}{(\ell+m'+1)!}\,, \tag{C.12}$$

$$C^y_{\ell mm'} = e^{-im'\phi_p}\delta_{m',m-1} - e^{im'\phi_p}\delta_{m',-(m+1)}(-1)^{m'+1}\frac{(\ell-m'-1)!}{(\ell+m'+1)!}\,, \tag{C.13}$$

$$C^z_{\ell mm'} = e^{-im'\phi_p}\delta_{m',m} + e^{im'\phi_p}\delta_{m',-m}(-1)^{m'}\frac{(\ell-m')!}{(\ell+m')!}\,, \tag{C.14}$$

$$\tilde{C}^x_{\ell mm'} = e^{-im'\phi_p}\delta_{m',m+1} + e^{im'\phi_p}\delta_{m',-(m-1)}(-1)^{m'-1}\frac{(\ell-m'+1)!}{(\ell+m'-1)!}\,, \tag{C.15}$$

$$\tilde{C}^y_{\ell mm'} = e^{-im'\phi_p}\delta_{m',m+1} - e^{im'\phi_p}\delta_{m',-(m-1)}(-1)^{m'-1}\frac{(\ell-m'+1)!}{(\ell+m'-1)!}\,. \tag{C.16}$$

Equation (C.6) reduces to the expression given in ref. [51] for polar angle $\theta_p = 0$, which corresponds to putting the relative momentum along the z-direction. Moreover, for the particular case of nS-states, for which $\ell = m = 0$, the squared matrix elements are

$$\begin{aligned} |\langle n\mathrm{S}|\boldsymbol{r}|\boldsymbol{p}\rangle|^2 &= |\langle n\mathrm{S}|\boldsymbol{r}|\boldsymbol{p} = p\boldsymbol{e}_z\rangle|^2\,, \\ |\langle n\mathrm{S}|z|\boldsymbol{p}\rangle|^2 &= |\langle n\mathrm{S}|\boldsymbol{r}|\boldsymbol{p}\rangle|^2\cos^2(\theta_p)\,. \end{aligned} \tag{C.17}$$

For excited states with non-vanishing orbital angular momentum, it holds that

$$\sum_{m=-\ell}^{\ell} |\langle n\ell m|\boldsymbol{r}|\boldsymbol{p}\rangle|^2 = \sum_{m=-\ell}^{\ell} |\langle n\ell m|\boldsymbol{r}|\boldsymbol{p} = p\boldsymbol{e}_z\rangle|^2 \,. \tag{C.18}$$

We provide some analytic expressions for the squared matrix elements in the center-of-mass frame for the particular bound states 1S, 2S and 2P used in this work:

$$|\langle 1\mathrm{S}|\boldsymbol{r}|\boldsymbol{p}\rangle|^2 = \frac{2^9\pi^2 a_0^4}{p(1+(a_0p)^2)^5} \frac{e^{-\frac{4}{a_0p}\arctan(a_0p)}}{1-e^{-\frac{2\pi}{a_0p}}} \,, \tag{C.19}$$

$$|\langle 1\mathrm{S}|z|\boldsymbol{p}\rangle|^2 = \frac{2^9\pi^2 a_0^4}{p(1+(a_0p)^2)^5} \frac{e^{-\frac{4}{a_0p}\arctan(a_0p)}}{1-e^{-\frac{2\pi}{a_0p}}} \cos^2(\theta_p) \,, \tag{C.20}$$

$$|\langle 2\mathrm{S}|\boldsymbol{r}|\boldsymbol{p}\rangle|^2 = \frac{2^{18}\pi^2 a_0^4 \left(1+(a_0p)^2\right)}{p\left(1+(2a_0p)^2\right)^6} \frac{e^{-\frac{4}{a_0p}\arctan(2a_0p)}}{1-e^{-\frac{2\pi}{a_0p}}} \,, \tag{C.21}$$

$$|\langle 2\mathrm{S}|z|\boldsymbol{p}\rangle|^2 = \frac{2^{18}\pi^2 a_0^4 \left(1+(a_0p)^2\right)}{p\left(1+(2a_0p)^2\right)^6} \frac{e^{-\frac{4}{a_0p}\arctan(2a_0p)}}{1-e^{-\frac{2\pi}{a_0p}}} \cos^2(\theta_p) \,, \tag{C.22}$$

$$\begin{aligned} |\langle 2\mathrm{P}_{m=0}|\boldsymbol{r}|\boldsymbol{p}\rangle|^2 = {} & \big[4(1+(a_0p)^{-2})(3\cos^2(\theta_p)+1) + 1 + (2a_0p)^{-2} \\ & -4\sqrt{1+(a_0p)^{-2}}\sqrt{1+(2a_0p)^{-2}}(3\cos^2(\theta_p)-1)\big] \\ & \times \frac{2^4\pi^2 e^{-\frac{4}{a_0p}\arctan(2a_0p)}}{3^2 a_0^8 p^{13}(1+(2a_0p)^{-2})^7\left(1-e^{-\frac{2\pi}{a_0p}}\right)} \,, \end{aligned} \tag{C.23}$$

$$\begin{aligned} |\langle 2\mathrm{P}_{m=0}|z|\boldsymbol{p}\rangle|^2 = {} & \left(\sqrt{1+(2a_0p)^{-2}} - 2\sqrt{1+(a_0p)^{-2}}(3\cos^2(\theta_p)-1)\right)^2 \\ & \times \frac{2^4\pi^2 e^{-\frac{4}{a_0p}\arctan(2a_0p)}}{3^2 a_0^8 p^{13}(1+(2a_0p)^{-2})^7\left(1-e^{-\frac{2\pi}{a_0p}}\right)} \,, \end{aligned} \tag{C.24}$$

$$\begin{aligned} |\langle 2\mathrm{P}_{m=\pm1}|\boldsymbol{r}|\boldsymbol{p}\rangle|^2 = {} & \Big[\frac{1}{2}(1+(a_0p)^{-2})(20-12\cos^2(\theta_p)) + 1 + (2a_0p)^{-2} \\ & -2\sqrt{1+(a_0p)^{-2}}\sqrt{1+(2a_0p)^{-2}}(1-3\cos^2(\theta_p))\Big] \\ & \times \frac{2^4\pi^2 e^{-\frac{4}{a_0p}\arctan(2a_0p)}}{3^2 a_0^8 p^{13}(1+(2a_0p)^{-2})^7\left(1-e^{-\frac{2\pi}{a_0p}}\right)} \,, \end{aligned} \tag{C.25}$$

$$\begin{aligned} |\langle 2\mathrm{P}_{m=\pm1}|z|\boldsymbol{p}\rangle|^2 = {} & 18\cos^2(\theta_p)\sin^2(\theta_p)\left(1+(a_0p)^{-2}\right) \\ & \times \frac{2^4\pi^2 e^{-\frac{4}{a_0p}\arctan(2a_0p)}}{3^2 a_0^8 p^{13}(1+(2a_0p)^{-2})^7\left(1-e^{-\frac{2\pi}{a_0p}}\right)} \,. \end{aligned} \tag{C.26}$$

Next we consider the quantum-mechanical matrix element $\langle n\ell m|\boldsymbol{r}|n'\ell'm'\rangle$ between two bound states with quantum numbers n and n'. Its solution in the center-of-mass frame

reads [51]

$$
\begin{aligned}
\langle n\ell m|\boldsymbol{r}|n'\ell'm'\rangle &= \int d^3r\, \boldsymbol{r}\, \Psi^*_{n\ell m}(\boldsymbol{r})\Psi_{n'\ell'm'}(\boldsymbol{r}) \\
&= \mathcal{N}\Bigg\{ -\delta_{\ell,\ell'-1}\sqrt{\frac{(n'+\ell+1)!}{(n'-\ell-2)!}}\sqrt{\frac{1}{4\pi(2\ell+3)}} \\
&\quad\times\Bigg[\sqrt{\frac{(\ell+m)!}{(\ell-m+2)!}}(\ell-m+1)(\ell-m+2)\delta_{m,m'+1}(-\boldsymbol{e}_x+i\boldsymbol{e}_y) \\
&\quad\quad+\sqrt{\frac{(\ell+m+2)!}{(\ell-m)!}}\delta_{m,m'-1}(\boldsymbol{e}_x+i\boldsymbol{e}_y)+2\sqrt{\frac{(\ell+m+1)!}{(\ell-m+1)!}}(\ell-m+1)\delta_{m,m'}\boldsymbol{e}_z\Bigg]\mathcal{G}_1 \\
&\quad+\delta_{\ell,\ell'+1}nn'\sqrt{\frac{(n'+\ell-1)!}{(n'-\ell)!}}\sqrt{\frac{2\ell-1}{4\pi}}\frac{(2\ell+1)\ell}{2(2\ell-1)} \\
&\quad\times\Bigg[\sqrt{\frac{(\ell+m-2)!}{(\ell-m)!}}(\ell+m-1)(\ell+m)\delta_{m,m'+1}(\boldsymbol{e}_x-i\boldsymbol{e}_y) \\
&\quad\quad+\sqrt{\frac{(\ell+m)!}{(\ell-m-2)!}}\delta_{m,m'-1}(-\boldsymbol{e}_x-i\boldsymbol{e}_y)+2\sqrt{\frac{(\ell+m-1)!}{(\ell-m-1)!}}(\ell+m)\delta_{m,m'}\boldsymbol{e}_z\Bigg]\mathcal{G}_2\Bigg\}\,,
\end{aligned}
\tag{C.27}
$$

where

$$
\begin{aligned}
\mathcal{N} &= \frac{(-1)^{n'-\ell}}{M\alpha}\frac{2^{2\ell+4}\pi}{2\ell+1}\sqrt{\frac{2\ell+1}{4\pi}\frac{(\ell-m)!}{(\ell+m)!}}\left(\frac{n-n'}{n+n'}\right)^{n+n'} \\
&\quad\times\sqrt{\frac{(n+\ell)!}{(n-\ell-1)!}}\frac{1}{(2\ell+1)!}\frac{n^\ell n'^\ell}{(n-n')^{2\ell+2}}\,,
\end{aligned}
\tag{C.28}
$$

$$
\begin{aligned}
\mathcal{G}_1 &= n^2n'^2\Bigg[\frac{{}_2F_1\left(\ell+2-n',\ell+1-n,2\ell+2,-\frac{4n'n}{(n'-n)^2}\right)}{(n-n')^2} \\
&\quad-\frac{{}_2F_1\left(\ell-n',\ell+1-n,2\ell+2,-\frac{4n'n}{(n'-n)^2}\right)}{(n+n')^2}\Bigg]\,,
\end{aligned}
\tag{C.29}
$$

$$
\begin{aligned}
\mathcal{G}_2 &= \Bigg[{}_2F_1\left(\ell+1-n,\ell-n',2\ell,-\frac{4n'n}{(n'-n)^2}\right) \\
&\quad-\left(\frac{n-n'}{n+n'}\right)^2\,{}_2F_1\left(\ell-1-n,\ell-n',2\ell,-\frac{4n'n}{(n'-n)^2}\right)\Bigg]\,.
\end{aligned}
\tag{C.30}
$$

As a special example, the transition matrix element squared between the ground state and the excited 2P state, which is used in this work, is

$$
|\langle 1\mathrm{S}|\boldsymbol{r}|2\mathrm{P}_{m=0}\rangle|^2 = |\langle 1\mathrm{S}|\boldsymbol{r}|2\mathrm{P}_{m=\pm1}\rangle|^2 = \frac{2^{17}}{3^{10}}\frac{1}{M^2\alpha^2}\,. \tag{C.31}
$$

We finally provide an analytical formula for the electric dipole matrix element between an incoming and outgoing scattering state entering the elastic scattering processes among unbound DM pairs. We rotate the coordinate system such that the relative momentum $\boldsymbol{p} = M\boldsymbol{v}_{\rm rel}^{(0)}/2$ of the incoming scattering state is oriented along the z-direction. Then the outcoming relative momentum $\boldsymbol{p}'$ of the unbound pair in the final state can be written as $\boldsymbol{p}' = (\cos(\phi_{p'})\sin(\theta_{p'}), \sin(\phi_{p'})\sin(\theta_{p'}), \cos(\theta_{p'}))Mv_{\rm rel}^{\prime(0)}/2$. The matrix element $\langle \boldsymbol{p}|\boldsymbol{r}|\boldsymbol{p}'\rangle$ reads[1]

$$\begin{aligned}
\langle \boldsymbol{p}|\boldsymbol{r}|\boldsymbol{p}'\rangle &= \int d^3r\, \boldsymbol{r}\, \Psi^*_{\boldsymbol{p}}(\boldsymbol{r})\Psi_{\boldsymbol{p}'}(\boldsymbol{r}) \\
&= \mathcal{M}\sum_{\ell=0}^{\infty}\mathcal{A}_\ell\Bigg\{\frac{\ell+1}{2\ell+1}\sqrt{(\ell+1)^2+(\alpha/v'_{\rm rel})^2} \\
&\quad\times\left[P_{\ell+1}(\cos(\theta_{p'}))\boldsymbol{e}_z + \frac{P^1_{\ell+1}(\cos(\theta_{p'}))}{\ell+1}\left[\cos(\phi_{p'})\boldsymbol{e}_x + \sin(\phi_{p'})\boldsymbol{e}_y\right]\right]\left(\frac{2}{v'_{\rm rel}+v_{\rm rel}}\right)^2\mathcal{X}_1 \\
&\quad - \frac{2\ell^2}{v'_{\rm rel}v_{\rm rel}\sqrt{\ell^2+(\alpha/v'_{\rm rel})^2}} \\
&\quad\quad\times\left[P_{\ell-1}(\cos(\theta_{p'}))\boldsymbol{e}_z + \frac{1}{\ell}P^1_{\ell-1}(\cos(\theta_{p'}))\left[\cos(\phi_{p'})\boldsymbol{e}_x + \sin(\phi_{p'})\boldsymbol{e}_y\right]\right]\mathcal{X}_2\Bigg\},
\end{aligned} \tag{C.32}$$

with

$$\begin{aligned}
\mathcal{M} &= \sqrt{\frac{2\pi\alpha/v_{\rm rel}}{1-e^{-2\pi\alpha/v_{\rm rel}}}}\sqrt{\frac{2\pi\alpha/v'_{\rm rel}}{1-e^{-2\pi\alpha/v'_{\rm rel}}}}e^{-\frac{\pi}{2}\alpha\left(\frac{1}{v'_{\rm rel}}+\frac{1}{v_{\rm rel}}\right)} \\
&\quad\times e^{\frac{\pi}{2}\alpha\left|\frac{1}{v'_{\rm rel}}-\frac{1}{v_{\rm rel}}\right|}\left|\frac{v'_{\rm rel}+v_{\rm rel}}{v'_{\rm rel}-v_{\rm rel}}\right|^{i\alpha\left(\frac{1}{v'_{\rm rel}}-\frac{1}{v_{\rm rel}}\right)},
\end{aligned} \tag{C.33}$$

$$\mathcal{A}_\ell = \frac{2^{2\ell+4}\pi}{M^4(2\ell)!}\frac{v'^{\ell}_{\rm rel}v^{\ell}_{\rm rel}}{(v'_{\rm rel}+v_{\rm rel})^{2\ell+2}}\prod_{\kappa=1}^{\ell}\sqrt{\kappa^2+(\alpha/v_{\rm rel})^2}\prod_{\kappa'=1}^{\ell}\sqrt{\kappa'^2+(\alpha/v'_{\rm rel})^2}, \tag{C.34}$$

and

$$\begin{aligned}
\mathcal{X}_1 = {}& {}_2F_1\left(\ell+2-i\frac{\alpha}{v'_{\rm rel}}, \ell+1+i\frac{\alpha}{v_{\rm rel}}, 2\ell+2, \frac{4v'_{\rm rel}v_{\rm rel}}{(v'_{\rm rel}+v_{\rm rel})^2}\right) \\
&- \left(\frac{v'_{\rm rel}+v_{\rm rel}}{v'_{\rm rel}-v_{\rm rel}}\right)^2 {}_2F_1\left(\ell-i\frac{\alpha}{v'_{\rm rel}}, \ell+1+i\frac{\alpha}{v_{\rm rel}}, 2\ell+2, \frac{4v'_{\rm rel}v_{\rm rel}}{(v'_{\rm rel}+v_{\rm rel})^2}\right),
\end{aligned} \tag{C.35}$$

$$\begin{aligned}
\mathcal{X}_2 = {}& {}_2F_1\left(\ell+1+i\frac{\alpha}{v_{\rm rel}}, \ell-i\frac{\alpha}{v'_{\rm rel}}, 2\ell, \frac{4v'_{\rm rel}v_{\rm rel}}{(v'_{\rm rel}+v_{\rm rel})^2}\right) \\
&- \left(\frac{v'_{\rm rel}+v_{\rm rel}}{v'_{\rm rel}-v_{\rm rel}}\right)^2 {}_2F_1\left(\ell-1+i\frac{\alpha}{v_{\rm rel}}, \ell-i\frac{\alpha}{v'_{\rm rel}}, 2\ell, \frac{4v'_{\rm rel}v_{\rm rel}}{(v'_{\rm rel}+v_{\rm rel})^2}\right).
\end{aligned} \tag{C.36}$$

[1] We abbreviate $v_{\rm rel}^{(0)} \equiv v_{\rm rel}$ and $v_{\rm rel}^{\prime(0)} \equiv v'_{\rm rel}$ in order to simplify the notation in the final result.

C.2 General expressions in SU(N)$_{\rm DM}$

The dipole matrix element in a non-abelian SU(N) model in the center-of-mass frame, $\langle n\ell m|\boldsymbol{r}|\boldsymbol{p}\rangle^{[\mathbf{adj}]}$, where $|n\ell m\rangle$ is the bound state of a color-singlet dark matter pair,[2] and $|\boldsymbol{p}\rangle^{[\mathbf{adj}]}$ is the color-adjoint state with arbitrary relative momentum vector $\boldsymbol{p} = M\boldsymbol{v}_{\rm rel}^{(0)}/2$, has the same analytic structure as the abelian equivalent in (C.6); they only differ in the factors $N_{n\ell m}(p)$, $X_{n\ell}^{1,2}(p)$ and $G_{n\ell}^{1,2}(p)$, which now read

$$\begin{aligned} N_{n\ell m}^{\mathrm{SU}(N)}(p) &= \frac{i^{\ell+3}2^{\ell}(-1)^{n-\ell+m}}{(2\ell+1)!}\sqrt{\left(\frac{2}{na_0}\right)^3\frac{(n+\ell)!}{2n(n-\ell-1)!}}\sqrt{\frac{2\pi/((N^2-1)a_0p)}{e^{\frac{2\pi}{(N^2-1)a_0p}}-1}} \\ &\quad\times\left(\frac{2}{na_0}\right)^{\ell}\sqrt{\frac{\pi}{2\ell+1}\frac{(\ell-m)!}{(\ell+m)!}}\frac{e^{\frac{2}{(N^2-1)a_0p}\left[1-i(\ell+1-n)(N^2-1)a_0p\right]\arctan\left(na_0p\right)}}{p^{\ell}\left(1+(na_0p)^{-2}\right)^{\ell}}\,, \end{aligned} \tag{C.37}$$

$$X_{n\ell}^{1,\mathrm{SU}(N)}(p) = \frac{ie^{-2i\arctan\left(na_0p\right)}}{p^4\left(1+(na_0p)^{-2}\right)^2}\prod_{\kappa=1}^{\ell+1}\sqrt{\kappa^2+((N^2-1)a_0p)^{-2}}\,, \tag{C.38}$$

$$X_{n\ell}^{2,\mathrm{SU}(N)}(p) = \frac{a_0n\ell(2\ell+1)}{2p^3\left(1+(na_0p)^{-2}\right)}\prod_{\kappa=1}^{\ell-1}\sqrt{\kappa^2+((N^2-1)a_0p)^{-2}}\,, \tag{C.39}$$

and

$$\begin{aligned} &G_{n\ell}^{1,\mathrm{SU}(N)}(p) \\ &= \left(1+\frac{iN}{2C_Fa_0p}\right){}_2F_1\left(\ell+2+\frac{i}{(N^2-1)a_0p},\ell+1-n,2\ell+2,\frac{4ina_0p}{(1+ina_0p)^2}\right) \\ &\quad-\frac{iN}{C_Fa_0p}e^{2i\arctan\left(na_0p\right)}{}_2F_1\left(\ell+1+\frac{i}{(N^2-1)a_0p},\ell+1-n,2\ell+2,\frac{4ina_0p}{(1+ina_0p)^2}\right) \\ &\quad-\left(1-\frac{iN}{2C_Fa_0p}\right)e^{4i\arctan\left(na_0p\right)} \\ &\qquad\qquad\times{}_2F_1\left(\ell+\frac{i}{(N^2-1)a_0p},\ell+1-n,2\ell+2,\frac{4ina_0p}{(1+ina_0p)^2}\right), \end{aligned} \tag{C.40}$$

$$\begin{aligned} &G_{n\ell}^{2,\mathrm{SU}(N)}(p) \\ &= \left(1-\frac{Nn}{2C_F}\right){}_2F_1\left(\ell+\frac{i}{(N^2-1)a_0p},\ell+1-n,2\ell,\frac{4ina_0p}{(1+ina_0p)^2}\right) \\ &\quad+N\frac{n}{C_F}e^{2i\arctan\left(na_0p\right)}{}_2F_1\left(\ell+\frac{i}{(N^2-1)a_0p},\ell-n,2\ell,\frac{4ina_0p}{(1+ina_0p)^2}\right) \\ &\quad-\left(1+\frac{Nn}{2C_F}\right)e^{4i\arctan\left(na_0p\right)}{}_2F_1\left(\ell+\frac{i}{(N^2-1)a_0p},\ell-1-n,2\ell,\frac{4ina_0p}{(1+ina_0p)^2}\right), \end{aligned} \tag{C.41}$$

[2]The color-singlet bound-state wavefunction in SU(N) has exactly the same analytic expression as the abelian analogue in (C.1)–(C.3), except the replacement $\alpha \to C_F\alpha$.

with $a_0 = 2/(C_F M\alpha)$. As a special case, in ref. [51] we provide an analytic expression for the dipole matrix element that holds for a coordinate system in which the relative momentum $\boldsymbol{p}$ of the dark matter pair in a color-adjoint state is chosen along the z-direction. The squared matrix element for the ground state is

$$|\langle 1\mathrm{S}|\boldsymbol{r}|\boldsymbol{p}\rangle^{[\mathbf{adj}]}|^2 = \frac{\pi^2}{M^5}\frac{2^{11}C_F^3\alpha^6}{Nv_{\mathrm{rel}}^{11}}\frac{(2C_F+N)^2}{\left[1+\left(\frac{C_F\alpha}{v_{\mathrm{rel}}}\right)^2\right]^6}\left[1+\left(\frac{1}{2N}\frac{\alpha}{v_{\mathrm{rel}}}\right)^2\right]\frac{e^{\frac{2\alpha}{Nv_{\mathrm{rel}}}\operatorname{arccot}\left(\frac{C_F\alpha}{v_{\mathrm{rel}}}\right)}}{e^{\frac{\pi}{N}\frac{\alpha}{v_{\mathrm{rel}}}}-1}\,, \tag{C.42}$$

which is in agreement with the result in ref. [50].

We complete the list by providing the analytic results for the scattering-state to scattering-state transitions corresponding to thermal absorption and bremsstrahlung processes, which in non-abelian theories are twofold. Those processes can happen between color-singlet, $|\boldsymbol{p}\rangle^{[\mathbb{1}]}$, and color-adjoint scattering states,[3] but in addition there are also transitions among color-adjoint configurations only. For color-adjoint to color-adjoint transitions, the dipole matrix element ${}^{[\mathbf{adj}]}\langle\boldsymbol{p}|\boldsymbol{r}|\boldsymbol{p}'\rangle^{[\mathbf{adj}]}$ in the center-of-mass frame, where $\boldsymbol{p}$ points along the z-direction, is simply eq. (C.32) with $\alpha \to -\alpha/(2N)$, whereas for the color-singlet to color-adjoint transitions it is

$$\begin{aligned}
&{}^{[\mathbf{adj}]}\langle\boldsymbol{p}|\boldsymbol{r}|\boldsymbol{p}'\rangle^{[\mathbb{1}]} = \int d^3r\,\boldsymbol{r}\,\Psi_{\boldsymbol{p}}^{*[\mathbf{adj}]}(\boldsymbol{r})\Psi_{\boldsymbol{p}'}^{[\mathbb{1}]}(\boldsymbol{r}) \\
&= \mathcal{M}^{\mathrm{SU}(N)}\sum_{\ell=0}^{\infty}\mathcal{A}_\ell^{\mathrm{SU}(N)}\left\{\frac{\ell+1}{2\ell+1}\sqrt{(\ell+1)^2+(C_F\alpha/v'_{\mathrm{rel}})^2}\right. \\
&\times\left[P_{\ell+1}(\cos(\theta_{p'}))\boldsymbol{e}_z + \frac{P^1_{\ell+1}(\cos(\theta_{p'}))}{\ell+1}\left[\cos(\phi_{p'})\boldsymbol{e}_x+\sin(\phi_{p'})\boldsymbol{e}_y\right]\right]\left(\frac{2}{v'_{\mathrm{rel}}+v_{\mathrm{rel}}}\right)^2\mathcal{X}_1^{\mathrm{SU}(N)} \\
&\quad -\frac{2\ell^2}{v'_{\mathrm{rel}}v_{\mathrm{rel}}\sqrt{\ell^2+(C_F\alpha/v'_{\mathrm{rel}})^2}} \\
&\quad\times\left.\left[P_{\ell-1}(\cos(\theta_{p'}))\boldsymbol{e}_z+\frac{1}{\ell}P^1_{\ell-1}(\cos(\theta_{p'}))\left[\cos(\phi_{p'})\boldsymbol{e}_x+\sin(\phi_{p'})\boldsymbol{e}_y\right]\right]\mathcal{X}_2^{\mathrm{SU}(N)}\right\},
\end{aligned} \tag{C.43}$$

[3] The color-singlet scattering-state wavefunction in SU(N) equals the abelian version in (C.4), except the replacement $\alpha \to C_F\alpha$. The color-adjoint wavefunction can be inferred from (C.4) by replacing the coupling $\alpha \to -\alpha/(2N)$, and reads

$$\begin{aligned}
\Psi_{\boldsymbol{p}}^{[\mathbf{adj}]}(\boldsymbol{r}) = \sum_{\ell=0}^{\infty}\Psi_{\boldsymbol{p}\ell}^{[\mathbf{adj}]}(\boldsymbol{r}) \quad &= \quad \sqrt{\frac{\pi\alpha/(Nv_{\mathrm{rel}})}{e^{\pi\alpha/(Nv_{\mathrm{rel}})}-1}}\sum_{\ell=0}^{\infty}i^\ell\frac{(2pr)^\ell}{(2\ell)!}P_\ell(\boldsymbol{e}_r\cdot\boldsymbol{e}_p)e^{ipr} \\
&\quad\times {}_1F_1\left(\ell+1+i\frac{\alpha}{2Nv_{\mathrm{rel}}},2\ell+2,-2ipr\right)\prod_{\kappa=1}^{\ell}\sqrt{\kappa^2+\left(\frac{\alpha}{2Nv_{\mathrm{rel}}}\right)^2}\,.
\end{aligned}$$

with

$$\mathcal{M}^{\mathrm{SU}(N)} = \sqrt{\frac{2\pi C_F\alpha/v'_{\mathrm{rel}}}{1-e^{-2\pi\alpha/v'_{\mathrm{rel}}}}}\sqrt{\frac{\pi\alpha/(Nv_{\mathrm{rel}})}{e^{\pi\alpha/(Nv_{\mathrm{rel}})}-1}}e^{-\frac{\pi}{2}\alpha\left(\frac{C_F}{v'_{\mathrm{rel}}}-\frac{1}{2Nv_{\mathrm{rel}}}\right)} \times e^{-\frac{\pi}{2}\alpha\left(\frac{C_F}{v'_{\mathrm{rel}}}+\frac{1}{2Nv_{\mathrm{rel}}}\right)\mathrm{sign}\,(v'_{\mathrm{rel}}-v_{\mathrm{rel}})}\left|\frac{v'_{\mathrm{rel}}+v_{\mathrm{rel}}}{v'_{\mathrm{rel}}-v_{\mathrm{rel}}}\right|^{i\alpha\left(\frac{C_F}{v'_{\mathrm{rel}}}+\frac{1}{2Nv_{\mathrm{rel}}}\right)}, \quad \text{(C.44)}$$

$$\mathcal{A}_\ell^{\mathrm{SU}(N)} = \frac{2^{2\ell+4}\pi}{M^4(2\ell)!}\frac{v'^{\ell}_{\mathrm{rel}}v^{\ell}_{\mathrm{rel}}}{(v'_{\mathrm{rel}}+v_{\mathrm{rel}})^{2\ell+2}}\prod_{s=1}^{\ell}\sqrt{s^2+(\alpha/(2Nv_{\mathrm{rel}}))^2}\prod_{s'=1}^{\ell}\sqrt{s'^2+(C_F\alpha/v'_{\mathrm{rel}})^2}, \quad \text{(C.45)}$$

and

$$\begin{aligned}
&\mathcal{X}_1^{\mathrm{SU}(N)} \\
&= \left(1-i\frac{N\alpha}{2v'_{\mathrm{rel}}}\right)\,{}_2F_1\left(\ell+2-i\frac{C_F\alpha}{v'_{\mathrm{rel}}},\ell+1-i\frac{\alpha}{2Nv_{\mathrm{rel}}},2\ell+2,\frac{4v'_{\mathrm{rel}}v_{\mathrm{rel}}}{(v'_{\mathrm{rel}}+v_{\mathrm{rel}})^2}\right) \\
&\quad -i\frac{N\alpha}{v'_{\mathrm{rel}}}\frac{v'_{\mathrm{rel}}+v_{\mathrm{rel}}}{v'_{\mathrm{rel}}-v_{\mathrm{rel}}}\,{}_2F_1\left(\ell+1-i\frac{C_F\alpha}{v'_{\mathrm{rel}}},\ell+1-i\frac{\alpha}{2Nv_{\mathrm{rel}}},2\ell+2,\frac{4v'_{\mathrm{rel}}v_{\mathrm{rel}}}{(v'_{\mathrm{rel}}+v_{\mathrm{rel}})^2}\right) \\
&\quad -\left(1+i\frac{N\alpha}{2v'_{\mathrm{rel}}}\right)\left(\frac{v'_{\mathrm{rel}}+v_{\mathrm{rel}}}{v'_{\mathrm{rel}}-v_{\mathrm{rel}}}\right)^2 \\
&\qquad\qquad \times\,{}_2F_1\left(\ell-i\frac{C_F\alpha}{v'_{\mathrm{rel}}},\ell+1-i\frac{\alpha}{2Nv_{\mathrm{rel}}},2\ell+2,\frac{4v'_{\mathrm{rel}}v_{\mathrm{rel}}}{(v'_{\mathrm{rel}}+v_{\mathrm{rel}})^2}\right), \quad \text{(C.46)}
\end{aligned}$$

$$\begin{aligned}
&\mathcal{X}_2^{\mathrm{SU}(N)} \\
&= \left(1-i\frac{N\alpha}{2v_{\mathrm{rel}}}\right)\,{}_2F_1\left(\ell+1-i\frac{\alpha}{2Nv_{\mathrm{rel}}},\ell-i\frac{C_F\alpha}{v'_{\mathrm{rel}}},2\ell,\frac{4v'_{\mathrm{rel}}v_{\mathrm{rel}}}{(v'_{\mathrm{rel}}+v_{\mathrm{rel}})^2}\right) \\
&\quad +i\frac{N\alpha}{v_{\mathrm{rel}}}\frac{v'_{\mathrm{rel}}+v_{\mathrm{rel}}}{v'_{\mathrm{rel}}-v_{\mathrm{rel}}}\,{}_2F_1\left(\ell-i\frac{\alpha}{2Nv_{\mathrm{rel}}},\ell-i\frac{C_F\alpha}{v'_{\mathrm{rel}}},2\ell,\frac{4v'_{\mathrm{rel}}v_{\mathrm{rel}}}{(v'_{\mathrm{rel}}+v_{\mathrm{rel}})^2}\right) \\
&\quad -\left(1+i\frac{N\alpha}{2v_{\mathrm{rel}}}\right)\left(\frac{v'_{\mathrm{rel}}+v_{\mathrm{rel}}}{v'_{\mathrm{rel}}-v_{\mathrm{rel}}}\right)^2 \\
&\qquad\qquad \times\,{}_2F_1\left(\ell-1-i\frac{\alpha}{2Nv_{\mathrm{rel}}},\ell-i\frac{C_F\alpha}{v'_{\mathrm{rel}}},2\ell,\frac{4v'_{\mathrm{rel}}v_{\mathrm{rel}}}{(v'_{\mathrm{rel}}+v_{\mathrm{rel}})^2}\right). \quad \text{(C.47)}
\end{aligned}$$

We recall that bound-state to bound-state and scattering-state to scattering-state transitions among color-singlet configurations cannot happen due to the non-abelian nature of the gauge fields. Moreover, we remind that in the abelian and non-abelian bound-state and scattering-state wavefunctions as well as in all the dipole matrix elements listed in this section and in section C.1, the natural renormalization scale of the coupling α is μ_{s}, which is of the order of the soft scale.

C.3 Continuum dipole matrix element: collinear divergence

The resulting abelian scattering-state to scattering-state transition matrix element in (C.32) turns out to behave singular in the limit of vanishing incoming or outgoing relative velocity $v_{\rm rel}, v'_{\rm rel} \to 0$, the *infrared* divergences, but also if the absolute values of the relative velocities approach each other, i.e. $v'_{\rm rel} \to v_{\rm rel}$, called *collinear* divergence (also referred to as the *diagonal* singularity [192–196]). The infrared singularity for vanishing $v'_{\rm rel}$ does not pose a problem, since it cancels out once the squared matrix element multiplies the rest of the integrand in the cross sections (6.110) and (6.111). Also the other infrared divergence, $v_{\rm rel} \to 0$, is cured once we thermally average the cross sections, since only those quantities enter in the evolution equations, cf. (7.1)–(7.3).[4]

The collinear singularity, however, still persists and on the first sight it is not clear how it can be removed. In fact, this peculiar divergence in the continuum dipole matrix element seems to be an artifact coming from the multipole expansion of the gauge fields in the center-of-mass frame of the heavy DM pair and, according to ref. [197], even exists in all higher mulipole matrix elements.[5] We build our analysis of this particular singularity on refs. [192, 193], and extract the divergence using proper analytical regularization techniques.

We reconsider the first line in eq. (C.32), which contains an integral over the scattering state wavefunctions $\Psi_{\boldsymbol{p}}(\boldsymbol{r}) = \sum\limits_{\ell=0}^{\infty} \sum\limits_{m=-\ell}^{\ell} i^{\ell} R_{p,\ell}(r) Y_{\ell}^{m}(\hat{\boldsymbol{r}}) Y_{\ell}^{m}(\hat{\boldsymbol{p}})$, with the real radial partial wavefunction $R_{p,\ell}(r)$ that can be inferred from (C.4).[6] Once the angular inte-

[4] Notice that possible contributions coming from taking the limits $v_{\rm rel}, v'_{\rm rel} \to \infty$, though not physically of interest since the underlying (p)NREFTs developed in this work are inherently valid only for non-relativistic DM particles, are always exponentially suppressed due to the statistical distribution functions.

[5] To be more precise, in [197] the authors claim that after multipole expanding the gauge fields $\boldsymbol{A}(\boldsymbol{R})$ in powers of small relative distances over large wavelengths, $\boldsymbol{r}/\boldsymbol{R} \ll 1$, the collinear divergence arises once the center-of-mass position dependence $\boldsymbol{R}$ of the gauge fields is put to zero, i.e. $\boldsymbol{A}(\boldsymbol{0})$. Hence it would be desirable to check quantitatively if the diagonal divergence is absent in a general reference frame, where $\boldsymbol{R} \neq \boldsymbol{0}$.

[6] $R_{p,\ell} \supset e^{ipr}\ {}_1F_1\left(\ell + 1 - \frac{i}{a_0 p}, 2\ell + 2, -2ipr\right)$, omitting the real prefactor, can be shown to be real by using the Cauchy product $\left(\sum\limits_{n=0}^{\infty} \alpha_n x^n\right)\left(\sum\limits_{n=0}^{\infty} \beta_n x^n\right) = \sum\limits_{n=0}^{\infty} x^n \left(\sum\limits_{k=0}^{n} \alpha_k \beta_{n-k}\right)$, with $x = -2ipr$:

$$
\begin{aligned}
R^{*}_{p,\ell} \supset e^{-ipr}\ {}_1F_1\left(\ell + 1 + \frac{i}{a_0 p}, 2\ell + 2, 2ipr\right) &= e^{ipr} e^{-2ipr} \sum_{n=0}^{\infty} \frac{(\ell + 1 + i/(a_0 p))^{(n)}\, (2ipr)^n}{(2\ell + 2)^{(n)} n!} \\
&= e^{ipr} \left(\sum_{n=0}^{\infty} \frac{(-2ipr)^n}{n!}\right)\left(\sum_{n=0}^{\infty} \frac{(\ell + 1 + i/(a_0 p))^{(n)}\, (-1)^n}{(2\ell + 2)^{(n)} n!} (-2ipr)^n\right) \\
&= e^{ipr} \sum_{n=0}^{\infty} (-2ipr)^n \left(\sum_{k=0}^{n} \frac{(\ell + 1 + i/(a_0 p))^{(k)}\, (-1)^k}{(2\ell + 2)^{(k)} k!\ (n-k)!}\right) = e^{ipr} \sum_{n=0}^{\infty} (-2ipr)^n \frac{(2\ell+1)!\ (\ell + n - i/(a_0 p))!}{(\ell - i/(a_0 p))!\ n!\ (2\ell + n + 1)!} \\
&= e^{ipr}\ {}_1F_1\left(\ell + 1 - \frac{i}{a_0 p}, 2\ell + 2, -2ipr\right) .
\end{aligned}
$$

gration has been done, it can be written as follows:

$$\begin{aligned}\langle \boldsymbol{p}|\boldsymbol{r}|\boldsymbol{p}'\rangle &= \int d^3r\, \boldsymbol{r}\, \Psi^*_{\boldsymbol{p}}(\boldsymbol{r})\Psi_{\boldsymbol{p}'}(\boldsymbol{r}) \\ &= 2\pi^2 i \sum_{\ell=0}^{\infty} \Bigg\{ (\ell+1) \\ &\qquad \times \left[P_{\ell+1}(\cos(\theta_{p'}))\boldsymbol{e}_z + \frac{P^1_{\ell+1}(\cos(\theta_{p'}))}{\ell+1}\left[\cos(\phi_{p'})\boldsymbol{e}_x + \sin(\phi_{p'})\boldsymbol{e}_y\right]\right] M^{\ell,(+)}_{p,p'} \\ &\quad + \ell \left[P_{\ell-1}(\cos(\theta_{p'}))\boldsymbol{e}_z + \frac{1}{\ell}P^1_{\ell-1}(\cos(\theta_{p'}))\left[\cos(\phi_{p'})\boldsymbol{e}_x + \sin(\phi_{p'})\boldsymbol{e}_y\right]\right] M^{\ell,(-)}_{p,p'} \Bigg\}, \end{aligned} \tag{C.48}$$

where the radial integrals are comprised in

$$\begin{aligned} M^{\ell,(+)}_{p,p'} &= \mathcal{C}^{\ell}_{p}\mathcal{C}^{\ell+1}_{p'} \lim_{\epsilon\to 0^+} \int_0^\infty dr\; e^{-\epsilon r} r^{2\ell+4} e^{ir(p+p')}\; {}_1F_1\left(\ell+1-\frac{i}{a_0 p}, 2\ell+2, -2ipr\right) \\ &\qquad \times {}_1F_1\left(\ell+2-\frac{i}{a_0 p'}, 2\ell+4, -2ip'r\right), \end{aligned} \tag{C.49}$$

$$\begin{aligned} M^{\ell,(-)}_{p,p'} &= \mathcal{C}^{\ell}_{p}\mathcal{C}^{\ell-1}_{p'} \lim_{\epsilon\to 0^+} \int_0^\infty dr\; e^{-\epsilon r} r^{2\ell+2} e^{ir(p+p')}\; {}_1F_1\left(\ell+1-\frac{i}{a_0 p}, 2\ell+2, -2ipr\right) \\ &\qquad \times {}_1F_1\left(\ell-\frac{i}{a_0 p'}, 2\ell, -2ip'r\right), \end{aligned} \tag{C.50}$$

where we introduced a dimensionfull regulator ϵ and[7]

$$\mathcal{C}^{\ell}_{p} = \frac{2^{\ell+1}}{(2\ell+1)!}\frac{p^{\ell}(a_0 p)^{-1/2}}{\sqrt{1-e^{-2\pi/(a_0 p)}}}\prod_{s=1}^{\ell}\sqrt{s^2+(a_0 p)^{-2}}\,. \tag{C.51}$$

In the following, we focus on (C.49), which can be written as[8]

$$\begin{aligned} M^{\ell,(+)}_{p,p'} &= \left|\ell+1+\frac{i}{a_0 p}\right| \frac{(2\pi)^3}{p^3}\delta(p-p') \\ &+ \frac{(2\ell+2)(2\ell+3)}{(2ip')^2}\mathcal{C}^{\ell}_{p}\mathcal{C}^{\ell+1}_{p'} \lim_{\epsilon\to 0^+}\int_0^\infty dr\; e^{-\epsilon r} r^{2\ell+2} e^{ir(p+p')}\, {}_1F_1\left(\ell+1-\frac{i}{a_0 p}, 2\ell+2, -2ipr\right) \\ &\quad \times \left[{}_1F_1\left(\ell+2-\frac{i}{a_0 p'}, 2\ell+2, -2ip'r\right) \;+\; {}_1F_1\left(\ell-\frac{i}{a_0 p'}, 2\ell+2, -2ip'r\right)\right]. \end{aligned} \tag{C.52}$$

---

[7] Notice that $\mathcal{C}^{\ell+1}_{p} = \mathcal{C}^{\ell}_{p}\frac{2p\sqrt{(\ell+1)^2+(a_0 p)^{-2}}}{(2\ell+2)(2\ell+3)}$ and $\mathcal{C}^{\ell-1}_{p} = \mathcal{C}^{\ell}_{p}\frac{2\ell(2\ell+1)}{2p\sqrt{\ell^2+(a_0 p)^{-2}}}$.

[8] Hereby we use two-times the recurrence relation ${}_1F_1(a,b+1,z) = \frac{b}{z}[{}_1F_1(a,b,z) - {}_1F_1(a-1,b,z)]$ and the orthogonality relation $\int_0^\infty dr\; r^2 R_{p,\ell}(r)R_{p',\ell}(r) = \frac{(2\pi)^3}{p^2}\delta(p-p')$.

Following the notation in ref. [193], we define [198]

$$\mathcal{I}_\epsilon(s,a,a') \equiv \int_0^\infty dr\ e^{-\epsilon r} r^{2\ell+1} e^{-sr}\ {}_1F_1\left(a, 2\ell+2, -2ipr\right)\ {}_1F_1\left(a', 2\ell+2, -2ip'r\right)$$
$$= \frac{\Gamma(2\ell+2)(\epsilon+s)^{a+a'-(2\ell+2)}}{(\epsilon+s+2ip)^{-a}(\epsilon+s+2ip')^{-a'}}\ {}_2F_1\left(a, a', 2\ell+2, \frac{-4pp'}{(\epsilon+s+2ip)(\epsilon+s+2ip')}\right), \quad \text{(C.53)}$$

where $s \equiv -i(p+p')$ and the result of the integral in the second line can be found for example in [199]. Then

$$\mathcal{J}_\epsilon(s,a,a') \equiv \int_0^\infty dr\ e^{-\epsilon r} r^{2\ell+2} e^{-sr}\ {}_1F_1\left(a, 2\ell+2, -2ipr\right)\ {}_1F_1\left(a', 2\ell+2, -2ip'r\right)$$
$$= -\frac{\partial}{\partial s}\mathcal{I}_\epsilon(s,a,a') = \frac{1}{\epsilon+s}\left(2\ell+2 - \frac{2iap}{\epsilon+s+2ip} - \frac{2ia'p'}{\epsilon+s+2ip'}\right)\mathcal{I}_\epsilon(s,a,a')\,. \quad \text{(C.54)}$$

In the collinear limit of the incoming and outgoing momenta, $p' \to p$, we expand the Gaussian hypergeometric function and obtain[9]

$$\mathcal{J}_\epsilon\left(-i(p+p'), \ell+1-\frac{i}{a_0 p}, \ell+2-\frac{i}{a_0 p'}\right)$$
$$= \frac{(\epsilon+i(p'-p))^{-2-\frac{i}{a_0}(\frac{1}{p}-\frac{1}{p'})}(\epsilon-i(p+p'))^{1-\frac{i}{a_0}(\frac{1}{p}+\frac{1}{p'})}}{(4pp')^{\ell+1-i/(a_0 p)}} \frac{\Gamma\left(1-\frac{i}{a_0}\left(\frac{1}{p'}-\frac{1}{p}\right)\right)\Gamma(2\ell+2)^2}{\Gamma\left(\ell+2-\frac{i}{a_0 p'}\right)\Gamma\left(\ell+1+\frac{i}{a_0 p}\right)}$$
$$+\frac{(\epsilon+i(p-p'))^{1+\frac{i}{a_0}(\frac{1}{p}-\frac{1}{p'})}(\epsilon-i(p+p'))^{1-\frac{i}{a_0}(\frac{1}{p}+\frac{1}{p'})}}{(4pp')^{\ell+2-i/(a_0 p')}(\epsilon+i(p'-p))} \frac{\Gamma\left(-1-\frac{i}{a_0}\left(\frac{1}{p}-\frac{1}{p'}\right)\right)\Gamma(2\ell+2)^2}{\Gamma\left(\ell+1-\frac{i}{a_0 p}\right)\Gamma\left(\ell+\frac{i}{a_0 p'}\right)}\,, \quad \text{(C.55)}$$

and

$$\mathcal{J}_\epsilon\left(-i(p+p'), \ell+1-\frac{i}{a_0 p}, \ell-\frac{i}{a_0 p'}\right)$$
$$= \frac{(\epsilon-i(p'-p))^{-2+\frac{i}{a_0}(\frac{1}{p}-\frac{1}{p'})}(\epsilon-i(p+p'))^{-1-\frac{i}{a_0}(\frac{1}{p}+\frac{1}{p'})}}{(4pp')^{\ell-i/(a_0 p')}} \frac{\Gamma\left(1+\frac{i}{a_0}\left(\frac{1}{p'}-\frac{1}{p}\right)\right)\Gamma(2\ell+2)^2}{\Gamma\left(\ell+1-\frac{i}{a_0 p}\right)\Gamma\left(\ell+2+\frac{i}{a_0 p'}\right)}$$
$$+\frac{(\epsilon+i(p'-p))^{1-\frac{i}{a_0}(\frac{1}{p}-\frac{1}{p'})}(\epsilon-i(p+p'))^{-1-\frac{i}{a_0}(\frac{1}{p}+\frac{1}{p'})}}{(4pp')^{\ell+1-i/(a_0 p)}(\epsilon-i(p'-p))} \frac{\Gamma\left(-1+\frac{i}{a_0}\left(\frac{1}{p}-\frac{1}{p'}\right)\right)\Gamma(2\ell+2)^2}{\Gamma\left(\ell+1+\frac{i}{a_0 p}\right)\Gamma\left(\ell-\frac{i}{a_0 p'}\right)}\,. \quad \text{(C.56)}$$

[9] In the limit $z \to \infty$ it holds that

$${}_2F_1\left(a, a', 2\ell+2, z\right) \to \frac{1}{(-z)^a}\frac{\Gamma(a'-a)\Gamma(2\ell+2)}{\Gamma(a')\Gamma(2\ell+2-a)} + \frac{1}{(-z)^{a'}}\frac{\Gamma(a-a')\Gamma(2\ell+2)}{\Gamma(a)\Gamma(2\ell+2-a')}\,.$$

Finally, taking the limit $\epsilon \to 0$, we can extract the collinear singularity from eq. (C.52), which reads

$$
\begin{aligned}
M^{\ell,(+)}_{p,p'}\Big|_{p'\to p} &= \left|\ell+1+\frac{i}{a_0 p}\right| \frac{(2\pi)^3}{p^3}\delta(p'-p) + \lim_{\epsilon\to 0^+} \frac{(2\ell+2)(2\ell+3)}{(2ip')^2}\mathcal{C}^\ell_p \mathcal{C}^{\ell+1}_{p'} \\
&\times\Big[\mathcal{J}_\epsilon\left(-i(p+p'),\ell+1-\tfrac{i}{a_0 p},\ell+2-\tfrac{i}{a_0 p'}\right)+\mathcal{J}_\epsilon\left(-i(p+p'),\ell+1-\tfrac{i}{a_0 p},\ell-\tfrac{i}{a_0 p'}\right)\Big]\Big|_{p'\to p} \\
&= \left|\ell+1+\frac{i}{a_0 p}\right| \frac{(2\pi)^3}{p^3}\delta(p'-p) \\
&+\Bigg\{\frac{(2\pi)^2}{p^2}\frac{\ell+1+\frac{i}{a_0 p}}{\left|\ell+1+\frac{i}{a_0 p}\right|}\frac{i}{(\epsilon+i(p'-p))^2}\Bigg[1-\frac{i}{a_0 p^2}(p'-p)\log\left(\tilde\epsilon+i(v'_{\rm rel}-v_{\rm rel})\right) \\
&\quad+\frac{p'-p}{p}\Bigg[\frac{i}{a_0 p}\log(2v_{\rm rel})-\frac{i}{a_0 p}\gamma_{\rm E}-\frac{3}{2} \\
&\qquad-\frac{i}{2a_0 p}\Bigg(\Psi_0\left(\ell+1-\frac{i}{a_0 p}\right)+\Psi_0\left(\ell+1+\frac{i}{a_0 p}\right) \\
&\qquad\quad+2(\ell+1)\left|\ell+1+\frac{i}{a_0 p}\right|^{-2}\Bigg)\Bigg]\Bigg]+\text{c.c.}\Bigg\} \\
&-\left\{\frac{\pi^2 a_0}{p^2}\frac{i}{\epsilon+i(p'-p)}\left(\ell+\frac{i}{a_0 p}\right)\left|\ell+1+\frac{i}{a_0 p}\right|+\text{c.c.}\right\},
\end{aligned}
\tag{C.57}
$$

where $\epsilon \equiv M\tilde\epsilon/2$ and, as a reminder, $p = Mv_{\rm rel}/2$ and $p' = Mv'_{\rm rel}/2$. One can factor out the collinear singularity from (C.50) in a similar way, and we obtain

$$
\begin{aligned}
M^{\ell,(-)}_{p,p'}\Big|_{p'\to p} &= \left|\ell+\frac{i}{a_0 p}\right| \frac{(2\pi)^3}{p^3}\delta(p'-p) \\
&-\Bigg\{\frac{(2\pi)^2}{p^2}\frac{\ell-\frac{i}{a_0 p}}{\left|\ell-\frac{i}{a_0 p}\right|}\frac{i}{(\epsilon+i(p'-p))^2}\Bigg[1-\frac{i}{a_0 p^2}(p'-p)\log\left(\tilde\epsilon+i(v'_{\rm rel}-v_{\rm rel})\right) \\
&\quad+\frac{p'-p}{p}\Bigg[\frac{i}{a_0 p}\log(2v_{\rm rel})-\frac{i}{a_0 p}\gamma_{\rm E}-\frac{1}{2} \\
&\qquad-\frac{i}{2a_0 p}\left(\Psi_0\left(\ell-\frac{i}{a_0 p}\right)+\Psi_0\left(\ell+\frac{i}{a_0 p}\right)\right)\Bigg]\Bigg]+\text{c.c.}\Bigg\} \\
&+\left\{\frac{\pi^2 a_0}{p^2}\frac{i}{\epsilon+i(p'-p)}\left(\ell-1-\frac{i}{a_0 p}\right)\left|\ell+\frac{i}{a_0 p}\right|+\text{c.c.}\right\}.
\end{aligned}
\tag{C.58}
$$

First of all, we notice that the divergence appears in a distributional sense in terms of a delta function and its derivative, since

$$
\frac{1}{(\epsilon+i(p'-p))^2} = -\frac{1}{((p'-p)-i\epsilon)^2} = -\mathrm{P}\left[\frac{1}{(p'-p)^2}\right]+i\pi\delta'(p'-p)\,. \tag{C.59}
$$

Second, we observe a deviation of the results (C.57) and (C.58) compared to those found in ref. [193], namely a mismatch in the constant terms $-3/2$ $(-1/2)$ in the fifth (third) line of (C.57) ((C.58)) compared to the analogous expressions in [193], but also the terms in the last line of each (C.57) and (C.58) are missing in [193]. Hence it remains to be checked, by how much those missing terms contribute to the overall integral result. Third, the results derived so far can be also directly used for color-adjoint to color-adjoint transitions in non-abelian gauge theories, cf. section C.2, by replacing $\alpha \to -\alpha/(2N)$ in the Bohr radius $a_0 = 2/(M\alpha)$, that enters at several places in (C.57) and (C.58). Finally, we do not write explicitly the result for the collinear singularity in the color-singlet to color-adjoint continuum dipole matrix element, cf. eq. (C.43), since it shares a similar structure as (C.57) and (C.58) with the same kind of divergence in terms of the Dirac delta function and its first derivative.

Appendix D

Thermal field theory: real-time formalism

This section is devoted to the cataloguing of the various two-point functions of the bosonic DM heavy pair and gauge fields as well as the fermionic fields of the dark light particles and, in addition, the computation of the radiative self-energy corrections of the dark photon propagator at zero and finite temperature for different hierarchies of energy scales, that are the basic ingredients used for the calculation of the interaction rates throughout this work. For a general introduction to quantum field theories (QFTs) at *finite temperature*, especially an extensive treatment of the fundamentals of the imaginary time formalism (also referred to as the *Matsubara* formalism) and the *real-time* formalism, we direct the reader to appropriate literature such as the following review papers [56, 200], or well-established textbooks (e.g. [201, 202]). The basic idea is to make a close connection between the principles of statistical mechanics and QFTs, due to the interpretation of the Boltzmann factor $e^{-H/T}$, where H is the Hamiltonian operator of the whole quantum system in a canonical ensemble, as a time evolution operator e^{-iHt}, i.e. by relating temperature with imaginary time, $t = -i/T$.[1] This work is based on the real-time formalism, where the expectation value of an observable $\mathcal{A}$,

$$\langle \mathcal{A} \rangle = \frac{\mathrm{Tr}\left[\mathcal{A} e^{-H/T}\right]}{\mathrm{Tr}\left[e^{-H/T}\right]}\,, \tag{D.1}$$

is evaluated on the complex *Schwinger-Keldysh* contour [203, 204], cf. figure D.1, starting from an initial time t_i along the path $\mathcal{C}_1$ to t_f, then along $\mathcal{C}_2$ back to $t_i - i\epsilon$, where it finally evolves on an imaginary time axis to the final time $t_i - iT$, because of the product of $\mathcal{A}$ and $e^{-H/T}$ within the trace in (D.1).[2]

[1] The Boltzmann factor equals the density operator of the full system in a canonical ensemble, $\rho = e^{-H/T}$, that solves the von-Neumann equation $\frac{\partial}{\partial t}\rho = -i\,[H, \rho]$ with the solution $\rho(t) = e^{-iHt}\rho(0)e^{iHt}$.

[2] In general, evaluating matrix elements $\langle \Psi | \mathcal{A} | \Psi \rangle$ in QFTs, like in eq. (D.1), with the same state $|\Psi\rangle$ at equal times on the left and on the right of an operator $\mathcal{A}$, goes under the name of the *in-in* formalism suited for thermal out-of-equilibrium processes, as opposed to the *in-out* (S-matrix) formalism used for in-vacuum scattering processes in QFTs at zero T.

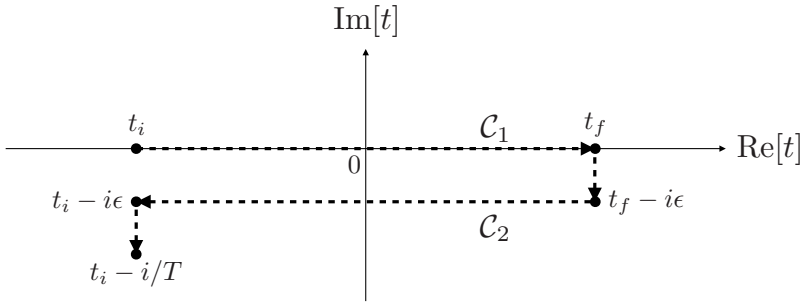

Figure D.1: Schwinger-Keldysh contour in the complex time-plane in the real-time formalism. According to the contour ordering $t_i \to t_f \to t_i - i/T$, time points on the lower branch $\mathcal{C}_2$ are always after those on the upper branch $\mathcal{C}_1$.

D.1 Greens functions on the Schwinger-Keldysh contour

In the real-time formalism, we evolve the system along the Schwinger-Keldysh contour, cf. figure D.1, which leads to a doubling of the degrees of freedom, since the quantum fields can live either on the upper time-ordered branch $\mathcal{C}_1$, corresponding to the physical time axis, or on the lower anti-time ordered branch $\mathcal{C}_2$. We denote accordingly the fields on the upper branch with a subscript 1, which are the physical fields, and the ones on the lower branch with a subscript 2, which are unphysical and can only enter via internal propagators within any Feynman diagram under consideration.[3] In the real-time formalism, the general procedure to determine and draw all Feynman diagrams is to assign all external lines to be of type 1, i.e. to consist only of fields of type 1, whereas the internal lines can be of type 1 or 2, and one needs to sum over all possible combinations of those assignments. Also the vertices can be either of type 1 or 2, where the type-1 vertices are those related to the familiar vertices in QFTs at zero temperature. The type-2 vertices differ by an additional negative sign.

Due to the doubling of the fields, there are four different kinds of two-point functions that can be constructed. In momentum space, the dark photon two-point function can be written in a matrix form as

$$D_{\mu\nu}(q) = \begin{pmatrix} D^{11}_{\mu\nu}(q) & D^{12}_{\mu\nu}(q) \\ D^{21}_{\mu\nu}(q) & D^{22}_{\mu\nu}(q) \end{pmatrix} = \begin{pmatrix} D^{T}_{\mu\nu}(q) & D^{<}_{\mu\nu}(q) \\ D^{>}_{\mu\nu}(q) & (D^{T}_{\mu\nu}(q))^* \end{pmatrix} , \tag{D.2}$$

where $D^{11}_{\mu\nu}(q)$ is the time-ordered two-point function, $D^{22}_{\mu\nu}(q)$ the anti-time-ordered two-point function and the off-diagonal elements are the Wightman functions, with mixed fields of each type 1 and 2 in the CTP-index space, that in case of a system in thermal equilibrium satisfy the KMS-relation

$$D^{<}_{\mu\nu}(q) = e^{-q_0/T} D^{>}_{\mu\nu}(q) \, . \tag{D.3}$$

[3]The additional subscript (1 or 2) on the fields in order to distinguish the two different time branches $\mathcal{C}_1$ and $\mathcal{C}_2$ to which the fields can belong to, is sometimes referred to as the CTP-index (CTP = Closed-time-path). The Schwinger-Keldysh formalism is also known as the closed-time-path formalism.

In the abelian theory,[4] the free (i.e. at leading order, superscript LO) thermal propagator in Coulomb gauge reads[5]

$$D_{00}^{\mathrm{LO}}(|\boldsymbol{q}|) = \begin{pmatrix} \dfrac{i}{\boldsymbol{q}^2} & 0 \\ 0 & \dfrac{-i}{\boldsymbol{q}^2} \end{pmatrix}, \tag{D.4}$$

$$\begin{aligned} D_{ij}^{\mathrm{LO}}(q) = \left(\delta_{ij} - \frac{q_i q_j}{|\boldsymbol{q}|^2}\right) \Bigg[& \begin{pmatrix} \dfrac{i}{q^2+i\epsilon} & \Theta(-q_0)2\pi\delta(q^2) \\ \Theta(q_0)2\pi\delta(q^2) & \dfrac{-i}{q^2-i\epsilon} \end{pmatrix} \\ & + 2\pi\delta(q^2)\, n_{\mathrm{B}}(|q_0|) \begin{pmatrix} 1 & 1 \\ 1 & 1 \end{pmatrix} \Bigg], \end{aligned} \tag{D.5}$$

where $n_{\mathrm{B}}(E) = 1/(e^{E/T}-1)$ is the Bose–Einstein distribution. In Coulomb-gauge it holds that $D_{0i}(q) = D_{i0}(q) = 0$. The 21- and time-ordered two-point functions, that are used in this work to determine the rates like the bsf cross section or the bsf width, can be derived from the retarded and advanced two-point functions $D^R_{\mu\nu}(q)$ and $D^A_{\mu\nu}(q)$, respectively, via

$$\begin{aligned} D^{>}_{\mu\nu}(q) &= [1+n_{\mathrm{B}}(q_0)][D^R_{\mu\nu}(q) - D^A_{\mu\nu}(q)] \\ &= 2[1+n_{\mathrm{B}}(q_0)]\mathrm{Re}[D^R_{\mu\nu}(q)]\big|_{q_0>0}\,, \end{aligned} \tag{D.6}$$

$$\begin{aligned} D^{11}_{\mu\nu}(q) &= D^R_{\mu\nu}(q) + D^<_{\mu\nu}(q) = D^A_{\mu\nu}(q) + D^>_{\mu\nu}(q) \\ &= \frac{D^R_{\mu\nu}(q) + D^A_{\mu\nu}(q)}{2} + \left[\frac{1}{2} + n_{\mathrm{B}}(q_0)\right][D^R_{\mu\nu}(q) - D^A_{\mu\nu}(q)] \\ &= \frac{1}{2}[D^R_{\mu\nu}(q) + D^A_{\mu\nu}(q) + D^S_{\mu\nu}(q)]\,. \end{aligned} \tag{D.7}$$

where in the last line we split the terms into a sum of symmetric, $D^S_{\mu\nu}(q)$, and anti-symmetric, $D^{AS}_{\mu\nu}(q) = D^R_{\mu\nu}(q) + D^A_{\mu\nu}(q)$, functions which are real and imaginary, respectively. The retarded and advanced free propagators in Coulomb gauge are

$$D^{R/A}_{00,\mathrm{LO}}(|\boldsymbol{q}|) = \frac{i}{\boldsymbol{q}^2}\,, \tag{D.8}$$

$$\begin{aligned} D^{R/A}_{ij,\mathrm{LO}}(q) &= \left(\delta_{ij} - \frac{q_i q_j}{\boldsymbol{q}^2}\right)\frac{i}{(q_0 \pm i\epsilon)^2 - \boldsymbol{q}^2} = \left(\delta_{ij} - \frac{q_i q_j}{\boldsymbol{q}^2}\right)\frac{i}{q^2 \pm i\,\mathrm{sign}(q_0)\epsilon} \\ &\equiv \left(\delta_{ij} - \frac{q_i q_j}{\boldsymbol{q}^2}\right)\Delta^{R/A}_{\mathrm{LO}}(q)\,. \end{aligned} \tag{D.9}$$

[4] In the SU(N) case, we need to multiply the color matrix δ^{AB} to the expressions in (D.4) and (D.5), where the trace of δ^{AB} is $\delta^{AA} = N^2 - 1$.

[5] Throughout this work, thermal propagators are assigned to particles that are in kinetic equilibrium with the thermal environment.

At higher order in perturbation theory, the free dark photon propagator gets modified by loop corrections due to interactions with the light dark fermions f_i from the thermal bath, cf. section D.2 for more explicit details.[6]

The two-point function can be expanded as a series in terms of the free propagator and one-loop polarization tensor,

$$D_{\mu\nu}(q) = D^{\mathrm{LO}}_{\mu\nu}(q) + D^{\mathrm{LO}}_{\mu\lambda}(q)\left[i\Pi^{\lambda\rho}(q)\right] D^{\mathrm{LO}}_{\rho\nu}(q) + \dots \,. \tag{D.10}$$

An analogous series can be written for all other functions, e.g. $D^{R/A}_{\mu\nu}(q)$, as well. If the series cannot be truncated, it needs to be resummed, and, using the geometric series, for the retarded and advanced functions it results in

$$\begin{aligned} D^{R/A}_{00}(q) &= \frac{i}{\boldsymbol{q}^2 + \Pi^{R/A}_{00}(q)}\,, & \text{(D.11)}\\ D^{R/A}_{ij}(q) &= \left(\delta_{ij} - \frac{q_i q_j}{\boldsymbol{q}^2}\right) \frac{i}{(q_0 \pm i\epsilon)^2 - \boldsymbol{q}^2 + \Pi^{R/A}_{\mathrm{trans}}(q)}\,, & \text{(D.12)} \end{aligned}$$

where the transverse retarded/advanced polarization tensor is defined as $\Pi^{R/A}_{\mathrm{trans}}(q) = (\delta^{ij} - q^i q^j/\boldsymbol{q}^2)\Pi^{R/A}_{ij}(q)/2$. The 21-Wightman function in an expanded form is given as

$$\begin{aligned} D^{>}_{\mu\nu}(q) &= 2[1+n_{\mathrm{B}}(q_0)]\ \mathrm{Re}\left[D^{R,\mathrm{LO}}_{\mu\nu}(q) + D^{R,\mathrm{LO}}_{\mu\lambda}(q)\left[i\Pi^{\lambda\rho}_R(q)\right] D^{R,\mathrm{LO}}_{\rho\nu}(q) + \dots\right]\Big|_{q_0>0} \\ &= 2[1+n_{\mathrm{B}}(q_0)]\ \mathrm{Re}\left[D^{R,\mathrm{LO}}_{\mu\nu}(q)\right]\Big|_{q_0>0} + 2[1+n_{\mathrm{B}}(q_0)]\ \mathrm{Im}\left[D^{R,\mathrm{LO}}_{\mu\lambda}(q)\Pi^{\lambda\rho}_R(q) D^{R,\mathrm{LO}}_{\rho\nu}(q)\right]\Big|_{q_0>0} \\ &\quad + \dots \\ &= D^{>,\mathrm{LO}}_{\mu\nu}(q) + D^{>,\mathrm{NLO}}_{\mu\nu}(q) + \dots \,. \end{aligned} \tag{D.13}$$

In the subsequent section D.2 we derive explicitly analytic expressions of the retarded thermal polarization tensor and give the results for the resummed dark photon propagator that were used in the main body of this work.

The free thermal bosonic propagator of the DM heavy fermion-antifermion field ϕ in $\mathrm{pNRQED}_{\mathrm{DM}}$ reads[7]

$$\begin{aligned} G(p_0) &= \begin{pmatrix} \dfrac{i}{p_0 - H + i\epsilon} & 0 \\ 2\pi\delta(p_0 - H) & \dfrac{-i}{p_0 - H - i\epsilon} \end{pmatrix} + 2\pi\delta(p_0 - H)\, n_{\mathrm{B}}(p_0) \begin{pmatrix} 1 & 1 \\ 1 & 1 \end{pmatrix} \\ &\approx \begin{pmatrix} \dfrac{i}{p_0 - H + i\epsilon} & 0 \\ 2\pi\delta(p_0 - H) & \dfrac{-i}{p_0 - H - i\epsilon} \end{pmatrix}. \end{aligned} \tag{D.14}$$

[6] Loop diagrams, which involve the heavy DM (anti-)particles $X, \bar{X}$ in the loop, are negligible (because of the decoupling theorem in the limit of very large DM masses) and hence can be neglected.

[7] In the non-abelian theory, the color-adjoint heavy-pair propagator is (D.14) $\times\ \delta^{AB}$, whereas the color-singlet heavy-pair propagator is simply (D.14).

where p_0 is the energy of the dark fermion-antifermion pair and in the heavy mass limit, recalling that $H = 2M + \ldots$, $n_{\rm B}(H)$ is exponentially suppressed as $e^{-2M/T}$. The real-time formalism is convenient when dealing with heavy fields, since the type-2 fermion-antifermion fields decouple from the type-1 fields due to the vanishing off-diagonal element in the matrix propagator in the second line of eq. (D.14), and hence may be ignored in the heavy-mass limit [48].

Finally, for the n_f dark fermionic fields f_i charged under $\mathrm{U}(1)_{\rm DM}$ with small masses m_i, the corresponding free thermal Dirac propagators are[8] (in SU(N): multiply by δ^{ab})

$$\begin{aligned} S_i^{\rm LO}(k) &= (\not{k} + m_i)\Bigg[\begin{pmatrix} \dfrac{i}{k^2 - m_i^2 + i\epsilon} & 0 \\ 2\pi\,\mathrm{sign}(k_0)\delta(k^2 - m_i^2) & \dfrac{-i}{k^2 - m_i^2 - i\epsilon} \end{pmatrix} \\ &\qquad -2\pi\,\mathrm{sign}(k_0)\delta(k^2 - m_i^2) n_{\rm F}(k_0) \begin{pmatrix} 1 & 1 \\ 1 & 1 \end{pmatrix} \Bigg], \end{aligned} \tag{D.15}$$

where $n_{\rm F}(E) = 1/(e^{E/T} + 1)$ is the Fermi–Dirac distribution and in practice we neglect the mass dependence for temperatures $T \gg m_i$. Hence, upon setting $m_i = 0$ in (D.15), each of the n_f light particles has parametrically the same thermal propagator expression, and we can omit the subscript i. The same relations among the different two-point functions, like the ones given in (D.6)–(D.7) for the bosonic case, apply also for the fermionic fields, except that one needs to replace the distribution function $n_{\rm B}$ by $-n_{\rm F}$. In particular, the symmetric massless fermion propagator is $S^S(k) = [1 - 2n_{\rm F}(|k_0|)]2\pi\not{k}\delta(k^2)$.

D.2 Thermal gauge-boson polarization tensor

In this section, we consider radiative corrections and resummation effects entirely in the abelian theory. The retarded dark photon self-energy, its diagram depicted in figure D.2, that enters in the next-to-leading order term of the 21-dark photon propagator in (D.13), with n_f massless dark particles in the loop, reads [205]

$$\begin{aligned} \Pi^R_{\mu\nu}(q) &= \Pi^{11}_{\mu\nu}(q) + \Pi^{12}_{\mu\nu}(q) \\ &= -ig^2 n_f \int \frac{d^4k}{(2\pi)^4} \left(\mathrm{Tr}\left[\gamma_\mu S^{11}(k-q)\gamma_\nu S^{11}(k)\right] - \mathrm{Tr}\left[\gamma_\mu S^{21}(k-q)\gamma_\nu S^{12}(k)\right] \right) \\ &= -i\frac{g^2}{2} n_f \int \frac{d^4k}{(2\pi)^4} \left(\mathrm{Tr}\left[\gamma_\mu S^{S}(k-q)\gamma_\nu S^{R}(k)\right] + \mathrm{Tr}\left[\gamma_\mu S^{A}(k-q)\gamma_\nu S^{S}(k)\right] \right. \\ &\qquad \left. + \mathrm{Tr}\left[\gamma_\mu S^{A}(k-q)\gamma_\nu S^{A}(k)\right] + \mathrm{Tr}\left[\gamma_\mu S^{R}(k-q)\gamma_\nu S^{R}(k)\right] \right), \end{aligned} \tag{D.16}$$

where the terms in the last line vanish after the integration over k_0 using the residue theorem. Shifting the momentum $k \to k + q$ in the first term and $k \to -k$ in the second

[8] We do not consider self-energy corrections to the light fermionic propagator in (D.15), that would involve dark photons in the loop, and hence we can omit the superscript LO in (D.15).

term, and using the explicit form of the massless fermion propagators (i.e. eq. (D.15) with $m_i = 0$), we get

$$\begin{aligned}\Pi^R_{\mu\nu}(q) &= n_f g^2 \int \frac{d^4k}{(2\pi)^3}[1-2n_{\rm F}(|k_0|)]{\rm Tr}[\gamma_\mu \not{k}\gamma_\nu(\not{k}+\not{q})]\frac{\delta(k^2)}{(k+q)^2+i\,{\rm sign}(k_0+q_0)\epsilon} \\ &= \Pi^{R,T=0}_{\mu\nu}(q) + \Pi^{R,T\neq 0}_{\mu\nu}(q)\,,\end{aligned} \tag{D.17}$$

where the vacuum polarization tensor, $\Pi^{R,T=0}_{\mu\nu}(q)$, stems from the first term in the square bracket and in the $\overline{\rm MS}$ scheme it reads

$$\Pi^{R,T=0}_{\mu\nu,\overline{\rm MS}}(q) = (q_\mu q_\nu - g_{\mu\nu}q^2)\frac{n_f g^2}{12\pi^2}\left[\ln\left(\frac{(q_0+i\epsilon)^2-\boldsymbol{q}^2}{-\mu^2}\right)-\frac{5}{3}\right]. \tag{D.18}$$

The thermal retarded polarization tensor is

$$\begin{aligned}\Pi^{R,T\neq 0}_{\mu\nu}(q) &= -2n_f g^2 \int \frac{d^4k}{(2\pi)^3} n_{\rm F}(|k_0|){\rm Tr}[\gamma_\mu \not{k}\gamma_\nu(\not{k}+\not{q})]\frac{\delta(k^2)}{(k+q)^2+i\,{\rm sign}(k_0+q_0)\epsilon} \\ &= -n_f g^2 \int \frac{d^3k}{(2\pi)^3}\frac{n_{\rm F}(|\boldsymbol{k}|)}{|\boldsymbol{k}|} \\ &\quad\times\left(\frac{{\rm Tr}[\gamma_\mu \not{k}\gamma_\nu(\not{q}+\not{k})]|_{k_0=|\boldsymbol{k}|}}{(q_0+|\boldsymbol{k}|)^2-|\boldsymbol{q}+\boldsymbol{k}|^2+i\epsilon_+}+\frac{{\rm Tr}[\gamma_\mu \not{k}\gamma_\nu(\not{q}+\not{k})]|_{k_0=-|\boldsymbol{k}|}}{(q_0-|\boldsymbol{k}|)^2-|\boldsymbol{q}+\boldsymbol{k}|^2+i\epsilon_-}\right),\end{aligned} \tag{D.19}$$

where we define $\epsilon_\pm \equiv {\rm sign}(\pm|k|+q_0)\epsilon$. Alternatively, using the relation[9]

$$\frac{1}{(k+q)^2+i\,{\rm sign}(k_0+q_0)\epsilon} = \int \frac{dk'_0}{2\pi}\frac{\Theta(k'_0)-\Theta(-k'_0)}{k_0+q_0-k'_0+i\epsilon}2\pi\delta(k'^2_0-|\boldsymbol{k}+\boldsymbol{q}|^2)\,, \tag{D.20}$$

it can be written as

$$\Pi^{R,T\neq 0}_{\mu\nu}(q) = n_f g^2 \int \frac{d^3k}{(2\pi)^3}\frac{n_F(|\boldsymbol{k}|)}{2|\boldsymbol{k}+\boldsymbol{q}||\boldsymbol{k}|}\left(\sum_{\sigma_{1,2}=\pm 1}\frac{\sigma_2 {\rm Tr}[\gamma_\mu \not{k}\gamma_\nu(\not{k}+\not{q})]|_{k_0=\sigma_1|\boldsymbol{k}|}}{q_0+\sigma_1|\boldsymbol{k}|+\sigma_2|\boldsymbol{k}+\boldsymbol{q}|+i\epsilon}\right), \tag{D.21}$$

which now contains poles only of first order. In the next step, we evaluate the trace appearing in the numerator,

$$\begin{aligned}T_{\mu\nu} &\equiv {\rm Tr}[\gamma_\mu \not{k}\gamma_\nu(\not{q}+\not{k})] \\ &= 4[k_\mu(q+k)_\nu + k_\nu(q+k)_\mu - g_{\mu\nu}k(q+k)]\,,\end{aligned} \tag{D.22}$$

and in terms of its temporal and spatial components it becomes

$$\begin{aligned}T_{00} &= 4(k_0q_0+k_0^2+|\boldsymbol{k}||\boldsymbol{q}|\cos\theta+|\boldsymbol{k}|^2)\,, \\ T_{ij} &= 4[2k_ik_j+k_iq_j+k_jq_i+\delta_{ij}(k^2+k_0q_0-|\boldsymbol{k}||\boldsymbol{q}|\cos\theta)]\,, \\ T_{\rm trans} &\equiv \frac{1}{2}\left(\delta^{ij}-\frac{q^iq^j}{\boldsymbol{q}^2}\right)T_{ij} \\ &= 4(k_0^2+k_0q_0-|\boldsymbol{k}||\boldsymbol{q}|\cos\theta-\boldsymbol{k}^2\cos^2\theta)\,,\end{aligned} \tag{D.23}$$

[9]Equation (D.20) follows from the relation $S^R(x-y) = \Theta(x_0-y_0)\left[S^>(x-y)-S^<(x-y)\right]$ between the retarded fermionic propagator and the fermionic Wightman functions in coordinate space.

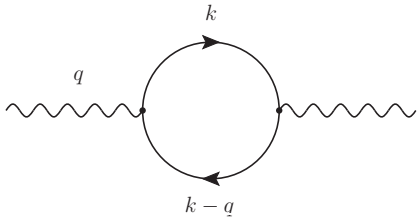

Figure D.2: One-loop self-energy diagram of the dark photon propagator. The polarization tensor is denoted by $\Pi^{\mu\nu}(q)$. Only the n_f dark light fermions run in the loop.

where θ denotes the angle between the momentum vectors $\boldsymbol{q}$ and $\boldsymbol{k}$. The longitudinal component of the thermal retarded polarization tensor in (D.19) reads

$$\begin{aligned}\Pi_{00}^{R,T\neq 0}(q) &= -4n_f g^2 \int \frac{d^3k}{(2\pi)^3}\frac{n_{\rm F}(|\boldsymbol{k}|)}{|\boldsymbol{k}|}\left[\frac{|\boldsymbol{k}|q_0+2\boldsymbol{k}^2+|\boldsymbol{k}||\boldsymbol{q}|\cos\theta}{q_0^2+2q_0|\boldsymbol{k}|-\boldsymbol{q}^2-2|\boldsymbol{k}||\boldsymbol{q}|\cos\theta+i\epsilon_+}\right.\\ &\qquad\left.+\frac{-|\boldsymbol{k}|q_0+2\boldsymbol{k}^2+|\boldsymbol{k}||\boldsymbol{q}|\cos\theta}{q_0^2-2q_0|\boldsymbol{k}|-\boldsymbol{q}^2-2|\boldsymbol{k}||\boldsymbol{q}|\cos\theta+i\epsilon_-}\right]\\ &= n_f\frac{g^2}{\pi^2}\int_0^\infty d|\boldsymbol{k}||\boldsymbol{k}|n_{\rm F}(|\boldsymbol{k}|)\left[\frac{4\boldsymbol{k}^2+q^2+4q_0|\boldsymbol{k}|}{4|\boldsymbol{k}||\boldsymbol{q}|}\ln\left(\frac{q^2+2q_0|\boldsymbol{k}|-2|\boldsymbol{q}||\boldsymbol{k}|+i\epsilon_+}{q^2+2q_0|\boldsymbol{k}|+2|\boldsymbol{q}||\boldsymbol{k}|+i\epsilon_+}\right)\right.\\ &\qquad\left.+\frac{4\boldsymbol{k}^2+q^2-4q_0|\boldsymbol{k}|}{4|\boldsymbol{k}||\boldsymbol{q}|}\ln\left(\frac{q^2-2q_0|\boldsymbol{k}|-2|\boldsymbol{q}||\boldsymbol{k}|+i\epsilon_-}{q^2-2q_0|\boldsymbol{k}|+2|\boldsymbol{q}||\boldsymbol{k}|+i\epsilon_-}\right)+2\right],\end{aligned} \tag{D.24}$$

and the transversal component is

$$\begin{aligned}\Pi_{\rm trans}^{R,T\neq 0}(q) &= -4n_f g^2 \int \frac{d^3k}{(2\pi)^3}\frac{n_{\rm F}(|\boldsymbol{k}|)}{|\boldsymbol{k}|}\left[\frac{\boldsymbol{k}^2+|\boldsymbol{k}|q_0-|\boldsymbol{k}||\boldsymbol{q}|\cos\theta-\boldsymbol{k}^2\cos^2\theta}{q_0^2+2q_0|\boldsymbol{k}|-\boldsymbol{q}^2-2|\boldsymbol{k}||\boldsymbol{q}|\cos\theta+i\epsilon_+}\right.\\ &\qquad\left.+\frac{\boldsymbol{k}^2-|\boldsymbol{k}|q_0-|\boldsymbol{k}||\boldsymbol{q}|\cos\theta-\boldsymbol{k}^2\cos^2\theta}{q_0^2-2q_0|\boldsymbol{k}|-\boldsymbol{q}^2-2|\boldsymbol{k}||\boldsymbol{q}|\cos\theta+i\epsilon_-}\right]\\ &= n_f\frac{g^2}{\pi^2}\int_0^\infty d|\boldsymbol{k}||\boldsymbol{k}|n_{\rm F}(|\boldsymbol{k}|)\left[-\frac{q_0^2+\boldsymbol{q}^2}{\boldsymbol{q}^2}\right.\\ &\quad+\frac{4\boldsymbol{q}^2(\boldsymbol{k}^2+|\boldsymbol{k}|q_0)+\boldsymbol{q}^4-(q_0^2+2q_0|\boldsymbol{k}|)^2}{8|\boldsymbol{k}||\boldsymbol{q}|^3}\ln\left(\frac{q^2+2q_0|\boldsymbol{k}|-2|\boldsymbol{q}||\boldsymbol{k}|+i\epsilon_+}{q^2+2q_0|\boldsymbol{k}|+2|\boldsymbol{q}||\boldsymbol{k}|+i\epsilon_+}\right)\\ &\quad\left.+\frac{4\boldsymbol{q}^2(\boldsymbol{k}^2-|\boldsymbol{k}|q_0)+\boldsymbol{q}^4-(q_0^2-2q_0|\boldsymbol{k}|)^2}{8|\boldsymbol{k}||\boldsymbol{q}|^3}\ln\left(\frac{q^2-2q_0|\boldsymbol{k}|-2|\boldsymbol{q}||\boldsymbol{k}|+i\epsilon_-}{q^2-2q_0|\boldsymbol{k}|+2|\boldsymbol{q}||\boldsymbol{k}|+i\epsilon_-}\right)\right].\end{aligned} \tag{D.25}$$

We split (D.24) and (D.25) into its real and imaginary parts,

$$\begin{aligned}{\rm Re}\left[\Pi_{00}^{R,T\neq 0}(q)\right] &= n_f\frac{g^2}{\pi^2}\int_0^\infty d|\boldsymbol{k}||\boldsymbol{k}|n_{\rm F}(|\boldsymbol{k}|)\left[\frac{4\boldsymbol{k}^2+q^2+4q_0|\boldsymbol{k}|}{4|\boldsymbol{k}||\boldsymbol{q}|}\ln\left|\frac{q^2+2q_0|\boldsymbol{k}|-2|\boldsymbol{q}||\boldsymbol{k}|}{q^2+2q_0|\boldsymbol{k}|+2|\boldsymbol{q}||\boldsymbol{k}|}\right|\right.\\ &\qquad\left.+\frac{4\boldsymbol{k}^2+q^2-4q_0|\boldsymbol{k}|}{4|\boldsymbol{k}||\boldsymbol{q}|}\ln\left|\frac{q^2-2q_0|\boldsymbol{k}|-2|\boldsymbol{q}||\boldsymbol{k}|}{q^2-2q_0|\boldsymbol{k}|+2|\boldsymbol{q}||\boldsymbol{k}|}\right|+2\right],\end{aligned} \tag{D.26}$$

$$\mathrm{Im}\left[\Pi_{00}^{R,T\neq 0}(q)\right] = n_f \frac{g^2}{\pi}\int_0^\infty d|\boldsymbol{k}||\boldsymbol{k}| n_{\mathrm{F}}(|\boldsymbol{k}|) \times\left[\frac{4\boldsymbol{k}^2+q^2+4q_0|\boldsymbol{k}|}{4|\boldsymbol{k}||\boldsymbol{q}|}\,\mathrm{sign}(\epsilon_+)\left[\Theta(2|\boldsymbol{k}|(q_0+|\boldsymbol{q}|)+\boldsymbol{q}^2)-\Theta(2|\boldsymbol{k}|(q_0-|\boldsymbol{q}|)+\boldsymbol{q}^2)\right]\right.$$
$$\left.+\,\frac{4\boldsymbol{k}^2+q^2-4q_0|\boldsymbol{k}|}{4|\boldsymbol{k}||\boldsymbol{q}|}\,\mathrm{sign}(\epsilon_-)\left[\Theta(2|\boldsymbol{k}|(q_0+|\boldsymbol{q}|)-\boldsymbol{q}^2)-\Theta(2|\boldsymbol{k}|(q_0-|\boldsymbol{q}|)-\boldsymbol{q}^2)\right]\right], \tag{D.27}$$

and

$$\mathrm{Re}\left[\Pi_{\mathrm{trans}}^{R,T\neq 0}(q)\right] = n_f \frac{g^2}{\pi^2}\int_0^\infty d|\boldsymbol{k}||\boldsymbol{k}| n_{\mathrm{F}}(|\boldsymbol{k}|)\left[-\frac{q_0^2+\boldsymbol{q}^2}{\boldsymbol{q}^2}\right.$$
$$+\,\frac{4\boldsymbol{q}^2(\boldsymbol{k}^2+|\boldsymbol{k}|q_0)+\boldsymbol{q}^4-(q_0^2+2q_0|\boldsymbol{k}|)^2}{8|\boldsymbol{k}||\boldsymbol{q}|^3}\ln\left|\frac{q^2+2q_0|\boldsymbol{k}|-2|\boldsymbol{q}||\boldsymbol{k}|}{q^2+2q_0|\boldsymbol{k}|+2|\boldsymbol{q}||\boldsymbol{k}|}\right|$$
$$\left.+\,\frac{4\boldsymbol{q}^2(\boldsymbol{k}^2-|\boldsymbol{k}|q_0)+\boldsymbol{q}^4-(q_0^2-2q_0|\boldsymbol{k}|)^2}{8|\boldsymbol{k}||\boldsymbol{q}|^3}\ln\left|\frac{q^2-2q_0|\boldsymbol{k}|-2|\boldsymbol{q}||\boldsymbol{k}|}{q^2-2q_0|\boldsymbol{k}|+2|\boldsymbol{q}||\boldsymbol{k}|}\right|\right], \tag{D.28}$$

$$\mathrm{Im}\left[\Pi_{\mathrm{trans}}^{R,T\neq 0}(q)\right] = n_f \frac{g^2}{\pi}\int_0^\infty d|\boldsymbol{k}||\boldsymbol{k}| n_{\mathrm{F}}(|\boldsymbol{k}|) \times\left[\frac{4\boldsymbol{q}^2(\boldsymbol{k}^2+|\boldsymbol{k}|q_0)+\boldsymbol{q}^4-(q_0^2+2q_0|\boldsymbol{k}|)^2}{8|\boldsymbol{k}||\boldsymbol{q}|^3}\,\mathrm{sign}(\epsilon_+)\right.$$
$$\times\left[\Theta(2|\boldsymbol{k}|(q_0+|\boldsymbol{q}|)+\boldsymbol{q}^2)-\Theta(2|\boldsymbol{k}|(q_0-|\boldsymbol{q}|)+\boldsymbol{q}^2)\right]$$
$$+\,\frac{4\boldsymbol{q}^2(\boldsymbol{k}^2-|\boldsymbol{k}|q_0)+\boldsymbol{q}^4-(q_0^2-2q_0|\boldsymbol{k}|)^2}{8|\boldsymbol{k}||\boldsymbol{q}|^3}\,\mathrm{sign}(\epsilon_-)$$
$$\left.\times\left[\Theta(2|\boldsymbol{k}|(q_0+|\boldsymbol{q}|)-\boldsymbol{q}^2)-\Theta(2|\boldsymbol{k}|(q_0-|\boldsymbol{q}|)-\boldsymbol{q}^2)\right]\right]. \tag{D.29}$$

The advanced polarization tensor can be obtained from the general relations $\mathrm{Re}\left[\Pi_{\mu\nu}^R\right] = \mathrm{Re}\left[\Pi_{\mu\nu}^A\right]$ and $\mathrm{Im}\left[\Pi_{\mu\nu}^R\right] = -\mathrm{Im}\left[\Pi_{\mu\nu}^A\right]$.

D.2.1 Hierarchy $T \sim |\mathbf{q}| \gg q_0$

We take the spatial loop momentum $\boldsymbol{k}$ in the photon self-energy, cf. figure D.2, to be of the order of the temperature T of the thermal bath, because we consider dark light fermions to be the constituents that form the thermal bath. Then for the particular hierarchy $T \sim |\boldsymbol{q}| \gg q_0$, which corresponds to interaction processes involving space-like dark photons, we may expand the eqs. (D.26)–(D.29) for small q_0, resulting in

$$\mathrm{Re}\left[\Pi_{00}^{R,T\neq 0}(q)\right] = n_f \frac{g^2}{\pi^2}\int_0^\infty d|\boldsymbol{k}||\boldsymbol{k}| n_{\mathrm{F}}(|\boldsymbol{k}|)\left[2-\frac{4\boldsymbol{k}^2-\boldsymbol{q}^2}{2|\boldsymbol{k}||\boldsymbol{q}|}\ln\left|\frac{|\boldsymbol{q}|-2|\boldsymbol{k}|}{|\boldsymbol{q}|+2|\boldsymbol{k}|}\right|\right], \tag{D.30}$$

$$\mathrm{Im}\left[\Pi_{00}^{R,T\neq 0}(q)\right] = 2n_f \frac{g^2}{\pi}\frac{q_0}{|\boldsymbol{q}|}\int_{|\boldsymbol{q}|/2}^\infty d|\boldsymbol{k}||\boldsymbol{k}| n_{\mathrm{F}}(|\boldsymbol{k}|), \tag{D.31}$$

$$\mathrm{Re}\left[\Pi^{R,T\neq 0}_{\mathrm{trans}}(q)\right] = n_f \frac{g^2}{\pi^2}\int_0^\infty d|\boldsymbol{k}||\boldsymbol{k}| n_{\mathrm{F}}(|\boldsymbol{k}|)\left[\frac{4\boldsymbol{k}^2+\boldsymbol{q}^2}{4|\boldsymbol{k}||\boldsymbol{q}|}\ln\left|\frac{|\boldsymbol{q}|-2|\boldsymbol{k}|}{|\boldsymbol{q}|+2|\boldsymbol{k}|}\right|-1\right], \tag{D.32}$$

$$\mathrm{Im}\left[\Pi^{R,T\neq 0}_{\mathrm{trans}}(q)\right] = n_f \frac{g^2}{\pi}\frac{q_0}{|\boldsymbol{q}|}\int_{|\boldsymbol{q}/2}^\infty d|\boldsymbol{k}||\boldsymbol{k}| n_{\mathrm{F}}(|\boldsymbol{k}|)\,. \tag{D.33}$$

The eqs. (D.30) and (D.31) are in agreement with the abelian versions of the expressions in [130, 150]. The thermal longitudinal symmetric polarization tensor then is

$$\begin{aligned}\Pi^{S,T\neq 0}_{00}(q) &= [1+2n_{\mathrm{B}}(q_0)]\left[\Pi^{R,T\neq 0}_{00}(q)-\Pi^{A,T\neq 0}_{00}(q)\right] = 2i[1+2n_{\mathrm{B}}(q_0)]\mathrm{Im}\left[\Pi^{R,T\neq 0}_{00}(q)\right]\\ &= 8in_f\frac{g^2}{\pi}\frac{T}{|\boldsymbol{q}|}\int_{|\boldsymbol{q}/2}^\infty d|\boldsymbol{k}||\boldsymbol{k}| n_{\mathrm{F}}(|\boldsymbol{k}|) = 2\Pi^{S,T\neq 0}_{\mathrm{trans}}(q)\,,\end{aligned} \tag{D.34}$$

where we expanded the Bose–Einstein distribution up to leading order in q_0/T, i.e. $n_{\mathrm{B}}(q_0) = T/q_0 + \dots$, and the second equality in the second line of (D.34) shows the relation between the longitudinal and transverse part.

D.2.2 Hierarchy $T \gg q_0, |\mathbf{q}|$

If the absolute value of the spatial momentum vector $\boldsymbol{q}$ is of the same order as q_0, we can expand the integrands in (D.26)–(D.29) both in $|\boldsymbol{q}|$ and q_0, and perform the integration over the loop momentum $|\boldsymbol{k}|$. The analytic results are

$$\mathrm{Re}\left[\Pi^{R,T\neq 0}_{00}(q)\right] = m_{\mathrm{D}}^2\left[1+\frac{q_0}{2|\boldsymbol{q}|}\ln\left|\frac{q_0-|\boldsymbol{q}|}{q_0+|\boldsymbol{q}|}\right|\right], \tag{D.35}$$

$$\mathrm{Im}\left[\Pi^{R,T\neq 0}_{00}(q)\right] = m_{\mathrm{D}}^2\frac{\pi q_0}{2|\boldsymbol{q}|}\Theta(-q^2)\,, \tag{D.36}$$

$$\mathrm{Re}\left[\Pi^{R,T\neq 0}_{\mathrm{trans}}(q)\right] = -m_{\mathrm{D}}^2\frac{q_0^2}{2\boldsymbol{q}^2}\left[1-\frac{q_0}{2|\boldsymbol{q}|}\left(1-\frac{\boldsymbol{q}^2}{q_0^2}\right)\ln\left|\frac{q_0+|\boldsymbol{q}|}{q_0-|\boldsymbol{q}|}\right|\right], \tag{D.37}$$

$$\mathrm{Im}\left[\Pi^{R,T\neq 0}_{\mathrm{trans}}(q)\right] = -m_{\mathrm{D}}^2\frac{\pi q_0^3}{4|\boldsymbol{q}|^3}\left(1-\frac{\boldsymbol{q}^2}{q_0^2}\right)\Theta(-q^2)\,, \tag{D.38}$$

where we computed the integral $\int_0^\infty d|\boldsymbol{k}||\boldsymbol{k}| n_{\mathrm{F}}(|\boldsymbol{k}|) = \pi^2T^2/(12)$, and introduced the *Debye* mass

$$m_{\mathrm{D}} = \sqrt{\frac{n_f}{3}g^2T^2} = \sqrt{\frac{4\pi}{3}n_f\alpha}\;T\,, \tag{D.39}$$

which depends on the coupling α, the temperature T and the total number n_f of massless dark particles. The thermal retarded polarization tensor develops an imaginary part only for space-like dark photons, where $q^2 < 0$. The results are in agreement with the abelian analogues in refs. [129, 130, 150, 206]. Finally, we give the analytic expressions for the longitudinal and transversal symmetric polarization tensors:

$$\Pi^{S,T\neq 0}_{00}(q) = 2i\pi m_{\mathrm{D}}^2\frac{T}{|\boldsymbol{q}|}\Theta(-q^2)\,, \tag{D.40}$$

$$\Pi^{S,T\neq 0}_{\mathrm{trans}}(q) = -i\pi m_{\mathrm{D}}^2\frac{Tq_0^2}{|\boldsymbol{q}|^3}\left(1-\frac{\boldsymbol{q}^2}{q_0^2}\right)\Theta(-q^2)\,. \tag{D.41}$$

D.2.3 Hierarchy $T \gg |\mathbf{q}| \gg q_0$

The hierarchy $T \gg |\mathbf{q}| \gg q_0$ is a special case of the one considered in section D.2.2, therefore we expand the expressions in (D.35)–(D.38) up to first order in $q_0 \ll |\boldsymbol{q}|$,

$$\begin{aligned}
\mathrm{Re}\left[\Pi_{00}^{R,T\neq 0}(q)\right] &= m_{\mathrm{D}}^2\,, && \text{(D.42)}\\
\mathrm{Re}\left[\Pi_{\mathrm{trans}}^{R,T\neq 0}(q)\right] &= m_{\mathrm{D}}^2 \times \mathcal{O}\left(\frac{q_0^2}{\boldsymbol{q}^2}\right)\,, && \text{(D.43)}\\
\mathrm{Im}\left[\Pi_{00}^{R,T\neq 0}(q)\right] &= m_{\mathrm{D}}^2 \frac{\pi q_0}{2|\boldsymbol{q}|}\,, && \text{(D.44)}\\
\mathrm{Im}\left[\Pi_{\mathrm{trans}}^{R,T\neq 0}(q)\right] &= m_{\mathrm{D}}^2 \frac{\pi q_0}{4|\boldsymbol{q}|}\,. && \text{(D.45)}
\end{aligned}$$

If the momentum $|\boldsymbol{q}|$ of the dark photon is of the order of the Debye mass, $T \gg |\boldsymbol{q}| \sim m_{\mathrm{D}} \gg q_0$, then the thermal loop corrections contributing to the dark photon propagator need to be resummed, which is known as the *Hard Thermal Loop* (HTL) resummation. For the particular hierarchy considered in this section, after performing the resummation which leads to the *dressed* propagators written in eqs. (D.11) and (D.12), we obtain for the longitudinal part

$$D_{00}^{R/A}(q) = \frac{i}{\boldsymbol{q}^2 + m_{\mathrm{D}}^2 \pm i m_{\mathrm{D}}^2 \frac{\pi q_0}{2|\boldsymbol{q}|}} = \frac{i}{\boldsymbol{q}^2 + m_{\mathrm{D}}^2} \pm \frac{\pi}{2}\frac{q_0}{|\boldsymbol{q}|}\frac{m_{\mathrm{D}}^2}{(\boldsymbol{q}^2 + m_{\mathrm{D}}^2)^2} + \mathcal{O}\left(\frac{q_0^2}{\boldsymbol{q}^2}\right)\,, \quad \text{(D.46)}$$

and for the transverse part

$$\begin{aligned}
D_{ij}^{R/A}(q) &= \left(\delta_{ij} - \frac{q_i q_j}{\boldsymbol{q}^2}\right) \frac{i}{(q_0 \pm i\epsilon)^2 - \boldsymbol{q}^2 \pm i m_{\mathrm{D}}^2 \frac{\pi q_0}{4|\boldsymbol{q}|}}\\
&= \left(\delta_{ij} - \frac{q_i q_j}{\boldsymbol{q}^2}\right) \left[\frac{i}{(q_0 \pm i\epsilon)^2 - \boldsymbol{q}^2} \pm \frac{\pi}{4}\frac{q_0}{|\boldsymbol{q}|}\frac{m_{\mathrm{D}}^2}{((q_0 \pm i\epsilon)^2 - \boldsymbol{q}^2)^2} + \mathcal{O}\left(\frac{q_0^2}{\boldsymbol{q}^2}\right)\right]\,. \quad \text{(D.47)}
\end{aligned}$$

In fact it turns out that, by comparing (D.46) with (D.47), only the longitudinal part gets dressed by the Debye mass, which removes the infrared divergence for $\boldsymbol{q}^2 \to 0$ at finite T, hence justifying the screening property of m_{D}. On the contrary, the spatial part in (D.47), upon expanding up to zeroth order in $q_0/|\boldsymbol{q}|$, reduces to the familiar leading-order expression in (D.9).

Then, using the relations in eq. (D.3) and in eqs. (D.6)–(D.7), the resummed longitudinal dark photon propagator becomes

$$D_{00}(q) = \frac{i}{\boldsymbol{q}^2 + m_{\mathrm{D}}^2}\begin{pmatrix}1 & 0\\ 0 & -1\end{pmatrix} + \pi\frac{T}{|\boldsymbol{q}|}\frac{m_{\mathrm{D}}^2}{(\boldsymbol{q}^2 + m_{\mathrm{D}}^2)^2}\begin{pmatrix}1 & 1\\ 1 & 1\end{pmatrix}\,, \quad \text{(D.48)}$$

and the resummed longitudinal symmetric propagator reads

$$D_{00}^{S}(q) = \frac{-i\Pi_{00}^{S}(q)}{(\boldsymbol{q}^2 + \Pi_{00}^{R}(q))(\boldsymbol{q}^2 + \Pi_{00}^{A}(q))} = 2\pi\frac{T}{|\boldsymbol{q}|}\frac{m_{\mathrm{D}}^2}{(\boldsymbol{q}^2 + m_{\mathrm{D}}^2)^2}\,. \quad \text{(D.49)}$$

On the other hand, for the less strict hierarchy considered in section D.2.2, if the dark photon energy q_0 is of the order of the Debye mass, such that $q_0, |\boldsymbol{q}| \sim m_{\rm D}$, both the longitudinal and transversal polarization tensors in (D.35)–(D.38) need to be resummed and one obtains

$$\begin{aligned} D_{00}^{R/A}(q) &= \frac{i}{\boldsymbol{q}^2 + m_{\rm D}^2 \left[1 + \frac{q_0}{2|\boldsymbol{q}|} \ln \left| \frac{q_0 - |\boldsymbol{q}|}{q_0 + |q|} \right| \right] \pm i\pi m_{\rm D}^2 \frac{q_0}{2|\boldsymbol{q}|} \Theta(-q^2)} \\ &= \frac{i}{\boldsymbol{q}^2 + m_{\rm D}^2 \left[1 + \frac{q_0}{2|\boldsymbol{q}|} \ln \left(\frac{q_0 - |\boldsymbol{q}| \pm i\epsilon}{q_0 + |\boldsymbol{q}| \pm i\epsilon} \right) \right]} \,, \end{aligned} \tag{D.50}$$

and

$$\begin{aligned} & D_{ij}^{R/A}(q) \\ &= \frac{i \left(\delta_{ij} - \frac{q_i q_j}{\boldsymbol{q}^2} \right)}{(q_0 \pm i\epsilon)^2 - \boldsymbol{q}^2 - m_{\rm D}^2 \frac{q_0^2}{2\boldsymbol{q}^2} \left[1 - \frac{q_0}{2|\boldsymbol{q}|} \left(1 - \frac{\boldsymbol{q}^2}{q_0^2} \right) \ln \left| \frac{q_0 + |\boldsymbol{q}|}{q_0 - |\boldsymbol{q}|} \right| \right] \mp i\pi m_{\rm D}^2 \frac{q_0^3}{4|\boldsymbol{q}|^3} \left(1 - \frac{\boldsymbol{q}^2}{q_0^2} \right) \Theta(-q^2)} \\ &= \left(\delta_{ij} - \frac{q_i q_j}{\boldsymbol{q}^2} \right) \frac{i}{q^2 \pm i\,\mathrm{sign}(q_0)\epsilon - \frac{m_{\rm D}^2}{2} \left[\frac{q_0^2}{\boldsymbol{q}^2} - \frac{q_0}{2|\boldsymbol{q}|^3} q^2 \ln \left(\frac{q_0 + |\boldsymbol{q}| \pm i\epsilon}{q_0 - |\boldsymbol{q}| \pm i\epsilon} \right) \right]} \,, \end{aligned} \tag{D.51}$$

from which one may compute the dressed symmetric propagator and, eventually, the full matrix-valued dark photon two-point function.[10]

[10] We remind that, according to (D.7), one can deduce that $D_{\mu\nu}^S(q) = [1 + 2n_{\rm B}(q_0)]\,[D_{\mu\nu}^R(q) - D_{\mu\nu}^A(q)]$.

Appendix E

Heavy two-pair system in OQS: dipole exchange diagrams

In this section, we address the impact of the *dipole exchange* diagrams, which connect a heavy particle-antiparticle pair (system I) with another heavy pair (system II) by an exchange of a dark photon via dipole interactions, on the evolution of the single-heavy pair reduced density $\rho_{\rm I}$ in the open quantum system (OQS) formalism. It follows up the discussion at the end of section 12.2, and underpins the arguments provided there with some concrete calculations. We consider a subset of the dipole exchange diagrams given in figure E.1, where only the electric dipole interactions are shown, and denote the four diagrams by $\mathcal{D}_1^{ee}$, $\mathcal{D}_2^{ee}$, $\mathcal{D}_3^{ee}$ and $\mathcal{D}_4^{ee}$, respectively.[1]

In the center-of-mass frame, neglecting the thermal bath motion, they are given by[2]

$$\begin{aligned}
\mathcal{D}_1^{ee} &= (ig)^2 \int_{t_0}^{t} dt_1 \; e^{-iH_{\rm I}(t-t_1)} r_{\rm I}^i e^{-iH_{\rm I}(t_1-t_0)} \rho_{\rm I}(t_0) e^{iH_{\rm I}(t-t_0)} \\
&\qquad \times \int_{t_0}^{t} dt_2 \; e^{-iH_{\rm II}(t-t_2)} r_{\rm II}^j e^{-iH_{\rm II}(t_2-t_0)} \rho_{\rm II}(t_0) e^{iH_{\rm II}(t-t_0)} \langle E_{\rm I}^i(t_1,\mathbf{0}) E_{\rm II}^j(t_2,\mathbf{0})\rangle_{11} \\
&\equiv -g^2 \int_{t_0}^{t} dt_1 \int_{t_0}^{t} dt_2 \; \mathcal{I}_{\rm I}(t,t_1,t_0,r_{\rm I}^i) \mathcal{I}_{\rm II}(t,t_2,t_0,r_{\rm II}^j) \langle E_{\rm I}^i(t_1) E_{\rm II}^j(t_2)\rangle_{11} \,, \qquad \text{(E.1)} \\
\mathcal{D}_2^{ee} &= (-ig)ig \int_{t_0}^{t} dt_1 \; e^{-iH_{\rm I}(t-t_0)} \rho_{\rm I}(t_0) e^{iH_{\rm I}(t_1-t_0)} r_{\rm I}^i e^{iH_{\rm I}(t-t_1)} \\
&\qquad \times \int_{t_0}^{t} dt_2 \; e^{-iH_{\rm II}(t-t_2)} r_{\rm II}^j e^{-iH_{\rm II}(t_2-t_0)} \rho_{\rm II}(t_0) e^{iH_{\rm II}(t-t_0)} \langle E_{\rm I}^i(t_1,\mathbf{0}) E_{\rm II}^j(t_2,\mathbf{0})\rangle_{21} \\
&\equiv g^2 \int_{t_0}^{t} dt_1 \int_{t_0}^{t} dt_2 \; \mathcal{I}_{\rm I}^\dagger(t,t_1,t_0,r_{\rm I}^i) \mathcal{I}_{\rm II}(t,t_2,t_0,r_{\rm II}^j) \langle E_{\rm I}^i(t_1) E_{\rm II}^j(t_2)\rangle_{21} \,, \qquad \text{(E.2)}
\end{aligned}$$

[1] The other set of diagrams, at order $\boldsymbol{r}^2$, includes exchanges between system I and system II through magnetic dipole interactions, cf. the Röntgen vertex in fig. 4.1 right, but also mixed exchanges between an electric and magnetic vertex.

[2] We adopt the notation used in the main body of this work, where the subscript I (II) denotes that the operators are with respect to system I (II).

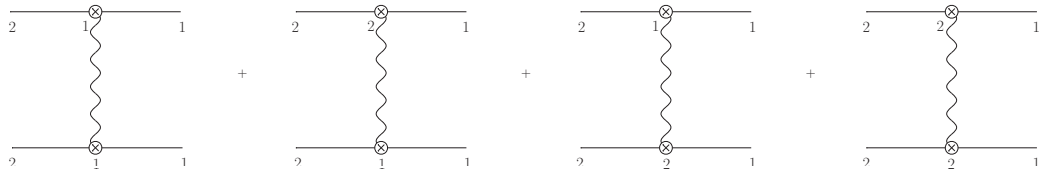

Figure E.1: Electric dipole exchange diagrams between a heavy DM pair (system I), the upper solid lines, and another heavy DM pair (system II), corresponding to the lower solid lines. The CTP-indices 1 or 2 denote that the fields and vertices are either along the temporal path $\mathcal{C}_1$ or $\mathcal{C}_2$, cf. figure D.1 for the Schwinger-Keldysh contour.

$$\begin{aligned}\mathcal{D}_3^{ee} &= ig(-ig)\int_{t_0}^{t} dt_1\; e^{-iH_{\rm I}(t-t_1)} r_{\rm I}^i e^{-iH_{\rm I}(t_1-t_0)} \rho_{\rm I}(t_0) e^{iH_{\rm I}(t-t_0)} \\ &\quad\times \int_{t_0}^{t} dt_2\; e^{-iH_{\rm II}(t-t_0)} \rho_{\rm II}(t_0) e^{iH_{\rm II}(t_2-t_0)} r_{\rm II}^j e^{iH_{\rm II}(t-t_2)} \langle E_{\rm I}^i(t_1,\mathbf{0}) E_{\rm II}^j(t_2,\mathbf{0})\rangle_{12} \\ &\equiv g^2 \int_{t_0}^{t} dt_1 \int_{t_0}^{t} dt_2\; \mathcal{I}_{\rm I}(t,t_1,t_0,r_{\rm I}^i) \mathcal{I}_{\rm II}^\dagger(t,t_2,t_0,r_{\rm II}^j) \langle E_{\rm I}^i(t_1) E_{\rm II}^j(t_2)\rangle_{12}\,, \end{aligned} \tag{E.3}$$

and

$$\begin{aligned}\mathcal{D}_4^{ee} &= (-ig)^2\int_{t_0}^{t} dt_1\; e^{-iH_{\rm I}(t-t_0)} \rho_{\rm I}(t_0) e^{iH_{\rm I}(t_1-t_0)} r_{\rm I}^i e^{iH_{\rm I}(t-t_1)} \\ &\quad\times \int_{t_0}^{t} dt_2\; e^{-iH_{\rm II}(t-t_0)} \rho_{\rm II}(t_0) e^{iH_{\rm II}(t_2-t_0)} r_{\rm II}^j e^{iH_{\rm II}(t-t_2)} \langle E_{\rm I}^i(t_1,\mathbf{0}) E_{\rm II}^j(t_2,\mathbf{0})\rangle_{22} \\ &\equiv -g^2 \int_{t_0}^{t} dt_1 \int_{t_0}^{t} dt_2\; \mathcal{I}_{\rm I}^\dagger(t,t_1,t_0,r_{\rm I}^i) \mathcal{I}_{\rm II}^\dagger(t,t_2,t_0,r_{\rm II}^j) \langle E_{\rm I}^i(t_1) E_{\rm II}^j(t_2)\rangle_{22}\,. \end{aligned} \tag{E.4}$$

Using a relation among the four dark photon propagators in the Schwinger-Keldysh formalism,[3] it follows for the electric-electric correlators that

$$\langle E^i E^j\rangle_{11} = \langle E^i E^j\rangle_{12} + \langle E^i E^j\rangle_{21} - \langle E^i E^j\rangle_{22}\,, \tag{E.5}$$

such that the sum of the four terms in (E.1)–(E.4) can be written as

$$\begin{aligned}\mathcal{D}_1^{ee} + \mathcal{D}_2^{ee} + \mathcal{D}_3^{ee} + \mathcal{D}_4^{ee} &= -g^2 \int_{t_0}^{t} dt_1 \int_{t_0}^{t} dt_2 \Big[\mathcal{I}_{\rm I}^i \left(\mathcal{I}_{\rm II}^j - \mathcal{I}_{\rm II}^{j,\dagger}\right) \langle E_{\rm I}^i(t_1) E_{\rm II}^j(t_2)\rangle_{12} \\ &\quad + \left(\mathcal{I}_{\rm I}^i - \mathcal{I}_{\rm I}^{i,\dagger}\right) \mathcal{I}_{\rm II}^j \langle E_{\rm I}^i(t_1) E_{\rm II}^j(t_2)\rangle_{21} - \left(\mathcal{I}_{\rm I}^i \mathcal{I}_{\rm II}^j - \mathcal{I}_{\rm I}^{i,\dagger} \mathcal{I}_{\rm II}^{j,\dagger}\right) \langle E_{\rm I}^i(t_1) E_{\rm II}^j(t_2)\rangle_{22}\Big]\,. \end{aligned} \tag{E.6}$$

[3] In the closed-time-path formalism, the time-ordered photon propagator can be split into a combination of the anti-time ordered propagator and the Wightman functions as follows, here in momentum space,

$$D_{11}^{\mu\nu}(q) = D_{12}^{\mu\nu}(q) + D_{21}^{\mu\nu}(q) - D_{22}^{\mu\nu}(q)\,,$$

which can be straightforwardly shown to be valid for the propagators at leading order given in eqs. (D.4) and (D.5).

The first two terms in eq. (E.6), which contain the factors $\mathcal{I}^j_{\rm II} - \mathcal{I}^{j,\dagger}_{\rm II} = 2i\,{\rm Im}\left[\mathcal{I}^j_{\rm II}\right]$ and $\mathcal{I}^i_{\rm I} - \mathcal{I}^{i,\dagger}_{\rm I} = 2i\,{\rm Im}\left[\mathcal{I}^i_{\rm I}\right]$, respectively, can be shown to vanish. We proof it for the first term:[4]

$$\begin{aligned}
{\rm Im}\left[\mathcal{I}^j_{\rm II}\right] &= {\rm Im}\left[e^{-iH_{\rm II}(t-t_2)} r^j_{\rm II} e^{-iH_{\rm II}(t_2-t_0)} \rho_{\rm II}(t_0) e^{iH_{\rm II}(t-t_0)}\right] \\
&= {\rm Im}\left[e^{-iH_{\rm II}(t-t_2)} r^j_{\rm II} e^{-iH_{\rm II}(t_2-t_0)} e^{iH_{\rm II}(t-t_0)} e^{-iH_{\rm II}(t-t_0)} \rho_{\rm II}(t_0) e^{iH_{\rm II}(t-t_0)}\right] \\
&= {\rm Im}\left[e^{-iH_{\rm II}(t-t_2)} r^j_{\rm II} e^{iH_{\rm II}(t-t_2)} \rho_{\rm II}(t)\right] \\
&= {\rm Im}\left[\left(r^j_{\rm II} - \frac{2p^j_{\rm II}}{M}(t-t_2)\right)\rho_{\rm II}(t)\right] = 0\,,
\end{aligned} \tag{E.7}$$

where in the third line we used $\rho_{\rm II}(t,t) = e^{-iH_{\rm II}(t-t_0)}\rho_{\rm II}(t_0,t_0)e^{iH_{\rm II}(t-t_0)}$, which is exact within the accuracy of order r^2. New terms arise at $\mathcal{O}(r^4)$, hence are beyond the dipole approximation [153]. All operators in the last line of (E.7) are hermitian, hence the imaginary part is zero. A similar computation gives ${\rm Im}\left[\mathcal{I}^i_{\rm I}\right] = 0$.

Concerning the last term in eq. (E.6), we will show that it vanishes once the partial trace over system II has been done, since we are eventually interested to proof that the mixed diagrams in fig. E.1 do not contribute to the evolution equation for the reduced density $\rho_{\rm I}$ of system I. Taking the partial trace of $\mathcal{I}^j_{\rm II}$, we obtain

$$\begin{aligned}
{\rm Tr}_{\rm II}\left[\mathcal{I}^j_{\rm II}\right] &= {\rm Tr}_{\rm II}\left[e^{-iH_{\rm II}(t-t_2)} r^j_{\rm II} e^{-iH_{\rm II}(t_2-t_0)} \rho_{\rm II}(t_0) e^{iH_{\rm II}(t-t_0)}\right] \\
&= {\rm Tr}_{\rm II}\left[r^j_{\rm II} e^{-iH_{\rm II}(t_2-t_0)} \rho_{\rm II}(t_0) e^{iH_{\rm II}(t-t_0)} e^{-iH_{\rm II}(t-t_2)}\right] \\
&= {\rm Tr}_{\rm II}\left[r^j_{\rm II} e^{-iH_{\rm II}(t_2-t_0)} \rho_{\rm II}(t_0) e^{iH_{\rm II}(t_2-t_0)}\right] \\
&= {\rm Tr}_{\rm II}\left[r^j_{\rm II}\rho_{\rm II}(t_2)\right]\,,
\end{aligned} \tag{E.8}$$

where in the second line we used the cyclicity of the trace. Following the same steps as in (E.8), but now for $\mathcal{I}^{j,\dagger}_{\rm II}$, we obtain

$${\rm Tr}_{\rm II}\left[\mathcal{I}^{j,\dagger}_{\rm II}\right] = {\rm Tr}_{\rm II}\left[r^j_{\rm II}\rho_{\rm II}(t_2)\right] = {\rm Tr}_{\rm II}\left[\mathcal{I}^j_{\rm II}\right]\,. \tag{E.9}$$

Therefore, when taking the partial trace of the sum of the exchange diagrams, eq. (E.6), over system II, we end up with the temporal integrals of the residual term

$$\begin{aligned}
&g^2\left(\mathcal{I}^i_{\rm I} - \mathcal{I}^{i,\dagger}_{\rm I}\right){\rm Tr}_{\rm II}\left[\mathcal{I}^j_{\rm II}\right]\langle E^i_{\rm I}(t_1)E^j_{\rm II}(t_2)\rangle_{22} \\
&= 2ig^2\,{\rm Im}\left[\mathcal{I}^i_{\rm I}\right]{\rm Tr}_{\rm II}\left[\mathcal{I}^j_{\rm II}\right]\langle E^i_{\rm I}(t_1)E^j_{\rm II}(t_2)\rangle_{22} = 0\,,
\end{aligned} \tag{E.10}$$

[4] In order to get from the third to the fourth line in eq. (E.7), we use

$$\begin{aligned}
e^{-iH_{\rm II}(t-t_2)} r^j_{\rm II} &= \left[e^{-iH_{\rm II}(t-t_2)}, r^j_{\rm II}\right] + r^j_{\rm II} e^{-iH_{\rm II}(t-t_2)} = -i\frac{\partial}{\partial p^j_{\rm II}}\left(e^{-iH_{\rm II}(t-t_2)}\right) + r^j_{\rm II} e^{-iH_{\rm II}(t-t_2)} \\
&= \left(r^j_{\rm II} - \frac{2p^j_{\rm II}}{M}(t-t_2)\right) e^{-iH_{\rm II}(t-t_2)}\,.
\end{aligned}$$

and hence we conclude with our statement that the dipole exchange diagrams decouple from system I, once we take the partial trace over system II, i.e.

$$\mathrm{Tr}_{\mathrm{II}}\left[\mathcal{D}_1^{ee} + \mathcal{D}_2^{ee} + \mathcal{D}_3^{ee} + \mathcal{D}_4^{ee}\right] = 0\,. \tag{E.11}$$

We expect the results shown in this section, that were derived in the center-of-mass frame without recoil effects, to be valid also when the motion of the thermal bath is included.

Appendix F

Annihilations: alternative viewpoint

Throughout the main body of this work, the observables have been computed by means of the the optical theorem, where the information about a specific scattering process can be extracted from the imaginary part of the corresponding forward scattering amplitude. In QFTs, it is closely connected to the sum of all possible Feynman diagrams that emerge due the cutting through internal propagators on the basis of the Cutkosky rules and the extended rules appropriate for diagrams in the real-time field theory [126, 207]. In this appendix, however, we aim to provide a different point of view on how to compute the interaction rates without the usage of the EFT-framework. We focus on annihilation processes in the $\mathrm{U}(1)_{\mathrm{DM}}$ model only, and compute the corresponding free annihilation cross section in section F.1, and in section F.2 we show how the Sommerfeld effect can be tackled by means of the Bethe–Salpeter approach [208]; it should serve as an alternative to the EFT techniques scrutinized in e.g. chapter 5.

F.1 Free annihilations in $\mathrm{QED}_{\mathrm{DM}}$

In section 5.1, we inferred the dark matter pair annihilations in the non-relativistic limit from the matching coefficients of the irrelevant four-fermion operators in $\mathrm{NRQED}_{\mathrm{DM}}$, which at leading order in the coupling encode the diagrams in fig. 5.1. But we can compute the annihilation cross section also directly, using the Feynman rules from the parent $\mathrm{U}(1)_{\mathrm{DM}}$ model. From Fermi's golden rule generalized to QFTs, we have for the annihilation into two dark photons $X + \bar{X} \to \gamma\gamma$[1]

$$d\sigma_{\mathrm{ann}} = \frac{1}{2}\frac{d^3k_1}{(2\pi)^3 2k_1^0}\frac{d^3k_2}{(2\pi)^3 2k_2^0}\frac{(2\pi)^4\delta^4(k_1+k_2-p_1-p_2)}{4\sqrt{(p_1p_2)^2-M^4}}|\mathcal{M}_{\mathrm{ann}}|^2\,, \tag{F.1}$$

where $\mathcal{M}_{\mathrm{ann}}$ is the dimensionless annihilation S-matrix amplitude and in the center-of-mass frame the incoming DM momenta are $p^\mu_{1/2} = (E, \pm\boldsymbol{p})$, with $E = \sqrt{M^2+\boldsymbol{p}^2}$ and

[1] In this section, we put $n_f = 0$ and consider only annihilations at leading order in α for simplicity.

$\boldsymbol{p} = (\boldsymbol{p}_1 - \boldsymbol{p}_2)/2$; the outgoing photon momenta are $k^\mu_{1/2} = (E, \pm\boldsymbol{k})$, and $|\boldsymbol{k}| = E$ due to energy-momentum conservation. The differential annihilation cross section then reads

$$\frac{d\sigma_{\rm ann}}{d\Omega} = \frac{|\mathcal{M}_{\rm ann}|^2}{512\pi^2 E|\boldsymbol{p}|} = \frac{\alpha^2}{16E|\boldsymbol{p}|}\left[\frac{3M^2 + \boldsymbol{p}^2(3+\cos^2\theta)}{M^2 + \boldsymbol{p}^2\sin^2\theta} - \left(\frac{M^2 - \boldsymbol{p}^2\sin^2\theta}{M^2 + \boldsymbol{p}^2\sin^2\theta}\right)^2\right] . \quad \text{(F.2)}$$

In the non-relativistic limit, upon expanding the terms in the square bracket in (F.2) up to first order in $\boldsymbol{p}^2/M^2$, we get $[\dots] \approx 2 + 4\boldsymbol{p}^2/M^2 = 2 + v_{\rm rel}^2$, where $p \equiv |\boldsymbol{p}| = Mv_{\rm rel}/2$. We expand also the energy up to first order, $E \approx M + \boldsymbol{p}^2/(2M) = M(1 + v_{\rm rel}^2/8)$. In this limit, the dependence on the scattering angles vanishes in (F.2), hence the angular integration can be done straightforwardly and the annihilation cross section up to $\mathcal{O}(\alpha^2, v_{\rm rel}^2)$ reads

$$\sigma^{\rm NR}_{\rm ann} v_{\rm rel} = \frac{\pi\alpha^2}{M^2}\left(1 + \frac{3}{8}v_{\rm rel}^2\right) . \quad \text{(F.3)}$$

We should get this result from the dimension eight four-fermion operators, with matching coefficients at order α^2, in the NRQED$_{\rm DM}$ model as well. We can take a different path, and use the result we obtained for the annihilation cross section, up to order $1/M^4$, in the pNRQED$_{\rm DM}$ theory, cf. (5.22), where we take the scattering wavefunction of the pair to be the one of a plane wave in the center-of-mass frame, i.e. $\psi_{\boldsymbol{p}}(\boldsymbol{r}) = \exp(i\boldsymbol{p}\cdot\boldsymbol{r})$, and hence discard the Sommerfeld effect, since $|\psi_{\boldsymbol{p}}(\boldsymbol{0})|^2 = 1$.[2] We obtain

$$(\sigma^{\rm NR}_{\rm ann} v_{\rm Møl})_{\rm cm} = \frac{\pi\alpha^2}{M^2} + \frac{\boldsymbol{p}^2}{3M^4}(3\pi\alpha^2 + 4\pi\alpha^2) + \frac{\boldsymbol{p}^2}{M^4}\left(-\frac{4}{3}\pi\alpha^2\right) = \frac{\pi\alpha^2}{M^2}\left(1 + \frac{\boldsymbol{p}^2}{M^2}\right) . \quad \text{(F.4)}$$

We finally insert the Møller velocity in the center-of-mass frame, written in eq. (5.8), into the left-hand side of (F.4), expand up to order $v_{\rm rel}^2$ and hereby verify that the result (F.3) from a direct computation in the parent QED$_{\rm DM}$ model agrees with the free annihilation cross section (F.4) in the lower EFT, that is a sum of S- and P-wave annihilations. We can go in a similar manner to higher order in the coupling $\alpha = \alpha(2M)$ and consider processes with more than two dark photon productions, or include non-relativistic corrections of higher order than $v_{\rm rel}^2$, or compute the cross section with respect to another reference frame. However, we will not be able to encounter the Sommerfeld effect. Despite the weak coupling α, it is a non-perturbative effect, where the perpetual t-channel soft-photon exchanges between the fermion and antifermion prior to its annihilation are enhanced if the pair is close to threshold. At this point one needs to resum the infinitely many *ladder* diagrams, which is not feasible in standard perturbation theory. In pNRQED$_{\rm DM}$, cf. section 4.2, the resummation is done at the Lagrangian level due to a multipole expansion of the soft dark photon fields, which in turn leads to a distortion of the plane wave function into a Coulombic scattering-state wavefunction (C.4), together with the emergence of bound-state configurations. In the next section, we pursue instead the resummation of the ladder diagrams at the diagrammatic level.

[2] The gradient and Laplace operator acting on a plane wave are $\boldsymbol{\nabla}_{\boldsymbol{r}}\psi^{(*)}_{\boldsymbol{p}}(\boldsymbol{r}) = \pm i\boldsymbol{p}\psi^{(*)}_{\boldsymbol{p}}(\boldsymbol{r})$ and $\boldsymbol{\Delta}_{\boldsymbol{r}}\psi^{(*)}_{\boldsymbol{p}}(\boldsymbol{r}) = -\boldsymbol{p}^2\psi^{(*)}_{\boldsymbol{p}}(\boldsymbol{r})$, respectively. Eq. (5.22) reduces to the result in the center-of-mass frame, once we set $\boldsymbol{P} = \boldsymbol{0}$.

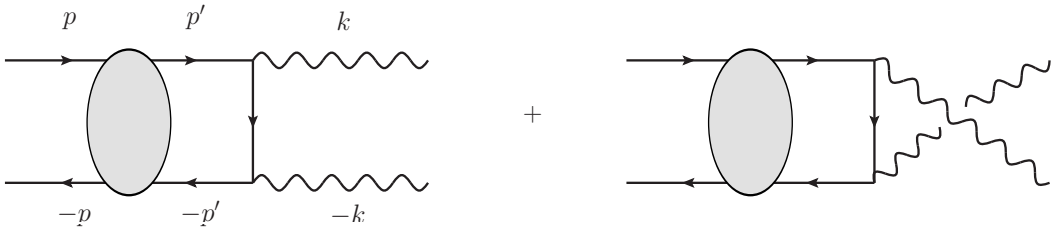

Figure F.1: Annihilation of a heavy fermion-antifermion dark matter pair into two dark photons in the center-of-mass frame. The grey shaded loop denotes that the resummation of the infinitely many ladder diagrams has been taken into account.

F.2 Sommerfeld-effect: Bethe–Salpeter ansatz

We consider once again annihilations at order α^2 and $n_f = 0$ in the center-of-mass frame, but now we resum the ladder diagrams with soft-photon exchanges, see the grey shaded loop in figure F.1, by means of the Bethe–Salpeter equation for the composite fermion-antifermion four-point Green function. The result for the S-matrix amplitude in momentum space reads

$$\mathcal{M}^{\rm Se}_{\rm ann}(\boldsymbol{p},\boldsymbol{k}) = \int \frac{d^3p'}{(2\pi)^3}\, \mathcal{M}_{\rm ann}(\boldsymbol{p}',\boldsymbol{k})\Psi_{\boldsymbol{p}}(\boldsymbol{p}') \tag{F.5}$$

where the superscript Se denotes that the resummation has been taken into account, and $\mathcal{M}_{\rm ann}(\boldsymbol{p}',\boldsymbol{k})$ is the S-matrix for annihilations without resummation - it corresponds to the amplitude $\mathcal{M}_{\rm ann}$ defined in section F.1 - and the relative momentum $\boldsymbol{p}'$ of the internal propagators is taken on-shell. [73,209] From eq. (F.5) it can be seen that the Sommerfeld-enhanced annihilation amplitude is written as a convolution of the free annihilation amplitude and the Bethe-Salpeter wavefunction, which in the non-relativistic limit is the momentum-space Coulomb wavefunction of the heavy pair above threshold, first derived in ref. [210]. It is the Fourier transform of the scattering-state wavefunction,[3]

$$\begin{aligned}
\Psi_{\boldsymbol{p}}(\boldsymbol{p}') &= \int d^3r\ \Psi_{\boldsymbol{p}}(\boldsymbol{r})e^{-i\boldsymbol{p}'\cdot\boldsymbol{r}} \\
&= \sum_{\ell=0}^{\infty}\sum_{m=-\ell}^{\ell} Y_\ell^m(\hat{\boldsymbol{p}}')Y_\ell^{m,*}(\hat{\boldsymbol{p}})\left[4\pi\int_0^\infty dr\ r^2 j_\ell(p'r)R_{p,\ell}(r)\right] \\
&= \sum_{\ell=0}^{\infty}\sum_{m=-\ell}^{\ell} Y_\ell^m(\hat{\boldsymbol{p}}')Y_\ell^{m,*}(\hat{\boldsymbol{p}})\mathcal{R}_{p,\ell}(p')\,,
\end{aligned} \tag{F.6}$$

[3] In order to get to the last line of (F.6), we inserted in the first line of eq. (F.6) the partial-wave decomposition of the scattering-state $\Psi_{\boldsymbol{p}}(\boldsymbol{r}) = \sum_{\ell=0}^{\infty}\sum_{m=-\ell}^{\ell} i^\ell R_{p,\ell}(r)Y_\ell^m(\hat{\boldsymbol{r}})Y_\ell^m(\hat{\boldsymbol{p}})$ and of the plane wave $e^{i\boldsymbol{p}\cdot\boldsymbol{r}} = \sum_{\ell=0}^{\infty}\sum_{m=-\ell}^{\ell} i^\ell R_{p,\ell}(r)\big|_{\alpha=0}Y_\ell^m(\hat{\boldsymbol{r}})Y_\ell^m(\hat{\boldsymbol{p}}) = 4\pi\sum_{\ell=0}^{\infty}\sum_{m=-\ell}^{\ell} i^\ell j_\ell(pr)Y_\ell^m(\hat{\boldsymbol{r}})Y_\ell^m(\hat{\boldsymbol{p}})$, and used the orthonormality relation $\int d\Omega_{\hat{\boldsymbol{r}}}\ Y_\ell^m(\hat{\boldsymbol{r}})Y_{\ell'}^{m'}(\hat{\boldsymbol{r}}) = \delta_{\ell\ell'}\delta_{mm'}$ for the spherical harmonics.

which is now expanded into partial waves, and $j_\ell(pr)$ are the spherical Bessel functions of the first kind. From the definition of $\mathcal{R}_{p,\ell}(p')$ in (F.6), it follows for the radial scattering-state wavefunction that[4]

$$R_{p,\ell}(r) = \int_0^\infty \frac{dp'}{2\pi^2}\; p'^2 j_\ell(p'r)\mathcal{R}_{p,\ell}(p')\,. \tag{F.7}$$

We can decompose the free annihilation amplitude in a similar way, i.e.[5]

$$\mathcal{M}_{\text{ann}}(\boldsymbol{p}', \boldsymbol{k}) = \sum_{\ell=0}^{\infty}\sum_{m=-\ell}^{\ell} Y_\ell^m(\hat{\boldsymbol{k}})Y_\ell^{m,*}(\hat{\boldsymbol{p}}')\mathcal{M}_{\text{ann}}^\ell(p', k)\,, \tag{F.8}$$

and obtain for the resummed annihilation amplitude, upon inserting (F.6) and (F.8) into equation (F.5) the following decomposition in partial-wave amplitudes:[6]

$$\mathcal{M}_{\text{ann}}^{\text{Se}}(\boldsymbol{p}, \boldsymbol{k}) = \sum_{\ell=0}^{\infty}\mathcal{M}_{\text{ann}}^{\ell,\text{Se}} = \sum_{\ell=0}^{\infty}\sum_{m=-\ell}^{\ell} Y_\ell^m(\hat{\boldsymbol{k}})Y_\ell^{m,*}(\hat{\boldsymbol{p}})\int_0^\infty \frac{dp'}{(2\pi)^3}\; p'^2\mathcal{M}_{\text{ann}}^\ell(p', k)\mathcal{R}_{p,\ell}(p')\,, \tag{F.9}$$

where we have performed the angular $\Omega_{\hat{\boldsymbol{p}}'}$-integration using the orthonormality relation for the spherical harmonics $Y_\ell^m(\boldsymbol{p}')$. One could in principle drop the $k = |\boldsymbol{k}|$-dependence in the partial scattering amplitude $\mathcal{M}_{\text{ann}}^\ell$ inside the integral in eq. (F.9), since $k = E = \sqrt{M^2 + p'^2} = k(p')$ due to energy-momentum conservation at the vertices. Likewise for the k-dependence on the left-hand side, i.e. $\mathcal{M}_{\text{ann}}^{\text{Se}} = \mathcal{M}_{\text{ann}}^{\text{Se}}(\boldsymbol{p}, \hat{\boldsymbol{k}})$. It can be advantageous to decompose the S-matrix into partial-wave amplitudes as in (F.9), because the entire angular dependencies are then factored out, which is only possible for rotationally symmetric potentials, and the remaining effort is in the computation of the one-dimensional momentum integral as soon as $\mathcal{M}_{\text{ann}}^\ell$ and $\mathcal{R}_{p,\ell}$ are known. This, however, can be a difficult task. In case of the Coulomb potential, it is known that the radial scattering-state wavefunction in momentum space possesses a collinear singularity due to the long-range behaviour of the massless dark photon [210]. This holds also for the individual partial waves in momentum space, i.e. $\mathcal{R}_{p,\ell}(p')$, which can be shown by rewriting the spherical Bessel function of the first kind in terms of the confluent hypergeometric function,[7] and inserting it together with the ℓth radial wavefunction in position

[4]Equation (F.7) can be proven to be consistent by inserting it into the definition for $\mathcal{R}_{p,\ell}(p')$ and using the orthogonality relation $\int_0^\infty dr\, r^2 j_\ell(pr)j_\ell(p'r) = \pi\delta(p'-p)/(2p^2)$.

[5]Equation (F.8) can be checked straightforwardly to hold if soft-scale resummation is discarded: $\psi_{\boldsymbol{p}}^{\alpha=0}(\boldsymbol{p}') = \int d^3r\; \psi_{\boldsymbol{p}}^{\alpha=0}(\boldsymbol{r})e^{-i\boldsymbol{p}'\cdot\boldsymbol{r}} = \int d^3r\; e^{i(\boldsymbol{p}-\boldsymbol{p}')\cdot\boldsymbol{r}} = (2\pi)^3\delta^3(\boldsymbol{p}-\boldsymbol{p}')$, which, upon plugging into (F.5), gives a consistency check $\mathcal{M}_{\text{ann}}^{\text{Se},\alpha=0} = \mathcal{M}_{\text{ann}}$.

[6]One can check that the decomposition in (F.9) is consistent when long-range interactions are absent, i.e. by setting α to zero: $\mathcal{R}_{p,\ell}^{\alpha=0}(p') = 4\pi\int_0^\infty dr\, r^2 j_\ell(p'r)R_{p,\ell}(r)\big|_{\alpha=0} = (4\pi)^2\int_0^\infty dr\, r^2 j_\ell(p'r)j_\ell(pr) = (2\pi)^3\delta(p'-p)/p^2$, then plugging into the integral in (F.9) gives $\mathcal{M}_{\text{ann}}^{\text{Se},\alpha=0} = \mathcal{M}_{\text{ann}}$.

[7]To be more explicit, we use the relation

$$j_\ell(p'r) = \frac{\sqrt{\pi}}{2}\left(\frac{p'r}{2}\right)^\ell \frac{\exp(ip'r)}{\Gamma(\ell+3/2)}\;{}_1F_1(\ell+1, 2\ell+2, -2ip'r)\,.$$

space (to be read out from eq. (C.4)) into $\mathcal{R}_{p,\ell}$. It reads

$$\mathcal{R}_{p,\ell}(p') = \frac{(4\pi)^2}{\Gamma\left(\ell+\frac{3}{2}\right)}\sqrt{\frac{2\pi/(a_0 p)}{1-e^{-2\pi/(a_o p)}}}\frac{\sqrt{\pi}}{2}\frac{(pp')^\ell}{(2\ell+1)!}\prod_{\kappa=1}^{\ell}\sqrt{\kappa^2+(a_0 p)^{-2}}$$
$$\times\int_0^\infty dr\; r^{2\ell+2}e^{i(p'+p)r}\;{}_1F_1(\ell+1,2\ell+2,-2ip'r)\;{}_1F_1(\ell+1-i/(a_0 p),2\ell+2,-2ipr)\,, \tag{F.10}$$

where the integral in the second line of (F.10) resembles one of the two integrals in equation (C.52).[8] The analytic result of the integral in (F.10) can be read off directly from the eqs. (C.53) and (C.54), and hence the Coulomb wavefunction in momentum space possesses the very same collinear divergence as the continuum dipole matrix element for a transition between two scattering states of momenta $\boldsymbol{p}$ and $\boldsymbol{p}'$. It can therefore be regularized in the very same manner as the matrix element, and we can expand around the collinear singularity $p' \approx p$, and obtain similar divergent terms $((p'-p)-i\epsilon)^{-1}$ and $((p'-p)-i\epsilon)^{-2}$. We refer the reader to the following refs. [211–213], where the authors regularize the momentum-space Coulomb wavefunction and partial waves with equivalent methods.

There is, however, a way to circumvent the collinear singularity $p' \approx p$ in $\mathcal{R}_{p,\ell}(p')$ that would spoil the integration over p' in (F.9). Following the arguments in refs. [209, 214], we assume that the free partial-wave amplitude $\mathcal{M}^\ell_{\rm ann}(p')$ can be Taylor expanded in powers of the relative velocity $v'_{\rm rel} \sim p'/M \ll 1$ of the annihilating non-relativistic fermion-antifermion pair,[9]

$$\mathcal{M}^\ell_{\rm ann}(p') = c_\ell\frac{p'^\ell}{M^\ell} + \frac{c_{\ell+2}}{2}\frac{p'^{\ell+2}}{M^{\ell+2}} + \ldots \equiv \sum_{n=0}^{\infty}\frac{\mathcal{C}_{\ell+2n}}{M^{\ell+2n}}p'^{\ell+2n}\,, \tag{F.11}$$

where the dimensionless coefficients $\mathcal{C}_{\ell+2n}$ depend on the coupling α and on the spin or polarization, but we are not interested in the explicit form of them. Instead we recognize that the polynomials $p'^{\ell+2n}$ can be of help in transforming the integral in (F.9) into a higher order derivative acting on the ℓth radial wavefunction in position space. According to ref. [209], we can write

$$\int_0^\infty\frac{dp'}{(2\pi)^3}\;p'^2\mathcal{M}^\ell_{\rm ann}(p',k)\mathcal{R}_{p,\ell}(p') = \sum_{n=0}^{\infty}\frac{\mathcal{C}_{\ell+2n}}{M^{\ell+2n}}\int_0^\infty\frac{dp'}{(2\pi)^3}\;p'^{\ell+2n+2}\mathcal{R}_{p,\ell}(p')$$
$$= \frac{1}{(2\pi)^3}\sum_{n=0}^{\infty}\frac{\mathcal{C}_{\ell+2n}}{M^{\ell+2n}}\frac{2^n n!(2\ell+2n+1)!!}{(-1)^n(\ell+2n)!}2\pi^2\frac{\partial^{\ell+2n}}{\partial r^{\ell+2n}}R_{p,\ell}(r)\bigg|_{r=0}\,, \tag{F.12}$$

[8] In fact the integral in (F.10) differs from the first integral in (C.52) only because of the first entry in the confluent hypergeometric function in the first term of the third line in (C.52), i.e. $\ell+1 \longleftrightarrow \ell+2-i/(a_0 p')$.

[9] In (F.11) we take into account that for a Coulombic potential the ℓth partial amplitude scales as $v^\ell_{\rm rel}$ at zeroth order in the non-relativistic expansion. Then for fixed orbital quantum number ℓ, higher order corrections come with powers of $2n$ in $v_{\rm rel}$, where n is a positive integer counting the order of accuracy in the expansion.

which can be checked straightforwardly upon inserting (F.7) into the second line of (F.12), and

$$\frac{\partial^{\ell+2n}}{\partial r^{\ell+2n}} j_\ell(p'r) = p'^{\ell+2n} \frac{\partial^{\ell+2n}}{\partial (p'r)^{\ell+2n}} j_\ell(p'r) = p'^{\ell+2n} \left[\frac{(-1)^n (\ell+2n)!}{2^n n! (2n+2\ell+1)!!} + \mathcal{O}(p'r) \right] . \tag{F.13}$$

Finally, we can write for the Sommerfeld-resummed amplitude (F.9), corresponding to the annihilation of a non-relativistic fermion-antifermion pair above threshold with relative momentum $\boldsymbol{p}$ in the center-of-mass frame:

$$\begin{aligned} \mathcal{M}_{\rm ann}^{\rm Se}(\boldsymbol{p}, \hat{\boldsymbol{k}}) &= \sum_{\ell=0}^{\infty} \mathcal{M}_{\rm ann}^{\ell,\rm Se}(\boldsymbol{p}, \hat{\boldsymbol{k}}) \\ &= \sum_{\ell=0}^{\infty} \sum_{m=-\ell}^{\ell} Y_\ell^m(\hat{\boldsymbol{k}}) Y_\ell^{m,*}(\hat{\boldsymbol{p}}) \sum_{n=0}^{\infty} \frac{\mathcal{C}_{\ell+2n}}{M^{\ell+2n}} \frac{(-1)^n}{4\pi} 2^n n! \frac{(2\ell+2n+1)!!}{(\ell+2n)!} \frac{\partial^{\ell+2n}}{\partial r^{\ell+2n}} R_{p,\ell}(r) \bigg|_{r=0} , \end{aligned} \tag{F.14}$$

which is now regular. Once the coefficients $\mathcal{C}_{\ell+2n}$ are known, the residual computational task is on the derivatives on the ℓth radial wavefunction, evaluated at $r = 0$, and one can include relativistic corrections up to the desired accuracy in n for each partial wave. The absolute value squared of (F.14), $|\mathcal{M}_{\rm ann}^{\rm Se}|^2$, can eventually be inserted into (F.1) or (F.2) in order to derive the Sommerfeld-enhanced annihilation cross section.

References

[1] G. Arcadi, M. Dutra, P. Ghosh, M. Lindner, Y. Mambrini, M. Pierre et al., *The waning of the WIMP? A review of models, searches, and constraints*, *Eur. Phys. J. C* **78** (2018) 203 [1703.07364].

[2] J. R. Ellis, J. S. Hagelin, D. V. Nanopoulos, K. A. Olive and M. Srednicki, *Supersymmetric Relics from the Big Bang*, *Nucl. Phys. B* **238** (1984) 453.

[3] G. Jungman, M. Kamionkowski and K. Griest, *Supersymmetric dark matter*, *Phys. Rept.* **267** (1996) 195 [hep-ph/9506380].

[4] R. Catena and L. Covi, *SUSY dark matter(s)*, *Eur. Phys. J. C* **74** (2014) 2703 [1310.4776].

[5] A. De Simone, G. F. Giudice and A. Strumia, *Benchmarks for Dark Matter Searches at the LHC*, *JHEP* **06** (2014) 081 [1402.6287].

[6] M. Garny, A. Ibarra and S. Vogl, *Signatures of Majorana dark matter with t-channel mediators*, *Int. J. Mod. Phys. D* **24** (2015) 1530019 [1503.01500].

[7] A. Albert et al., *Towards the next generation of simplified Dark Matter models*, *Phys. Dark Univ.* **16** (2017) 49 [1607.06680].

[8] Planck collaboration, N. Aghanim et al., *Planck 2018 results. I. Overview and the cosmological legacy of Planck*, *Astron. Astrophys.* **641** (2020) A1 [1807.06205].

[9] G. Bertone, D. Hooper and J. Silk, *Particle dark matter: Evidence, candidates and constraints*, *Phys. Rept.* **405** (2005) 279 [hep-ph/0404175].

[10] J. L. Feng, *Dark Matter Candidates from Particle Physics and Methods of Detection*, *Ann. Rev. Astron. Astrophys.* **48** (2010) 495 [1003.0904].

[11] N. Brambilla, A. Pineda, J. Soto and A. Vairo, *Effective field theories for heavy quarkonium*, *Rev. Mod. Phys.* **77** (2005) 1423 [hep-ph/0410047].

[12] M. Pospelov, A. Ritz and M. B. Voloshin, *Secluded WIMP Dark Matter*, *Phys. Lett. B* **662** (2008) 53 [0711.4866].

[13] M. Duerr, F. Kahlhoefer, K. Schmidt-Hoberg, T. Schwetz and S. Vogl, *How to save the WIMP: global analysis of a dark matter model with two s-channel mediators*, *JHEP* **09** (2016) 042 [1606.07609].

[14] J. A. Evans, S. Gori and J. Shelton, *Looking for the WIMP Next Door*, *JHEP* **02** (2018) 100 [1712.03974].

[15] B. von Harling and K. Petraki, *Bound-state formation for thermal relic dark matter and unitarity*, *JCAP* **1412** (2014) 033 [1407.7874].

[16] M. Beneke, C. Hellmann and P. Ruiz-Femenia, *Heavy neutralino relic abundance with Sommerfeld enhancements - a study of pMSSM scenarios*, *JHEP* **03** (2015) 162 [1411.6930].

[17] K. Petraki, M. Postma and J. de Vries, *Radiative bound-state-formation cross-sections for dark matter interacting via a Yukawa potential*, *JHEP* **04** (2017) 077 [1611.01394].

[18] S. Kim and M. Laine, *On thermal corrections to near-threshold annihilation*, *JCAP* **1701** (2017) 013 [1609.00474].

[19] M. Beneke, A. Bharucha, F. Dighera, C. Hellmann, A. Hryczuk, S. Recksiegel et al., *Relic density of wino-like dark matter in the MSSM*, *JHEP* **03** (2016) 119 [1601.04718].

[20] S. Biondini and M. Laine, *Re-derived overclosure bound for the inert doublet model*, *JHEP* **08** (2017) 047 [1706.01894].

[21] J. Harz and K. Petraki, *Radiative bound-state formation in unbroken perturbative non-Abelian theories and implications for dark matter*, *JHEP* **07** (2018) 096 [1805.01200].

[22] S. Biondini and M. Laine, *Thermal dark matter co-annihilating with a strongly interacting scalar*, *JHEP* **04** (2018) 072 [1801.05821].

[23] T. Binder, L. Covi and K. Mukaida, *Dark Matter Sommerfeld-enhanced annihilation and Bound-state decay at finite temperature*, *Phys. Rev.* **D98** (2018) 115023 [1808.06472].

[24] R. Oncala and K. Petraki, *Dark matter bound states via emission of scalar mediators*, *JHEP* **01** (2019) 070 [1808.04854].

[25] R. Oncala and K. Petraki, *Dark matter bound state formation via emission of a charged scalar*, *JHEP* **02** (2020) 036 [1911.02605].

[26] J. Harz and K. Petraki, *Higgs-mediated bound states in dark-matter models*, *JHEP* **04** (2019) 130 [1901.10030].

[27] T. Binder, K. Mukaida and K. Petraki, *Rapid bound-state formation of Dark Matter in the Early Universe*, *Phys. Rev. Lett.* **124** (2020) 161102 [1910.11288].

[28] S. Biondini, S. Kim and M. Laine, *Non-relativistic susceptibility and a dark matter application*, *JCAP* **10** (2019) 078 [1908.07541].

[29] T. Binder, B. Blobel, J. Harz and K. Mukaida, *Dark matter bound-state formation at higher order: a non-equilibrium quantum field theory approach*, *JHEP* **09** (2020) 086 [2002.07145].

[30] S. Biondini and V. Shtabovenko, *Bound-state formation, dissociation and decays of darkonium with potential non-relativistic Yukawa theory for scalar and pseudoscalar mediators*, *JHEP* **03** (2022) 172 [2112.10145].

[31] S. Biondini and V. Shtabovenko, *Non-relativistic and potential non-relativistic effective field theories for scalar mediators*, *JHEP* **08** (2021) 114 [2106.06472].

[32] T. Binder, M. Garny, J. Heisig, S. Lederer and K. Urban, *Excited bound states and their role in dark matter production*, *Phys. Rev. D* **108** (2023) 095030 [2308.01336].

[33] J. D. March-Russell and S. M. West, *WIMPonium and Boost Factors for Indirect Dark Matter Detection*, *Phys. Lett. B* **676** (2009) 133 [0812.0559].

[34] R. Laha, *Directional detection of dark matter in universal bound states*, *Phys. Rev. D* **92** (2015) 083509 [1505.02772].

[35] L. Pearce, K. Petraki and A. Kusenko, *Signals from dark atom formation in halos*, *Phys. Rev. D* **91** (2015) 083532 [1502.01755].

[36] M. Cirelli, P. Panci, K. Petraki, F. Sala and M. Taoso, *Dark Matter's secret liaisons: phenomenology of a dark U(1) sector with bound states*, *JCAP* **1705** (2017) 036 [1612.07295].

[37] H. An, M. B. Wise and Y. Zhang, *Strong CMB Constraint On P-Wave Annihilating Dark Matter*, *Phys. Lett. B* **773** (2017) 121 [1606.02305].

[38] A. Mitridate, M. Redi, J. Smirnov and A. Strumia, *Cosmological Implications of Dark Matter Bound States*, *JCAP* **1705** (2017) 006 [1702.01141].

[39] S. Biondini and S. Vogl, *Coloured coannihilations: Dark matter phenomenology meets non-relativistic EFTs*, *JHEP* **02** (2019) 016 [1811.02581].

[40] I. Baldes, F. Calore, K. Petraki, V. Poireau and N. L. Rodd, *Indirect searches for dark matter bound state formation and level transitions*, *SciPost Phys.* **9** (2020) 068 [2007.13787].

[41] M. Garny and J. Heisig, *Bound-state effects on dark matter coannihilation: Pushing the boundaries of conversion-driven freeze-out*, *Phys. Rev. D* **105** (2022) 055004 [2112.01499].

[42] M. Becker, E. Copello, J. Harz, K. A. Mohan and D. Sengupta, *Impact of Sommerfeld effect and bound state formation in simplified t-channel dark matter models*, *JHEP* **08** (2022) 145 [2203.04326].

[43] M. Baumgart, N. L. Rodd, T. R. Slatyer and V. Vaidya, *The Quintuplet Annihilation Spectrum*, 2309.11562.

[44] S. Biondini, J. Bollig and S. Vogl, *Indirect detection of dark matter with (pseudo)-scalar interactions*, 2308.14594.

[45] S. Biondini, T. A. Chowdhury and S. Saad, *Non-perturbative effects for dark sectors with QCD portals*, *JHEP* **08** (2023) 002 [2306.09428].

[46] W. E. Caswell and G. P. Lepage, *Effective Lagrangians for Bound State Problems in QED, QCD, and Other Field Theories*, *Phys. Lett.* **167B** (1986) 437.

[47] A. Pineda and J. Soto, *Potential NRQED: The Positronium case*, *Phys. Rev.* **D59** (1999) 016005 [hep-ph/9805424].

[48] N. Brambilla, J. Ghiglieri, A. Vairo and P. Petreczky, *Static quark-antiquark pairs at finite temperature*, *Phys. Rev.* **D78** (2008) 014017 [0804.0993].

[49] M. A. Escobedo and J. Soto, *Non-relativistic bound states at finite temperature (I): The Hydrogen atom*, *Phys. Rev. A* **78** (2008) 032520 [0804.0691].

[50] N. Brambilla, M. A. Escobedo, J. Ghiglieri and A. Vairo, *Thermal width and gluo-dissociation of quarkonium in pNRQCD*, *JHEP* **12** (2011) 116 [1109.5826].

[51] S. Biondini, N. Brambilla, G. Qerimi and A. Vairo, *Effective field theories for dark matter pairs in the early universe: cross sections and widths*, *JHEP* **07** (2023) 006 [2304.00113].

[52] S. Biondini, N. Brambilla, G. Qerimi and A. Vairo, *Effective field theories for dark matter pairs in the early universe: center-of-mass recoil effects*, *JHEP* **07** (2024) 021 [2402.12787].

[53] S. Biondini, N. Brambilla, G. Qerimi and A. Vairo, *Effective Field Theories for Dark Matter Pairs in the Early Universe*, *LHEP* **2023** (2023) 375 [2304.07180].

[54] S. Biondini, N. Brambilla, G. Qerimi and A. Vairo, *Center-of-mass recoil effects on the annihilation and formation of dark matter bound pairs*, *PoS* **EPS-HEP2023** (2024) 112 [2402.14199].

[55] S. Biondini, N. Brambilla, A. Dashko, G. Qerimi and A. Vairo, *Effective field theories for dark matter pairs in the early universe: Debye mass effects*, 2501.03327.

[56] M. Laine and A. Vuorinen, *Basics of Thermal Field Theory*, vol. 925. Springer, 2016, 10.1007/978-3-319-31933-9, [1701.01554].

[57] P. Gondolo and G. Gelmini, *Cosmic abundances of stable particles: Improved analysis*, *Nucl. Phys.* **B360** (1991) 145.

[58] J. D. Bjorken, *Highly relativistic nucleus-nucleus collisions: The central rapidity region*, *Phys. Rev. D* **27** (1983) 140.

[59] N. Brambilla, M. A. Escobedo, J. Soto and A. Vairo, *Heavy quarkonium suppression in a fireball*, *Physical Review D* **97** (2018) .

[60] R. J. Scherrer, *How slowly can the early universe expand?*, *Physical Review D* **106** (2022) .

[61] B. W. Lee and S. Weinberg, *Cosmological Lower Bound on Heavy Neutrino Masses*, *Phys. Rev. Lett.* **39** (1977) 165.

[62] K. Griest and D. Seckel, *Three exceptions in the calculation of relic abundances*, *Phys. Rev.* **D43** (1991) 3191.

[63] Particle Data Group collaboration, R. L. Workman et al., *Review of Particle Physics*, *PTEP* **2022** (2022) 083C01.

[64] C. Patrignani, *Review of particle physics*, *Chinese Physics C* **40** (2016) 100001.

[65] A. Sommerfeld, *Über die Beugung und Bremsung der Elektronen*, *Ann. Phys.(1931)* **403** (1931) .

[66] J. Hisano, S. Matsumoto, M. M. Nojiri and O. Saito, *Non-perturbative effect on dark matter annihilation and gamma ray signature from galactic center*, *Phys. Rev. D* **71** (2005) 063528 [hep-ph/0412403].

[67] J. L. Feng, M. Kaplinghat, H. Tu and H.-B. Yu, *Hidden Charged Dark Matter*, *JCAP* **0907** (2009) 004 [0905.3039].

[68] J. Ellis, F. Luo and K. A. Olive, *Gluino Coannihilation Revisited*, *JHEP* **09** (2015) 127 [1503.07142].

[69] K. Petraki, M. Postma and J. de Vries, *Radiative bound-state-formation cross-sections for dark matter interacting via a yukawa potential*, *Journal of High Energy Physics* **2017** (2017) .

[70] H. An, M. B. Wise and Y. Zhang, *Effects of bound states on dark matter annihilation*, *Physical Review D* **93** (2016) .

[71] H. An, M. B. Wise and Y. Zhang, *Strong cmb constraint on p-wave annihilating dark matter*, *Physics Letters B* **773** (2017) 121–124.

[72] S. Biondini, *Bound-state effects for dark matter with Higgs-like mediators*, *JHEP* **06** (2018) 104 [1805.00353].

[73] K. Petraki, M. Postma and M. Wiechers, *Dark-matter bound states from feynman diagrams*, *Journal of High Energy Physics* **2015** (2015) .

[74] D. Feldman, B. Kors and P. Nath, *Extra-weakly Interacting Dark Matter*, *Phys. Rev. D* **75** (2007) 023503 [hep-ph/0610133].

[75] P. Fayet, *U-boson production in e+ e- annihilations, psi and Upsilon decays, and Light Dark Matter*, *Phys. Rev. D* **75** (2007) 115017 [hep-ph/0702176].

[76] M. Goodsell, J. Jaeckel, J. Redondo and A. Ringwald, *Naturally Light Hidden Photons in LARGE Volume String Compactifications*, *JHEP* **11** (2009) 027 [0909.0515].

[77] D. E. Morrissey, D. Poland and K. M. Zurek, *Abelian Hidden Sectors at a GeV*, *JHEP* **07** (2009) 050 [0904.2567].

[78] S. Andreas, M. D. Goodsell and A. Ringwald, *Dark matter and dark forces from a supersymmetric hidden sector*, *Phys. Rev. D* **87** (2013) 025007 [1109.2869].

[79] B. Holdom, *Two U(1)'s and Epsilon Charge Shifts*, *Phys. Lett. B* **166** (1986) 196.

[80] R. Foot and X.-G. He, *Comment on Z Z-prime mixing in extended gauge theories*, *Phys. Lett. B* **267** (1991) 509.

[81] S. Koren and R. McGehee, *Freezing-in twin dark matter*, *Phys. Rev. D* **101** (2020) 055024 [1908.03559].

[82] M. A. Escobedo and J. Soto, *Non-relativistic bound states at finite temperature (II): the muonic hydrogen*, *Phys. Rev. A* **82** (2010) 042506 [1008.0254].

[83] E. Braaten and R. D. Pisarski, *Simple effective Lagrangian for hard thermal loops*, *Phys. Rev. D* **45** (1992) R1827.

[84] N. Brambilla, M. A. Escobedo, J. Ghiglieri, J. Soto and A. Vairo, *Heavy Quarkonium in a weakly-coupled quark-gluon plasma below the melting temperature*, *JHEP* **09** (2010) 038 [1007.4156].

[85] N. Brambilla, M. A. Escobedo, J. Ghiglieri and A. Vairo, *Thermal width and quarkonium dissociation by inelastic parton scattering*, *JHEP* **05** (2013) 130 [1303.6097].

[86] T. Kinoshita and M. Nio, *Radiative corrections to the muonium hyperfine structure: The $\alpha^2(z\alpha)$ correction*, *Phys. Rev. D* **53** (1996) 4909.

[87] P. Labelle, S. M. Zebarjad and C. P. Burgess, *Nonrelativistic qed and next-to-leading hyperfine splitting in positronium*, *Physical Review D* **56** (1997) 8053–8061.

[88] A. V. Manohar, *The HQET / NRQCD Lagrangian to order α/m^3*, *Phys. Rev.* **D56** (1997) 230 [hep-ph/9701294].

[89] M. E. Luke and A. V. Manohar, *Reparametrization invariance constraints on heavy particle effective field theories*, *Phys. Lett. B* **286** (1992) 348 [hep-ph/9205228].

[90] N. Brambilla, D. Gromes and A. Vairo, *Poincaré invariance constraints on NRQCD and potential NRQCD*, *Phys. Lett. B* **576** (2003) 314 [hep-ph/0306107].

[91] A. Pineda and J. Soto, *Matching at one loop for the four quark operators in NRQCD*, *Phys. Rev.* **D58** (1998) 114011 [hep-ph/9802365].

[92] A. Pineda and J. Soto, *Effective field theory for ultrasoft momenta in NRQCD and NRQED*, *Nucl. Phys. Proc. Suppl.* **64** (1998) 428 [hep-ph/9707481].

[93] A. Pineda and J. Soto, *The Lamb shift in dimensional regularization*, *Phys. Lett.* **B420** (1998) 391 [hep-ph/9711292].

[94] N. Brambilla, A. Pineda, J. Soto and A. Vairo, *Potential NRQCD: An Effective theory for heavy quarkonium*, *Nucl. Phys.* **B566** (2000) 275 [hep-ph/9907240].

[95] A. Barchielli, E. Montaldi and G. M. Prosperi, *On a Systematic Derivation of the Quark - Anti-quark Potential*, *Nucl. Phys. B* **296** (1988) 625.

[96] A. Barchielli, N. Brambilla and G. M. Prosperi, *Relativistic Corrections to the Quark - anti-Quark Potential and the Quarkonium Spectrum*, *Nuovo Cim. A* **103** (1990) 59.

[97] N. Brambilla, D. Gromes and A. Vairo, *Poincare invariance and the heavy quark potential*, *Phys. Rev. D* **64** (2001) 076010 [hep-ph/0104068].

[98] J. D. Cresser and S. M. Barnett, *The rate of spontaneous decay of a moving atom*, *Journal of Physics B: Atomic, Molecular and Optical Physics* **36** (2003) 1755.

[99] X. Yao and T. Mehen, *Quarkonium in-medium transport equation derived from first principles*, *Phys. Rev. D* **99** (2019) 096028 [1811.07027].

[100] G. T. Bodwin, E. Braaten and G. P. Lepage, *Rigorous QCD analysis of inclusive annihilation and production of heavy quarkonium*, *Phys. Rev.* **D51** (1995) 1125 [hep-ph/9407339].

[101] E. Braaten, *Introduction to the NRQCD factorization approach to heavy quarkonium*, in *3rd International Workshop on Particle Physics Phenomenology*, 11, 1996, hep-ph/9702225.

[102] A. Petrelli, M. Cacciari, M. Greco, F. Maltoni and M. L. Mangano, *NLO production and decay of quarkonium*, *Nucl. Phys. B* **514** (1998) 245 [hep-ph/9707223].

[103] A. Vairo, *A Theoretical review of heavy quarkonium inclusive decays*, *Mod. Phys. Lett.* **A19** (2004) 253 [hep-ph/0311303].

[104] N. Baro, F. Boudjema, G. Chalons and S. Hao, *Relic density at one-loop with gauge boson pair production*, *Phys. Rev.* **D81** (2010) 015005 [0910.3293].

[105] A. Chatterjee, M. Drees and S. Kulkarni, *Radiative Corrections to the Neutralino Dark Matter Relic Density - an Effective Coupling Approach*, *Phys. Rev.* **D86** (2012) 105025 [1209.2328].

[106] J. Harz, B. Herrmann, M. Klasen, K. Kovarik and Q. L. Boulc'h, *Neutralino-stop coannihilation into electroweak gauge and Higgs bosons at one loop*, *Phys. Rev.* **D87** (2013) 054031 [1212.5241].

[107] C. Hellmann and P. Ruiz-Femenía, *Non-relativistic pair annihilation of nearly mass degenerate neutralinos and charginos II. P-wave and next-to-next-to-leading order S-wave coefficients*, *JHEP* **08** (2013) 084 [1303.0200].

[108] P. Ciafaloni, D. Comelli, A. De Simone, E. Morgante, A. Riotto and A. Urbano, *The Role of Electroweak Corrections for the Dark Matter Relic Abundance*, *JCAP* **1310** (2013) 031 [1305.6391].

[109] G. Ovanesyan, N. L. Rodd, T. R. Slatyer and I. W. Stewart, *One-loop correction to heavy dark matter annihilation*, *Phys. Rev.* **D95** (2017) 055001 [1612.04814].

[110] S. Schmiemann, J. Harz, B. Herrmann, M. Klasen and K. Kovařík, *Squark-pair annihilation into quarks at next-to-leading order*, *Phys. Rev.* **D99** (2019) 095015 [1903.10998].

[111] S. Banerjee, F. Boudjema, N. Chakrabarty, G. Chalons and H. Sun, *Relic density of dark matter in the inert doublet model beyond leading order: The heavy mass case*, *Phys. Rev.* **D100** (2019) 095024 [1906.11269].

[112] P. A. M. Dirac, *On the Annihilation of Electrons and Protons*, *Proc. Cambridge Phil. Soc.* **26** (1930) 361.

[113] M. Beneke, C. Hellmann and P. Ruiz-Femenia, *Non-relativistic pair annihilation of nearly mass degenerate neutralinos and charginos I. General framework and S-wave annihilation*, *JHEP* **03** (2013) 148 [1210.7928].

[114] C. Hellmann and P. Ruiz-Femenía, *Non-relativistic pair annihilation of nearly mass degenerate neutralinos and charginos II. P-wave and next-to-next-to-leading order S-wave coefficients*, *JHEP* **08** (2013) 084 [1303.0200].

[115] N. Brambilla, E. Mereghetti and A. Vairo, *Electromagnetic quarkonium decays at order v7*, *Journal of High Energy Physics* **2006** (2006) 039.

[116] N. Brambilla, D. Eiras, A. Pineda, J. Soto and A. Vairo, *Inclusive decays of heavy quarkonium to light particles*, *Phys. Rev. D* **67** (2003) 034018 [hep-ph/0208019].

[117] N. Brambilla, E. Mereghetti and A. Vairo, *Hadronic quarkonium decays at order v**7*, *Phys. Rev. D* **79** (2009) 074002 [0810.2259].

[118] M. Berwein, N. Brambilla, S. Hwang and A. Vairo, *Poincaré invariance in NRQCD and potential NRQCD revisited*, *Phys. Rev. D* **99** (2019) 094008 [1811.05184].

[119] N. Brambilla, D. Eiras, A. Pineda, J. Soto and A. Vairo, *New predictions for inclusive heavy-quarkonium p-wave decays*, *Physical Review Letters* **88** (2001) .

[120] R. Iengo, *Sommerfeld enhancement: General results from field theory diagrams*, *JHEP* **05** (2009) 024 [0902.0688].

[121] S. Cassel, *Sommerfeld factor for arbitrary partial wave processes*, *J. Phys.* **G37** (2010) 105009 [0903.5307].

[122] J. Hisano, S. Matsumoto and M. M. Nojiri, *Unitarity and higher order corrections in neutralino dark matter annihilation into two photons*, *Phys. Rev. D* **67** (2003) 075014 [hep-ph/0212022].

[123] K. Blum, R. Sato and T. R. Slatyer, *Self-consistent Calculation of the Sommerfeld Enhancement*, *JCAP* **06** (2016) 021 [1603.01383].

[124] P. V. Landshoff and A. Rebhan, *Covariant gauges at finite temperature*, *Nucl. Phys. B* **383** (1992) 607 [hep-ph/9205235].

[125] M. A. Escobedo, J. Soto and M. Mannarelli, *Non-relativistic bound states in a moving thermal bath*, *Phys. Rev. D* **84** (2011) 016008 [1105.1249].

[126] R. Kobes and G. Semenoff, *Cutkosky rules for condensed-matter systems*, *Phys. Rev. B* **34** (1986) 4338.

[127] K. Petraki, M. Postma and M. Wiechers, *Dark-matter bound states from Feynman diagrams*, *JHEP* **06** (2015) 128 [1505.00109].

[128] T. Binder, K. Mukaida, B. Scheihing-Hitschfeld and X. Yao, *Non-Abelian electric field correlator at NLO for dark matter relic abundance and quarkonium transport*, *JHEP* **01** (2022) 137 [2107.03945].

[129] N. Brambilla, M. A. Escobedo, J. Ghiglieri, J. Soto and A. Vairo, *Heavy quarkonium in a weakly-coupled quark-gluon plasma below the melting temperature*, *Journal of High Energy Physics* **2010** (2010) .

[130] N. Brambilla, J. Ghiglieri, A. Vairo and P. Petreczky, *Static quark-antiquark pairs at finite temperature*, *Physical Review D* **78** (2008) .

[131] M. A. Escobedo, F. Giannuzzi, M. Mannarelli and J. Soto, *Heavy Quarkonium moving in a Quark-Gluon Plasma*, *Phys. Rev. D* **87** (2013) 114005 [1304.4087].

[132] H. A. Weldon, *Covariant Calculations at Finite Temperature: The Relativistic Plasma*, *Phys. Rev. D* **26** (1982) 1394.

[133] S. S. Costa and G. E. A. Matsas, *Temperature and relativity*, *Phys. Lett. A* **209** (1995) 155 [gr-qc/9505045].

[134] F. Brezinski and G. Wolschin, *Gluodissociation and Screening of υ States in PbPb Collisions at $\sqrt{s_{NN}} = 2.76$ TeV*, *Phys. Lett. B* **707** (2012) 534 [1109.0211].

[135] T. Binder, A. Filimonova, K. Petraki and G. White, *Saha equilibrium for metastable bound states and dark matter freeze-out*, *Phys. Lett. B* **833** (2022) 137323 [2112.00042].

[136] J. E. Juknevich, D. Melnikov and M. J. Strassler, *A Pure-Glue Hidden Valley I. States and Decays*, *JHEP* **07** (2009) 055 [0903.0883].

[137] J. E. Juknevich, *Pure-glue hidden valleys through the Higgs portal*, *JHEP* **08** (2010) 121 [0911.5616].

[138] K. K. Boddy, J. L. Feng, M. Kaplinghat and T. M. P. Tait, *Self-Interacting Dark Matter from a Non-Abelian Hidden Sector*, *Phys. Rev. D* **89** (2014) 115017 [1402.3629].

[139] J. M. Cline, Z. Liu, G. D. Moore and W. Xue, *Composite strongly interacting dark matter*, *Phys. Rev. D* **90** (2014) 015023 [1312.3325].

[140] T. Song, Y. Park, S. H. Lee and C.-Y. Wong, *The Thermal width of heavy quarkonia moving in quark gluon plasma*, *Phys. Lett. B* **659** (2008) 621 [0709.0794].

[141] N. Brambilla, A. Pineda, J. Soto and A. Vairo, *Effective-field theories for heavy quarkonium*, *Reviews of Modern Physics* **77** (2005) 1423–1496.

[142] N. Brambilla, S. Eidelman, B. K. Heltsley, R. Vogt, G. T. Bodwin, E. Eichten et al., *Heavy quarkonium: progress, puzzles, and opportunities*, *The European Physical Journal C* **71** (2011) .

[143] N. Brambilla, S. Eidelman, P. Foka, S. Gardner, A. S. Kronfeld, M. G. Alford et al., *Qcd and strongly coupled gauge theories: challenges and perspectives*, *The European Physical Journal C* **74** (2014) .

[144] S. Navas, C. Amsler, T. Gutsche, C. Hanhart, J. J. Hernández-Rey, C. Lourenço et al., *Review of particle physics ,* particle data group collaboration, *Phys. Rev. D* **110** (2024) 030001.

[145] G. T. Bodwin, E. Braaten and G. P. Lepage, *Rigorous qcd predictions for decays of p-wave quarkonia*, *Phys. Rev. D* **46** (1992) R1914.

[146] F. Maltoni, *Quarkonium phenomenology*, Ph. D. thesis, University of Pisa (1999) .

[147] S. El Hedri, A. Kaminska and M. de Vries, *A Sommerfeld Toolbox for Colored Dark Sectors*, *Eur. Phys. J. C* **77** (2017) 622 [1612.02825].

[148] S. Titard and F. J. Yndurain, *Rigorous QCD evaluation of spectrum and ground state properties of heavy q anti-q systems: With a precision determination of m(b) M(eta(b))*, *Phys. Rev. D* **49** (1994) 6007 [hep-ph/9310236].

[149] T. Binder, K. Mukaida, B. Scheihing-Hitschfeld and X. Yao, *Non-abelian electric field correlator at nlo for dark matter relic abundance and quarkonium transport*, *Journal of High Energy Physics* **2022** (2022) .

[150] N. Brambilla, M. A. Escobedo, J. Ghiglieri and A. Vairo, *Thermal width and quarkonium dissociation by inelastic parton scattering*, *Journal of High Energy Physics* **2013** (2013) .

[151] N. Brambilla, M. Escobedo, J. Ghiglieri and A. Vairo, *Thermal width and gluo-dissociation of quarkonium in pnrqcd*, *Journal of High Energy Physics* **2011** (2011) .

[152] N. Brambilla, M. A. Escobedo, J. Soto and A. Vairo, *Quarkonium suppression in heavy-ion collisions: an open quantum system approach*, *Phys. Rev.* **D96** (2017) 034021 [1612.07248].

[153] N. Brambilla, M. A. Escobedo, J. Soto and A. Vairo, *Heavy quarkonium suppression in a fireball*, *Phys. Rev.* **D97** (2018) 074009 [1711.04515].

[154] R. A. Bertlmann, W. Grimus and B. C. Hiesmayr, *An Open-quantum-system formulation of particle decay*, *Phys. Rev.* **A73** (2006) 054101 [quant-ph/0602116].

[155] E. Braaten, H. W. Hammer and G. P. Lepage, *Open Effective Field Theories from Deeply Inelastic Reactions*, *Phys. Rev. D* **94** (2016) 056006 [1607.02939].

[156] G. Lindblad, *On the Generators of Quantum Dynamical Semigroups*, *Commun. Math. Phys.* **48** (1976) 119.

[157] V. Gorini, A. Kossakowski and E. C. G. Sudarshan, *Completely Positive Dynamical Semigroups of N Level Systems*, *J. Math. Phys.* **17** (1976) 821.

[158] E. Braaten, H.-W. Hammer and G. P. Lepage, *Lindblad equation for the inelastic loss of ultracold atoms*, *Physical Review A* **95** (2017) .

[159] N. N. Bogoliubov, *Kinetic equations*, *Journal of Physics USSR* **10** (1946) 265.

[160] J. G. Kirkwood, *The statistical mechanical theory of transport processes I. general theory*, *The Journal of Chemical Physics* **14** (1946) 180.

[161] J. Yvon, *La Théorie Statistique des Fluides et l'Équation d'Etat, Actualités Scientifiques et Industrialles*, vol. 203. Hermann, Paris, 1935.

[162] M. Born and H. S. Green, *A general kinetic theory of liquids I. the molecular distribution functions*, *Proc. R. Soc. Lond.* **A** (1946) 10.

[163] X. Yao and T. Mehen, *Quarkonium semiclassical transport in quark-gluon plasma: factorization and quantum correction*, *Journal of High Energy Physics* **2021** (2021) .

[164] X. Yao, W. Ke, Y. Xu, S. A. Bass and B. Müller, *Coupled boltzmann transport equations of heavy quarks and quarkonia in quark-gluon plasma*, *Journal of High Energy Physics* **2021** (2021) .

[165] D.-L. Yang and X. Yao, *Quarkonium polarization in medium from open quantum systems and chromomagnetic correlators*, *Physical Review D* **110** (2024) .

[166] E. Wigner, *On the quantum correction for thermodynamic equilibrium*, *Phys. Rev.* **40** (1932) 749.

[167] I. F. Valtierra, A. B. Klimov, G. Leuchs and L. L. Sánchez-Soto, *Quasiprobability currents on the sphere*, *Phys. Rev. A* **101** (2020) 033803.

[168] R. J. Glauber, *Coherent and incoherent states of the radiation field*, *Phys. Rev.* **131** (1963) 2766.

[169] E. C. G. Sudarshan, *Equivalence of semiclassical and quantum mechanical descriptions of statistical light beams*, *Phys. Rev. Lett.* **10** (1963) 277.

[170] K. Usimi, *Some formal properties of the density matrix*, *Proceedings of the Physico-Mathematical Society of Japan. 3rd Series* **22** (1940) 264.

[171] P. Carruthers and F. Zachariasen, *Quantum Collision Theory with Phase Space Distribution Functions*, *Rev. Mod. Phys.* **55** (1983) 245.

[172] W. B. Case, *Wigner Functions and Weyl Transforms for Pedestrians*, *Am. J. Phys.* **76** (2008) 937.

[173] H. Breuer and F. Petruccione, *The Theory of Open Quantum Systems*. Oxford University Press, 2002.

[174] N. Brambilla, M. A. Escobedo, A. Vairo and P. Vander Griend, *Transport coefficients from in medium quarkonium dynamics*, *Phys. Rev. D* **100** (2019) 054025 [1903.08063].

[175] J. Hisano, S. Matsumoto, M. Nagai, O. Saito and M. Senami, *Non-perturbative effect on thermal relic abundance of dark matter*, *Phys. Lett. B* **646** (2007) 34 [hep-ph/0610249].

[176] M. Cirelli, A. Strumia and M. Tamburini, *Cosmology and Astrophysics of Minimal Dark Matter*, *Nucl. Phys.* **B787** (2007) 152 [0706.4071].

[177] M. Beneke, A. Bharucha, A. Hryczuk, S. Recksiegel and P. Ruiz-Femenia, *The last refuge of mixed wino-Higgsino dark matter*, *JHEP* **01** (2017) 002 [1611.00804].

[178] N. G. Deshpande and E. Ma, *Pattern of Symmetry Breaking with Two Higgs Doublets*, *Phys. Rev. D* **18** (1978) 2574.

[179] R. Barbieri, L. J. Hall and V. S. Rychkov, *Improved naturalness with a heavy Higgs: An Alternative road to LHC physics*, *Phys. Rev. D* **74** (2006) 015007 [hep-ph/0603188].

[180] L. Lopez Honorez, E. Nezri, J. F. Oliver and M. H. G. Tytgat, *The Inert Doublet Model: An Archetype for Dark Matter*, *JCAP* **02** (2007) 028 [hep-ph/0612275].

[181] L. Lopez Honorez and C. E. Yaguna, *A new viable region of the inert doublet model*, *JCAP* **01** (2011) 002 [1011.1411].

[182] Y. Akamatsu, *Heavy quark master equations in the Lindblad form at high temperatures*, *Phys. Rev. D* **91** (2015) 056002 [1403.5783].

[183] A. Rothkopf, *Heavy Quarkonium in Extreme Conditions*, *Phys. Rept.* **858** (2020) 1 [1912.02253].

[184] Y. Akamatsu, *Quarkonium in quark–gluon plasma: Open quantum system approaches re-examined*, *Prog. Part. Nucl. Phys.* **123** (2022) 103932 [2009.10559].

[185] N. Brambilla, M. Escobedo, M. Strickland, A. Vairo, P. V. Griend and J. H. Weber, *Bottomonium suppression in an open quantum system using the quantum trajectories method*, *Journal of High Energy Physics* **2021** (2021) .

[186] N. Brambilla, M. Escobedo, M. Strickland, A. Vairo, P. Vander Griend and J. H. Weber, *Bottomonium production in heavy-ion collisions using quantum trajectories: Differential observables and momentum anisotropy*, *Physical Review D* **104** (2021) .

[187] H. Ba Omar, M. Escobedo, A. Islam, M. Strickland, S. Thapa, P. Vander Griend et al., *Qtraj 1.0: A lindblad equation solver for heavy-quarkonium dynamics*, *Computer Physics Communications* **273** (2022) 108266.

[188] N. Brambilla, M. Escobedo, A. Islam, M. Strickland, A. Tiwari, A. Vairo et al., *Heavy quarkonium dynamics at next-to-leading order in the binding energy over temperature*, *Journal of High Energy Physics* **2022** (2022) .

[189] G. Arcadi, O. Lebedev, S. Pokorski and T. Toma, *Real Scalar Dark Matter: Relativistic Treatment*, *JHEP* **08** (2019) 050 [1906.07659].

[190] W. Gordon, *Zur berechnung der matrizen beim wasserstoffatom*, *Annalen der Physik* **394** (1929) 1031.

[191] M. Stobbe, *Zur quantenmechanik photoelektrischer prozesse*, *Annalen der Physik* **399** (1930) 661.

[192] J. L. Madajczyk and M. Trippenbach, *Singular part of the hydrogen dipole matrix element*, *Journal of Physics A: Mathematical and General* **22** (1989) 2369.

[193] V. Véniard and B. Piraux, *Continuum-continuum dipole transitions in femtosecond-laser-pulse excitation of atomic hydrogen*, *Phys. Rev. A* **41** (1990) 4019.

[194] S. D. Oh and R. H. Pratt, *Positiveness and monotonicity of continuum-continuum coulomb dipole matrix elements*, *Phys. Rev. A* **45** (1992) 1583.

[195] T. Mercouris, Y. Komninos, S. Dionissopoulou and C. A. Nicolaides, *Effects on observables of the singularity in the multiphoton free - free dipole matrix elements*, *Journal of Physics B: Atomic, Molecular and Optical Physics* **29** (1996) L13.

[196] Y. Komninos, T. Mercouris and C. A. Nicolaides, *Structure and calculation of field-induced free-free transition matrix elements in many-electron atoms*, *Phys. Rev. A* **86** (2012) 023420.

[197] S. J. van Enk, J. Zhang and P. Lambropoulos, *On the free - free dipole moment*, *Journal of Physics B: Atomic, Molecular and Optical Physics* **30** (1997) L17.

[198] I. S. Gradshteyn and I. M. Ryzhik, *Table of integrals, series, and products*. Amsterdam: Elsevier/Academic Press, 7th ed. ed., 2007.

[199] A. Quattropani, F. Bassani and S. Carillo, *Two-photon transitions to excited states in atomic hydrogen*, *Phys. Rev. A* **25** (1982) 3079.

[200] J. Ghiglieri, A. Kurkela, M. Strickland and A. Vuorinen, *Perturbative Thermal QCD: Formalism and Applications*, *Phys. Rept.* **880** (2020) 1 [2002.10188].

[201] J. I. Kapusta and C. Gale, *Finite-temperature field theory: Principles and applications*, Cambridge Monographs on Mathematical Physics. Cambridge University Press, 2011, 10.1017/CBO9780511535130.

[202] M. L. Bellac, *Thermal Field Theory*, Cambridge Monographs on Mathematical Physics. Cambridge University Press, 3, 2011, 10.1017/CBO9780511721700.

[203] J. S. Schwinger, *Brownian motion of a quantum oscillator*, *J. Math. Phys.* **2** (1961) 407.

[204] L. V. Keldysh, *Diagram technique for nonequilibrium processes*, *Zh. Eksp. Teor. Fiz.* **47** (1964) 1515.

[205] S. Carignano, C. Manuel and J. Soto, *Power corrections to the htl effective lagrangian of qed*, *Physics Letters B* **780** (2018) 308.

[206] M. Carrington, H. Defu and M. Thoma, *Equilibrium and non-equilibrium hard thermal loop resummation in the real time formalism*, *The European Physical Journal C* **7** (1999) 347.

[207] R. E. Cutkosky, *Singularities and discontinuities of feynman amplitudes*, *J. Math. Phys.* **1** (1960) 429.

[208] E. E. Salpeter and H. A. Bethe, *A relativistic equation for bound-state problems*, *Phys. Rev.* **84** (1951) 1232.

[209] S. Cassel, D. Ghilencea and G. Ross, *Electroweak and dark matter constraints on a in models with a hidden valley*, *Nuclear Physics B* **827** (2010) 256–280.

[210] E. Guth and C. J. Mullin, *Momentum representation of the coulomb scattering wave functions*, *Phys. Rev.* **83** (1951) 667.

[211] V. Eremenko, N. J. Upadhyay, L. Hlophe, F. M. Nunes, C. Elster, G. Arbanas et al., *Coulomb problem in momentum space without screening*, *Phys. Rev. C* **90** (2014) 014615.

[212] V. Eremenko, N. Upadhyay, I. Thompson, C. Elster, F. Nunes, G. Arbanas et al., *Coulomb wave functions in momentum space*, *Computer Physics Communications* **187** (2015) 195.

[213] N. Michel, *Precise coulomb wave functions for a wide range of complex l, η and z*, *Computer Physics Communications* **176** (2007) 232–249.

[214] S. El Hedri, A. Kaminska and M. de Vries, *A sommerfeld toolbox for colored dark sectors*, *The European Physical Journal C* **77** (2017) .